

Measurement of W bosons in p-Pb at 8.16 TeV and charmonia in Pb-Pb at 5.02 TeV with the CMS detector at the LHC

Mesure des bosons W en p-Pb à 8.16 TeV et
des charmonia en Pb-Pb à 5.02 TeV avec le
déTECTeur CMS auprès du LHC

Thèse de doctorat de l'Université de Paris-Saclay
préparée à École Polytechnique

École doctorale n°576
Particules, Hadrons, Énergie, Noyau, Instrumentation, Imagerie,
Cosmos et Simulation (PHENIICS)
Spécialité de doctorat: Physique hadronique

Thèse présentée et soutenue à l'ÉcolePolytechnique, le 8 octobre 2018, par

André Govinda Ståhl Leiton

Composition du Jury :

?????????????????????	?????????????????????	Président du Jury
Lydia Roos	LPNHE, Paris	Rapporteuse
Boris Hippolyte	IPHC, Strasbourg	Rapporteur
Albert de Roeck	University of Antwerp	Examinateur
Begoña de la Cruz Martínez	CIEMT, Madrid	Examinatrice
Carlos Salgado Lopez	Universidad de Santiago de Compostela	Examinateur
Sophie Henrot Versille	LAL, Orsay	Examinatrice
Raphaël Granier de Cassagnac	LLR, Palaiseau	Directeur de thèse

Titre : Mesure des bosons W en p-Pb à 8.16 TeV et des charmonia en Pb-Pb à 5.02 TeV avec le détecteur CMS auprès du LHC.

Mots clés : Boson W, charmonia, physique de ions lourds, plasma des quarks et gluons, CMS

Résumé :

Title : Measurement of W bosons in p-Pb at 8.16 TeV and charmonia in Pb-Pb at 5.02 TeV with the CMS detector at the LHC

Keywords : W boson, charmonia, heavy-ion physics, quark-gluon plasma, CMS

Abstract : Heavy ions are collided at the Large Hadron Collider at high energies, allowing to inspect the properties of nuclear matter and to produce the hot and dense state of deconfined matter known as the Quark-Gluon Plasma (QGP). In order to probe the nuclear matter effects present in heavy-ion collisions, this thesis study the production of two important hard probes: W bosons and charmonia (J/ψ and $\psi(2S)$ mesons).

The cold nuclear matter effects, associated to the nuclear modification of the parton distribution functions (PDFs), can be characterised by studying the formation of W bosons in heavy-ion collisions. The production of W bosons represents an important tool to asses the PDF modifications, which impact the initial hard scattering, since these bosons do not interact strongly with the collision-induced medium. The analysis of the W-boson production in p-Pb collisions at $\sqrt{s_{NN}} = 8.16$ TeV with the CMS detector is presented in the first part of this thesis. The results are in good agreement with PDF calculations including nuclear modifications, while they strongly disfavour the free-proton hypothesis at forward lepton rapidity. Since the measurements are more precise than the model calculations, the W-boson results have the potential to constrain the nuclear PDF parametrisations, which could eventually improve our understanding of the PDF effects on other hard probes, such as charmonia.

The production of charmonia is sensitive to the formation and evolution of the strongly-interacting medium formed in heavy-ion collisions, thus making of it an excellent probe of the QGP. The suppression or enhancement of the different charmonium states is considered a signature of the presence of the QGP. In this thesis, the production of prompt and nonprompt J/ψ mesons is measured in Pb-Pb collisions at $\sqrt{s_{NN}} = 5.02$ TeV. In addition, the modification of the $\psi(2S)$ mesons relative to J/ψ mesons is reported for the same collision system. The nuclear modification factor of charmonia is determined as a function of centrality, rapidity and transverse momentum p_T . The prompt J/ψ meson yields are suppressed in Pb-Pb collisions compared to binary-scaled p-p collisions, although a weaker suppression is observed at $3 < p_T < 6.5$ GeV/c in central collisions. The yields of b hadrons, probed by the nonprompt charmonia, are also suppressed over the full kinematic region measured, and a reduced suppression is observed at high p_T . Regarding the $\psi(2S)$ mesons, they are found to be more strongly suppressed than J/ψ mesons in Pb-Pb collisions.



TABLE OF CONTENTS

Table of Contents	v
	Page
Introduction	1
1 High energy nuclear physics	3
1.1 The strong interaction	3
1.1.1 The standard model	3
1.1.2 Quantum chromodynamics	5
1.1.3 Parton distribution functions	10
1.1.4 QCD phase diagram	13
1.2 Relativistic heavy-ion collisions	14
1.2.1 History of heavy-ion accelerators	15
1.2.2 Geometry of nucleus-nucleus collisions	17
1.2.3 Evolution of heavy-ion collisions	20
1.2.4 Experimental probes of the QGP	21
2 Experimental setup	35
2.1 The Large Hadron Collider	35
2.1.1 Accelerator complex	36
2.1.2 Detectors	37
2.1.3 Luminosity	39
2.1.4 LHC schedule	39
2.1.5 Heavy-ion schemes in 2015-2016	40
2.2 The Compact Muon Solenoid	41
2.2.1 Subdetectors	45
2.2.2 Trigger system	53
2.2.3 Reconstruction	60

TABLE OF CONTENTS

3 W-boson production in proton-lead collisions	65
3.1 Introduction	65
3.1.1 A brief history of the weak theory	66
3.1.2 The modern electroweak theory	69
3.1.3 Production of W bosons in p-Pb and decay into muons	71
3.1.4 Nuclear PDFs	74
3.1.5 Experimental results at LHC	80
3.2 Analysis	84
3.2.1 Dataset	84
3.2.2 Next-to-leading order simulations	86
3.2.3 Event selection	88
3.2.4 Correction for weak-boson transverse momentum	93
3.2.5 Corrections for missing transverse momentum	94
3.2.6 Signal efficiency	105
3.2.7 Signal extraction	114
3.2.8 Observables	123
3.2.9 Systematic uncertainties	126
3.3 Results	136
3.3.1 W-boson production in p-Pb at 8.16 TeV	136
3.3.2 Comparison with theoretical models	140
4 Charmonium production in lead-lead collisions	145
4.1 Introduction	145
4.1.1 Spectrum of charmonium states	145
4.1.2 Hadroproduction of charmonia	147
4.1.3 Charmonia in heavy-ion collisions	153
4.2 Analysis	159
4.2.1 Dataset	160
4.2.2 Charmonium simulations	161
4.2.3 Event selection	163
4.2.4 Extraction of prompt and nonprompt J/ψ mesons	168
4.2.5 Extraction of prompt $\psi(2S)/J/\psi$ ratio	180
4.2.6 Charmonium acceptance and efficiency	186
4.2.7 Systematic uncertainties of J/ψ -meson yields	192
4.2.8 Systematic uncertainties on the $\psi(2S)/J/\psi$ ratio	199

TABLE OF CONTENTS

4.3 Results	202
4.3.1 Nonprompt fraction of J/ψ mesons	202
4.3.2 Cross section of prompt and nonprompt J/ψ mesons	203
4.3.3 Nuclear modification factor of J/ψ mesons	205
4.3.4 Double ratio of prompt $\psi(2S)/J/\psi$ yields	209
Conclusion	213
A Results of the fits for the W boson analysis	215
B Analysis bins used in the charmonia analyses	219
Bibliography	225
List of Tables	249
List of Figures	253

INTRODUCTION

2 The progress made by the scientific community over the last century have pushed the
 3 boundaries of our understanding of the subatomic world and have led to the formulation
 4 of one the most successful theories of physics, the so-called Standard Model (SM) of
 5 particle physics. Even though the SM framework is able to describe, with great accuracy,
 6 the interactions and properties of most known particles, some fundamental phenomena
 7 are still not fully understood, such as the phase states of matter or the evolution of
 8 particles in a nuclear environment.

9 Under normal circumstances, the main constituents of matter, called partons (i.e.
 10 quarks and gluons), are confined by the strong nuclear force into hadrons. However, at
 11 high enough temperatures or densities, it is expected that matter undergoes a phase
 12 transition to a state where quarks and gluons become asymptotically free, known as the
 13 Quark Gluon Plasma (QGP). Such extreme state of matter is believed to have existed
 14 during the creation of the Universe and to be part of the core of neutron stars. To
 15 recreate the QGP in the laboratory, heavy ions are collided in accelerator facilities at
 16 high energies. The QGP can be probed in heavy-ion experiments by measuring different
 17 observables, such as the production yield of particles that interact strongly with the
 18 QGP medium (e.g. quarkonia, jets, ...). In addition, the environment present in a nucleus
 19 can also affect the production of particles produced in heavy-ion collisions, even in the
 20 absence of QGP. The measurement of electroweak particles that do not interact with
 21 the QGP medium (photons, Z and W bosons) allow to study the nuclear modification of
 22 Parton Distribution Functions (PDF). The PDFs of nuclei are crucial inputs to theory
 23 predictions for heavy-ion colliders and their precise determination with experimental
 24 data is indispensable for calculations of the initial stage of nucleus-nucleus reactions.

25 Three analyses are presented in this thesis. The first one measure the production of W
 26 bosons in p-Pb collisions at a center-of-mass energy per nucleon pair of $\sqrt{s_{\text{NN}}} = 8.16 \text{ TeV}$,
 27 with the goal to provide precise experimental constrains to the nuclear modifications of
 28 the quark PDFs. I am the *contact person* of the analysis and have conducted all the work
 29 except the tag-and-probe and the weak boson p_T corrections. I presented the preliminary

TABLE OF CONTENTS

30 results at the Quark Matter [1] and ICHEP [2] conferences in 2018. The work is expected
31 to be published in a peer-reviewed journal in the near future [3]. The second and third
32 analyses probe quark deconfinement in the QGP by measuring the J/ψ and $\psi(2S)$ (i.e.
33 charmonium) production in Pb-Pb collisions at $\sqrt{s_{NN}} = 5.02\text{ TeV}$. My main contributions
34 to the J/ψ and $\psi(2S)$ analyses include the optimization of the muon kinematic selection,
35 the signal extraction and the systematic uncertainties associated to the fitting. The
36 results of the $\psi(2S)$ and J/ψ analyses have been published in PRL [4] and EPJC [5],
37 respectively, and I presented them at the Hot Quarks 2016 [6] and EPS-HEP 2017 [7]
38 conferences.

39 The manuscript is organised as follows. The general concepts of the strong interac-
40 tions and heavy-ion collisions are introduced in Chapter 1. A brief description of the
41 main probes of the QGP concludes the chapter. Chapter 2 describes the experimental
42 apparatus, where the operational conditions of the Large Hadron Collider and character-
43 istics of the Compact Muon Solenoid detector are detailed. The chapter also describes the
44 trigger and reconstruction algorithms employed to select and process the data. Chapter 3
45 presents in details the samples generated, event selection, corrections to the missing
46 transverse momentum, estimation of the muon efficiency, signal extraction, systematic
47 uncertainties and results of the W -boson analysis, accompanied by a short introduction
48 on electroweak physics. The charmonium analysis in Pb-Pb collisions is exposed in Chap-
49 ter 4. The chapter contains details on the charmonium samples, the event selection, the
50 J/ψ efficiency estimation, the extraction of the J/ψ yields and the $\psi(2S)/J/\psi$ ratios, the
51 systematic uncertainties and the results, including a brief introduction to the physics of
52 charmonia in heavy-ion collisions.

HIGH ENERGY NUCLEAR PHYSICS

55 This chapter introduces some key concepts of high energy nuclear physics com-
56 mon to the analysis of the production of W bosons and charmonia in heavy-ion
57 collisions. The quantum field theory of the strong interactions is described in
58 Section 1.1. The state of hot dense hadronic matter, known as the quark-gluon plasma,
59 and the study of its properties in heavy-ion collisions are reviewed in Section 1.2.

60 1.1 The strong interaction

61 The strong interaction is one of the three fundamental interactions described by the
62 standard model of particle physics introduced in Section 1.1.1. Its underlying theory is
63 Quantum Chromodynamics (QCD) presented in Section 1.1.2. It binds quarks and gluons
64 in hadrons, which are distributed inside the hadron as described by PDFs (Section 1.1.3).
65 Depending on the temperature and density of the system, it is expected to exhibit a
66 complex phase diagram (Section 1.1.4).

67 1.1.1 The standard model

68 The standard model is a theoretical framework that describes the properties of elemen-
69 tary particles and their interactions. The SM was developed during the 20th century
70 through the collaborative effort of many physicists. According to the SM, the most ele-
71 mentary particles are fermions and bosons. Fermions are particles with half-integer spin

72 which behave according to Fermi-Dirac statistics formulated by Enrico Fermi [8] and
 73 Paul Dirac [9] in 1926. As a consequence, fermions are restricted by the Pauli exclusion
 74 principle [10] which dictates that two or more fermions with the same quantum numbers
 75 cannot occupy the same quantum state.

76 In addition, fermions can be classified as leptons or quarks. There are six leptons
 77 arranged in three "generations": the electron (e^-) and the electron neutrino (ν_e), the
 78 muon (μ^-) and the muon neutrino (ν_μ), and the tau (τ^-) and the tau neutrino (ν_τ).
 79 The neutrinos are electrically neutral and almost massless, while the other leptons
 80 have negative electric charge (-1) and sizeable masses. In the case of quarks, there are
 81 six "flavours" paired also in three generations of increasing mass. The up and down
 82 quarks belong to the first generation, while the more heavier quarks are included in the
 83 second generation (charm and strange quarks) and third generation (top and bottom
 84 quarks). The up (u), charm (c) and top (t) quarks have positive electric charge ($+2/3$)
 85 while the down (d), strange (s) and bottom (b) quarks have negative electric charge
 86 ($-1/3$). Each quark also carry another quantum number called colour charge that can
 87 have three different values labelled as red, green and blue. Moreover, each fermion has
 88 an associated antiparticle with the same mass but with opposite charges. The positron
 89 (e^+) is the antiparticle of the electron, while the name of the rest of antiparticles simply
 90 starts with the prefix "anti" (e.g. anti-quarks \bar{q} , anti-neutrinos $\bar{\nu}$ or anti-leptons ℓ^+).

91 The interactions between fermions are described in the standard model by three
 92 fundamental forces: electromagnetism, strong nuclear force and the weak nuclear force.
 93 The gravitational force is currently not included in the SM but the effect of gravity at the
 94 quantum level is too small to be observed. In the SM, each fundamental force is mediated
 95 by the exchange of bosons, which are integer spin particles that follows the Bose-Einstein
 96 statistics proposed in 1924 by Sateyndra Bose [11] and Albert Einstein [12].

97 The electromagnetic and the weak nuclear forces are described in the SM by the
 98 electroweak theory. The electromagnetic interactions between particles with electric
 99 charge are mediated by photons which are massless and chargeless spin one particles.
 100 On the other hand, the weak interactions can act on all fermions but the strength of
 101 the weak force is roughly 10^{-4} times weaker than the electromagnetic force and 10^{-6}
 102 times weaker than the strong nuclear force¹. The weak interactions are mediated by
 103 three massive vector bosons: the electrically charged W^\pm bosons² and the electrically
 104 neutral Z boson. Processes involving neutrinos or the change of quark flavour are only

¹The strength of the interactions is determined for two up quarks separated by a distance of 3×10^{-17} m.

²Since the W bosons are used to probe the nuclear PDF, the theory of the weak interaction is further described, together with the analysis in p-Pb collisions, in Chapter 3.

105 possible through the weak interactions. Last, the strong nuclear force is responsible for
106 the interactions between colour charged particles (i.e. quarks) described by the theory of
107 Quantum Chromodynamics (QCD). The strong interactions are mediated by spin one
108 bosons called gluons which carry colour and anti-colour charge. Unlike the photon, gluons
109 can interact with themselves leading to a strong attraction that confines the quarks in
110 colourless configurations known as hadrons. Hadrons composed of three (anti-)quarks are
111 called baryons while those made of a quark and an anti-quark are called mesons. Exotic
112 hadrons containing four and five quarks have been recently observed by the Belle [13]
113 and LHCb [14] collaborations, respectively.

114 The generation of mass of the elementary particles is explained in the SM by the
115 Brout-Englert-Higgs (BEH) mechanism [15, 16]. The weak bosons and the fermions
116 acquire their mass by interacting with the Higgs field. The stronger a particle couples
117 to the Higgs field, the more massive it becomes. The quantum excitation of the Higgs
118 field corresponds to a scalar boson, the so-called Higgs boson. The BEH mechanism was
119 experimentally confirmed after the CMS [17] and ATLAS [18] collaborations announced
120 the discovery of the Higgs boson in 2012. The basic properties of leptons, quarks and
121 bosons of the SM are summarised in Table 1.1.

122 1.1.2 Quantum chromodynamics

123 The development of new experimental techniques, such as the synchrocyclotron and the
124 bubble chamber, led to the discovery of many hadronic resonances starting from the
125 late 1940s. In an attempt to organise these new hadrons, Murray Gell-Mann [20] and
126 Yuval Ne’eman [21] proposed in 1961 the Eightfold Way classification. The Eightfold Way
127 scheme managed to sort the hadrons into representations of the SU(3) group leading to
128 the creation of the quark model. The quark model, developed in 1964 by Gell-Mann [22]
129 and George Zweig [23], considered the hadrons as composite objects made of valence
130 quarks and anti-quarks. Even though the quark model was successful at describing the
131 properties of most hadrons known at the time, it had problems explaining the structure
132 of the Ω^- baryon. The Ω^- baryon is made of three strange quarks with parallel spins
133 but such configuration was forbidden by the Pauli exclusion principle. To solve the
134 spin-statistics paradox, Oscar Greenberg [24] proposed that each quark also carried
135 a 3-valued quantum number named the colour charge. The description of the strong
136 interactions using the concept of colour charges was formally developed in the theory of
137 QCD by Harald Fritzsch, Heinrich Leutwyler and Murray Gell-Mann [25] in 1973.

	Name	Symbol	Mass	Charge	Spin	Interactions
Quarks	1 st Up	u	2.2 MeV	2/3	1/2	All
	Down	d	4.7 MeV	-1/3	1/2	All
	2 nd Charm	c	1.28 GeV	2/3	1/2	All
	Strange	s	96 MeV	-1/3	1/2	All
	3 rd Top	t	173.5 GeV	2/3	1/2	All
	Bottom	b	4.18 GeV	-1/3	1/2	All
Leptons	1 st Electron	e^-	511 keV	-1	1/2	Electroweak
	Electron neutrino	ν_e	<2 eV	0	1/2	Weak
	2 nd Muon	μ^-	106 MeV	-1	1/2	Electroweak
	Muon neutrino	ν_μ	<2 eV	0	1/2	Weak
	3 rd Tau	τ^-	1.78 GeV	-1	1/2	Electroweak
	Tau neutrino	ν_τ	<2 eV	0	1/2	Weak
Bosons	Photon	γ	$< 10^{-18}$ eV	0	1	Electromagnetic
	Gluon	g	0	0	1	Strong
	W boson	W^\pm	80.4 GeV	± 1	1	Electroweak
	Z boson	Z	91.2 GeV	0	1	Electroweak
	Higgs boson	H	125.1 GeV	0	0	BEH mechanism

Table 1.1: Basic properties of quarks, leptons and bosons from the SM. The table includes the mass, electric charge, spin and type of interactions of each particle. The values are taken from Ref. [19].

138 Quantum chromodynamics is a non-abelian quantum field theory with gauge symmetry group $SU(3)$, that describes the strong interactions between colour charged particles.
 139 The primary objects of QCD are the quarks which carry one colour charge (e.g. green)
 140 and the gluons which carry a colour and an anti-colour charge (e.g. red-antiblue). There
 141 are eight different gluons which form an octet representation of $SU(3)$ ³. The Lagrangian
 142 of QCD is:
 143

$$L_{QCD} = \sum_f \bar{q}_{f,i} \left(i\gamma^\mu D_\mu^{i,j} - m_f \delta^{a,b} \right) q_{f,j} - \frac{1}{4} F_{\mu,\nu}^a F_a^{\mu,\nu} \quad (1.1)$$

144 where g_s is the strong gauge coupling constant, and γ^μ are the Dirac γ -matrices. The
 145 $q_{f,i}$ represents the Dirac spinor of a quark with flavour f , mass m_f and colour index i
 146 running from $i = 1$ to 3. The QCD gauge covariant derivative $D_\mu^{i,j}$ and the gluon field
 147 strength tensor $F_{\mu,\nu}^a$ are given by:

³The fully symmetric colour-anticolour combination is colourless and thus, can not mediate colour.

$$D_\mu^{i,j} = \delta^{i,j} \partial_\mu - i \frac{g_s}{2} \lambda_a^{i,j} G_\mu^a \quad (1.2)$$

$$F_{\mu,\nu}^a = \partial_\mu G_\nu^a - \partial_\nu G_\mu^a + g_s f_{bc}^a G_\mu^b G_\nu^c$$

148 where f_{bc}^a are the SU(3) structure constants, $\lambda_a^{i,j}$ are the Gell-Mann matrices, and G_μ^a
 149 is the vector field of a gluon with index a that runs from 1 to 8.

150 Expanding the terms in Eq. (1.1), one can derive three different types of vertices
 151 representing the interaction between quarks and gluons, and the gluon self-interactions
 152 as shown in Figure 1.1.

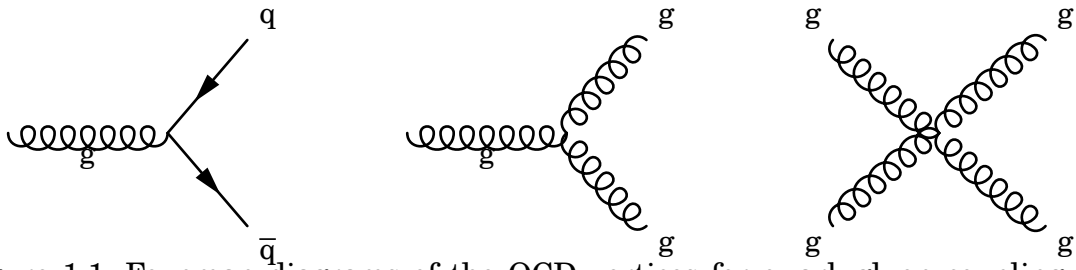


Figure 1.1: Feynman diagrams of the QCD vertices for quark-gluon coupling (left), triple-gluon self-coupling (middle) and quadri-gluon self-coupling (right).

153 1.1.2.1 Running coupling constant

154 In quantum field theory, physical quantities are calculated by performing a perturbative
 155 expansion of the theory in terms of its coupling constant. The first order of the expansion
 156 is called the leading order (LO). At higher orders, some of the terms contain loops (infinite
 157 integrals) which diverge due to high momentum particles in the loop. The ultraviolet
 158 (UV) divergences can be removed from the perturbation series by renormalising the
 159 Lagrangian.

160 The renormalisation procedure consists in replacing the bare parameters of the La-
 161 grangian by finite renormalised parameters, and then treat the divergences by applying a
 162 regularisation scheme. There are many regularisation schemes but one of the most often
 163 used is Minimal Subtraction (MS) based on dimensional regularisation. The MS scheme
 164 consists in solving the loop integrals in d arbitrary spacetime dimensions introducing a
 165 scale μ in the process [26]. In order to keep the physical observables independent of the
 166 renormalisation scale, the dependence of the renormalised parameters on the scale μ is
 167 fixed by renormalisation group equations (RGE) [26].

168 In the case of QCD, the strength of the strong interactions is parametrised by the
 169 strong coupling constant $\alpha_s = 4\pi g_s^2$. The UV divergences in perturbative QCD (pQCD)
 170 appears from loop diagrams like those shown in Figure 1.2.

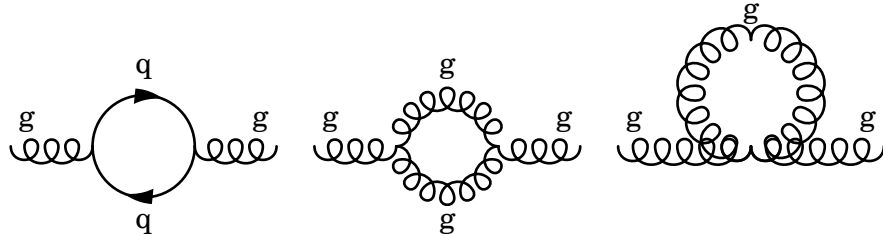


Figure 1.2: Feynman diagrams of 1-loop contributions to pQCD.

171 The renormalised strong coupling constant $\alpha_s(\mu^2)$ satisfies the following RGE [19]:

$$\mu^2 \frac{d\alpha_s(\mu^2)}{d\mu^2} = \beta(\alpha_s) = -\alpha_s^2 (\beta_0 + \beta_1 \alpha_s + \dots) \quad (1.3)$$

172 where $\beta_0 = 7/(4\pi)$ and $\beta_1 = 13/(8\pi^2)$ are the 1-loop and the 2-loop coefficients of the
 173 β -function, respectively [19]. In the one-loop approximation, $\alpha_s(\mu^2)$ can be expressed as:

$$\alpha_s(\mu^2) = \frac{1}{\beta_0 \ln\left(\frac{\mu^2}{\Lambda_{\text{QCD}}^2}\right)} \quad (1.4)$$

174 where $\Lambda_{\text{QCD}} \approx 255 \text{ MeV}$ [27]⁴ is the QCD Landau pole (i.e. the scale at which the
 175 coupling becomes infinite). The factorisation scale μ is generally associated to the energy
 176 scale Q of a given process. This means that $\alpha_s(\mu^2)$ is not really a constant but depends
 177 on the energy scale, so it is also known as the QCD running coupling constant. Figure 1.3
 178 presents the latest results on the measurement of $\alpha_s(Q^2)$ as a function of the energy
 179 scale Q [19].

180 1.1.2.2 Asymptotic freedom

181 One important consequence of the non-abelian nature of QCD is the asymptotic freedom
 182 of colour charged particles discovered in 1973 by David Gross and Frank Wilczek [28],
 183 and also by David Politzer [29]. As can be observe in Figure 1.3, the strength of the strong
 184 nuclear force gets asymptotically reduced as the energy scale is increased. Perturbative

⁴Derived in the $\overline{\text{MS}}$ scheme for 2 quark flavours.

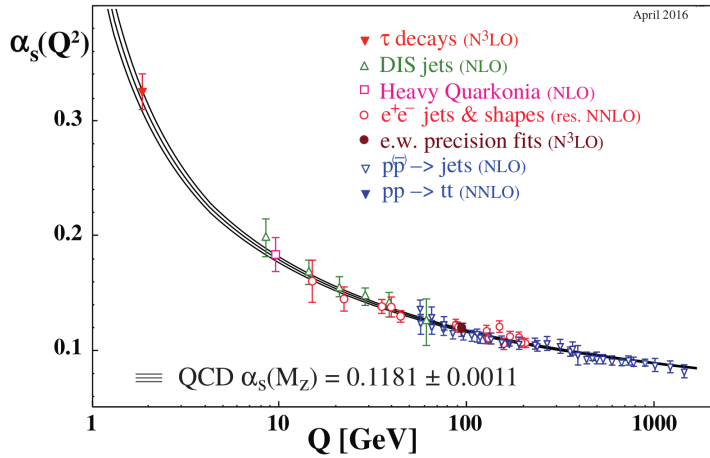


Figure 1.3: Summary of measurements of α_s as a function of the energy scale Q . Figure taken from the PDG [19]

185 QCD can then be fully applied in the asymptotic free regime since the strong coupling
 186 constant is small.

187 Considering the inverse relation between the wavelength of particles and their mo-
 188 mentum (the de Broglie hypothesis [30]), asymptotic freedom implies that the strong
 189 nuclear interactions between quarks gets weaker at larger momentum or at shorter dis-
 190 tances. This phenomenon can be understood qualitatively as derived from the interaction
 191 with the QCD vacuum. The presence of virtual quark-antiquark pairs from the vacuum
 192 acts as colour dipoles reducing (screening) the strength of the colour charge field. In
 193 addition, virtual gluons can couple to other gluons increasing (anti-screening) the net
 194 effect of the colour charge seen at larger distances. Thus, there is an interplay between
 195 quark-antiquark colour screening and gluon colour anti-screening, where the later effect
 196 dominates in QCD.

197 1.1.2.3 Colour confinement

198 The fact that quarks and gluons have never been observed isolated in normal conditions is
 199 due to another phenomenon of QCD called colour confinement. The intensity of the strong
 200 nuclear force increases when the energy scale is reduced or the distance is increased as
 201 seen in Figure 1.3. The large strong interactions between colour charged particles force
 202 the quarks and gluons to be confined in hadrons. The divergent behaviour of α_s at the
 203 Landau pole shown in Eq. (1.4), is a consequence of the inability of pQCD to describe the
 204 low energy regime, which becomes non-perturbative.

205 The strong nuclear force can be described qualitatively as a string. When a quark

and anti-quark gets separated, the gluon string that mediates their strong interaction elongates, increasing the energy. The string eventually breaks when it becomes more energetically favourable to create a light quark-antiquark pair, splitting the original meson into two mesons as shown in Figure 1.4. This leads to a process called hadronisation where quarks and gluons produce a cascade of hadrons. The presence of colour charged particles in high energy collisions can be measured experimentally using jets derived by clustering the final state hadrons in narrow cones.

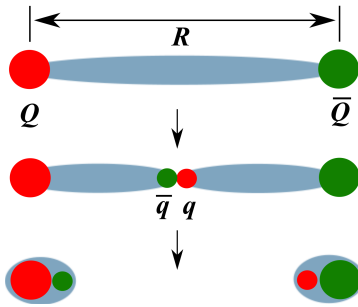


Figure 1.4: Sketch of the gluon string breaking between a quark Q and an anti-quark \bar{Q} due to $q\bar{q}$ pair creation. Figure taken from Ref. [31].

1.1.3 Parton distribution functions

The production of particles in hadronic collisions depends on the evolution of the partons (i.e. quarks and gluons) inside the hadrons and the parton momentum transfer during the hard scattering. Since the strong coupling constant decreases with increasing momentum scales, partons can be considered asymptotically free within the hadron during collisions involving large momentum transfer. In this case, each parton carries a fraction of the total momentum of the hadron, represented by the quantity called Bjorken x [32] (labelled simply as x), given by:

$$p_{parton} = x p_{proton} \quad (1.5)$$

The net quantum properties of hadrons, such as the electric or colour charge, are derived from the valence quarks. The interaction between valence quarks is mediated by the exchange of gluons. Gluons can also produce virtual quark-antiquark pairs and other gluons through self interactions. The virtual quarks produced inside the hadrons are called sea quarks. The gluons and sea quarks do not contribute to the net quantum numbers of the hadron but they can contribute to its mass and they also play a key role in the interaction of hadrons with other particles.

228 A convenient way of studying the partonic content of hadrons is through the parton
 229 distribution functions. The PDF of a hadron represents the probability that a parton
 230 carries a given fraction x of the total momentum of the hadron.

231 According to the QCD factorisation theorem [33], the cross section of a given hard
 232 scattering process in hadronic collisions can be split in a partonic cross section times the
 233 PDFs of each incoming hadron. On one hand, the partonic cross section can be derived
 234 using perturbative QCD and does not depend on the colliding hadrons. On the other
 235 hand, the PDFs can not be calculated from first principles due to the non-perturbative
 236 nature of QCD, but they can be determined from global fits to experimental data since the
 237 PDFs are independent of the initial scattering process (i.e. universal). The hadronic cross
 238 section in a given final state can be expressed at LO, using the factorisation theorem, as:

$$\sigma_{h_1, h_2} = \sum_{f_1, f_2 = (q, \bar{q}, g)} \int_0^1 dx_1 dx_2 f_1^{h_1}(x_1, Q^2) f_2^{h_2}(x_2, Q^2) \hat{\sigma}_{f_1 f_2} \quad (1.6)$$

239 where Q^2 is the momentum scale, $f^{h_1}(x, Q^2)$ is the PDF of a given incoming hadron
 240 h_1 , and $\hat{\sigma}_{f_1 f_2}$ represents the partonic cross section of the scattering process between
 241 partons f_1 and f_2 .

242 The Q^2 dependence of the PDFs is described by the parton evolution equations
 243 developed by Dokshitzer, Gribov, Lipatov, Altarelli and Parisi (DGLAP) [34–36]. In the
 244 DGLAP formalism, the PDFs can be expressed in terms of kernels $P_{q_1 q_2}$ (called splitting
 245 functions), and the evolution equations of the parton densities can be written as:

$$\begin{aligned} \frac{d}{dt} q_i(x, t) &= \frac{\alpha_s(Q)}{2\pi} [q_i \circledast P_{qq} + g \circledast P_{qg}] \\ \frac{d}{dt} g(x, t) &= \frac{\alpha_s(Q)}{2\pi} \left[\sum_i (q_i + \bar{q}_i) \circledast P_{gq} + g \circledast P_{gg} \right] \\ [q \circledast P] &= \int_x^1 dy \frac{q(y, t)}{y} \times P\left(\frac{x}{y}\right) \end{aligned} \quad (1.7)$$

246 where $t = \log(Q^2/\mu_F^2)$, μ_F is the factorisation scale (energy scale that separates the
 247 PDFs from the partonic cross sections), and $P_{q_1 q_2}$ represents the probability that a parton
 248 of type q_1 emits a parton of type q_2 . In other words, the DGLAP evolution equations
 249 state that the PDF of a given parton q at an x value is determined from the contribution
 250 of all the partons at higher momentum fraction considering their probability of decaying
 251 into the parton q .

252 From the definition of the PDFs, one can also formulate a set of structure functions
 253 defined as:

$$F_2^P(x) = \sum_q e_q^2 f(x, Q^2) x \quad (1.8)$$

where e_q is the electric charge of a given quark flavour q . The structure functions were extensively measured in deep-inelastic scattering (DIS) collisions at the Hadron-Elektron-Ring-Anlage (HERA) accelerator. The DIS process consists in the inelastic scattering of electrons off protons as presented in Figure 1.5. In the DIS process, the momentum transferred from the electron to the proton is defined as $Q^2 = -q^2 = -(k - k')^2$ and the corresponding Bjorken x fraction is $x = Q^2/(2p \cdot q)$, where all 4-momenta are defined in the figure.

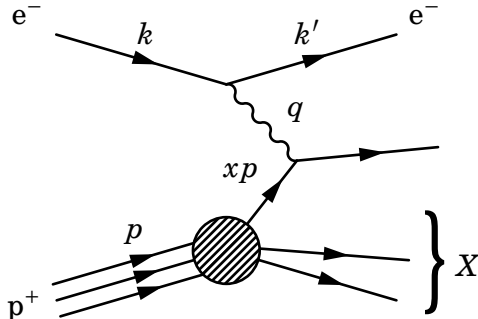


Figure 1.5: Feynman diagram of deep inelastic scattering of electrons against protons.

The measurements of the F_2 structure function performed by the ZEUS collaboration [37] at HERA are shown in Figure 1.6. Even though DIS experiments were not able to probe the gluons directly, the DIS data showed that valence quarks only carry half of the proton momentum, the other half being carried by the gluons.

Another important process used to constrain PDFs is the Drell-Yan (DY) process or the production of W bosons. In the DY process, a quark from one hadron and an anti-quark from another hadron annihilate into a virtual photon (γ^*) or a Z boson, which then decays to a particle-antiparticle pair as shown in Figure 1.7. The measurement of DY production can be used to constrain the quark PDFs in a wide range of momentum fraction x depending on the invariant mass of the dilepton pair. In addition, the measurement of the production of positive and negative charged W bosons in hadronic collisions is used to disentangle the flavour dependence of the quark PDFs. More details about the W boson production will be provided in Chapter 3, since the present thesis report a measurement of W bosons in p-Pb collisions that provide strong constraints on nuclear PDF.

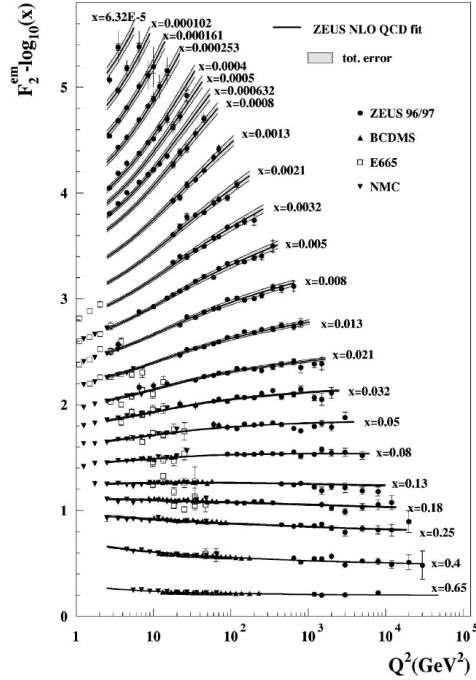


Figure 1.6: Next-to-leading order QCD fits to the ZEUS F_2 structure function data from 1996, 1997 and proton fixed-target at HERA. The error bands of the fit represent the total experimental uncertainty from both correlated and uncorrelated sources. Figure taken from Ref. [37].

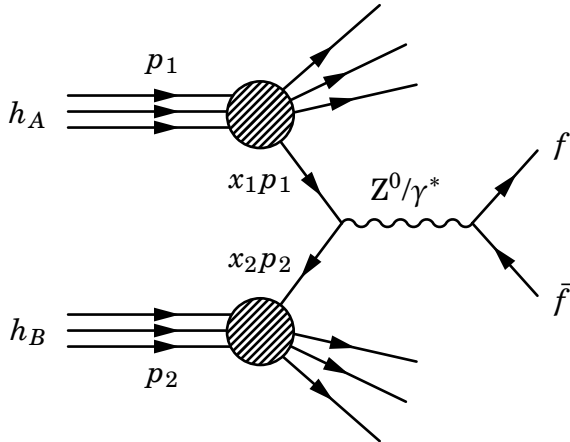


Figure 1.7: Feynman diagram of the Drell-Yan process.

275 1.1.4 QCD phase diagram

276 The first attempt to describe the temperature evolution of matter at high energies
 277 was performed by Rolf Hagedorn in 1965 [38]. Hagedorn considered matter at high

278 energies as a gas made of hadrons and he employed a thermodynamical bootstrap
279 approach to describe the hadron gas. After studying the mass spectrum of all the hadron
280 species measured at the time, Hagedorn realised that the density of hadron species
281 grows exponentially until it diverges at a temperature of $T_H \approx 158$ MeV, known as the
282 Hagedorn temperature. Years later, with the advent of QCD, it was understood that the
283 Hagedorn temperature described a transition from a hadron gas to a state of matter
284 where quarks and gluons are asymptotically free called the quark-gluon plasma.

285 The description of the QCD phase transition turned out to be complicated because the
286 critical temperature is close to the QCD scale $\Lambda_{\text{QCD}} \approx 255$ MeV [27], where perturbative
287 calculations are no longer reliable. An alternative method to study the non-perturbative
288 regime of QCD consists of solving numerically the QCD field equations on a discrete
289 space-time grid using a method called lattice QCD. Nowadays, lattice QCD is able to
290 describe the evolution of matter at finite temperatures and low densities. A sketch of the
291 QCD phase diagram in terms of the temperature T and the baryon chemical potential
292 μ_B ⁵. is shown in Figure 1.8.

293 Normal nuclear matter exists in nature at low temperatures and high μ_B (900 MeV).
294 At higher μ_B , matter undergoes a phase transition to a degenerate gas of fermions,
295 known as neutron gas, which is present in neutron stars. It is theorised that at even
296 higher μ_B , matter could reach a state of colour superconductivity where quarks bind
297 together into Cooper pairs [40]. On the other hand, matter present at the beginning of
298 the universe or produced in TeV-scale particle collisions has very low baryon chemical
299 potential. Matter is described at low temperatures as a hadron gas and it becomes a
300 QGP when the temperature exceeds some critical value. At low μ_B , the phase transition
301 between the hadron gas and the QGP has been established, using lattice QCD, to be a
302 crossover where the two states coexist [41, 42].

303 1.2 Relativistic heavy-ion collisions

304 Heavy-ion colliders have become essential tools to explore the fundamental properties of
305 matter. Collisions of nuclei are used to probe the phase transitions of QCD and to recreate
306 the QGP in the laboratory. The QGP is believed to have existed at the beginning of the
307 Universe and to be part of the core of some astrophysical objects such as neutron stars.
308 The study of the QGP allows to test QCD in the most extreme regimes and provides an

⁵The baryon chemical potential can be viewed as a measure of the excess of matter over anti-matter and it is proportional to the baryon density.

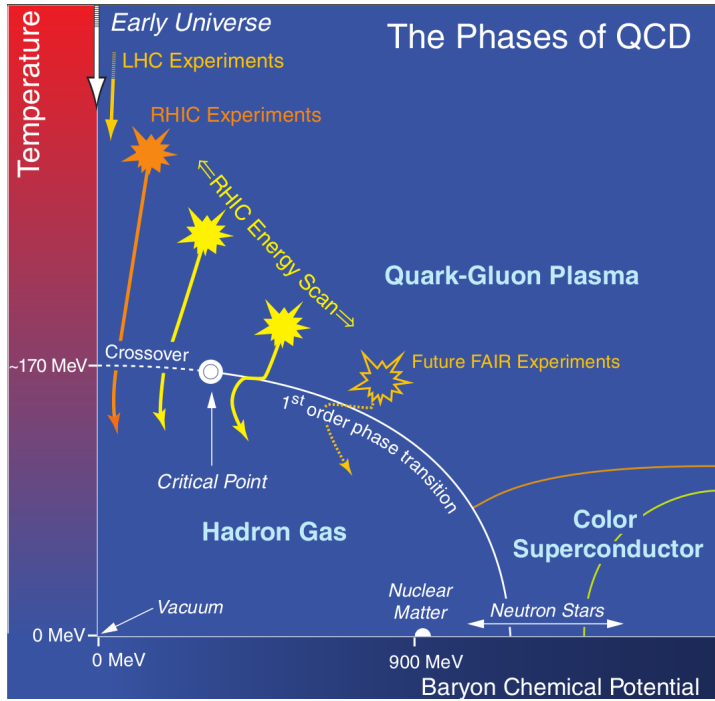


Figure 1.8: Sketch of the QCD phase diagram for nuclear matter. The solid lines show the phase boundaries and the solid circle represents the critical point. Figure taken from Ref. [39].

309 insight on the evolution of the Universe. Some of the primary research goals of the heavy-
 310 ion physics programme is to understand the formation and properties of the QGP, and
 311 how does matter interact with the nuclear medium. Nowadays, the experimental study of
 312 ultra-relativistic (i.e. at energies above $\sqrt{s_{NN}} > 10 \text{ GeV}$) heavy-ion collisions is performed
 313 at the Brookhaven National Laboratory (BNL) and at the European Organization for
 314 Nuclear Research (CERN).

315 1.2.1 History of heavy-ion accelerators

316 The interest in probing the QCD phase diagram in the laboratory arose in the 1970s
 317 after Werner Scheid, Hans Müller and Walter Greiner predicted that nuclear matter
 318 could be compressed in heavy-ion collisions at nucleus-nucleus energies larger than
 319 100 MeV/nucleon [43]. The shock compression mechanism could reach matter densities
 320 up to five times higher than the density of atomic nuclei ($\rho_0 = 0.16 \text{ baryons/fm}^3$) [43].
 321 Coinciding in time, the Lawrence Berkeley National Laboratory (LBNL) decided to
 322 transform their proton synchrotron accelerator Bevatron into a heavy-ion experiment
 323 called Bevalac. Heavy ions were produced in the Bevalac using the heavy-ion linear

324 accelerator SuperHILAC and then sent to the Bevatron, where the ions were further
325 accelerated against a fixed target with energies of up to 2.6 GeV/nucleon [44]. The goal
326 at the time was to investigate the equation of state (EoS) of hadronic matter at high
327 densities. The understanding of the relation between the pressure and the energy density
328 of dense matter was a key element needed to describe the dynamics of astrophysical
329 objects such as neutron stars [45, 46].

330 The successful creation of compressed nuclear matter at the Bevatron motivated
331 the construction of several heavy-ion accelerators at higher energies. The first one was
332 the Alternating Gradient Synchrotron (AGS) particle accelerator at the Brookhaven
333 National Laboratory (BNL). The AGS became the first facility in 1960 to accelerate
334 protons to an energy of 33 GeV, which allowed to discover the muon neutrino in 1962
335 and to observe the CP violation of the weak interactions in Kaon decays in 1964. An
336 electrostatic accelerator called the Tandem Van de Graaf was built in 1970 to provide
337 beams of ions to the AGS. The relativistic heavy-ion programme started at AGS in 1986
338 and lasted for 12 years during which several experiments were performed (e.g. E802,
339 E858, E866, E896 and E917). The AGS accelerated Si beams at 14.6 GeV/nucleon and
340 Au beams at 11.1 GeV/nucleon, and collided them against different types of fixed targets
341 (e.g. Al and Au).

342 In parallel, CERN built the Super Proton Synchrotron (SPS) in 1976. To study the QGP,
343 CERN added an Electron-Cyclotron Resonance (ERC) ion source in 1986 which initially
344 accelerated ions of oxygen and sulphur at 200 GeV/nucleon. A subsequent upgrade of
345 the ion injector in 1994 allowed to accelerate up to an energy of 158 GeV/nucleon the Pb
346 ions, which were collided against fixed targets located in two experimental halls: one in
347 the SPS north area (NA) and the other in the SPS west area (WA). Several fixed target
348 experiments were built at the SPS between 1986 and 2005. After years of analysing the
349 Pb-Pb and Pb-Au fixed target collision data from SPS, CERN announced in 2000 that
350 the combined results of the experiments NA44, NA45, NA49, NA50, NA52, WA97/NA57
351 and WA98, provided a first evidence of the creation of a new state of matter consistent
352 with the QGP [47].

353 In the meantime, the first nucleus-nucleus collider, known as the Relativistic Heavy
354 Ion Collider (RHIC), started operations at the BNL in 2000. Two beams of Au are pre-
355 accelerated at the AGS to an energy of 8.86 GeV/nucleon and then sent to RHIC where
356 the Au beams were first collided at $\sqrt{s_{NN}} = 130$ GeV, and later at 200 GeV. Other collision
357 systems explored at RHIC include: p-p, p-Au, d-Au, Cu-Cu, Cu-Au and U-U [48]. There
358 were four detectors at RHIC called BRAHMS, PHENIX, STAR, and PHOBOS. Currently,

359 only the STAR and PHENIX collaborations are still active, while PHOBOS ceased
 360 operations in 2005 and BRAHMS in 2006. After four years of meticulously studying the
 361 system produced in Au-Au collisions with the four detectors, RHIC finally announced
 362 in 2005 the discovery of a strongly coupled QGP. Contrary to the expected gaseous
 363 behaviour, the QGP observed at RHIC turned out to resemble more a liquid with very
 364 little viscosity [49–52].

365 Currently, the largest heavy-ion collider is the Large Hadron Collider (LHC) at CERN,
 366 whose construction finished in 2008. The SPS is used as injector to the LHC, accelerating
 367 the Pb beams to energies of 1.38 TeV. The first nucleus-nucleus collisions at LHC took
 368 place in 2010 using Pb beams at 2.76 TeV. Since then, the LHC has collided different
 369 configurations involving ions, including p-Pb at 2.76 TeV (2013), Pb-Pb at 5.02 TeV
 370 (2015), p-Pb at 8.16 TeV (2016), Xe-Xe at 5.44 TeV (2017), and at the end of 2018 LHC is
 371 planning to provide a larger set of Pb-Pb collisions at 5.02 TeV. There are four detectors
 372 at the LHC called ALICE, CMS, ATLAS and LHCb. The four experiments are nowadays
 373 participating in the heavy-ion programme at LHC. Due to the large beam energies, the
 374 LHC is an ideal collider to study the QGP at very high temperatures, where one expects
 375 smaller QGP formation times and larger hot medium densities, compared to RHIC.

376 1.2.2 Geometry of nucleus-nucleus collisions

377 The number of particles produced in a nucleus-nucleus collision depends on the geometry
 378 of the collision. Since nuclei are extended objects made of nucleons (i.e. protons and
 379 neutrons), the number of nucleon-nucleon (NN) interactions increases the more head-
 380 on or central is the collision. The nucleons that participate in the collision are called
 381 participants while those that do not participate are referred to as spectators. The overlap
 382 region of the collision depends on the impact parameter \vec{b} , which is the transverse
 383 distance between the centres of the two colliding nuclei as shown in Figure 1.9.

384 The formation and characteristics of the QGP in nucleus-nucleus collisions depends
 385 on the number of colliding nucleons. To study the dynamics of the nuclear medium, the
 386 heavy-ion collisions are classified based on their centrality. The centrality c is defined as
 387 the fraction of the total nucleus-nucleus inelastic cross section $\sigma_{AB}^{\text{inel}}$ determined within
 388 the area defined by the impact parameter b , and it is expressed as:

$$c = \frac{\pi b^2}{\sigma_{AB}^{\text{inel}}} \quad (1.9)$$

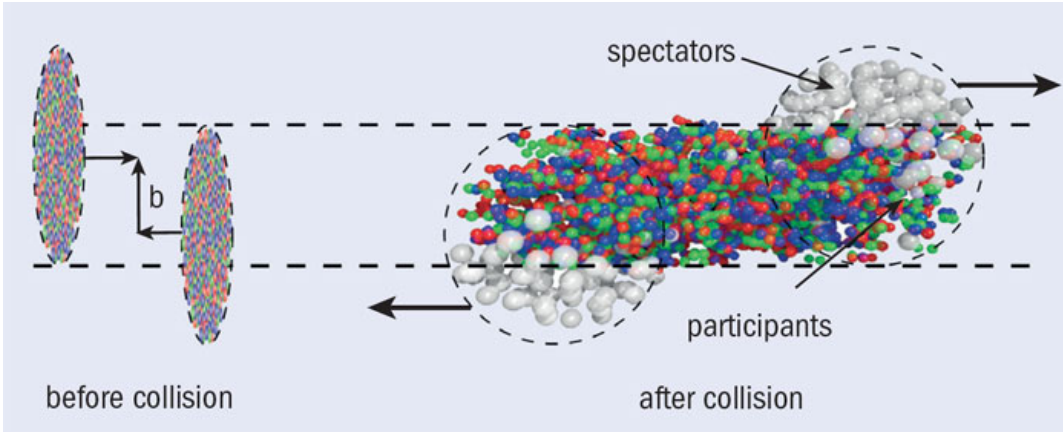


Figure 1.9: Illustration of two nucleus with impact parameter b before (left) and after (right) colliding. Figure taken from Ref. [39].

389 The collision centrality can be related to the number of participants N_{part} and the
 390 number of binary nucleon-nucleon collisions N_{coll} using a Glauber model. The Glauber
 391 model, developed in the 1950s by Roy Glauber, describes the collision between two nuclei
 392 as a superposition of independent NN interactions [53].

393 There are two ways of implementing the Glauber model, the optical and the Monte
 394 Carlo approaches. In the optical approach, the physical observables are computed using
 395 the optical limit which assumes a continuous nucleon density distribution. On the
 396 other hand, in the Monte Carlo approach, the two nuclei are simulated by distributing
 397 the nucleons according to their nuclear density profile, and then the nucleus-nucleus
 398 collisions are modelled, at random impact parameters, by computing the individual NN
 399 collisions [53].

400 An example of a heavy-ion collision described by the optical Glauber model geometry
 401 is shown in Figure 1.10. It represents the collision between a nucleus A with A nucleons
 402 and a nucleus B with B nucleons.

403 The tube located at a distance \vec{s} from the center of the nucleus A overlaps the tube
 404 located at a distance $\vec{b} - \vec{s}$ from the center of the nucleus B. In this case, the nuclear
 405 overlap function $T_{AB}(b)$ is defined as:

$$T_{AB}(b) = \int d\vec{s}^2 T_A(\vec{s}) T_B(\vec{b} - \vec{s}) \quad (1.10)$$

406 where T_A and T_B are the nuclear thickness functions of the nucleus A and B, respec-
 407 tively.

408 The nuclear thickness function is given by $T(\vec{r}) = \int dz \rho(\vec{r}, z)$, where ρ is the nuclear

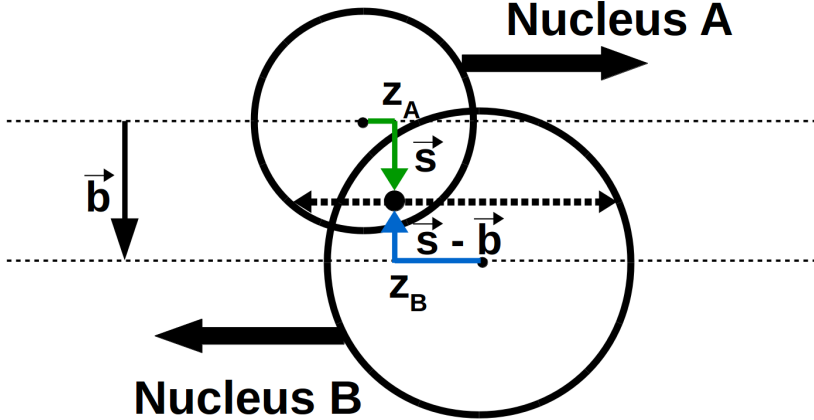


Figure 1.10: Schematic representation of the optical Glauber model geometry.

409 density distribution of a given nucleus, which is generally parametrised with a Wood-
410 Saxon density profile [53]:

$$\rho(r) = \frac{\rho_0}{1 + \exp\left(\frac{r-r_0}{a}\right)} \quad (1.11)$$

411 where r is the distance to the center of the nucleus, a represents the width of the
412 edge region of the nucleus called the skin depth, r_0 is the mean radius of the nucleus
413 and ρ_0 is the nuclear density at the center of the nucleus. The average number of binary
414 NN collisions $\langle N_{\text{coll}} \rangle$ for a given impact parameter b is defined as:

$$\langle N_{\text{coll}}(b) \rangle = AB \cdot \langle T_{AB}(b) \rangle \cdot \sigma_{\text{nn}}^{\text{inel}} \quad (1.12)$$

415 where $\sigma_{\text{nn}}^{\text{inel}}$ is the inelastic nucleon-nucleon cross section and $\langle T_{AB}(b) \rangle$ is the average
416 nuclear overlap function. Hence, the Glauber model provides a quantitative description
417 of the geometry of the nuclear collision and can be used to estimate the variables (N_{part} ,
418 N_{coll} and T_{AB}) for a given centrality class.

419 Experimentally, the impact parameter of the collision can not be determined directly.
420 However, the distribution of the number of soft particles scales with N_{part} . As a result,
421 one can classify the events in different centrality classes by binning the measured
422 distribution of charged particles, so that each bin contain the same fraction of the
423 total integral. The mean parameters $\langle N_{\text{part}} \rangle$ and $\langle N_{\text{coll}} \rangle$, can be then derived, for each
424 centrality class, by simulating the charged-particle distribution using a MC Glauber
425 model. In addition, the collision centrality can sometimes be also inferred from the

426 number of spectators determined from the measurement of the transverse energy in the
427 forward region.

428 **1.2.3 Evolution of heavy-ion collisions**

429 The evolution of a nucleus-nucleus collision undergoes several steps, starting from the
430 collision of the nuclei to the final production of hadrons. Figure 1.11 illustrates the
431 different processes that occur during a heavy-ion collision associated to the production of
432 the QGP.

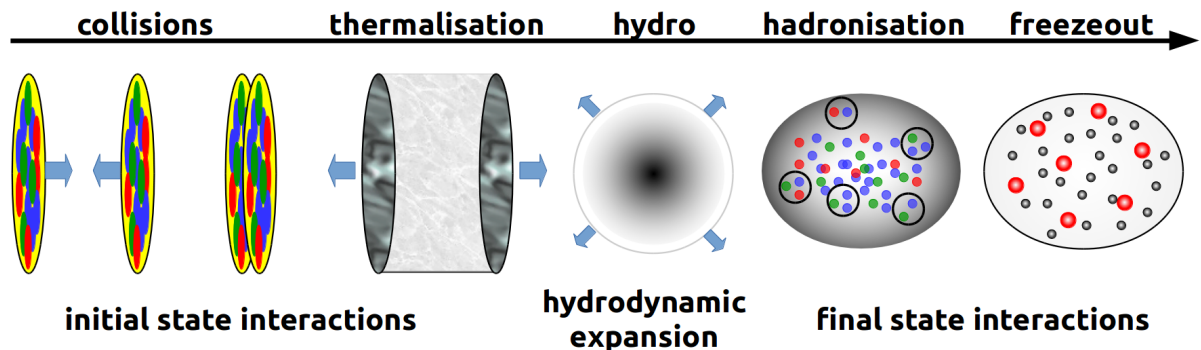


Figure 1.11: Sketch of the evolution of a relativistic heavy-ion collision.

433 1. Initial stage: At high energies, the two nuclei are Lorentz contracted along the
434 axis of motion while approaching each other at almost the speed of light. As a
435 consequence, the nucleons of each nuclei are also contracted increasing the number
436 of gluons until it reaches the gluon saturation scale. The initial conditions can be
437 described in various ways, depending on the physics to be addressed: the Glauber
438 model or the effective theory called the Color Glass Condensate are often used.
439 When the two nuclei collide, the partons inside the geometrical overlap region of
440 the two nuclei undergo parton-parton interactions.

441

442 2. QGP formation and thermalisation: The parton-parton interactions quickly start
443 producing new particles increasing the density of the system until a phase tran-
444 sition is reached forming the QGP. After some time, the system reaches thermal
445 equilibrium.

446

447 3. Hydrodynamical expansion: After reaching the thermal equilibrium, the system
448 evolves as a nearly-perfect fluid. It first expands longitudinally along the beam
449 direction and then it expands in all directions until the QGP cools down back to
450 the critical temperature.

451

452 4. Hadronisation: The medium undergoes a second phase transition back to a hadronic
453 gas where the partons recombine into hadrons. In this phase, the system keeps
454 expanding via hadron-hadron interactions until the average path length of the
455 hadrons is as large as the size of the system.

456

457 5. Freeze-out: The hadron gas experience first a chemical freeze-out when the in-
458 elastic collisions between hadrons cease, fixing the composition of the particles.
459 Subsequently, the system reaches a kinetic freeze-out when the elastic scattering
460 between the hadrons also stop, fixing the kinematic distributions of the parti-
461 cles. Subsequently, the particles escape the medium and are reconstructed in the
462 detector.

463 1.2.4 Experimental probes of the QGP

464 The QGP can not be directly measured experimentally, since once it is created it only
465 exists for a very short amount of time. Nonetheless, the QGP can be studied indirectly
466 by measuring how the particles and the system produced in the collision are modified by
467 the presence of the QGP. There are many experimental *signatures* that has been used
468 to asses the different properties of the QGP, such as the enhancement of the strange
469 quark production, suppression of the quarkonium yields, attenuation of the energy of jets,
470 anisotropies in the azimuthal distribution of particles, among others. The production
471 mechanism of each experimental probe depends on the momentum scale of the process.
472 Signatures produced in processes involving large momentum transfer are called hard
473 probes while those produced at low momentum scales are called soft probes.

474 The majority of the particles produced in heavy-ion collisions are soft and constitute
475 the bulk of the system. Soft probes are used to study the thermal and hydrodynamical
476 evolution of the medium. The production yields of soft particles scales with N_{part} . The
477 strange hadron yields and the elliptic flow are two examples of soft probes. On the
478 other hand, hard probes are produced from the parton-parton hard scattering during
479 the initial stage of the collision. Hard probes are ideal tools to study the structure of

480 the system since they are produced early in a well-controlled manner⁶ and often living
 481 through the QGP. The number of hard particles produced in the medium scales with N_{coll} .
 482 Some important hard probes used to study the nuclear medium includes the electroweak
 483 bosons, quarkonia and jets. The following subsections present a brief description on some
 484 of the soft and hard probes of the QGP.

485 **1.2.4.1 Elliptic flow**

486 When the QGP is formed, it undergoes a collective expansion due to the large pressure
 487 gradient produced by the multiple partonic interactions during the heavy-ion collision.
 488 This collective expansion is known as flow. The magnitude of the flow tend to grow with
 489 the number of parton-parton interactions and it depends on the initial conditions of the
 490 collision. If the nucleus-nucleus collision is completely central ($b = 0$) then the particles
 491 develop a radial flow, but if the collision is non-central ($b \neq 0$) then the spacial anisotropy
 492 of the overlap region leads to an additional anisotropic flow as shown in Figure 1.12.

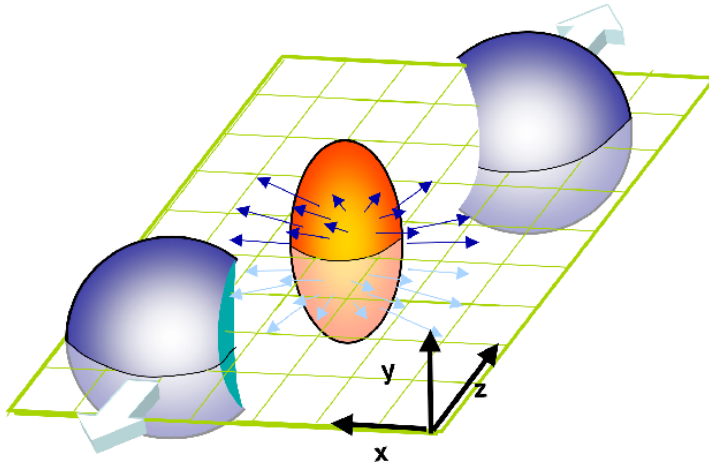


Figure 1.12: Sketch of the elliptic flow produced in non-central heavy-ion collisions.
 Figure taken from Ref. [54].

493 Experimentally, the anisotropic flow can be determined from the Fourier decomposi-
 494 tion of the particle azimuthal angle ϕ distribution with respect to the reaction plane
 495 ψ_{RP} [55]:

$$\frac{d^3N}{d^3\vec{p}} = \frac{1}{2\pi} \frac{d^2N}{p_T dp_T dy} \left(1 + 2 \sum_{n=1}^{\infty} v_n \cos[n(\phi - \psi_{RP})] \right) \quad (1.13)$$

⁶The production cross section of hard probes can be computed using the QCD factorisation theorem.

496 where the Fourier coefficient v_2 measures the strength of the elliptic flow and the
 497 reaction plane is derived from the direction of the beam (z -axis) and the impact parameter
 498 (x -axis) as presented in Figure 1.12.

499 An alternative way to derive the flow coefficients is by computing the Fourier decom-
 500 position of the two-particle azimuthal distribution defined as [55]:

$$v_n \{2\}^2 = c_n \{2\} = \langle \cos[n(\phi_1 - \phi_2)] \rangle \quad (1.14)$$

501 where $c_n \{2\}$ is called the two-particle cumulant and the brackets represent the
 502 average over all particles and events. The advantage of using particle correlations is that
 503 the Fourier coefficients do not depend on the reaction plane determination, but non-flow
 504 contributions (e.g. resonance decays or back-to-back jets) can affect the measurements.
 505 Correlating more than two particles, such as four-particle correlations, can reduce the
 506 impact of the non-flow effects.

507 The elliptic flow of the medium is sensitive to the equation of states of the QGP [55]
 508 and bulk viscosity [56]. Furthermore, relativistic hydrodynamic calculations [57] predicts
 509 that the elliptic flow of hadrons can approximately be expressed as $v_2 \propto (p_T - \beta \cdot m_T)$,
 510 where β is the average flow velocity and m_T is the transverse mass of the hadron, which
 511 is defined as $m_T^2 = m^2 + p_T^2$. As a consequence, the elliptic flow is expected to show a mass
 512 ordering where the more massive hadrons would have lower v_2 values compared to the
 513 lighter hadrons.

514 The low p_T -dependence of the elliptic flow of strange hadrons measured at RHIC in
 515 Au-Au collisions at $\sqrt{s_{NN}} = 200$ GeV is presented in Figure 1.13. The measurement of
 516 the elliptic flow of π^\pm mesons, K_s^0 mesons, antiprotons and Λ baryons (with masses of
 517 140, 495, 940 and 1,115 MeV, respectively), shows the expected mass ordering pattern.
 518 Moreover, the good agreement between the RHIC results and the predictions using
 519 relativistic hydrodynamics assuming that the fluid flow is non-viscous, supported the
 520 conclusion that the QGP behaves as a nearly ideal fluid [58].

521 At the start of the LHC, the CMS collaboration performed a measurement of the two-
 522 particle angular correlations in p-p collisions producing high number of particles (referred
 523 as high-multiplicity collisions). Figure 1.14 presents the two-particle $\Delta\eta$ - $\Delta\phi$ correlation
 524 function measured by the CMS collaboration in p-p collisions at $\sqrt{s} = 7$ TeV [59], where
 525 $\Delta\phi$ is the azimuthal angle difference between the two particles and $\Delta\eta$ is the difference
 526 in their pseudorapidity. The results show a long-range structure ($2.0 < \Delta\eta < 4.8$) of
 527 near-side ($\Delta\phi \sim 0$) two-particle correlations, often called "ridge". The structure is seen
 528 for particles with $1 \text{ GeV}/c < p_T < 3 \text{ GeV}/c$, produced in high-multiplicity ($N > 110$) p-p

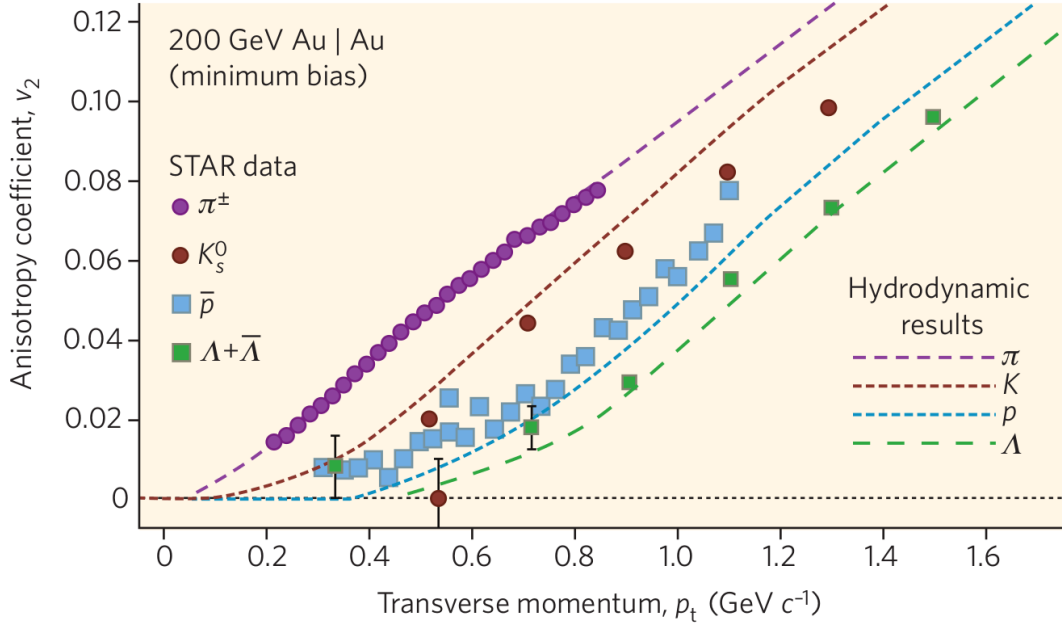


Figure 1.13: Elliptic flow distribution of as a function of transverse momentum for π^\pm mesons, K_s^0 mesons, antiprotons and Λ baryons measured by STAR collaboration in Au-Au collisions at $\sqrt{s_{\text{NN}}} = 200$ GeV. The results are compared with relativistic hydrodynamic calculations. Figure taken from Ref. [58].

529 collisions. A similar ridge-like structure had already been observed at RHIC in heavy-ion
 530 collisions [60], which was understood as a result of the hydrodynamic expansion of the
 531 QGP, but the phenomenon found in p-p collisions was completely unexpected at the time
 532 and it is still not fully understood yet.

533 **1.2.4.2 Strangeness enhancement**

534 Strange quarks belongs to the second generation of quarks and are roughly 20-40 times
 535 more massive than up and down quarks. The number of strange quarks involved in a
 536 decay can be quantified through the quantum number called strangeness, which can take
 537 values of $+1$, -1 and 0 , for strange quarks, strange anti-quarks, and the other quarks,
 538 respectively. Strangeness is conserved in strong and electromagnetic interactions, while
 539 it is not conserved in weak decays. In hadronic collisions, strange quark-antiquark
 540 pairs ($s\bar{s}$) are produced in parton-parton interactions via gluon fusion ($gg \rightarrow s\bar{s}$) or quark
 541 annihilation ($q\bar{q} \rightarrow s\bar{s}$), and through gluon splitting ($g \rightarrow s\bar{s}$) during the evolution of the
 542 medium. The production of strange hadrons in proton-proton collisions is suppressed
 543 relative to hadrons made of light quarks (i.e. pions), due to the higher mass of the strange

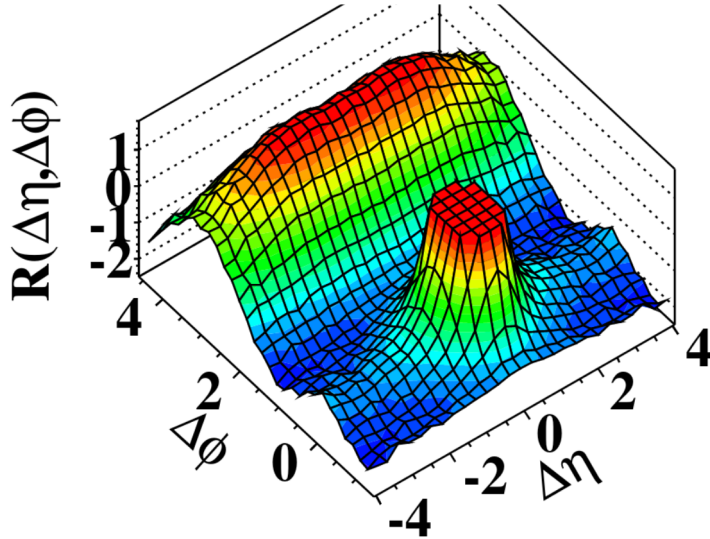


Figure 1.14: 3D display of the $\Delta\eta$ - $\Delta\phi$ correlation function between two charged particles with $1 \text{ GeV}/c < p_T < 3 \text{ GeV}/c$, measured by the CMS collaboration in high multiplicity ($N \geq 110$) p-p collisions at $\sqrt{s} = 7 \text{ TeV}$. Figure taken from Ref. [59].

544 quark.

545 In heavy-ion collisions, where the QGP is formed, it was proposed by Johann Rafelski
 546 and Rolf Hagedorn [61] in 1980, that the enhancement of strangeness could serve as
 547 a signature of the QGP. Due to the large gluon density and energy present in the hot
 548 medium, the gluon fusion becomes the dominant production mode of strange-quark pairs
 549 in the QGP. When the temperature of the QGP decreases and the partons hadronise,
 550 the production of hadrons containing strange (anti-)quarks is enhanced relative to the
 551 production of pions. Moreover, at high collision energies, the strange quarks can also bind
 552 to charm and bottom quarks during hadronisation, producing many exotic hadrons (e.g.
 553 strange D_s or B_s mesons) that would otherwise be rarely seen without the presence of
 554 the QGP. In summary, one expects an overall increase of strange-quark pair production,
 555 leading to an enhancement of the production of strange hadrons in central heavy-ion
 556 collisions compared to proton-proton collisions [62].

557 The enhancement of strange hadrons has been observed at SPS [63, 64] and RHIC [65].
 558 The production yields in heavy-ion collisions of strange hadrons measured at RHIC and
 559 SPS are shown in Figure 1.15. The results show a clear enhancement of the production
 560 of strange baryons in heavy-ion collisions relative to p-p (at RHIC) or p-Be (at SPS)
 561 collisions, increasing for higher N_{part} (more central collisions) and strangeness content
 562 ($\Omega^-[\text{sss}] > \Xi^-[\text{dss}] > \Lambda[\text{uds}]$). This strangeness enhancement can be described using a

563 thermal model based on a grand canonical ensemble approach, suggesting the presence
 564 of a hot medium [62].

565 Recently, the ALICE collaboration published in [66] the observation of enhanced
 566 production of strange hadrons in high-multiplicity proton-proton collisions at $\sqrt{s} =$
 567 7 TeV, as presented in the right plot of Figure 1.15. The results at LHC show that the
 568 enhancement of the strangeness production increases as a function of charged-particle
 569 multiplicity from high-multiplicity p-p to p-Pb to Pb-Pb collisions. Therefore, further
 570 studies of the mechanism of strangeness production at high multiplicities are necessary
 571 to understand the evolution of small systems.

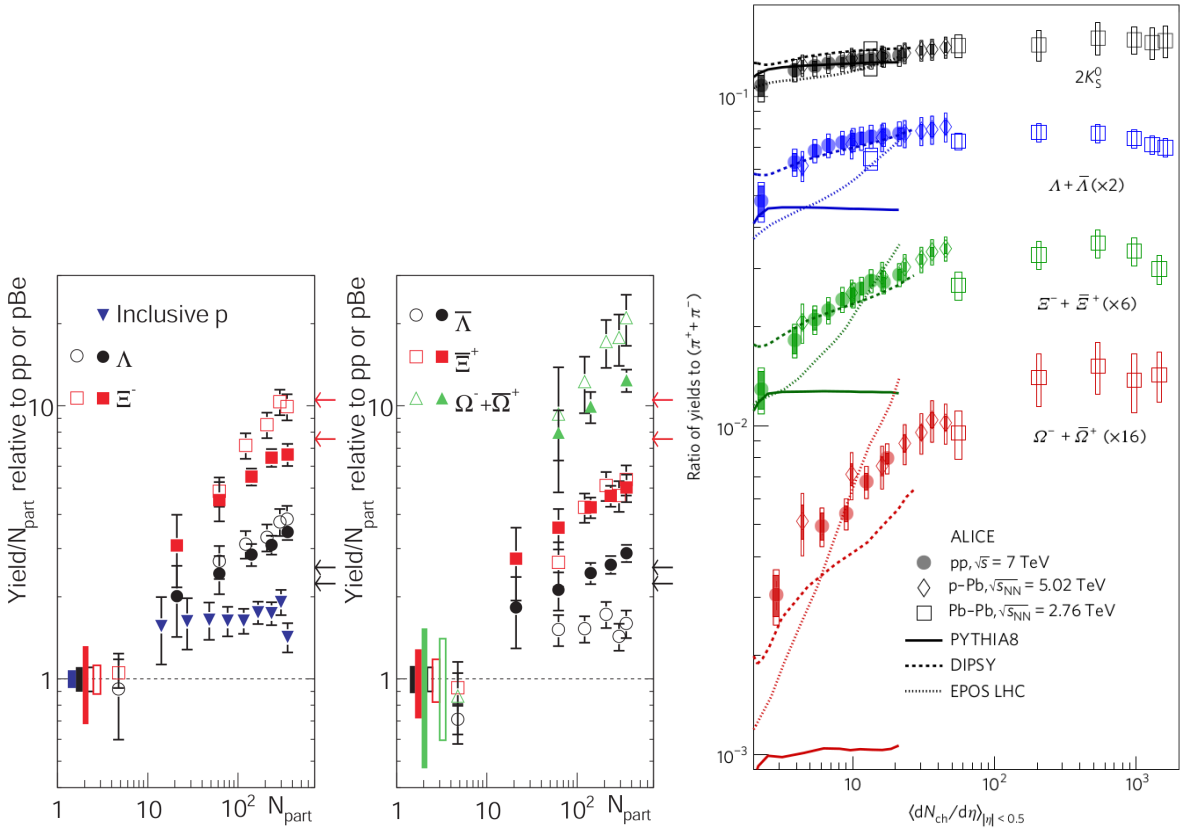


Figure 1.15: Left: Distribution of the yield of inclusive protons and strange baryons, measured by the STAR collaboration in Au-Au collisions at $\sqrt{s_{\text{NN}}} = 200$ GeV (solid symbols) and by the NA57 collaboration in Pb-Pb collisions at $\sqrt{s_{\text{NN}}} = 17.3$ GeV (empty symbols), relative to the corresponding yield in p-p (at RHIC) or p-Be (at SPS) collisions scaled by N_{part} . Figure from Ref. [65]. Right: Distribution of the p_T -integrated yield ratios of strange hadrons to pions as a function of the average charged-particle multiplicity measured in $|\eta| < 0.5$ by the ALICE collaboration in p-p, p-Pb and Pb-Pb collisions at $\sqrt{s} = 7$ TeV, $\sqrt{s_{\text{NN}}} = 5.02$ TeV and $\sqrt{s_{\text{NN}}} = 2.56$ TeV, respectively. Figure from Ref. [66].

572 **1.2.4.3 Jet quenching**

573 Energetic partons are produced in the hard scattering at the beginning of the collision.
 574 These scattered partons fragment into other colour-charged particles, which then create
 575 an ensemble of hadrons during the hadronisation process. The baryons and mesons
 576 produced at the end of the collision tend to move along the same direction as the original
 577 fragmented parton, forming a localised spray of particles called jet. The jets can be
 578 reconstructed by clustering hadrons and other particles around a given direction using a
 579 jet sequential recombination algorithm (e.g. anti- k_t [67]).

580 In heavy-ion collisions, the hard partons lose energy when they traverse the hot
 581 medium either by multiple scattering with the medium constituents or by medium-
 582 induced gluon radiation. As a consequence, the energy of the jets is attenuated and the
 583 jets are considered quenched by the medium. The phenomenon of jet quenching in the
 584 QGP was first proposed in 1982 by James Bjorken. Bjorken suggested in [68] that the
 585 observation of events with two jets, where one of the jets escape the QGP without loosing
 586 energy while the other jet is fully quenched as shown in Figure 1.16, could be used as a
 587 probe to determine the presence of the QGP.

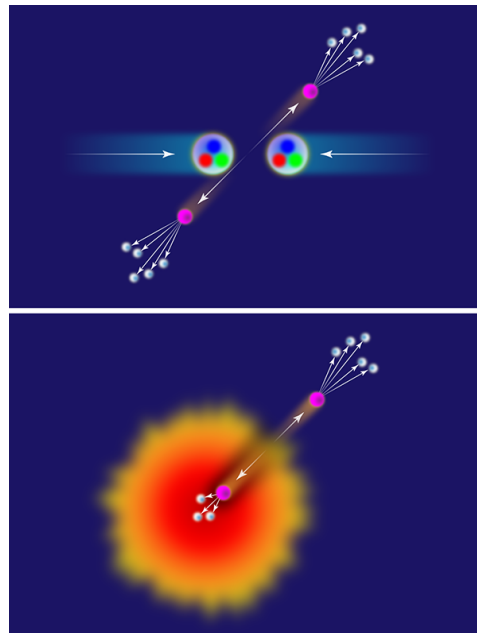


Figure 1.16: Sketch of the production mechanism of two jets in proton-proton (top) and heavy-ions (bottom) collisions. Figure taken from Ref. [69].

588 In order to quantify how the hot nuclear medium modifies the production of a given
 589 particle, one can measure the nuclear modification factor R_{AA} defined as:

$$R_{AA} = \frac{N_{AA}}{\langle N_{coll} \rangle N_{pp}} \quad (1.15)$$

590 where N_{AA} is the yield of particles measured per nucleus-nucleus collision, N_{pp} is
 591 the same yield measured per p-p collision, and $\langle N_{coll} \rangle$ is the average number of binary
 592 nucleon-nucleon collisions. Proton-proton collisions are used as a reference since most of
 593 the events do not produce a QGP, even though it is not excluded that a hot medium could
 594 be formed in the most rare and violent p-p collisions.

595 The first direct observation of jet quenching was determined at RHIC, where the
 596 production of hadrons were found to be suppressed in central Au-Au collisions compared
 597 to p-p collisions. Figure 1.17 shows the nuclear modification factor of direct photons⁷,
 598 pions, η mesons, and charged hadrons measured at RHIC in central Au-Au collisions at
 599 $\sqrt{s_{NN}} = 200 \text{ GeV}$. The results show a strong suppression ($R_{AA} \sim 0.2$) of the production of
 600 hadrons consistent with parton energy loss in the QGP⁸. In addition, the R_{AA} of direct
 601 photons is found to be consistent with unity (expected since photons do not interact
 602 strongly), which serves as a sanity check of the N_{coll} scaling.

603 In the case of LHC, an enhanced dijet asymmetry was observed in Pb-Pb collisions
 604 compared to proton-proton collisions. The dijet asymmetry is quantified by measuring the
 605 jet energy imbalance between the two highest transverse energy jets with an azimuthal
 606 angle separation of $\Delta\phi = |\phi_1 - \phi_2| > \pi/2$. The jet energy imbalance A_J is derived as:

$$A_J = \frac{E_{T1} - E_{T2}}{E_{T1} + E_{T2}} \quad (1.16)$$

607 where E_{T1} is the transverse energy of the most energetic jet among the pair of
 608 jets. 1.18 presents the results, published by the ATLAS collaboration [72], of the dijet
 609 asymmetry distribution and the azimuthal angle between the two jets in different bins
 610 of centrality. The dijet asymmetry measured in Pb-Pb collisions at $\sqrt{s_{NN}} = 2.76 \text{ TeV}$ are
 611 compared to the measurements from p-p collisions at $\sqrt{s} = 7 \text{ TeV}$ and the simulated
 612 results derived using events from the Heavy Ion Jet INteraction Generator (HIJING)
 613 superimposed with PYTHIA events. The LHC results show a significant dijet energy
 614 imbalance in Pb-Pb collisions which increases with the centrality of the collision. The
 615 missing jet energy was later found in the form of low-momentum particles emitted at
 616 larger angles [73]. This dijet asymmetry is not seen in p-p collisions evidencing the
 617 strong jet energy loss present in the QGP.

⁷Photons not originating from the decay of hadrons.

⁸At low p_T , extra thermal photons can be created by the medium providing insights on its average temperature [70].

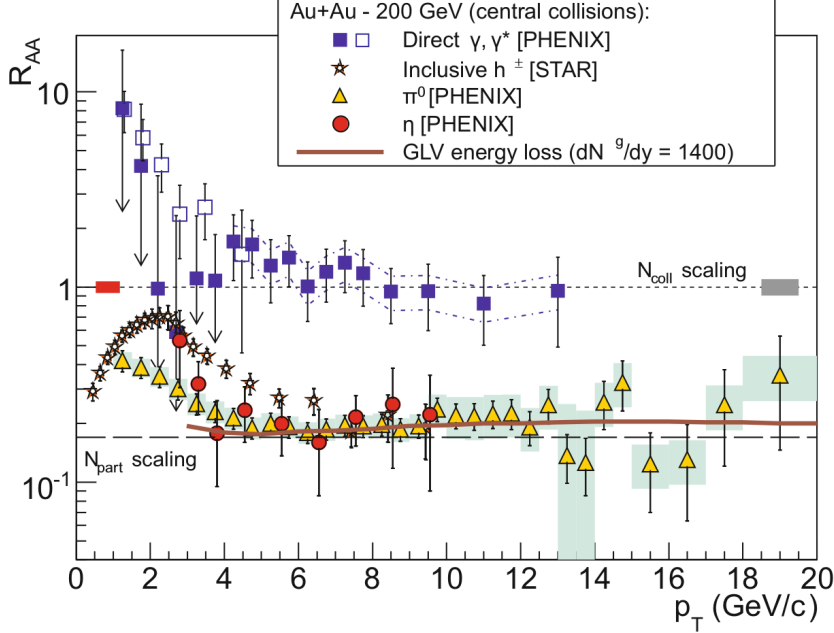


Figure 1.17: Distribution of the nuclear modification factor R_{AA} of direct photons, pions, η mesons and charged hadrons, measured at RHIC in central Au-Au collisions at $\sqrt{s_{NN}} = 200$ GeV. Theoretical predictions of radiative parton energy loss are also included. Figure taken from Ref. [71].

618 1.2.4.4 Quarkonium production

619 Quarkonia ($Q\bar{Q}$) are mesons composed of a heavy quark and its own anti-quark. Quarko-
 620 nia can be classified as charmonia or bottomonia if they are made of charm quarks or
 621 bottom quarks, respectively. The first excited state of charmonia is called J/ψ meson while
 622 for bottomonia is called $\Upsilon(1S)$ meson. The properties of quarkonia are non-perturbative
 623 but since the mass of the heavy quarks is comparable to the mass of the quarkonia, the
 624 quarks move inside the quarkonia much slower than the speed of light. As a result, the
 625 properties of quarkonia can be computed using an effective non-relativistic model. For
 626 instance, one way to describe the binding of the quarks is by using a Cornell potential [74]
 627 given by:

$$V_{Q\bar{Q}}(r) = -\frac{a}{r} + br \quad (1.17)$$

628 where r is the binding radius of the quarkonium, a is the coulombic interaction
 629 coupling, and b is the string tension. By solving the Schrödinger equation for the $Q\bar{Q}$
 630 potential, one finds several higher excited states of charmonia (e.g. $\psi(2S)$) and bottomonia

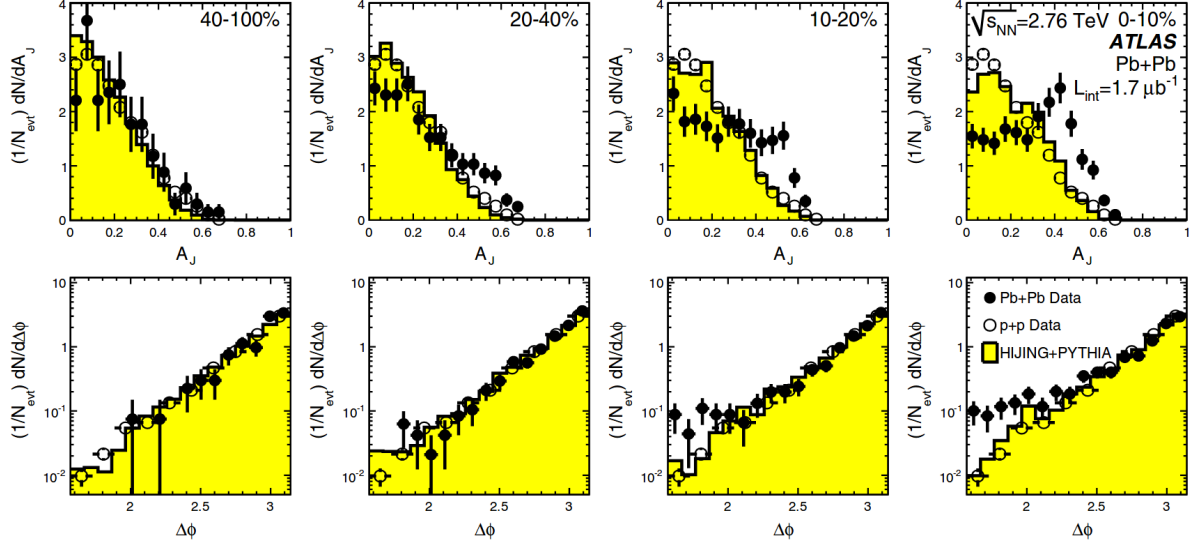


Figure 1.18: Dijet asymmetry measured by the ATLAS collaboration in lead-lead collisions at $\sqrt{s_{NN}} = 2.76$ TeV (points) and proton-proton collisions at $\sqrt{s} = 7$ TeV (open circles). The top panel shows the dijet asymmetry distributions and unquenched HIJING with superimposed PYTHIA dijets (solid yellow histograms), as a function of collision centrality. The bottom panel shows the distribution of the azimuthal angle between the two jets $\Delta\phi$, for data and HIJING+PYTHIA, also as a function of centrality. Figure taken from Ref. [72].

631 (e.g. $\Upsilon(2S)$ and $\Upsilon(3S)$), with lower binding energies and larger radius (i.e. $r_{\Upsilon(1S)} < r_{\Upsilon(2S)} <$
632 $r_{\Upsilon(3S)}$).

633 One of the first signatures suggested to probe the QGP was the suppression of J/ψ
634 meson production. In 1986, Tetsuo Matsui and Helmut Satz [75] proposed that the
635 J/ψ meson binding potential gets screened in the QGP due to the interactions with
636 the free colour charged constituents of the hot medium. The Debye colour screening
637 potential increases with the temperature of the medium until the binding potential can
638 no longer hold the quarks together, and the quarkonium "melts". The binding potential
639 of quarkonium states gets weaker for larger binding radius. As a result, the higher
640 excited states of quarkonium are expected to be more dissociated at a given temperature
641 compared to the ground state, leading to a sequential suppression of quarkonia.

642 The sequential suppression of bottomonium states has been observed at the LHC.
643 Figure 1.19 shows the invariant mass distribution of dimuons measured by the CMS
644 collaboration in Pb-Pb collisions at $\sqrt{s_{NN}} = 5.02$ TeV [76]. The result is compared to the
645 invariant mass distribution obtained by adding the bottomonium mass peaks extracted

from p-p collisions at $\sqrt{s} = 5.02$ TeV on top of the Pb-Pb background and normalised to the $\Upsilon(1S)$ mass peak in Pb-Pb. The comparison shows a clear suppression pattern where the $\Upsilon(3S)$ meson is completely melted while part of the $\Upsilon(2S)$ mass peak still survives. In the case of the $\Upsilon(1S)$ meson, the feed-down contributions from excited state decays of $\chi_b(nP) \rightarrow \Upsilon(1S)$ and $\nu(nS) \rightarrow \Upsilon(1S)$, can reach values up to 40% as measured by the LHCb collaboration for $p_T^\Upsilon > 6$ GeV/c [77]. As a result, it is not clear if the observed suppression of the $\Upsilon(1S)$ meson is due to deconfinement in the QGP or the dissociation of the excited states that decays to the $\Upsilon(1S)$ meson.

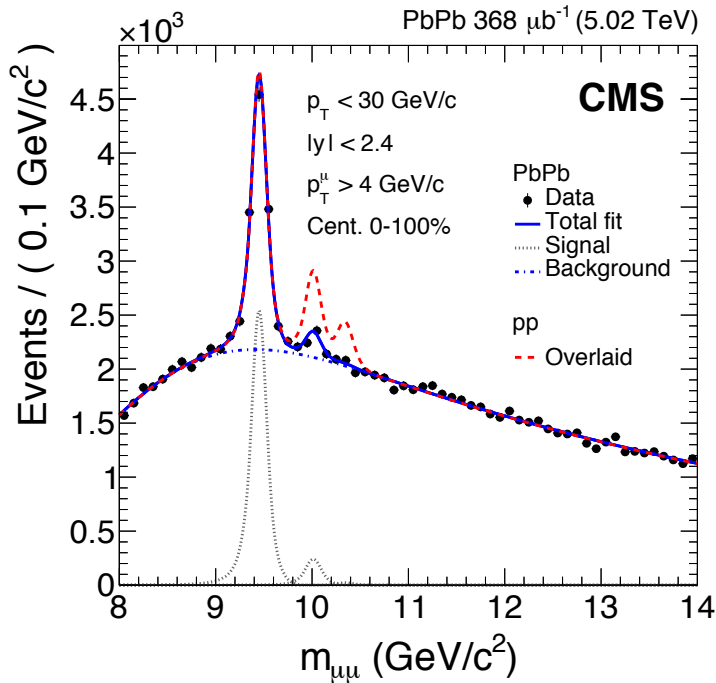


Figure 1.19: Dimuon invariant mass distribution measured by the CMS collaboration in Pb-Pb collisions at $\sqrt{s_{NN}} = 5.02$ TeV. The total fit (solid blue line), the background component (dot-dashed blue line) and the individual $\Upsilon(1S)$, $\Upsilon(2S)$ and $\Upsilon(3S)$ mass peaks (dotted gray lines) are shown. The dashed red line represents the p-p signal shapes added on top of the Pb-Pb background and normalised to the $\Upsilon(1S)$ mass peak in Pb-Pb. Figure taken from Ref. [76].

The first evidence of J/ψ -meson anomalous suppression (i.e. beyond nuclear effects) was observed in Pb-Pb collisions at 158 GeV/nucleon by the NA50 collaboration at SPS [78]. The results at SPS showed that the J/ψ -meson cross section measured in peripheral collisions was consistent with the expectations from nuclear absorption while in central collisions it was more suppressed [79]. The measurement of the J/ψ -meson production in Au-Au collisions at $\sqrt{s_{NN}} = 200$ GeV at RHIC [80] showed a similar level of

660 suppression at mid-rapidity ($|y| < 0.35$) compared to SPS, despite the higher energy den-
661 sity at RHIC. In addition, the production of J/ψ mesons at forward rapidity ($1.2 < |y| < 2.2$)
662 was found to be more suppressed than at mid-rapidity.

663 To understand the measurements of J/ψ -meson production at SPS and RHIC, two
664 explanations were proposed. The first one suggested that, apart from the anomalous
665 suppression, the J/ψ meson production could also be enhanced at RHIC energies. Ac-
666 cording to [81], the J/ψ mesons could be regenerated in the most central collisions from
667 the combination of initially uncorrelated charm quarks (i.e. not produced in the same
668 hard scattering). The number of directly produced $c\bar{c}$ pairs in central nucleus-nucleus
669 collisions is expected to be small at SPS energies, but it can reach values around 10 (200)
670 charm-quark pairs at RHIC (LHC) energies [82, 83]. The second explanation proposed
671 that the production of J/ψ mesons at RHIC was mainly affected by an interplay between
672 initial state effects (e.g. nuclear PDFs or CGC) and the dissociation of the excited states
673 (e.g. χ_c and $\psi(2S)$) that contributes to the feed-down of the J/ψ meson.

674 The measurements of the J/ψ -meson production have also been performed at the
675 LHC. The results of the J/ψ -meson nuclear modification factor measured by the ALICE
676 collaboration in the 0% – 20% most central Pb-Pb collisions at $\sqrt{s_{NN}} = 2.76 \text{ TeV}$ are
677 compared in Figure 1.20 to the results measured by the PHENIX collaboration in the
678 0% – 20% most central Au-Au collisions at $\sqrt{s_{NN}} = 200 \text{ GeV}$. The $J/\psi R_{AA}$ measured at
679 the LHC is larger than the one measured at RHIC at low J/ψ meson p_T , which can so far
680 only be explained by the presence of regeneration.

681 **1.2.4.5 Electroweak boson production**

682 Electroweak particles, such as W bosons and Z bosons, are produced in the parton-parton
683 hard scattering and they do not interact strongly with the nuclear medium produced in
684 the heavy-ion collisions. As a result, electroweak bosons are good probes of the initial
685 stage of the proton-nucleus (p-A) and nucleus-nucleus (A-A) collisions, but they do not
686 probe the QGP. The dominant production mode of electroweak bosons in heavy-ion
687 collisions is via the annihilation of a light quark and anti-quark. The large momentum
688 scales involved in the production of weak bosons allows to derive precise calculations of
689 their partonic cross sections using pQCD.

690 The production yields of electroweak bosons in p-A or A-A collisions are affected by
691 the mix of protons and neutrons in the colliding nucleus (isospin effect), and the depletion
692 (shadowing) or enhancement (anti-shadowing) of the PDFs in the nucleus. Thus, the
693 measurement of the electroweak boson production in heavy-ion collisions can be used

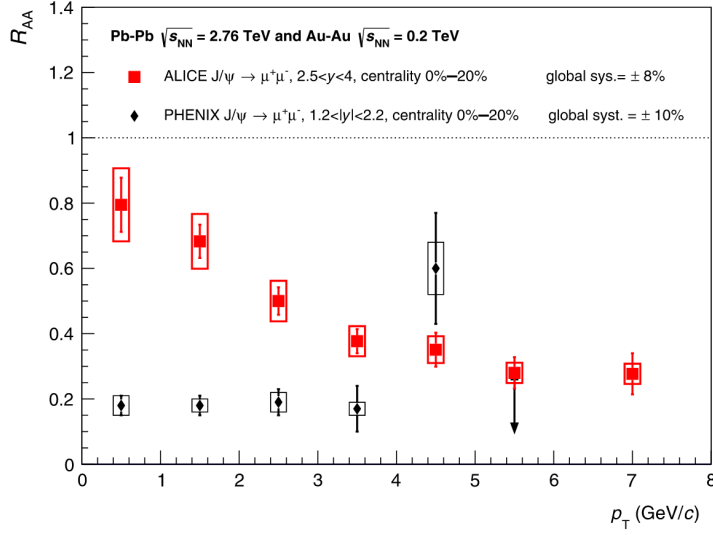


Figure 1.20: Nuclear modification factor of J/ψ meson as a function of transverse momentum measured by the ALICE collaboration in the 0% – 20% most central Pb-Pb collisions at $\sqrt{s_{\text{NN}}} = 2.76 \text{ TeV}$ compared to results from the PHENIX collaboration measured in the 0% – 20% most central Au-Au collisions at $\sqrt{s_{\text{NN}}} = 200 \text{ GeV}$. Figure taken from Ref. [84].

694 to set constraints to the global fits of the nuclear PDFs. In the case of A-A collisions,
 695 the measurement of the nuclear modification factor of Z bosons at the LHC in Pb-Pb
 696 collisions at $\sqrt{s_{\text{NN}}} = 2.56 \text{ TeV}$ [85], presented in Figure 1.21, shows that the production
 697 of weak bosons is not modified by the hot nuclear medium and can then be used as
 698 a *standard candle* to check, at first order, the binary scaling ($R_{\text{AA}} = 1$) and indirectly
 699 determine the centrality of the collision.

700 Summary

701 Our understanding of the QGP has expanded substantially since the last 20 years.
 702 The first evidence of its existence was found at SPS, after studying the suppression
 703 of J/ψ mesons and the strangeness enhancement in Pb-Pb collisions. Years after, the
 704 first observation of the QGP was claimed at RHIC, supported by a vast amount of
 705 experimental signatures such as jet quenching, charmonium suppression, strangeness
 706 enhancement and collectivity. The QGP found at RHIC turns out to behave as a nearly
 707 perfect dense fluid. The QGP was later also observed at the LHC, which has provided
 708 further knowledge on the properties of the QGP at TeV energies. In addition, the LHC
 709 experiments have also observed hints of the formation of a collective medium in small
 710 systems such as high-multiplicity p-p collisions, which is still not fully understood.

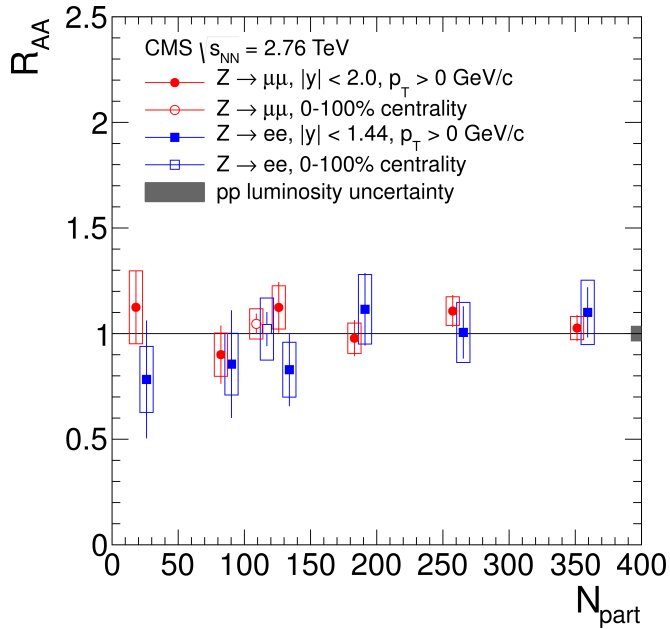


Figure 1.21: Nuclear modification factor R_{AA} of $Z \rightarrow e^+e^-$ (blue squares) and $Z \rightarrow \mu^+\mu^-$ (red circles) events as a function of N_{part} measured by the CMS collaboration in Pb-Pb collisions at $\sqrt{s_{\text{NN}}} = 2.56 \text{ TeV}$. The open points represent the centrality-integrated R_{AA} and the vertical lines (boxes) correspond to statistical (systematic) uncertainties. Figure taken from Ref. [85].

711 The production of J/ψ mesons in heavy-ion collisions has shown a rich phenomenology
 712 and will be the main topic of Chapter 4, where the analysis of charmonia in Pb-Pb
 713 collisions will be presented. These results provide new insights on the production of
 714 non-prompt J/ψ mesons (i.e. from b-hadron decays) and $\psi(2S)$ mesons, extending the
 715 coverage to higher charmonium p_T ranges.

716 Electroweak bosons are sensitive probes of the initial state of the collision and
 717 the measurement of their production in heavy-ion collisions can be used to constrain
 718 the nuclear PDFs, which are crucial theoretical inputs for a better description of the
 719 formation of the QGP. In Chapter 3, this thesis reports the first measurement of significant
 720 nuclear modification of W-boson production.

721

722

EXPERIMENTAL SETUP

723 This chapter provides a brief overview of the experimental setup employed to ac-
724 quire the data used in this thesis. The data is derived from high energy collisions
725 of protons and lead ions recorded by the Compact Muon Solenoid (CMS) detector.
726 The Large Hadron Collider (LHC) and the settings of the particle collisions are described
727 in Section 2.1. The main features of the CMS detector and its components are detailed in
728 Section 2.2.

729 2.1 The Large Hadron Collider

730 The Large Hadron Collider is currently the largest and highest-energy particle accelera-
731 tor in the world. It is installed in an underground tunnel of 26.7 km in circumference,
732 located as deep as 175 m underground beneath the border between France and Switzer-
733 land. The construction of the LHC was handled by CERN and took almost 30 years.
734 The LHC is designed to accelerate and collide beams of protons or heavy ions (e.g Pb
735 nuclei). Before being injected into the LHC, particles are accelerated through a chain of
736 accelerators housed at CERN. Each accelerator boosts the energy of the particles and
737 transfers them to the next machine. The accelerator complex for the LHC is presented
738 in Section 2.1.1 and a short description of the LHC detectors is given in Section 2.1.2.
739 The concept of luminosity is introduced in Section 2.1.3, and brief overview of the LHC
740 schedule and heavy-ion schemes used during 2015-2016, are presented in Section 2.1.4
741 and Section 2.1.5, respectively.

2.1.1 Accelerator complex

There are two main injection chains for the LHC, one optimised for protons and the other for Pb nuclei (Pb^{82+}). Figure 2.1 shows a schematic diagram of the LHC injection chains for protons and Pb ions represented with red and blue arrows, respectively.

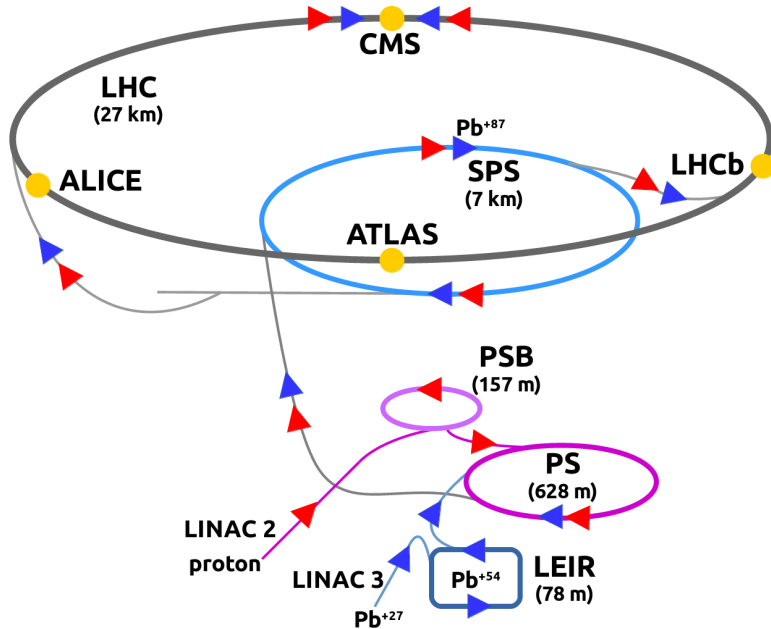


Figure 2.1: Schematic diagram of the LHC injection chain for protons and Pb nuclei. The proton and Pb ion trajectories are indicated with red and blue arrows, accordingly. The location of each LHC detector is also included.

Protons are extracted from a gas of hydrogen atoms by stripping off their electrons in a duoplasmatron, and are initially accelerated to an energy of 50 MeV with radio-frequency (RF) cavities in the linear accelerator Linac-2. Afterwards, they are sent to the Proton Synchrotron Booster (PSB), which is composed of four superimposed synchrotron rings that groups the protons into bunches and accelerates them to 1.4 GeV. Six proton bunches from the PSB are sequentially fed into the Proton Synchrotron (PS), where they are accelerated to 25 GeV and further splitted into 72 bunches separated in time by 25 ns. The proton beam is further accelerated to 450 GeV in the Super Proton Synchrotron (SPS) and alternately injected in the two LHC beam pipes, one beam pipe in the clockwise direction and the other in the counter-clockwise direction. Conventional electromagnets are used to keep the particles circulating in the PSB, PS and SPS accelerators.

The heavy-ion accelerator chain was initially designed in the 1990s for the SPS fixed-

target experiments and then upgraded in the 2000s for the LHC. The Electron Cyclotron Resonance Ion Source (ECRIS) is used to produce heavy ions. In the case of lead, a beam of Pb^{27+} ions with an energy of 2.5 keV/nucleon is extracted from the ECRIS every 200 μs , and then accelerated to 250 keV/nucleon with a 100 MHz RF quadrupole (RFQ). The ion beam is sent afterwards to the linear accelerator Linac-3, which accelerates the Pb ions to 4.2 MeV/nucleon and transfers them to the Low Energy Ion Ring (LEIR). The Pb^{27+} ions are passed through a 0.3 μm -thick carbon foil in the Linac-3–LEIR transfer line, stripping them to Pb^{54+} ions. The LEIR accelerates the Pb^{54+} ions to 72 MeV/nucleon and packs them in bunches using electron cooling. Every 3.6 s, the LEIR feeds two bunches into the PS ring and up to 16 bunches are accumulated, forming a batch, before being transferred to the SPS. The PS batch is compressed to a time interval of 100 ns, and accelerated to 5.9 GeV/nucleon. When the Pb^{54+} ions are sent to the SPS, they are fully stripped (Pb^{82+} ions) through an aluminium foil. The SPS accelerates up to twelve Pb^{82+} ion batches from the PS to 176.4 GeV/nucleon and then injects them into the LHC.

The LHC consists of eight straight sections called insertion regions (IR), connected by eight arc sections as shown in Figure 2.2. The size and trajectory of the particle beams are controlled, in each arc section of the LHC, with a series of superconducting magnets made of Niobium-Titanium and kept at a temperature of 1.9 K with superfluid Helium-4. Dipole magnets are used to bend the particles, while quadrupole magnets focus the beam. Moreover, each particle beam is accelerated in IR4 with eight RF superconducting cavities operated at 400 MHz. The LHC beam dumping system, employed to safely stop the particle beams, is located at IR6. In addition, to protect the LHC from beam losses and absorb the beam halo, a collimation system is installed at IR3 and IR7, dedicated for beam momentum and betatron cleaning, respectively. The other four insertion regions house each of the four main LHC detectors, where the beams are collided in their corresponding interaction point (IP).

2.1.2 Detectors

The four main detectors installed in the LHC ring are:

- A Large Ion Collider Experiment (ALICE) [87]: a particle detector located at IP2, specialised on the measurement of the properties of nuclear matter at high densities. The main interest of the ALICE collaboration is the study of the QGP and the different aspects of heavy-ion physics. The ALICE detector is divided in three sets of subdetectors: the global event detectors are used to characterise

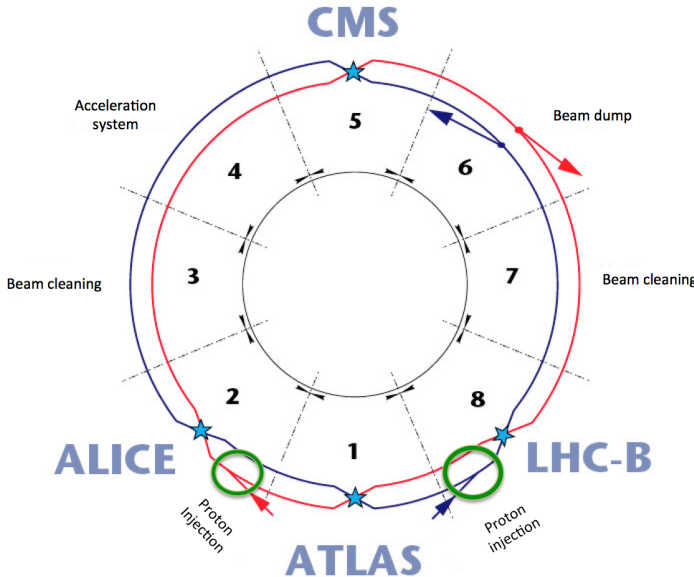


Figure 2.2: Schematic diagram of the LHC layout. Figure taken from Ref. [86].

791 the geometry of the collisions, the central barrel detectors can track charged
792 particles down to low momentum and identify hadrons and electrons, and the
793 muon spectrometer can reconstruct muons in the forward region.

- 794 • A Toroidal LHC ApparatuS (ATLAS) [88]: a general-purpose particle detector
795 located at IP1, optimised for particle collisions at the highest rates and energies
796 achieved in the LHC. It consists of a toroidal magnetic system, an inner tracker,
797 an electromagnetic and hadronic calorimeter, and a muon spectrometer. It is able
798 to measure the energy of electromagnetic particles and hadrons, determine the
799 momentum of charged particles, reconstruct jets, and identify muons with high
800 precision. The ATLAS collaboration is involved in different physic areas including
801 the discovery of the Higgs boson, searches for physics beyond the SM, precision
802 measurements of electroweak and top-quark properties, and heavy-ion physics.
- 803 • Compact Muon Solenoid (CMS) [89]: a multi-purpose particle detector located at
804 IP5. It has a similar design as the ATLAS detector covering the same physics areas.
805 The CMS detector and its inner components are detailed in Section 2.2.
- 806 • LHCb [90]: a single-arm forward spectrometer located at IP8, designed to precisely
807 measure the decays of hadrons containing bottom quarks. It is able to distinguish

between the interaction point and the b-hadron decay vertex, perform particle identification, measure the energy of electrons, photons and hadrons, and reconstruct the trajectories of charged particles. The research programme of the LHCb experiment nowadays covers heavy-flavour, QCD, electroweak and heavy-ion physics. LHCb can also operate in fixed-target mode by injecting a small amount of a noble gas (e.g. helium) around its collision region inside the beam pipe.

2.1.3 Luminosity

The performance of the LHC can be characterised based on its delivered luminosity. The higher the luminosity of the collider, the more particle interactions occur when the beams are collided. The number of interactions per unit time dN/dt , produced in a given reaction, is proportional to the cross section σ_r of the corresponding process, as defined in:

$$\frac{dN}{dt} = \mathcal{L} \sigma_r \quad (2.1)$$

where \mathcal{L} represents the instantaneous luminosity of the particle collisions. In the case of circular beam profiles, the instantaneous luminosity depends on several factors:

$$\mathcal{L} = \frac{k_b N_{b,1} N_{b,2} f_{rev} \gamma}{4\pi \epsilon_n \beta^*} F \quad (2.2)$$

where k_b is the number of bunches collided, $N_{b,1}$ and $N_{b,2}$ are the number of particles per bunch in the two beams, $f_{rev} = 11245$ Hz is the revolution frequency at the LHC, ϵ_n is the normalised transverse beam emittance, β^* is the beta-function defined at the interaction point, and F is a geometric reduction factor due to the angle at which the two beams collide. The integrated luminosity is derived by integrating the instantaneous luminosity over a given period of time.

2.1.4 LHC schedule

The LHC started operations in 2008, and delivered collision data during its first running period (labelled as Run-1) until 2013, followed by a long shut-down (LS1) period of 2 years dedicated to upgrade the machine. The second period of LHC operations (Run-2) started on 2015 and will conclude at the end of 2018. During Run-1, the LHC performed proton-proton (p-p) collisions at a center-of-mass (CM) energy of $\sqrt{s} = 2.36$ TeV in 2009, and p-p collisions at $\sqrt{s} = 7$ TeV and lead-lead (Pb-Pb) collisions at a nucleon-nucleon CM

835 energy of $\sqrt{s_{\text{NN}}} = 2.56 \text{ TeV}$ between 2010 and 2011. In addition, the LHC collided protons
836 at $\sqrt{s} = 8 \text{ TeV}$ in 2012, and proton-lead (p-Pb) at $\sqrt{s_{\text{NN}}} = 5.02 \text{ TeV}$ in 2013. Afterwards,
837 the Run-2 period started with p-p collisions at $\sqrt{s} = 13 \text{ TeV}$ and Pb-Pb collisions at
838 $\sqrt{s} = 5.02 \text{ TeV}$ in 2015, p-Pb collisions at $\sqrt{s} = 8.16 \text{ TeV}$ in 2016, p-p collisions at $\sqrt{s_{\text{NN}}} =$
839 5.02 TeV in 2017, Xenon-Xenon (Xe-Xe) collisions at $\sqrt{s_{\text{NN}}} = 5.16 \text{ TeV}$, and will finish with
840 Pb-Pb collisions at $\sqrt{s_{\text{NN}}} = 5.02 \text{ TeV}$ at the end of 2018.

841 2.1.5 Heavy-ion schemes in 2015-2016

842 The LHC heavy-ion physics programme began in 2010, and has since then provided
843 data from p-Pb and Pb-Pb collisions at various beam energies. The results presented in
844 this thesis are based on heavy-ion data taken between 2015 and 2016. The charmonium
845 analysis, detailed in Chapter 4, uses data from p-p and Pb-Pb collision at $\sqrt{s_{\text{NN}}} = 5.02 \text{ TeV}$
846 taken in 2015, while the W-boson analysis, described in Chapter 3, utilises p-Pb collision
847 data recorded in 2016.

848 In 2015, the LHC programme dedicated to heavy-ion physics took place during four
849 weeks between November and December. The first week was dedicated to p-p collisions at
850 $\sqrt{s} = 5.02 \text{ TeV}$ to create a reference sample for the Pb-Pb collision data. Each proton beam
851 was accelerated to 2.51 TeV. The number of proton bunches were initially 44 and was
852 sequentially increased during the week to a maximum of 1825 bunches. The subsequent
853 week, the LHC beam settings were modified to collide two beams of Pb^{82+} ions at
854 $\sqrt{s_{\text{NN}}} = 5.02 \text{ TeV}$. The LHC started accelerating ten Pb bunches to 2.51 TeV/nucleon, and
855 then progressively increased the number of Pb bunches until it reached 518 at the end
856 of the Pb-Pb data taking. The Pb beam lifetime was shorter than for protons due to the
857 large ultraperipheral electromagnetic interactions between Pb ions, requiring to refill
858 the beams more often. All experiments took Pb-Pb collision data, including LHCb for the
859 first time [91]. The integrated luminosity of the Pb-Pb collision data is shown in the left
860 plot of Figure 2.3.

861 The following year, asymmetric collisions of Pb^{82+} nuclei with protons were performed
862 between November 7th and December 4th. Several beam configurations were imple-
863 mented in 2016 to fulfil the interests of each experiment: ALICE requested p-Pb data
864 at $\sqrt{s_{\text{NN}}} = 5.02 \text{ TeV}$, CMS and ATLAS asked for p-Pb data at $\sqrt{s_{\text{NN}}} = 8.16 \text{ TeV}$ with an
865 integrated luminosity of at least $\mathcal{L} = 100 \text{ nb}^{-1}$, and LHCb requested p-Pb collisions at
866 $\sqrt{s_{\text{NN}}} = 8.16 \text{ TeV}$ complemented with a reversal of the beam direction. After careful plan-
867 ning, the first ten days were dedicated to p-Pb collisions at $\sqrt{s_{\text{NN}}} = 5.02 \text{ TeV}$ optimised
868 for ALICE. Afterwards, the LHC spent two weeks on p-Pb collisions at $\sqrt{s_{\text{NN}}} = 8.16 \text{ TeV}$.

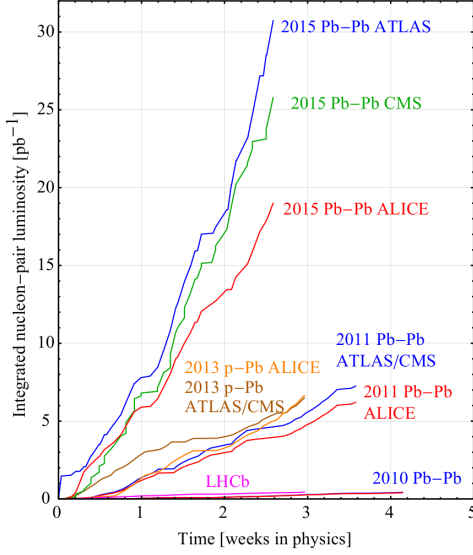


Figure 2.3: Integrated nucleon-pair luminosity delivered by the LHC to each experiment during Pb-Pb collisions at $\sqrt{s_{NN}} = 5.02\text{ TeV}$. The integrated luminosity of p-Pb collisions at $\sqrt{s_{NN}} = 5.02\text{ TeV}$ and Pb-Pb collisions at $\sqrt{s_{NN}} = 2.76\text{ TeV}$ are included for comparison. Figure taken from Ref. [91].

At the beginning of the p-Pb collisions at $\sqrt{s_{NN}} = 8.16\text{ TeV}$, the proton beam was composed of 702 bunches at 6.5 TeV moving in the clockwise direction, while the Pb beam was made of 548 bunches at 2.56 TeV/nucleon moving in the anti-clockwise direction, around the LHC rings. The LHC then proceeded to reverse the beam directions after the integrated luminosity accumulated in CMS and ATLAS reached half of the requested value ($\sim 60\text{ nb}^{-1}$), and kept colliding 540 Pb bunches with 684 proton bunches during the last nine days. At the end of the heavy-ion data taking period, the LHC managed to deliver a total integrated luminosity of $\mathcal{L} = 188\text{ nb}^{-1}$ of p-Pb data to the CMS experiment as shown in Figure 2.4. The beam settings used by LHC during the heavy-ion collision programme performed in 2015 and 2016 are summarised in Table 2.1.

2.2 The Compact Muon Solenoid

The CMS [89] is a multi-purpose particle detector housed in an underground cavern at IP5 of the LHC. The CMS experiment is integrated, at the time of writing this thesis, by an international collaboration of over 5600 members from around 215 institutes from 46 countries. The CMS is composed of a central barrel in the mid-rapidity region closed by two endcap disks, one on each side of the IP, forming a hermetic cylindrical detector.

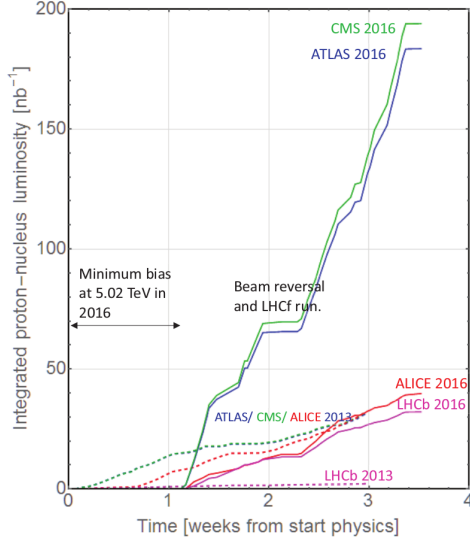


Figure 2.4: Integrated proton-nucleus luminosity delivered by the LHC to each experiment during p-Pb collisions at $\sqrt{s_{NN}} = 8.16 \text{ TeV}$ (solid lines). The integrated luminosity of p-Pb collisions at $\sqrt{s_{NN}} = 5.02 \text{ TeV}$ (dashed lines) is included for comparison. Figure taken from Ref. [92].

Variable	p-p 2015	Pb-Pb 2015	p-Pb 2016
Fill no.	4647	4720	5562
Collision energy $\sqrt{s_{NN}}$ [TeV]	5.02	5.02	8.16
Pb beam energy E_{Pb} [TeV/nucleon]	-	2.51	2.56
Beam energy E_p [TeV/proton]	2.56	6.37	6.5
Pb ions per bunch N_b^{Pb} [10^8]	-	2.0	2.1
Protons per bunch N_b^p [10^{10}]	10.1	-	2.7
No. of Pb bunches k_b^{Pb}	-	518	540
No. of proton bunches k_b^p	1825	-	684
No. of colliding bunches k_c	1813	491	513
β^* [m]	4	0.8	0.6
Crossing angle [μrad]	170	145	140
Pb beam emittance $\epsilon_n^{\text{Pb}}(x, y)$ [μm]	-	2.1	1.6
Pb bunch length σ_z^{Pb} [m]	-	0.09	0.9
CMS peak lumi. $\mathcal{L}^{\text{peak}}$ [$10^{27} \text{ cm}^{-2} \text{ s}^{-1}$]	3.4×10^5	3	869
CMS integrated lumi. \mathcal{L}_{int} [nb^{-1}]	28820	0.6	188

Table 2.1: LHC beam parameters during the highest luminosity physics fills. The luminosity values are averages for CMS. Information extracted from Ref. [93].

2.2. THE COMPACT MUON SOLENOID

The CMS detector consists of four main subdetector systems: the silicon tracker, the Electromagnetic CALorimeter (ECAL), the Hadronic CALorimeter (HCAL) and the muon chambers. A superconducting solenoid magnet placed in the barrel section generates a magnetic field of 3.8 T. The tracking system, the ECAL and the HCAL, are located within the solenoid volume, while the muon system is placed between the layers of the flux-return yoke, which confines the magnetic flux. A sectional view of the CMS detector including the number of channels per subdetector, in its 2016 configuration, is shown in Figure 2.5.

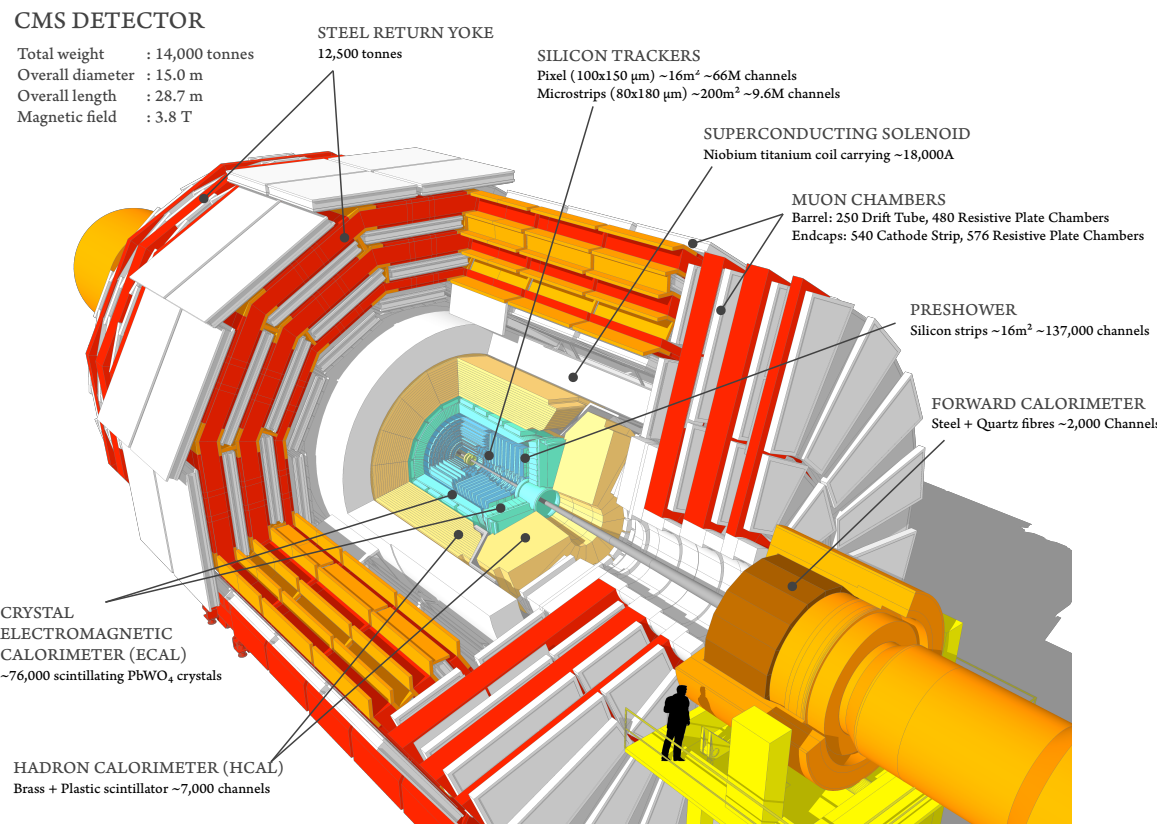


Figure 2.5: Cutaway view of the CMS detector in its configuration used during 2015 and 2016. Labels and basic details of each subdetector are included. [94]

One of the main components of the CMS detector is its superconducting solenoid magnet of 6 m internal diameter and 12.5 m length. The magnet produce a uniform magnetic field of 3.8 T in the central region by supplying an electric current of 18.1 kA through a four-layer winding coil made of NbTi wire. To be able to sustain the large electric currents, the solenoid coil is thermally insulated within a vacuum volume and

898 operated in superconducting mode at a temperature of 4.6 K with a thermal-siphon
 899 cooling system fed with liquid helium. The flux of the magnetic field outside the barrel
 900 is returned through a massive steel yoke of 10000 tons divided in five barrel wheels
 901 and four endcap disks at each end. In case there is a major system fault or the magnet
 902 suffers a superconducting-to-resistive transition (quench), the electric power source is
 903 immediately disconnected and the stored magnetic energy is quickly discharged through
 904 a 30 mΩ dump resistor placed outdoors.

905 The coordinate system of the CMS detector is centred at the interaction point. It
 906 is oriented in such a way that the x -axis points radially inward to the centre of the
 907 LHC ring while the y -axis points upward perpendicular to the LHC plane. The z -axis
 908 is defined parallel to the beam. By convention, the positive z -direction is defined along
 909 the counter-clockwise beam direction. For asymmetric collisions, such as p-Pb, it is
 910 later reversed (if necessary) to match the proton-going direction, so that the "forward"
 911 (low Bjorken-x) physics corresponds to the "forward" ($\eta > 0$) part of the detector (see
 912 Section 3.2.1).

913 The trajectory of particles measured at CMS is described in the coordinate system
 914 displayed in Figure 2.6. The polar angle θ is measured from the z -axis while the az-
 915 imuthal angle ϕ is measured from the x -axis in the x - y plane, called the transverse
 916 plane. The radial coordinate r is also measured in the transverse plane. The polar angle
 917 is replaced by the pseudorapidity η which, for massless particles, matches the rapidity
 918 and is Lorentz invariant under longitudinal boosts. The pseudorapidity is zero in the
 919 transverse plane and approaches infinity towards the z -axis, according to:

$$\eta = -\ln \left[\tan \left(\frac{\theta}{2} \right) \right] \quad (2.3)$$

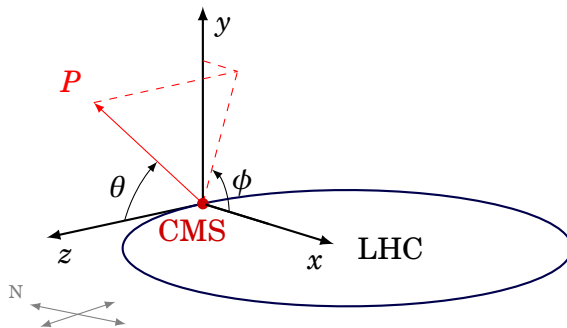


Figure 2.6: Schematic diagram of the coordinate system used in the CMS experiment.

920 The details of the original configuration of the CMS detector can be found in Ref. [89].
921 After Run-1 was over, the CMS underwent several improvements as part of the planned
922 upgrades for the LS1 shut-down period (2013-2014). The systems upgraded during LS1
923 include the muon endcap stations, the hadron calorimeter, and the L1 trigger. In the
924 case of the muon system, an additional disk of muon detectors was installed on the
925 outermost part of each endcap section providing a fourth measurement in the forward
926 region [95]. Moreover, the photosensors of the forward (outer-barrel) hadron calorimeter
927 were replaced with multi-anode photomultiplier tubes (silicon photomultipliers), and the
928 corresponding readout electronics were upgraded to handle the new sensors [96]. And
929 finally, the framework and electronics of the L1 trigger system were completely changed
930 to sustain the increasing interaction rate of the LHC beam collisions [97].

931 **2.2.1 Subdetectors**

932 The CMS detector [89] is composed of several subdetectors which provide a precise
933 measurement of the trajectory and energy of the particles emitted from the LHC collisions.
934 The superconducting solenoid volume contains the inner tracker close to the beam line
935 followed radially outwards by the electromagnetic and hadronic calorimeters. The muon
936 chambers are installed outside of the solenoid, interspersed with layers of the flux-return
937 yoke. An electromagnetic preshower is installed in the endcaps complementing the ECAL
938 to improve the identification of photons and electrons.

939 **2.2.1.1 Tracker**

940 The CMS tracking system is designed to measure the trajectory of charged particles and
941 reconstruct the 3D vertex position of the primary interaction and the secondary decays.
942 It is completely surrounded by the volume of the solenoid magnet in the barrel region,
943 and has a diameter of 2.5 m and a length of 5.8 m, centred on the interaction point. The
944 CMS tracker is made of a pixel detector and a silicon strip tracker. A schematic cross
945 section of the CMS tracker is presented in Figure 2.7.

946 The pixel detector is made of 1440 pixel modules installed in the tracker section
947 closest to the interaction region. It covers the pseudorapidity range $|\eta| < 2.5$ with three
948 Barrel Pixel (BPix) layers and two Forward Pixel (FPix) disks. The BPix layers are placed
949 at a radii of 4.4 cm, 7.3 cm and 10.2 cm from the beam axis, while the FPix disks are
950 located, on each side of the IP, at a longitudinal distance of $z = \pm 34.5$ cm and $z = \pm 46.5$ cm.
951 The BPix (FPix) detectors contain 48 (18) million silicon pixels, each with a cell size of

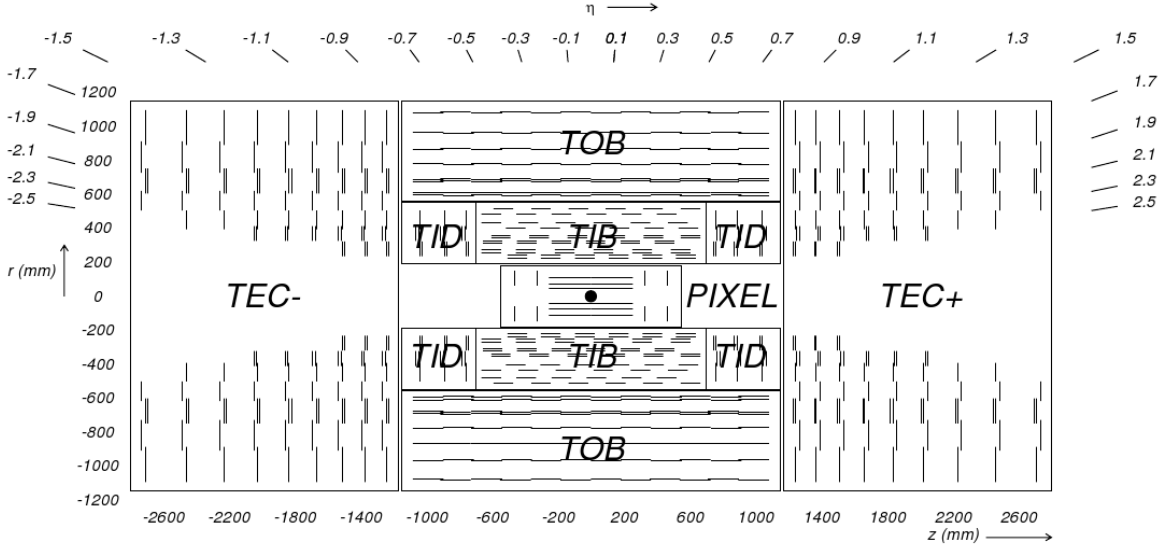


Figure 2.7: View of the CMS tracker in the r - z plane. Each line represents a detector module. Figure taken from Ref. [89].

952 $100 \times 150 \mu\text{m}^2$. The arrangement of the pixel detector modules in the forward)
 953 region provides, over the full tracker coverage, three tracking hits per track and a
 954 position resolution of 15-20 (15) μm in the z -coordinate.

955 The silicon-strip tracker contains 9.3 million strips divided in 24244 silicon sensors,
 956 covering the region between the pixel detector and the ECAL. In the barrel region, the
 957 strip tracker is composed of the Tracker Inner Barrel (TIB), made of four concentric
 958 cylinders placed at a radius between 25.5 cm and 49.8 cm, and the Tracker Outer Barrel
 959 (TOB), which consists of a wheel-like structure containing six cylinders with an inner
 960 (outer) radius of 55.5 (116) cm. The pseudorapidity coverage of the strip tracker is
 961 extended up to $|\eta| = 2.5$ with three Tracker Inner Disks (TID) and nine Tracker EndCap
 962 (TEC) disks, installed on each endcap section along $80 \text{ cm} < |z| < 90 \text{ cm}$ and $124 \text{ cm} < |z| <$
 963 282 cm , accordingly. The strip detector modules used in the TIB, TID and inner four
 964 TEC rings are made of one $320 \mu\text{m}$ -thick sensor, while those used in the TOB and outer
 965 five TEC rings are made of two $500 \mu\text{m}$ -thick sensors. The strip pitch varies between
 966 $80\text{-}120 \mu\text{m}$, $100\text{-}141 \mu\text{m}$, $122\text{-}183 \mu\text{m}$, and $97\text{-}184 \mu\text{m}$, in the TIB, TID, TOB and TEC,
 967 respectively. The strip tracker can achieve a position resolution in the TIB (TOB) of 23-35
 968 ($35\text{-}53$) μm in the transverse plane and 230 (530) μm in the z -coordinate.

969 **2.2.1.2 Electromagnetic calorimeter**

970 The ECAL of the CMS is a hermetic homogeneous calorimeter composed of 75848 lead-
 971 tungstate (PbWO_4) crystals. The ECAL is designed to fully absorb and measure the
 972 energy of electrons and photons. The PbWO_4 material was chosen for its small Molière
 973 radius (2.2 cm), a short radiation length (0.89 cm), and a high density (8.28 g cm^{-3}).
 974 When a high-energy electron or photon interacts with the nuclei of the ECAL crystals, it
 975 generates a cascade of electromagnetic particles (e^- , e^+ and γ) and induces the emission
 976 of blue scintillation light ($\lambda \approx 420 \text{ nm}$), which is then measured in photodetectors. The
 977 total amount of scintillation light produced is proportional to the energy deposited in
 978 the crystals by the electrons and photons. In order to cope with the running conditions
 979 of the LHC, the crystals are designed to have a fast response (25 ns), and be optically
 980 transparent and radiation-hard.

981 The ECAL is installed between the silicon-strip tracker and the HCAL. It is divided
 982 in a cylindrical-barrel section (EB) and two endcap rings (EE), one on each side of the
 983 IP. The EB is made of 61200 crystals of 23 cm long, covering the pseudorapidity range
 984 $|\eta| < 1.48$ with a granularity of 170-fold in η and 360-fold in ϕ . The crystals are grouped
 985 in modules of either 400 or 500 units, and four modules are assembled in so-called
 986 supermodules. The EB has a total of 36 supermodules, each covering 20° in ϕ with 1700
 987 crystals. The scintillation light is measured in the EB with Avalanche PhotoDiodes
 988 (APD), mounted in pairs on the back of each crystal. Each APD is operated, with a
 989 high-voltage power supply system, at gain 50 and a voltage between 340-430 V. The
 990 schematic layout and geometric view of the ECAL are shown in Figure 2.8.

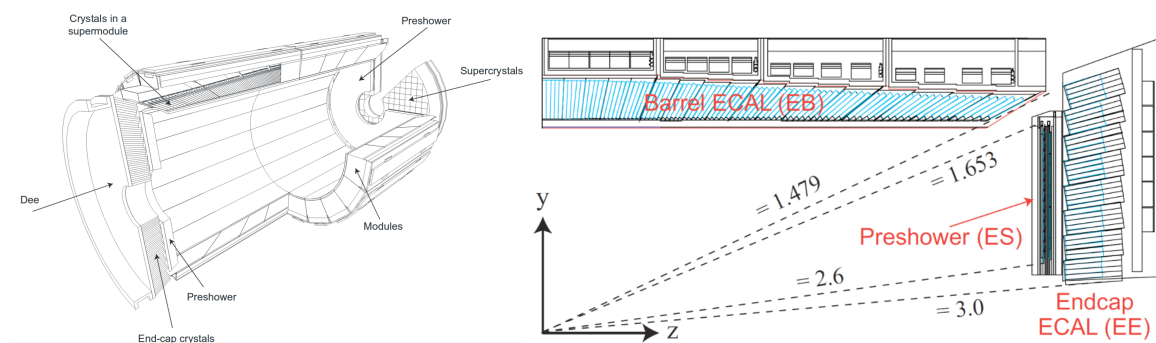


Figure 2.8: Schematic layout [89] (left) of the CMS electromagnetic calorimeter, and its corresponding one-quarter geometric view [98] (right).

991 The EE rings are installed at $z = \pm 3.15 \text{ m}$, extending the coverage of the ECAL up
 992 to $|\eta| = 3.0$. The EE consists of 14648 crystals of 22 cm long, assembled in units of 5×5

993 crystals known as SuperCrystals (SC). Each EE ring is divided in two halves, each
994 containing 156 SCs. A single-stage photomultiplier called Vacuum PhotoTriodes (VPT),
995 attached to the back of each EE crystal, is used to measure the scintillation photons. The
996 VPT has a diameter of 25 mm, a quantum efficiency of 22% at a wavelength of 430 nm,
997 and a gain of 10.2 at zero magnetic field.

998 An additional calorimeter called the Preshower detector is installed in the endcap
999 rings between the tracker and the EE. The Preshower is an electromagnetic sampling
1000 calorimeter of 20 cm thickness, optimised to identify photons from neutral pion decays.
1001 It is composed of two layers of lead absorbers interleaved with 4300 silicon sensors
1002 organised in 32 strips. Each silicon sensor has a thickness of 320 μm and an active area
1003 of $63 \times 63 \text{ mm}^2$. Incoming photons and electrons initiate an electromagnetic shower when
1004 they interact with the lead absorbers. The energy deposited in the absorbers and the
1005 transverse profile of the shower are measured in the silicon strips.

1006 The response of the crystals and the signal amplification of the APDs depend on
1007 the operating temperature. As a result, a water flow cooling system is installed to
1008 keep the crystals and sensors at a stable temperature of $18.00 \pm 0.05^\circ\text{C}$. Moreover, the
1009 transparency of the crystals to scintillation light is affected by the radiation dose due
1010 to the formation of colour centres which absorbs part of the light. The variation of the
1011 crystal transparency is monitored using laser pulses introduced into the crystals at a
1012 frequency of 80 Hz. The laser monitoring system uses two blue lasers ($\lambda \approx 440 \text{ nm}$) to
1013 track the radiation-induced transparency variations, which are then corrected for by
1014 recalibrating the detector.

1015 The energy resolution of the ECAL is affected by several sources, such as the fluc-
1016 tuations in the shower, crystal non-uniformities, calibration errors, and noise in the
1017 photodetectors. The relative energy resolution of the ECAL is parametrised as a function
1018 of the measured energy E via:

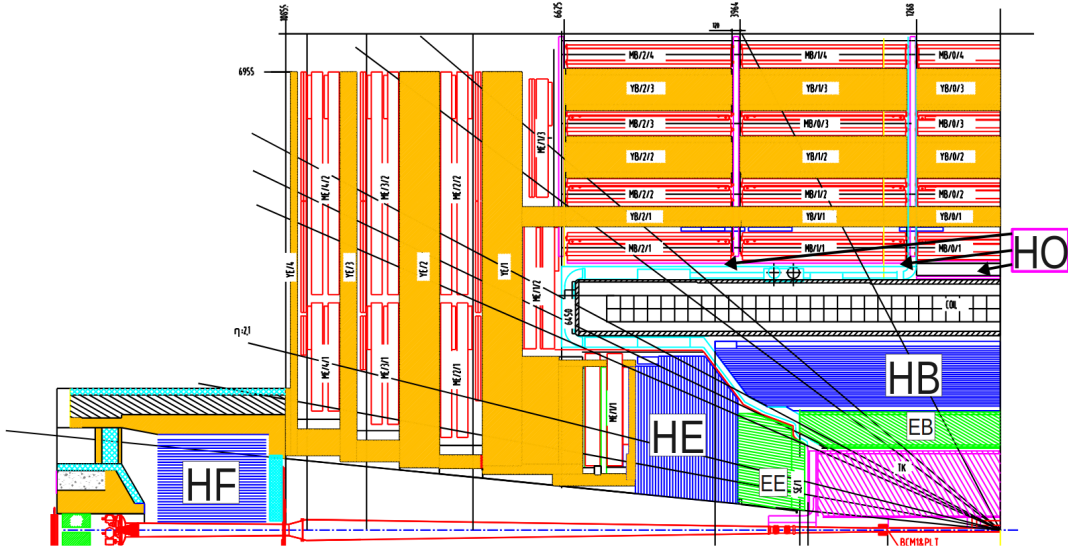
$$\left(\frac{\sigma_E}{E}\right)^2 = \left(\frac{2.8\%}{\sqrt{E/\text{GeV}}}\right)^2 + \left(\frac{12\%}{E/\text{GeV}}\right)^2 + (0.3\%) \quad (2.4)$$

1019 **2.2.1.3 Hadronic calorimeter**

1020 The HCAL is a hermetic sampling calorimeter made of 70000 plastic-scintillator tiles
1021 interleaved with absorber plates. The goal of the HCAL is to completely absorb and
1022 measure the energy of hadrons. When a hadron hits an absorber plate, it induces a
1023 shower of particles through the successive absorber layers. The secondary particles

2.2. THE COMPACT MUON SOLENOID

produced in the cascade pass through the plastic tiles, located in between the absorbers, leading to the emission of scintillator light at a peak wavelength of $\sim 440\text{ nm}$. Photons generated on each tile are collected with WaveLength-Shifting (WLS) fibres fabricated in a double-clad configuration with a diameter of 0.94 mm. The WLS fibres shifts the scintillator light to the green spectrum (515 nm) and pass it to fibre-optic waveguides which then transfers the light to a phototransducer. The scintillator tiles are grouped in trays that are 5° wide in ϕ . A geometric view of CMS, highlighting the different components of the HCAL, is presented in Figure 2.9.



trays. The HO has 2730 scintillator tiles of 10 mm thick organised in 422 trays, offering the same $\Delta\eta \times \Delta\phi$ granularity as the HB. The HO uses a multipixel Geiger-mode APD, known as Silicon PhotoMultiplier (SiPM), to detect photons.

The coverage of the HCAL is extended in the forward region to $|\eta| = 3$ with the Hadron-Endcap (HE) calorimeter and up to $|\eta| = 5.2$ with the Hadron-Forward (HF) calorimeter. The HE is located in the endcap rings and its absorber is made of two 79 mm-thick plates of cartridge brass separated by 9 mm. The HE contains 20916 plastic tiles and has a $\Delta\eta \times \Delta\phi$ granularity of 0.17×0.17 . The HE also uses HPDs to measure the scintillator light.

The HF is divided in 36 wedges that are 20° wide in ϕ , and its front face is located at $z = \pm 11.2$ m, on each side of the IP. Since the HF experience a large energy deposit from the beam collisions, its design has been optimised to handle high levels of radiation. The HF absorber consists of a 1.7 m-depth cylindrical structure made of 5 mm-thick steel-grooved plates, while the HF active medium is composed of quartz fibres of polymer hard-cladding and fused-silica core. The signal consists of Cherenkov light generated when energetic charged particles from the shower traverse the quartz fibres. The Cherenkov light is measured by multi-anode PhotoMultiplier Tubes (PMT) shielded behind 40 cm of steel. The HF fibres are inserted in the absorber grooves along the beam line in two longitudinal segments. Long fibres are inserted over the full absorber depth while short fibres starts at a depth of 22 cm from the front face covering the back of the absorber. Since most of the energy of electrons and photons is deposited in the first 22 cm while hadrons are able to penetrate more in the HF absorber, the difference in energy measured in the long and short fibres is used to estimate the electromagnetic and hadronic components of the shower.

2.2.1.4 Muon detectors

The CMS muon tracking system measures the momentum and charge of muons in the fiducial region $|\eta| < 2.4$. It is divided in four stations corresponding to four concentric cylinders in the barrel region and to four disks on each endcap section. Figure 2.10 shows a geometric view of one quadrant of the CMS muon system. The dense material of the calorimeters and the solenoid magnet absorbs most of the hadrons, electrons and photons, while energetic muons are able to reach the muon stations loosing only a small fraction of their energy. Muons are detected in CMS using three type of gaseous technologies: Drift Tubes (DT), Cathode Strip Chambers (CSC) and Resistive Plate Chambers (RPC).

The DT detectors are used in the barrel region of the muon system ($|\eta| < 1.2$). A

2.2. THE COMPACT MUON SOLENOID

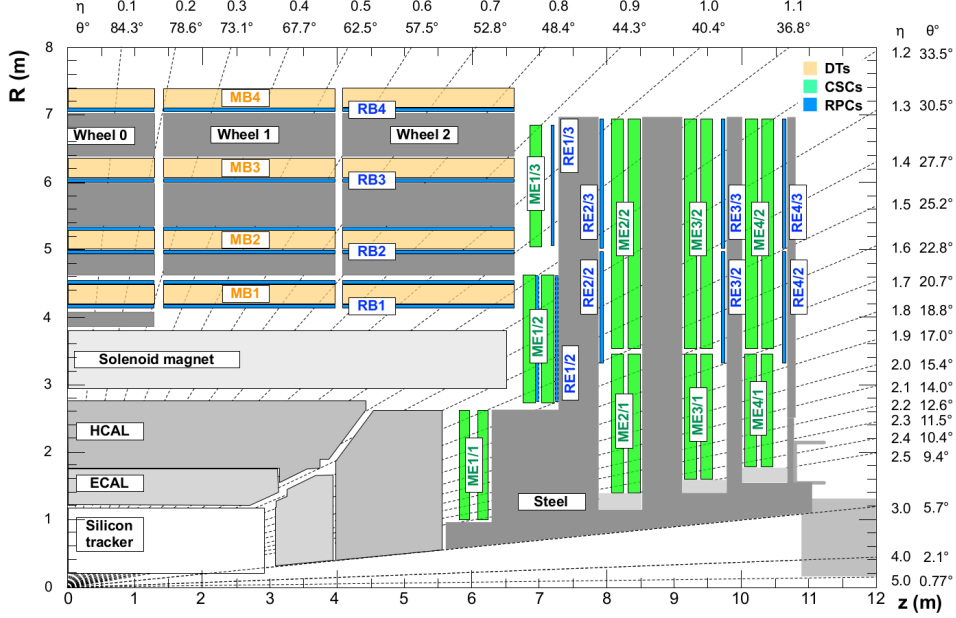


Figure 2.10: Geometric view of one quadrant the CMS detector in the r - z plane. Each chamber of the muon system is shown in blue (RPC), green (CSC) and orange (DT). Figure taken from Ref. [99].

DT consists of a 50 μm -diameter anode wire placed inside a rectangular tube connected to two cathode strips and filled with a gas mixture of 85% of Ar and 15% of CO₂. The layout of a DT cell is displayed on the left of Figure 2.11. When a charged particle passes through a DT, it ionises the gas releasing electrons that are then detected in the anode wire. The DT system is composed of 172000 anode wires of 2.4 m length. There are four DT chambers in each of the five barrel wheels and twelve azimuthal sectors. In total, the fourth station contain 70 DT chambers and the first three stations contain 60 DT chambers each. Four layers, each containing up to 60 DTs, are grouped in units called SuperLayers (SL). The DT chambers of the three inner stations (outermost station) are made of three (two) SLs. The first and third SL, as shown on the right of Figure 2.11, have their anode wires installed parallel to the z -axis to measure the bending in the transverse plane, while the anode wires of the second SL are placed orthogonal to the beam line to measure the position in the z -coordinate. The SLs of the fourth station only have anode wires parallel to the z -axis. The SLs measure the position and angle of the track segments with a precision of 1.5 mm and 20 mrad, respectively.

Instead of DTs, the two endcap sections use 540 CSCs covering a pseudorapidity range $0.9 < |\eta| < 2.4$. The CSC system is designed to cope with the higher rate of particles and the large non-uniform magnetic field present in the forward region. A CSC is made

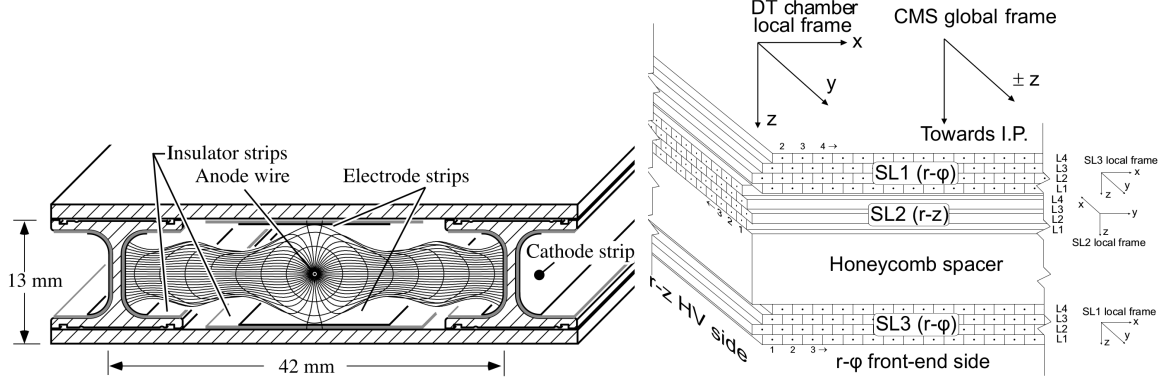


Figure 2.11: Schematic layout of a DT cell (left) and a DT chamber (right). Figures taken from [100].

of six anode wire planes crossed with seven cooper cathode strips within a gas mixture of 40% Ar, 50% CO₂, and 10% CF₄, forming a multiwire proportional chamber. The CSCs are operated at 3.6 kV with a gas gain of 7×10^4 , and are organised in chambers installed perpendicular to the beam pipe. The CSC chambers are trapezoidal and cover either 10° or 20° in ϕ , and they overlap providing contiguous coverage in ϕ . The cathode strips are milled in panels along constant $\Delta\phi$ -width and provide measurements in the transverse plane, while the anode wires are placed azimuthally and measure the pseudorapidity of muons. The CSC system has a total of 266112 cathode-strip and 210816 anode-wire read-out channels. A schematic layout of a CSC is shown in Figure 2.12.

To allow fast muon triggering, the barrel and endcap regions are complemented with RPC detectors. A RPC module consists of an anode plate parallel to a cathode plate, as shown in Figure 2.13. The RPC plates are separated by a gap filled with a gas mixture of 96.2% C₂H₂F₄, 3.5% iC₄H₁₀ and 0.3% SF₆, and operated in avalanche mode with read-out strips in between. There are 480 (576) RPC chambers in the barrel (endcap) region. Each RPC chamber consists of two or three modules of up to 96 strips each. Each RPC strip covers 0.31° in ϕ . The RPC chambers are organised in six coaxial cylinders in the barrel region and four rings in the endcaps, covering the pseudorapidity region up to $|\eta| = 1.9$. The innermost ring span 20° in ϕ while the other rings span 10°. The RPC modules are optimised for fast muon triggering by detecting ionising events faster than the time interval between two bunch crossings (25 ns). They provide a good timing resolution but with a coarser spatial granularity compared to DTs and CSCs. The RPCs also allow to resolve ambiguities between tracks made from multiple hits in the muon chambers.

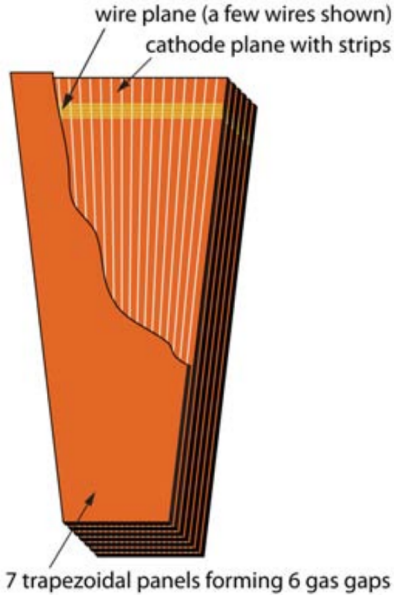


Figure 2.12: Schematic layout of a CSC. Figure taken from [89].

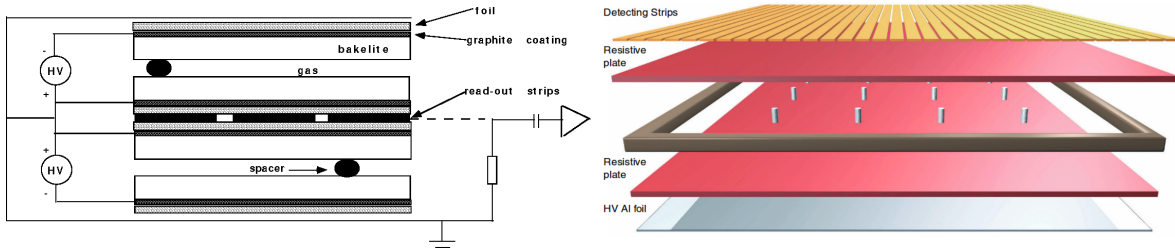


Figure 2.13: Cross section view (left) [101] and exploded view (right) [102] of a RPC module.

1119 2.2.2 Trigger system

1120 At LHC design conditions, the two beams crosses each IP every 25 ns, equivalent to a
 1121 frequency of 40 MHz. Once a collision is recorded by CMS, all detector channels are read
 1122 out and the data is sent to the CERN main computing farm, known as the Tier-0, to be
 1123 further processed with the CMS SoftWare (CMSSW). However, the Tier-0 processing
 1124 rate is limited by its CPU performance and storage capacity. As a result, the input rate
 1125 of data transferred to the Tier-0 has to be kept below 1 kHz to avoid overflowing the
 1126 computing centre.

1127 To reach this goal, CMS has implemented a two-level trigger system designed to select
 1128 events of interest for physics analysis. The first level, known as the Level-1 (L1) trigger,
 1129 lowers the collision rate to an output rate of 100 kHz by filtering events using custom

hardware. The next trigger level, called the High Level Trigger (HLT), is performed in a cluster of computers located in the CMS experimental cavern. The HLT software algorithms further reduce the data rate down the limit required by the Tier-0.

2.2.2.1 **Level-1 trigger**

The L1 trigger system [103] is designed to handle the large collision rate of the LHC. To accomplish this goal, the L1 trigger is made of custom hardware modules optimised to process the events with a latency of less than 4 μ s. The L1 trigger is divided in two parts: the calorimeter and muon triggers.

The data from each subdetector are organised in units called Trigger Primitives (TP). The calorimeter TP are derived from the Trigger Towers (TT), each corresponding to a region of 0.087×0.087 in $\eta\phi$ (represents 5×5 crystals in the ECAL). While for muons, a TP corresponds to a segment in either the DT or CSC systems. The information of the inner tracker is not used in the L1 trigger since the tracker data can not be currently read out within a bunch crossing time of 25 ns. As a result, the L1 calorimeter trigger cannot discriminate between electrons and photons. The output of the L1 muon and calorimeter triggers is combined in the L1 Global Trigger (GT), which then takes the final decision to either reject or accept the event.

The L1 trigger decision is determined according to a set of user-defined L1 trigger conditions. The L1 criteria are organised in a menu made of different algorithms which are programmed by the users and hard-coded in the firmware of a Field-Programmable Gate Array (FPGA). Some typical conditions used to define the L1 algorithms include setting a minimum p_T threshold or η range on the L1 objects, or requiring events to have a given amount of L1 candidates. If an event passes the conditions of at least one of the L1 algorithms, the whole CMS detector is read out and the data is then sent to the HLT computers. The L1 menu is updated several times during data taking, to adapt to the changes in the LHC beam conditions and physics requirements.

In order to reduce the contribution from cosmic muons and also suppresses pre-firing from the calorimeters caused by particles interacting in the photomultipliers, the events processed by the L1 trigger are required to be associated to a bunch crossing. The Beam Pick-up Timing eXperiment (BPTX) detectors, installed at a distance of $z = \pm 175$ m on each side of the IP, are used to select valid bunch crossings by checking for a coincidence of the signals on each side.

The L1 system underwent, between 2014 and 2015, an extensive upgrade that included a complete replacement of the electronics and the data acquisition system. The

1164 previous L1 trigger, used during LHC Run-1 and 2015, is referred in this manuscript as
 1165 the legacy L1 trigger, while the L1 trigger deployed before the pPb collision run in 2016,
 1166 is called the upgraded L1 trigger.

1167 **Legacy L1 trigger.** The legacy L1 trigger [103] was used in CMS until the end of 2015,
 1168 covering the entire LHC Run-1 and beginning of Run-2 data taking periods. The events
 1169 from p-p and Pb-Pb collisions at $\sqrt{s_{\text{NN}}} = 5.02 \text{ TeV}$, in particular the data used for the
 1170 charmonium analysis reported in Chapter 4, were selected using the legacy L1 trigger.
 1171 Figure 2.14 shows a diagram of the legacy L1 trigger system.

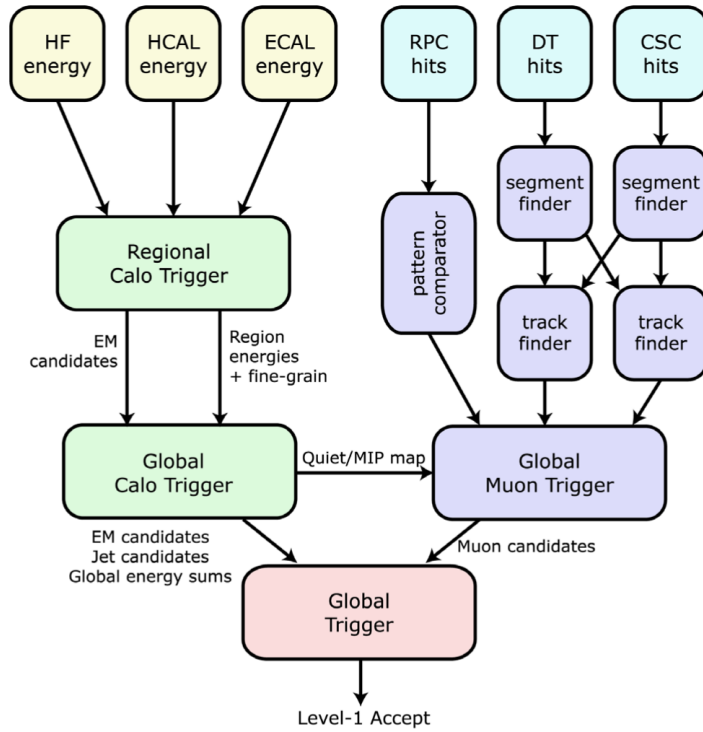


Figure 2.14: Diagram of the legacy L1 trigger of CMS. Figure taken from Ref. [104].

1172 In the legacy L1 trigger, the transverse energy E_T values are read out from each
 1173 ECAL, HF and HCAL TT, and then sent to the Regional Calorimeter Trigger (RCT). The
 1174 RCT processes the raw data and produces 72 electron-photon (e/γ) candidates (identified
 1175 as energy clusters mainly deposited in the ECAL), computes the E_T in the HF region
 1176 and derives 396 E_T sums of 4×4 TT regions. The Global Calorimeter Trigger (GCT) then
 1177 receives the objects from the RCT and reconstructs jets and hadronic tau decays based on
 1178 the regional E_T sums, sorts the e/γ candidates according to their E_T , and computes global

1179 quantities such as the total E_T . Eight e/γ candidates, eight jets, four tau candidates, the
1180 HF E_T , and the global quantities are then sent to the GT.

1181 The legacy L1 muon trigger follows a detector-based design. The DT and CSC hit
1182 measurements are used by the front-end trigger electronics to reconstruct track segments
1183 in each muon station. Regional track finders (TF), one for each muon subsystem, sort the
1184 track segments and identify muons using pattern recognition algorithms. The hardware
1185 modules of the DT (CSC) TFs consists of 72 (12) Versa Module Eurocard (VME) boards.
1186 The muon momentum is estimated based on the bending of the track along the magnetic
1187 field. The position of each muon detector hit is converted to $\eta\text{-}\phi$ coordinates using lookup
1188 tables derived from simulation. To cover the overlap region between the CSC and DT
1189 muon systems, the information of their TFs is combined. The RPC hits are directly sent
1190 to a pattern comparator trigger (PACT), which find muon candidates by comparing the
1191 RPC measurements to predefined patterns. Each muon TF determines the $\eta\text{-}\phi$ position
1192 and the p_T of the muon candidates, and also assigns a quality value based on the position
1193 and number of muon stations used to form the muon track.

1194 On every bunch crossing, the CSC and DT TFs transfer, each one, four muon can-
1195 didates to the Global Muon Trigger (GMT), while the RPC trigger sends eight muon
1196 candidates. The GMT then proceeds to merge the muon tracks if they have been identi-
1197 fied by several muon subsystems, and assigns a three-bit quality code to the muon tracks
1198 depending on the information provided by each TF. All muon candidates are ranked in
1199 the GMT based on their quality code, and those with the same quality are then ranked
1200 based on their p_T . The four highest ranked candidates are then transferred to the GT.
1201 The quality bits assigned to the L1 muon candidates are:

- 1202 • **Bits 0 to 4:** Represent empty, halo or very low quality muon tracks. Not used for
1203 physics.
- 1204 • **Bit 5:** Muon candidate found by the DT or CSC TFs, but not confirmed by the RPC
1205 PACT.
- 1206 • **Bit 6:** Muon candidate found by the RPC PACT, but not confirmed by the DT or
1207 CSC TFs.
- 1208 • **Bit 7:** Muon candidate detected by the DT or CSC TFs, and also by the RPC PACT.

1209 Finally, legacy GT takes the final L1 decision based on the information provided by
1210 the GMT and the GCT. It is able to evaluate up to 128 L1 algorithms.

1211 **Upgraded L1 trigger.** The upgraded L1 trigger system [97], deployed in CMS at
1212 the beginning of 2016, was used during the data taking period of p-Pb collisions at

1213 $\sqrt{s_{\text{NN}}} = 8.16 \text{ TeV}$, and thus for the W-boson analysis reported in Chapter 3. A diagram of
 1214 the upgraded L1 trigger system is shown in Figure 2.15.

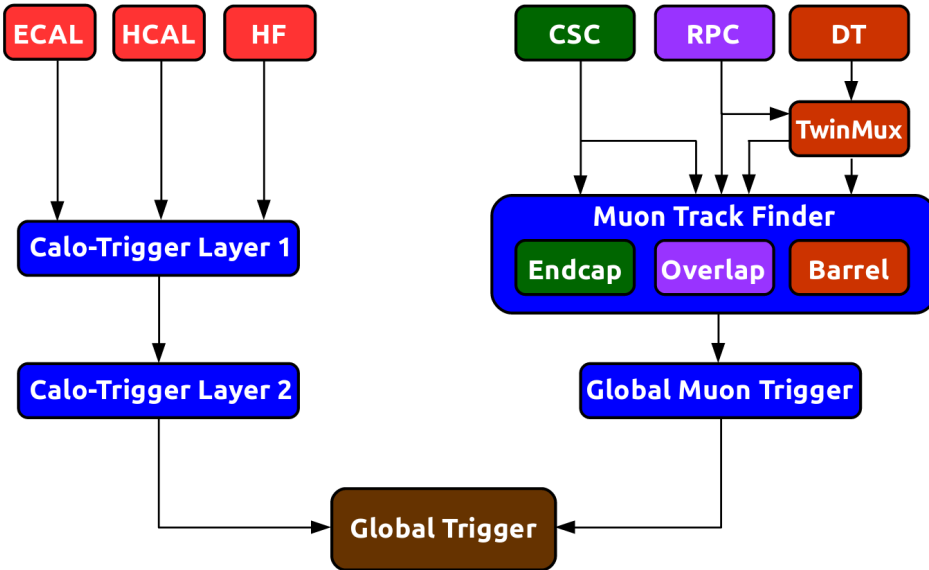


Figure 2.15: Diagram of the CMS L1 trigger used in 2016.

1215 The electronic system of the upgraded L1 trigger consists of Xilinx Virtex-7 FPGAs
 1216 mounted on Advanced Mezzanine Cards (AMC), designed according to the micro Telecom-
 1217 munications Computing Architecture (μ TCA) standard. Compared to the VME standard
 1218 employed in its predecessor, the μ TCA standard provides higher scalability, flexibility
 1219 and bandwidth. The communication links between the L1 boards were upgraded from
 1220 copper serial links (limited to 1.2 Gb/s in the legacy L1 trigger) to high speed optical
 1221 serial links capable of handling a bandwidth of up to 10 Gb/s.

1222 The upgraded L1 calorimeter [105] trigger is divided in two separate processing
 1223 layers and its architecture follows a time-multiplexed trigger design (the data is splitted
 1224 in bunch-crossing intervals instead of detector regions). The first layer (Layer-1) collects
 1225 data from the calorimeter TTs with 36 trigger processor cards and then distributes all
 1226 data for a given bunch crossing to one of the nine multi-purpose FPGAs of the second
 1227 layer (Layer-2). The Layer-2 use the TT data to reconstruct e/γ candidates, jets, and taus
 1228 (decaying to hadrons), and compute global energy quantities. Lookup tables are used to
 1229 perform the shape pattern recognition and the energy calibration.

1230 In the case of the L1 muon trigger [106], its architecture is upgraded following a
 1231 regional approach. The data from the different muon subsystems are combined at an
 1232 earlier stage than in the legacy trigger, and L1 muon tracks are reconstructed in three

regions: barrel ($|\eta| < 0.8$), overlap ($0.8 < |\eta| < 1.25$), and endcap ($1.25 < |\eta| < 2.4$). The Endcap-Muon TF (EMTF) is designed to process the information from the CSC and RPC modules, however it only received data from the CSC system during 2016 since the RPC concentrator card was still been commissioning. The Barrel-Muon TF (BMTF) builds muon candidates using RPC hits and DT segments reconstructed in the central region. The transition area ($|\eta| \approx 1.04$) between the endcap and barrel sections is covered with the Overlap-Muon TF (OMTF), which takes into account the data from the three muon subsystems. The DT and RPC segments from the barrel region are collected by an intermediate layer called the TwinMux system, which concentrates data and distributes it to the BMTF and OMTF.

The upgraded GMT, referred as μ GMT, receives up to 36 L1 muon candidates from each L1 muon TF. The μ GMT sorts the muon tracks, removes duplicate muons found by different TFs and ranks the muon candidates by their p_T and track quality. The eight highest ranked L1 muon candidates are then sent to the GT. The information from the μ GMT and the Layer-2 is used by the upgraded GT to evaluate up to 512 L1 algorithms and determine the final L1 decision.

2.2.2.2 High level trigger

The HLT is executed on a processor farm composed of an array of multi-core computers running a Linux-based operating system known as Scientific Linux. During 2016, approximately 20000 cores were employed to run the HLT [107]. The HLT software is organised in readout, builder and filter units. The readout unit extracts the information from all CMS subsystems once an event passes the L1 trigger. The builder unit assembles the raw data provided by the readout unit to build detector segments, hits and clusters. The assembled data are subsequently sent to the filter unit which performs the reconstruction of physics objects and selects events for data analysis. The logic of the HLT reconstruction framework is similar to what is used in offline reconstruction but optimised to handle high input data rates ($\leq 100\text{kHz}$).

The structure of the HLT algorithms is organised in a set of processing steps, called HLT path, that runs the reconstruction and selection of events. Each HLT path consists of a sequence of processing units that runs in a predefined order and selects events based on user-defined conditions, such as requiring the presence of muons with p_T larger than a given threshold. Once an event has been accepted by the HLT, the CMS data is kept temporarily on disk and eventually sent to the Tier-0 computing facility for further offline processing. The HLT output rate is constrained by the size of the event data and

1267 the Tier-0 processing power. The average data size of an event in p-p collisions is around
1268 500 kb, while in central Pb-Pb collisions can reach values as large as 3 Mb due to the
1269 higher particle multiplicity.

1270 For the analyses presented in this manuscript, the data was triggered requiring
1271 the presence of identified muons. The reconstruction of muon candidates in the HLT is
1272 performed in two steps. The first one, referred as the Level-2 (L2), reconstructs muon
1273 tracks using data from the muon system only, while the next step, known as the Level-3
1274 (L3), combines the information from both the inner tracker and the muon stations.

1275 **HLT L2 muon reconstruction.** The L2 muon algorithm starts by performing a local
1276 reconstruction of the muon detectors to determine the hits on each muon chamber. The
1277 CSC and DT hits are then combined to form segments, which are only kept if found near
1278 a L1 muon candidate. The muon segments are then recursively fitted with a Kalman
1279 Filter (KF) technique [108] to build the L2 muon tracks. Duplicate tracks are filtered by
1280 removing L2 muon tracks that share hits. The KF fit is constrained to the position of the
1281 IP to improved the p_T resolution of L2 muon candidates.

1282 **HLT L3 muon reconstruction.** The L3 muon reconstruction improves the momen-
1283 tum resolution by combining the measurements from the inner tracker and the muon
1284 chambers. The reconstruction of all tracks in the inner tracker (hereafter called tracker
1285 tracks) cannot be done at HLT due to timing constrains. Instead, a regional tracking is
1286 performed by only reconstructing tracker tracks close to the L2 muon candidates using
1287 three different seeding algorithms. In the first case, the seeds are defined by extrapo-
1288 lating the parameters (position and p_T) of the L2 muon tracks to the outer surface of
1289 the inner tracker. The second seeding procedure takes the extrapolated L2 muon tracks
1290 and updates their parameters with the hit information from the outermost layers of
1291 the silicon-strip tracker. And the third seeding algorithm uses segments from two pixel
1292 hits measured in consecutive layers found in a narrow η - ϕ region around each L2 muon
1293 track. Each seed is then used to build the tracker tracks with a KF fit. The reconstructed
1294 tracker and L2 muon tracks are propagated to a common surface, and then matched by
1295 comparing their goodness-of-fit χ^2 . If a L2 muon track and a tracker track is matched,
1296 the hits of both tracks are then combined and refitted to form the L3 muon track.

2.2.3 Reconstruction

The aim of the CMS event reconstruction algorithms is to build and identify the physics objects generated during the collision by processing the raw data recorded by the CMS detector. The reconstruction algorithms are implemented in CMSSW framework. Once an event is selected by the HLT, the detector information is then transferred to the Tier-0 computing centre and processed with CMSSW. The reconstruction software starts by building the hits, segments and clusters, measured in each of the CMS subdetectors. Afterwards, it processes the detector information to form physics objects such as charged-particle tracks, muons, electrons, photons and jets. Global event quantities, like the missing transverse momentum (p_T^{miss}), are computed by combining the information from the different reconstructed objects. Only the reconstruction of muons and the p_T^{miss} are described hereafter, since they are the only objects used in the W-boson and charmonium analyses presented in Chapter 3 and Chapter 4, respectively.

2.2.3.1 Muon reconstruction

Muon candidates are reconstructed in CMS using the information from the inner tracker and the muon system. Tracks formed in the muon system only are called *standalone-muon* tracks, while those built in the inner tracker and matched to a hit in the muon system are referred to as *tracker-muon* tracks. *Global-muon* tracks are reconstructed by matching a tracker track with a standalone-muon track [109]. The three different types of muon tracks used in CMS are displayed in Figure 2.16.

Standalone muons. The standalone muon reconstruction starts with the formation of segments made from a linear interpolation of the position of hits measured in the DT or CSC layers. Each track segment has an associated state vector representing its position, direction and p_T . The state vector of the segments built in the innermost muon station is used to seed the muon track fit.

In the barrel region, tracks are built by fitting the DT segments with a KF algorithm [108], starting from the innermost muon chamber. Moreover, since the magnetic field in the endcap sections is not uniform, the hits of the CSC segments are used directly to perform the KF fit. The RPC hits are also included in the KF. In the case that no hits are found between muon layers, the state vector of the muon track is propagated to the next layer taking into account the magnetic field and the interaction of muons with the CMS detector material.

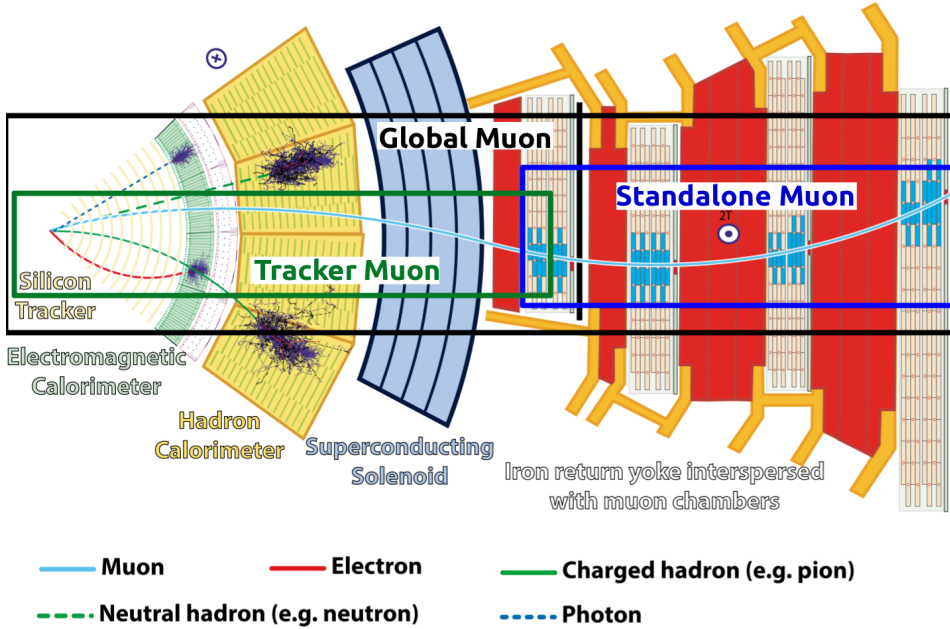


Figure 2.16: Cross section view of the CMS detector showing how particles interact in the CMS. The different types of muon tracks are indicated by boxes. Figure taken from Ref. [110].

1329 The track building procedure is iterated while progressing towards the outer muon
 1330 chambers. The χ^2 value between the detector hits and the position of the track projected
 1331 onto the muon chambers is computed in each step. The hits with large χ^2 values are
 1332 excluded from the KF fit and the parameters of the track are updated accordingly. The
 1333 track fit algorithm stops when it reaches the last muon station. Subsequently, the KF
 1334 algorithm is performed backwards working from the outermost to the innermost muon
 1335 chambers, completing the standalone-muon track. Finally, the standalone-muon tracks
 1336 are extrapolated to the closest approach to the beam line and their position is required
 1337 to be close to the IP.

1338 **Global muons.** The global muon reconstruction improves the momentum measure-
 1339 ment by including the information from the inner tracker. The global muon tracking
 1340 begins by propagating the standalone-muon tracks to the outer surface of the silicon-strip
 1341 tracker, and a tracker layer consistent with the position of the propagated standalone
 1342 muon then defines a common surface.

1343 Tracker-track segments are built from pairs (triplets), made of two (three), hits
 1344 reconstructed in adjacent inner-tracker layers. These segments are then employed to seed

1345 an iterative KF combinatorial track finder. The sophisticated tracking procedure runs
1346 ten different iterations. The first two iterations reconstruct low- p_T and high- p_T tracks
1347 seeded with pixel-hit triplets. The third iteration uses pixel-hit triplets to reconstruct
1348 tracks from secondary vertices displaced, within a radial distance $R < 5$ cm, from the
1349 primary vertex. The next iteration is meant to recover tracks with one or two missing
1350 hits by seeding with pixel-hit pairs instead. The fifth iteration build displaced tracks
1351 ($R < 7$ cm) seeded by triplets from pixel and strip hits. The following two iterations
1352 reconstruct very displaced tracks ($R < 60$ cm) seeded by strip-hit triplets. The eighth
1353 iteration aims to find tracks within the core of high- p_T jets seeded by pairs of pixel and
1354 strip hits. And the last two iterations build tracks seeded with hits and segments from
1355 the muon chambers, to improve the muon reconstruction efficiency. The hits associated
1356 to tracks formed in a given iteration are excluded in the subsequent iterations to avoid
1357 duplicating tracks. The rate of mis-reconstructed tracks is kept low in each step by
1358 applying a set of quality criteria on the goodness-of-fit χ^2 and the number of hits used,
1359 and by requiring the tracks to be consistent with a charged-particle trajectory originating
1360 from the primary vertex.

1361 The tracker track and the propagated standalone-muon track are matched in the
1362 common surface according to their p_T , position and direction measured in the common
1363 plane, and the hits from both tracks are then refitted to derive the ultimate global-muon
1364 candidate. If multiple global-muon tracks are found for the same standalone muon, the
1365 track with the best χ^2 fit value is kept.

1366 **Tracker muons.** The tracker-muon candidates are built by propagating all tracker
1367 tracks with $p_T > 0.5$ GeV/c and total momentum $p > 2.5$ GeV/c, outward to the innermost
1368 muon station. The propagated track is then considered a tracker-muon track if it matches,
1369 along the transverse plane, at least one hit reconstructed in the inner muon chambers.

1370 **Tracking in Pb-Pb collisions.** A modified version of the tracker-track reconstruction
1371 was employed during Pb-Pb collisions at $\sqrt{s_{\text{NN}}} = 5.02$ TeV, to cope with the large number
1372 of charged particles produced in central heavy-ion collisions. The tracking algorithm used
1373 to build the tracker tracks consists of seven iterations and is called Regional Iterative
1374 tracking (RegIt). Instead of using all pixel hits reconstructed in the inner tracker, RegIt
1375 performs a regional track reconstruction using only those hits found in a η - ϕ area around
1376 each standalone-muon track. The RegIt iterations follow the same logic as the standard
1377 tracking, excluding the three iterations corresponding to low- p_T , very displaced, and

1378 high- p_T jet tracks. In each iteration, tracks made with RegIt are required to have a
 1379 $p_T > 0.8 \text{ GeV}/c$ and at least eight hits, which is a tighter criteria compared to the standard
 1380 track reconstruction.

1381 **2.2.3.2 Missing transverse momentum reconstruction**

1382 Since neutrinos cannot be detected, their presence is inferred from the overall particle
 1383 momentum imbalance in the transverse plane, known as missing transverse momentum
 1384 (p_T^{miss}). The p_T^{miss} is defined as the magnitude of \vec{p}_T^{miss} , which represents the negative
 1385 vector sum of the transverse momentum of all particles identified by CMS in an event,
 1386 as described in:

$$\begin{aligned}\vec{p}_T^{\text{miss}} &= - \sum_{\text{particles}} \vec{p}_T \\ p_T^{\text{miss}} &= \left| \vec{p}_T^{\text{miss}} \right|\end{aligned}\tag{2.5}$$

1387 The Particle-Flow (PF) algorithm [111] is used to identify the particles produced in a
 1388 given event. The PF algorithm is optimised to reconstruct stable particles by taking into
 1389 account the information from all CMS subdetectors. The algorithm determines the mo-
 1390 mentum of the reconstructed objects and classify them in five categories: electron, muon,
 1391 photon, charged hadron and neutral hadron, as shown in Figure 2.16. The transverse
 1392 momentum of all PF particles is used to compute the p_T^{miss} . The performance of the p_T^{miss}
 1393 reconstruction in p-p collision data has been documented in [112, 113].

W-BOSON PRODUCTION IN PROTON-LEAD COLLISIONS

1396 This chapter reports the measurement of the production of W bosons in proton-
1397 lead collisions at a nucleon-nucleon center-of-mass energy $\sqrt{s_{\text{NN}}} = 8.16 \text{ TeV}$ with
1398 the CMS detector. A brief introduction to the theory of electroweak interactions
1399 and the W-boson production in p-Pb collisions is presented in Section 3.1. This section
1400 concludes with a overview of the latest measurements of weak-boson production in
1401 heavy-ion collisions at the LHC. The W-boson analysis is then described in detailed
1402 in Section 3.2. In Section 3.3, the results of the W-boson analysis are presented and
1403 compared to theoretical calculations based on PDFs.

1404 3.1 Introduction

1405 This section provides a short introduction to the W-boson analysis. It starts with a
1406 brief historical overview of the weak theory (Section 3.1.1) and continues with a short
1407 description of the modern theory of electroweak interactions (Section 3.1.2). The process
1408 of interest in this analysis, $p\text{Pb} \rightarrow W \rightarrow \mu\nu_\mu$, is detailed in Section 3.1.3. Section 3.1.4
1409 introduces the nuclear PDFs and describes the most recent nuclear PDF sets. Finally,
1410 Section 3.1.5 present some of the latest results on weak boson production in heavy-ion
1411 collisions at the LHC.

3.1.1 A brief history of the weak theory

In the early 20th century, quantum mechanics was the standard framework of atomic physics but certain processes such as the β decay, discovered by Ernest Rutherford in 1899 [114], were not fully understood yet. At the time, the β decay was characterized by the process $A_i \rightarrow A_f + e^-$, where an initial nucleus A_i decays into another nucleus A_f emitting an electron during the process. In order to conserve energy, the electron is required to have a fixed kinetic energy, but James Chadwick observed in 1914 that the β rays produced a continuous energy spectrum [115, 116] in disagreement with what was expected. Another puzzle was the apparently wrong statistics of ^{14}Ni ($A = 14$, $Z = 7$), which was thought at the time to be composed of 14 protons and 7 electrons (behaving as a fermion), but was experimentally proven to have spin 1. As a way to solve the problem of the continuous β decay spectrum and the statistics problem of nitrogen, Wolfgang Pauli proposed in 1930 the existence of a new particle [117, 118]. Pauli named his particle initially the neutron, but was later renamed to neutrino by Enrico Fermi after the discovery of a new heavy neutral particle by Chadwick in 1932 [119], that ended up solving the ^{14}Ni statistics problem by explaining the nitrogen nucleus as made of 7 protons and 7 neutrons (even number of fermions). Pauli described the neutrino as a neutral fermion with mass close to zero and spin 1/2 capable of penetrating matter deeper than photons [117].

Enrico Fermi, after attending the 7th Solvay conference, where the discovery of the neutron and the neutrino hypothesis were presented, proposed a new theory to explain the β decay [120]. Fermi's theory defined the β decay as a process in which the neutron decays to a proton, emitting an electron and a neutrino. Fermi formulated his theory using an analogous approach as in Quantum Electrodynamics (QED), by proposing the following Lagrangian for β decay [121]:

$$L_\beta = G_F (\bar{u}_p \gamma_\mu u_n) (\bar{u}_e \gamma^\mu u_\nu) \quad (3.1)$$

where u is the Dirac spinor of each particle, γ_μ is the Dirac matrix and G_F is the Fermi coupling constant. Fermi's theory of weak interactions assumed the same conservation rules as QED, including the symmetry under reflection in space [121]. A system that is invariant under reflections conserve a quantity called parity.

In the upcoming years, the physicists Tsung Dao Lee and Chen Ning Yang started to suspect that the weak interactions could violate parity conservation, after not finding any experimental evidence of its conservation so far [122]. In an attempt to test the

1444 conservation of parity in weak interactions, Lee and Yang proposed in 1956 to study
1445 the β decays of Cobalt (^{60}Co) and measure the projection of the momentum of electrons
1446 along the spin axis of the Cobalt nucleus [122]. If the decay process conserves parity then
1447 electrons would be produced in both directions: parallel and anti-parallel to the magnetic
1448 field. The experiment to test the conservation of parity was realized by Chien-Shiung
1449 Wu in 1957. The results of Wu's research showed that electrons were preferentially
1450 produced in the opposite direction to the Cobalt spin [123], which meant that parity was
1451 not conserved in weak interactions, and even maximally violated.

1452 Apart from parity, one can also associate a helicity to particles. The particle's helicity
1453 is considered right-handed if the projection of the spin on the particle momentum is
1454 aligned, and left-handed otherwise. In 1958, Goldhaber, Grodzins and Sunyar measured
1455 the neutrino helicity at Brookhaven National Laboratory (BNL) and discovered that
1456 neutrinos were always left-handed and anti-neutrinos were right-handed [124]. As a
1457 consequence of the discovery of parity violation and the neutrino helicity, Robert Marshak
1458 and George Sudarshan modified Fermi's weak theory and introduced an axial vector
1459 term, giving rise to the V-A (vector-axial) theory of weak interactions [125]. Even though
1460 parity (P) and charge conjugation (C) (transforms particles into their anti-particles)
1461 were violated separately, it was then assumed that the combined CP operation was still
1462 conserved by the weak interaction.

1463 The assumption of the conservation of CP did not last long. An experiment performed
1464 at BNL by James Christenson, James Cronin, Val Fitch and René Turlay [126] in
1465 1964 concluded that a small proportion of long-lived K_L meson ($\text{CP} = -1$) was able to
1466 decay to two pions ($\text{CP} = +1$) violating CP in the process. To explain the CP violation
1467 in weak theory, Makoto Kobayashi and Toshihide Maskawa [127] extended in 1973
1468 the formulation of the Cabibbo angle to include three generation of quarks and a CP-
1469 violating phase term. The Cabibbo angle was originally computed by Nicola Cabibbo [128]
1470 to explain the different amplitudes observed between the up, down and strange quark
1471 transitions. The charm quark was not yet discovered but was strongly hypothesized,
1472 through the Glashow-Iliopoulos-Maiani (GIM) mechanism [129]. The Cabibbo, Kobayashi
1473 and Maskawa (CKM) matrix supposed the existence of the charm, bottom and top quarks,
1474 discovered later in 1977 [130, 131], 1977 [132] and 1995 [133], respectively.

1475 Following Paul Dirac's formulation of QED [134], Sheldon Glashow [135], Steven
1476 Weinberg [136] and Abdus Salam [137] managed in 1968 to build a gauge-invariant
1477 unified theory of the electromagnetic and weak interactions. In order to make the elec-
1478 troweak theory symmetric under local phase transformations, it required the presence

of four spin-1 massless bosons: two charged particles called W^\pm bosons and two neutral particles corresponding to the Z boson and photon. But since the weak interactions are short range, it has to be mediated by massive bosons. The addition of mass to the bosons was realized after introducing the spontaneous local breaking of the underlying SU(2) symmetry through the Higgs mechanism [15, 16]. In the following years, Gerardus t’Hooft and Martinus Veltman managed to renormalise the electroweak theory [138, 139], allowing to calculate more precisely the theoretical masses of the weak bosons.

The Z boson was then missing, but a single event was found in the Gargamelle experiment [140], exhibiting a flavour-changing neutral current that could only be mediated by a virtual Z boson ($\nu_\mu + e^- \rightarrow \nu_\mu + e^-$). The experimental study of weak bosons required the development of new particle acceleration technologies. In 1976, Carlo Rubbia, Peter McIntyre and David Cline suggested to transform CERN’s circular proton accelerator, the SPS, into a proton-antiproton collider (Sp \bar{p} S) [141]. The upgrade to Sp \bar{p} S was made possible thanks to the stochastic cooling technology invented by Simon Van der Meer [142] in 1972, which allowed to cool down and collect anti-protons. Several experiments were built in the Underground Area (UA) to study the proton-antiproton collisions at the Sp \bar{p} S. The UA1 and UA2 collaborations observed on-shell W bosons [143, 144] in 1983, via reporting the observation of electrons with large transverse energy and the presence of missing momentum in p \bar{p} collisions at $\sqrt{s} = 540\text{ GeV}$. And few months later, both collaborations also reported the observation of on-shell Z bosons in the dilepton decay channel [145, 146].

After the major success of the Sp \bar{p} S project, CERN constructed in 1983 a new lepton circular collider called the Large Electron-Positron (LEP) collider [147]. LEP was designed to accelerate electrons and positrons to an energy of half the Z-boson mass (45 GeV), in order to perform precision measurements of the Z-boson line-shape. Precise measurements of the W-boson mass [148] were later performed by the experiments in the Fermi National Accelerator Laboratory (FNAL). The FNAL experiments analysed data collected between 1983 and 2011 from the Tevatron [149], a proton-antiproton synchrotron collider that operated at energies up to $\sqrt{s} = 1.96\text{ TeV}$.

The successful programs of LEP and Tevatron produced the most precise measurements of the properties of the electroweak theory, but there was still a missing piece to complete the picture, the Higgs boson. The discovery of the Higgs boson was finally achieved in 2012 by the CMS [17] and ATLAS [18] collaborations at the Large Hadron Collider (LHC).

1513 3.1.2 The modern electroweak theory

1514 The interactions between elementary particles mediated by the weak and electromagnetic
 1515 forces are described in the Standard Model using the electroweak theory developed by
 1516 Glashow, Weinberg and Salam [135–137]. The unification of these two fundamental
 1517 forces of nature is accomplished mathematically using a non-abelian $SU(2) \times U(1)_Y$ gauge
 1518 theory. The electroweak theory requires four massless gauge bosons: three bosons with
 1519 weak isospin (called W_1 , W_2 and W_3) from $SU(2)$ and one boson (named B) with weak
 1520 hypercharge from $U(1)_Y$.

1521 Since weak bosons have mass, a full description of the electroweak interactions
 1522 requires the inclusion of massive vector bosons. The problem is that one can not naively
 1523 add a mass term of the form $m^2 W^\mu W_\mu$ into the electroweak Lagrangian since this
 1524 would break gauge invariance making the theory divergent. Thus, this issue is instead
 1525 solved by spontaneously breaking the $SU(2) \times U(1)_Y$ electroweak symmetry into a $U(1)_{EM}$
 1526 symmetry using the Higgs mechanism [15, 16]. The overall idea is that the electroweak
 1527 gauge bosons couple to a scalar field called the Higgs field which is present in all space.
 1528 When this field induces a spontaneous breaking of the gauge symmetry, it is split into
 1529 one dynamic part corresponding to the Higgs boson, and another constant part called the
 1530 vacuum expectation value (VEV). The symmetry breaking of $SU(2) \times U(1)_Y$ to $U(1)_{EM}$
 1531 generates three massless Goldstone bosons. The Goldstone bosons are then absorbed
 1532 by the electroweak gauge bosons producing the W^+ , W^- and Z bosons with masses
 1533 proportional to the VEV, while the photon remains massless. The W^\pm , Z and γ bosons
 1534 are correlated with the W_1 , W_2 , W_3 and B gauge bosons in the following way:

$$\begin{aligned} W^\pm &= \frac{1}{\sqrt{2}} (W_1 \pm W_2) \\ \begin{pmatrix} Z \\ \gamma \end{pmatrix} &= \begin{pmatrix} \cos \theta_W & \sin \theta_W \\ -\sin \theta_W & \cos \theta_W \end{pmatrix} \begin{pmatrix} B \\ W_3 \end{pmatrix} \end{aligned} \tag{3.2}$$

1535 where θ_W represents the weak mixing angle. In addition, quarks and leptons ac-
 1536 quire mass through the Yukawa interaction with the Higgs field. Since the quark weak
 1537 eigenstates are not the same as their mass eigenstates, weak interactions can induce a
 1538 transition from an up-like quark (u , c , t) to a down-like quark (d , s , b). The strength of the
 1539 quark-flavour mixing in weak decays is parametrised by the CKM matrix V_{CKM} via:

$$\begin{pmatrix} d' \\ s' \\ b' \end{pmatrix} = \begin{pmatrix} V_{ud} & V_{us} & V_{ub} \\ V_{cd} & V_{cs} & V_{cb} \\ V_{td} & V_{ts} & V_{tb} \end{pmatrix} \begin{pmatrix} d \\ s \\ b \end{pmatrix} \quad (3.3)$$

where (d', s', b') are the down-like quark weak eigenstates and (d, s, b) are the corresponding mass eigenstates. The latest values of the magnitude of the CKM matrix elements are [19]:

$$\begin{pmatrix} |V_{ud}| & |V_{us}| & |V_{ub}| \\ |V_{cd}| & |V_{cs}| & |V_{cb}| \\ |V_{td}| & |V_{ts}| & |V_{tb}| \end{pmatrix} = \begin{pmatrix} 0.97417 & 0.2248 & 0.00409 \\ 0.220 & 0.995 & 0.0405 \\ 0.0082 & 0.04 & 1.009 \end{pmatrix} \quad (3.4)$$

The Lagrangian of the electroweak theory includes several components that describe the interactions between the fermions, electroweak bosons and the Higgs boson. In the case of the Z boson, the term of the Lagrangian that represents the interactions between fermions and neutral-charged electroweak bosons is:

$$L_{NC} = \alpha_{em} \theta_W \sum_{\text{fermions}} \bar{f} \gamma^\mu A_\mu f + \frac{g}{\cos \theta_W} \sum_{\text{fermions}} \bar{f} \gamma^\mu \frac{(g_v^f - g_a^f \gamma^5)}{2} Z_\mu f \quad (3.5)$$

where g is the coupling constant of $SU(2)_L$, f is the Dirac spinors of fermions, A_μ is the electromagnetic field, and g_v^f (g_a^f) is the fermion vector (axial) weak coupling constants. Eq. (3.5) specify that the Z bosons and photons conserve flavour, always decaying into a fermion and its corresponding anti-fermion. While photons do not distinguish the helicity of particles, the Z-boson couplings are different for left- and right-handed fermions.

Furthermore, the component of the Lagrangian that represents the interaction between W bosons and fermions is given by:

$$L_{CC} = \frac{g}{2\sqrt{2}} \left((\bar{u}, \bar{c}, \bar{t})_R W_\mu^+ \gamma^\mu V^{\text{CKM}} \begin{pmatrix} d_L \\ s_L \\ b_L \end{pmatrix} + (\bar{\nu}_e, \bar{\nu}_\mu, \bar{\nu}_\tau)_R W_\mu^+ \gamma^\mu \begin{pmatrix} e_L^- \\ \mu_L^- \\ \tau_L^- \end{pmatrix} \right) \quad (3.6)$$

where f_L correspond to left-handed fermions and \bar{f}_R represents right-handed anti-fermions. Thus, W bosons only couple to right-handed anti-fermions and left-handed fermions organized in pairs of lepton-neutrino or quark-antiquark, where the electric charge of the of particles differ by one unit. Since the top-quark mass (178 GeV) is larger than the W-boson mass (80 GeV), the W boson can not decay to a virtual top quark.

1559 Figure 3.1 shows the possible decays of weak bosons to fermions. The measured values
 1560 of the mass, width and couplings of weak vector bosons are summarized in Table 3.1.

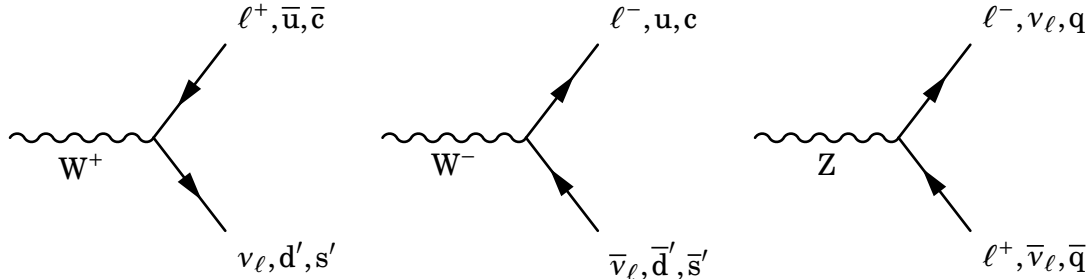


Figure 3.1: Feynman diagram of the decay modes of W^+ (left), W^- (middle) and Z (right) bosons to fermions.

Variable	Description	Value
M_W	W boson mass	$80.385 \pm 0.015 \text{ GeV}$
Γ_W	W boson width	$2.085 \pm 0.042 \text{ GeV}$
$\text{BR}(W \rightarrow \ell\nu)$	Branching fraction of W boson semileptonic decays	$(10.86 \pm 0.09)\%$
$\text{BR}(W \rightarrow q\bar{q}')$	Branching fraction of W boson hadronic decays	$(67.41 \pm 0.27)\%$
M_Z	Z boson mass	$91.1876 \pm 0.0021 \text{ GeV}$
Γ_Z	Z boson width	$2.4952 \pm 0.0023 \text{ GeV}$
$\text{BR}(Z \rightarrow \ell^+\ell^-)$	Fraction of Z boson charged-lepton decays	$(3.3658 \pm 0.0023)\%$
$\text{BR}(Z \rightarrow \nu\bar{\nu})$	Fraction of Z boson neutrino decays	$(20.00 \pm 0.06)\%$
$\text{BR}(Z \rightarrow q\bar{q})$	Fraction of Z boson hadronic decays	$(69.91 \pm 0.06)\%$

Table 3.1: Experimental values of the mass, width and branching fractions of weak bosons extracted from the PDG [19].

1561 3.1.3 Production of W bosons in p-Pb and decay into muons

1562 In this thesis, the inclusive production of W bosons is measured in p-Pb collisions through
 1563 the muonic decay channel, which is represented by the process $p\text{Pb} \rightarrow W + x \rightarrow \mu + \nu_\mu + x$.
 1564 Since the mass of the W boson is large ($M_W = 80.385 \text{ GeV}$), the W bosons are formed
 1565 during the initial hard scatterings between the partons from the incoming proton and
 1566 those from the nucleons bound in the Pb ion.

1567 The cross section for the inclusive production of W bosons in p-Pb collisions can be
 1568 expressed, assuming that the QCD factorisation holds for a nucleus, as:

$$\sigma[pPb \rightarrow W + X] = \sum_{a,i,j} \int dx_p dPb_2 f_i^p(x_p, Q^2) \cdot f_j^{a/Pb}(x_{Pb}, Q^2) \hat{\sigma}[i + j \rightarrow W + X] \quad (3.7)$$

1569 where $f^{a/Pb}$ are the PDFs of a nucleon a bound in the Pb ion, f^p are the PDFs of
 1570 the incoming proton and $\hat{\sigma}$ is the partonic cross section. The partonic cross section is
 1571 evaluated using pQCD by expanding it in terms of α_s , as given by:

$$\hat{\sigma} = \sum_i (\alpha_s^i \cdot \hat{\sigma}^i) = \hat{\sigma}^{\text{LO}} + \alpha_s \hat{\sigma}^{\text{NLO}} + \dots \quad (3.8)$$

1572 In practice, the expansion of the partonic cross section is truncated at a given order
 1573 (e.g. NLO). At leading order, the production of W bosons in proton-nucleon collisions is
 1574 accomplished through the process of quark-antiquark annihilation ($q + \bar{q} \rightarrow W$), as shown
 1575 in Figure 3.2. On the other hand, the NLO cross section includes contributions from the
 1576 processes shown in Figure 3.3.

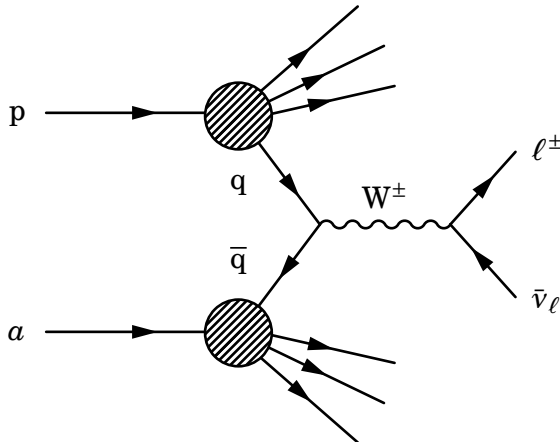


Figure 3.2: Leading order Feynman diagram of W boson production to final state leptons, from a collision between an incoming proton (p) and a bound nucleon (a) in a Pb nucleus.

1577 The total partonic cross section at LO for $pPb \rightarrow W \rightarrow \mu\nu_\mu$ can be computed using
 1578 electroweak theory and is given by [19]:

$$\hat{\sigma}^{\text{LO}}[ij \rightarrow W \rightarrow \mu\nu_\mu](Q^2) = \frac{|V_{ij}^{\text{CMK}}|^2}{N_c} \frac{8G_F^2 M_W^4}{16\sqrt{2}\pi} \left(\frac{Q^2}{(Q^2 - M_W^2)^2 + Q^2 \Gamma_W^2} \right) \quad (3.9)$$

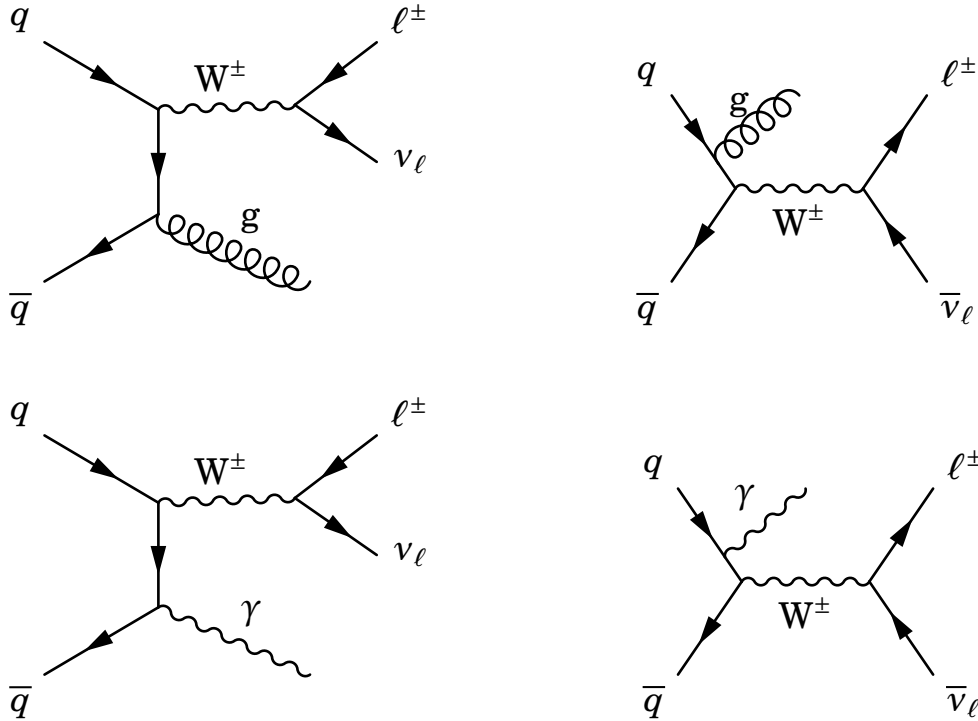


Figure 3.3: Next-to-leading order Feynman diagrams of W boson partonic production to final state leptons.

1579 where M_W is the mass of the W boson, Γ_W is the width of the W boson, $N_c = 3$ is the
 1580 number of colour charges of quarks, and $|V_{ij}^{\text{CKM}}|$ is the magnitude of the CKM matrix
 1581 element associated to the interaction between the quarks i and j.

1582 In pPb collisions, the W bosons are mainly produced from interactions between the
 1583 valence quarks and sea anti-quarks of the proton and nucleons. The dominant production
 1584 modes of W^+ bosons correspond to up quark and down anti-quark annihilation ($u\bar{d} \rightarrow W^+$)
 1585 while for W^- bosons correspond to down quark and up anti-quark annihilation ($d\bar{u} \rightarrow W^-$).
 1586 The next relevant contributions come from $c\bar{s}$ and $s\bar{c}$, while the other quark-antiquark
 1587 contributions are suppressed according to the off-diagonal CKM matrix elements. Thus,
 1588 the inclusive W boson cross section measured in p-Pb data is mostly sensitive to the
 1589 proton and nuclear PDFs of light quarks and anti-quarks.

1590 In addition, the direction of the outgoing muons and anti-muons is different with
 1591 respect to the scattered quarks. In weak interactions, the W^+ boson couples to left-handed
 1592 neutrinos while the W^- boson couples to right-handed anti-neutrinos. As a consequence,
 1593 in order to conserve helicity, the anti-muons are preferentially produced in the same
 1594 direction as the W^+ boson while muons are preferentially produced in the opposite

1595 direction, as shown in Figure 3.4.

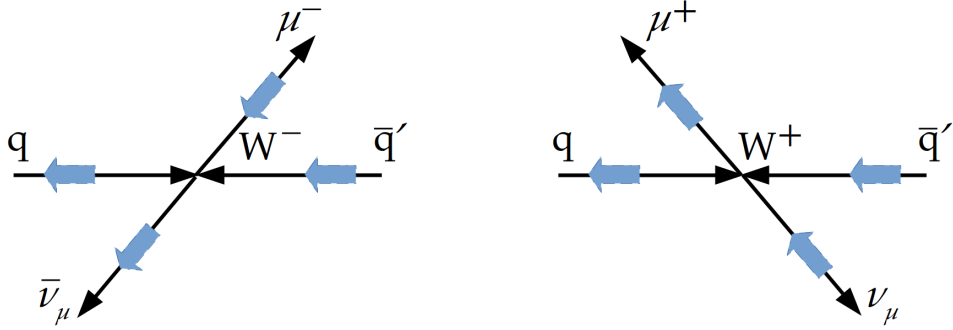


Figure 3.4: Schematic diagram of the production of W^- (left) and W^+ (right) bosons to muonic decays. The black arrows represent the particle direction of motion whereas the blue arrows correspond to its spin. The spin of the W^\pm boson points in the direction of the anti-quark.

1596 At LO, the rapidity of W bosons (y_W) is related to the Bjorken- x of the proton and
1597 Pb nucleon via:

$$x_p = \frac{M_W}{\sqrt{s_{NN}}} e^{y_W} , \quad x_{Pb} = \frac{M_W}{\sqrt{s_{NN}}} e^{-y_W} \quad (3.10)$$

1598 And since the W -boson rapidity is correlated to the muon η , then the pseudorapidity
1599 distribution of muons arising from W -boson decays in p-Pb collisions is sensitive to
1600 different x regions of the light quark nuclear PDF that are described in the next section.

1601 3.1.4 Nuclear PDFs

1602 The parton distribution functions can not be determined from first principles due to the
1603 non-perturbative behaviour of the strong interactions. Nevertheless, their dependence
1604 on x can be derived by fitting observables (e.g. structure functions or asymmetries) to
1605 experimental data from different processes since PDFs do not depend on the initial hard
1606 scattering. The Q^2 dependence of the PDFs is determined using the DGLAP evolution
1607 equations. The most common processes used to constrain the PDFs correspond to DY,
1608 DIS, vector boson and jet production, which have been measured by various experiments,
1609 including data from HERA, SLAC and LHC.

1610 There are several proton PDF global fits currently available. In this thesis we use
1611 the NLO CT14 PDF sets published in 2016 [150] by the collaboration of theorists and
1612 experimentalist on QCD (CTEQ). The global fits of CT14 PDFs include data of vector
1613 bosons and jets from LHC p-p collisions at 7 TeV and 8 TeV, charm quark DIS production

3.1. INTRODUCTION

from HERA, and electron charge asymmetry from Tevatron. The x -dependence of the CT14 PDF is parametrised at low Q^2 by [150]:

$$x f_a(x, Q^2) = x^{c_1} (1-x)^{c_2} P_a(x) \quad (3.11)$$

where f_a is the PDF of a parton a , c_i are parameters and P_a is a polynomial function. In total, the CT14 proton PDFs are described by 26 parameters including: 8 parameters for the valence quarks, 5 parameters for the gluon and 13 parameters for the sea quarks [150].

Figure 3.5 presents the CT14 proton PDF results at $Q = 10\text{ GeV}$ and $Q = 100\text{ GeV}$. One can observe that the light valence quarks carry most of the momentum of the proton while the gluons and sea quarks are mainly distributed at low x . When the energy is increased, the distribution of partons gets significantly enhanced at low x , predominantly dominated by gluons.

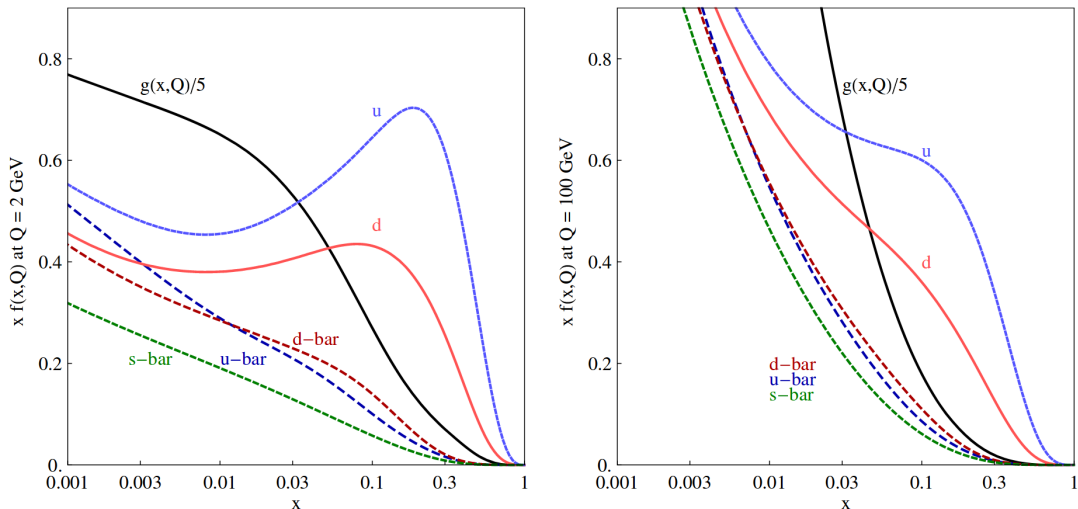


Figure 3.5: Results of the CT14 proton PDFs at NNLO derived at $Q = 10\text{ GeV}$ (left) and $Q = 100\text{ GeV}$ (right). Figure taken from Ref. [150].

In heavy-ion collisions, the PDFs of the protons and neutrons bound in the nucleus are modified by the presence of the nuclear medium environment. The PDFs of nuclei were initially analysed in charged-lepton DIS experiments using nuclear targets by measuring the nuclear structure function per nucleon (F_2^A) for a heavy-ion target (A) relative to the one for deuterium (F_2^D)¹ ($R_{F_2}^A = F_2^A/F_2^D$).

The European Muon Collaboration (EMC) measured at CERN the structure function of muon DIS from iron and deuterium targets, and published in 1983 the first observation

¹Deuterium is approximately considered to be composed of a free proton and a free neutron.

1632 of a depletion of the DIS cross section from iron relative to the one from deuterium in the
 1633 high x -region $0.3 < x < 0.65$ [151], which was named the EMC region. Afterwards, further
 1634 DIS measurements at CERN and SLAC found a suppression of the nuclear structure
 1635 function compared to deuterium in the low- x region $x < 0.1$ and an enhancement in
 1636 the intermediate x -region $0.1 < x < 0.3$, which are referred as the shadowing and anti-
 1637 shadowing regions [152]. Moreover, the measurements at SLAC using data at higher x
 1638 observed an increase of $R_{F_2}^A$ while approaching $x = 1$, which was expected from the motion
 1639 of nucleons inside the nuclei, called Fermi motion. Figure 3.6 presents an illustration of
 1640 the different regions of nuclear modifications found experimentally.

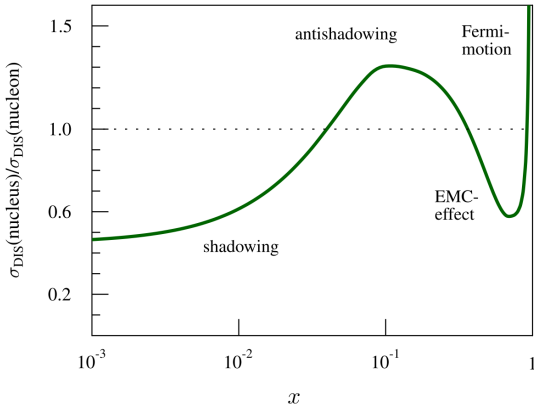


Figure 3.6: Illustration of the different nuclear PDF effects. Figure taken from Ref. [153].

1641 In the case of heavy-ion collisions, the different nuclear modifications can be qualita-
 1642 tively described as follows:

- 1643 • **Shadowing:** corresponds to the suppression seen in $x \lesssim 0.1$, and it arises from
 1644 the multiple interactions between the scattered partons and the ones from the
 1645 different nucleons. The multiple parton scatterings shifts the momentum transfer
 1646 x of the partons towards higher values, effectively reducing the parton densities at
 1647 low x .
- 1648 • **Anti-shadowing:** corresponds to an enhancement in $0.1 \lesssim x \lesssim 0.3$, and it can be
 1649 understood as a consequence of the multiple parton scatterings that occur in the
 1650 nucleus.
- 1651 • **EMC effect:** corresponds to the suppression in $0.3 \lesssim x \lesssim 0.7$. Some models have
 1652 been proposed to explain this phenomenon which consider modifications of the nu-

1653 cleon structure due to the nuclear medium and also due to short-range correlations
 1654 between nucleons.

- 1655 • **Fermi-motion effect:** corresponds to a enhancement in $x > 0.7$, and it is due to
 1656 the motion of nucleons inside the nucleus.

1657 The first global fit to describe leading-order nuclear effects was the EKS98 nPDF [154],
 1658 which employed the nuclear DIS data measured at CERN and Fermilab, and the DY
 1659 dimuon data from Fermilab proton-nucleus collisions. The pion data collected by RHIC
 1660 was later included in subsequent global nPDF fits, such as EPS08 [155], EPS09 [156]
 1661 and DSSZ [157], which provided constrains to the gluon nPDF.

1662 The nPDFs or the nuclear modification are defined for protons bound in a nucleus. The
 1663 bound neutron nPDFs are derived from the bound proton PDFs using isospin symmetry
 1664 (i.e. by exchanging the up and down quark PDFs). The full nPDFs for a nucleus of Z
 1665 protons and $A - Z$ neutrons can be derived using the bound proton nPDFs $f^{p/A}$ and the
 1666 bound neutron nPDFs $f^{n/A}$, according to:

$$f^A = \frac{Z}{A} f^{p/Pb} + \frac{A-Z}{A} f^{n/Pb} \quad (3.12)$$

1667 From now on, we will focus on the latest nuclear PDF sets: the EPPS16 and nCTE15
 1668 nPDFs, which are used in this thesis.

1669 **EPPS16 nPDF.** The EPPS16 nuclear PDFs were published in 2017 by Eskola, Paakki-
 1670 nen, Paukkunen and Salgado (EPPS) [158]. The EPPS16 nPDF calculations updates
 1671 their previous EPS09 global fits [156].

1672 The EPPS16 global fits includes the same data sets as EPS09 (charged-lepton-nucleus
 1673 DIS data from SLAC, DY dilepton production from EMC proton-nucleus collisions,
 1674 and inclusive pion production from RHIC deuteron-nucleus collisions), as well as the
 1675 CHORUS neutrino-nucleus DIS data, low-mass DY production from RHIC pion-nucleus
 1676 collisions, and the results using dijet and electroweak boson production in LHC pPb
 1677 collisions at $\sqrt{s_{NN}} = 5.02\text{TeV}$. The addition of the new LHC, RHIC and CHORUS data
 1678 into the global fit is not in tension with the previous EPS09 data sets, reassuring the
 1679 validity of the universality of the nuclear PDFs. Moreover, the inclusion of the CMS
 1680 measurements of dijet production in pPb collisions at $\sqrt{s_{NN}} = 5.02\text{TeV}$ highly constrained
 1681 the gluon nPDF. On the other hand, the LHC measurements of the electroweak boson
 1682 production in pPb data did not significantly constrain the nPDF fits, mostly due to the
 1683 limited statistical precision, but the the results of the W-boson production from the CMS

1684 collaboration suggested possible differences in the modifications of the quark nPDFs.
 1685 The measurements of the electroweak boson production in heavy-ion collisions at LHC
 1686 will be presented in the next subsection.

1687 The EPPS16 includes five additional parameters compared to EPS09, to account for
 1688 possible flavour dependence of the quark nuclear modifications seen at LHC. The nuclear
 1689 PDFs are parametrised in EPPS16 as:

$$f_i^{p/A}(x, Q^2) = R_i^A(x, Q^2) f_i^p(x, Q^2) \quad (3.13)$$

1690 where $f_i^{p/A}$ represents the bound proton nPDF of parton i in a nucleus A, f_i^p is the
 1691 free proton PDF of parton i and R_i^A is the corresponding nuclear correction factor. The
 1692 EPPS16 nuclear modifications are derived using the NLO CT14 PDF as the free proton
 1693 baseline. The parameters of R_i^A are determined in three regions: the shadowing region
 1694 $x \rightarrow 0$, the anti-shadowing maximum point x_a and the EMC minimum point x_e (see
 1695 Figure 3.6). The dependence on the number of nucleons A is parametrised along the
 1696 three x regions in the following way:

$$R_i^A(x, Q_0^2) = R_i^{A_{\text{ref}}}(x, Q_0^2) \left(\frac{A}{A_{\text{ref}}} \right)^{\gamma_i [R_i^{A_{\text{ref}}}(x, Q_0^2) - 1]} \quad (3.14)$$

1697 where Q_0 is a parametrisation scale fixed at the charm pole mass (1.3 GeV), γ_i is
 1698 a positive parameter and $A_{\text{ref}} = 12$. The Q^2 dependence above Q_0^2 is determined by
 1699 solving the DGLAP parton evolution equations. The EPPS16 nuclear modifications are
 1700 parametrised in total by 20 parameters.

1701 The EPPS16 nuclear correction factors for Pb ions R^{Pb} extracted from the global PDF
 1702 fit are shown in Figure 3.7. The EPPS16 results are compared against a baseline derived
 1703 by performing the EPPS16 fits on the reduced dataset used in EPS09. The inclusion of
 1704 these CHORUS, RHIC p-A and LHC data improves the uncertainties of the gluon R^A at
 1705 high x and the strange-quark R^{Pb} at low x .

1706 **nCTEQ15 nPDF.** The nCTEQ15 nuclear PDFs, published by Kovarik et al. in 2016 [159],
 1707 were derived using the CTEQ framework. The nCTEQ15 nPDF global fits make use of
 1708 the charged-lepton DIS data, DY dilepton data and RHIC inclusive pion data. In contrast
 1709 with EPPS16, where the nuclear modification factor $R_i^{p/A}$ is fitted, the nCTEQ15 global
 1710 analysis parametrises the nuclear PDF $f_i^{p/A}$ directly (i.e. no free proton PDF is used as
 1711 baseline). The nCTEQ nPDFs are parametrised as:

3.1. INTRODUCTION

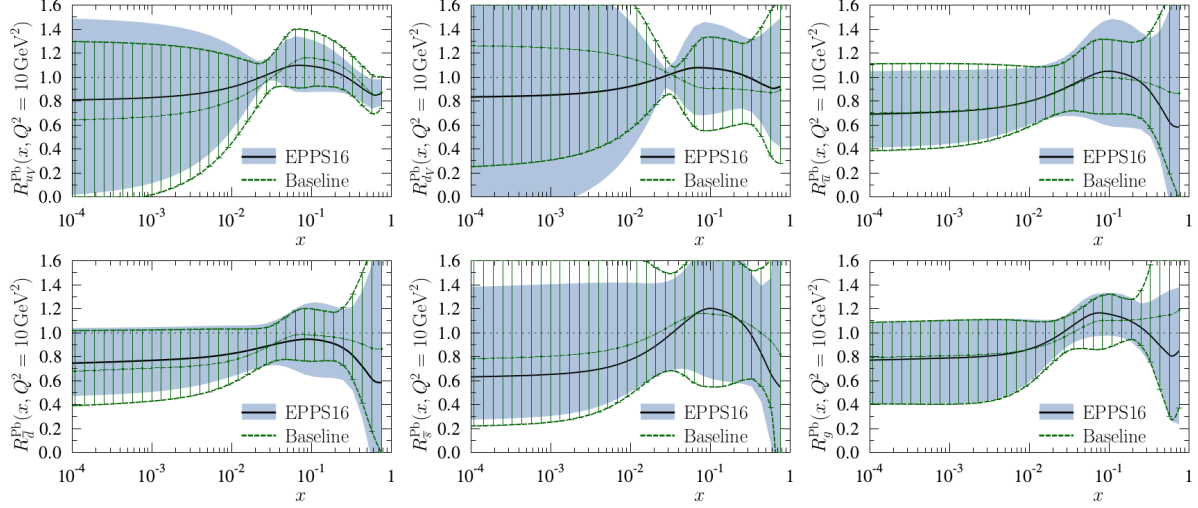


Figure 3.7: Results of the EPPS16 nuclear correction factor R^A for Pb ions at $Q^2 = 10 \text{ GeV}^2$. The black curve represents the central fit while the blue bands shows the total uncertainty of the PDF fit. The results are compared against a baseline made by performing the EPPS16 fits on the same datasets used for EPS09. Figure taken from Ref. [158].

$$x f_a^{p/A}(x, Q_0^2) = c_0 x^{c_1} (1-x)^{c_2} e^{c_3 x} (1 + e^{c_4 x})^{c_5} \\ \frac{\bar{d}(x, Q_0^2)}{\bar{u}(x, Q_0^2)} = c_0 x^{c_1} (1-x)^{c_2} + (1 + c_3 x)(1-x)^{c_4} \quad (3.15)$$

where $f_a^{p/A}$ is the bound proton nPDF of a parton a in a nucleus A, \bar{d} and \bar{u} are the down and up anti-quark nPDFs, respectively, c_i are parameters, and the parametrisation scale Q_0 is fixed at 1.3 GeV . The strange quark and anti-quark nPDFs are assumed to be the same. The A-dependence of the nPDFs is parametrised in nCTEQ15 using the coefficients c_i , according to:

$$c_i(A) = c_{i,0} + c_{i,1} (1 - A^{-c_{i,2}}) \quad (3.16)$$

The nCTEQ15 fits are performed using 16 free parameters. In addition, the nCTEQ15 treats the up and down valence quark PDFs independently but it assumes no flavour dependence for nuclear modifications of the up and down anti-quarks.

Figure 3.8 shows the nCTEQ15 results of the full nuclear lead PDFs f^{Pb} compared to the results from the EPS09 and HKN07 nPDFs. One can see that at $x \gtrsim 0.05$ and

1722 $Q^2 = 10 \text{ GeV}^2$ the up and down valence quark nPDFs dominates while at $x < 0.01$ the sea
 1723 quarks and the gluons nPDFs becomes dominant.

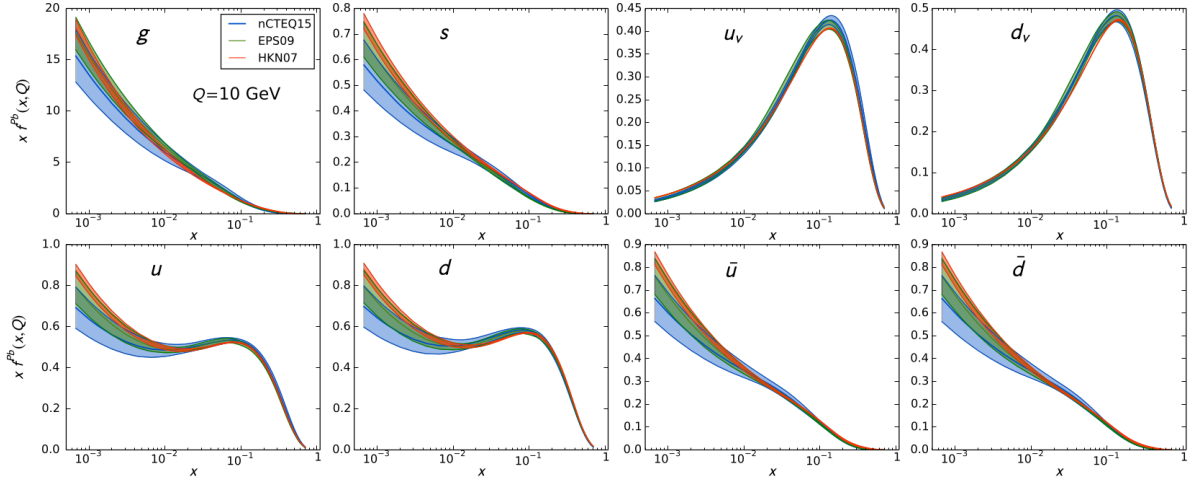


Figure 3.8: Results of the nCTEQ15 full nuclear PDFs for Pb ions f^{Pb} at $Q = 10 \text{ GeV}$.
 Figure taken from Ref. [159].

1724 A comparison between the results of the nCTEQ15 and EPPS16 nuclear modifications
 1725 is shown in Figure 3.9. The nCTEQ15 expects more shadowing than EPPS16 for the
 1726 down valence quarks and light sea quarks, while the opposite trend is observed for
 1727 up valence quarks. Moreover, the uncertainties of the EPPS16 results are much larger
 1728 than the nCTEQ15 results because the EPPS16 uses more parameters to fit the nuclear
 1729 modifications.

1730 The main characteristics of the EPS09, EPPS16 and nCTEQ15 nuclear PDFs are
 1731 summarized in Table 3.2.

1732 3.1.5 Experimental results at LHC

1733 Measurements of the weak boson production in heavy-ion collisions have been performed
 1734 by the LHC experiments. The latest results have been derived from p-Pb collisions
 1735 at $\sqrt{s_{\text{NN}}} = 5.02 \text{ TeV}$ and Pb-Pb collisions at $\sqrt{s_{\text{NN}}} = 2.56 \text{ TeV}$ and $\sqrt{s_{\text{NN}}} = 5.02 \text{ TeV}$. This
 1736 subsection gives a brief summary on some of the results.

1737 **Pb-Pb results.** The CMS [160, 161] and ATLAS [162, 163] collaboration measured
 1738 the W- and Z-boson production in Pb-Pb collisions at $\sqrt{s_{\text{NN}}} = 2.56 \text{ TeV}$ in the lepton
 1739 decay channel. The ATLAS and CMS measurements were performed in the mid-rapidity

3.1. INTRODUCTION

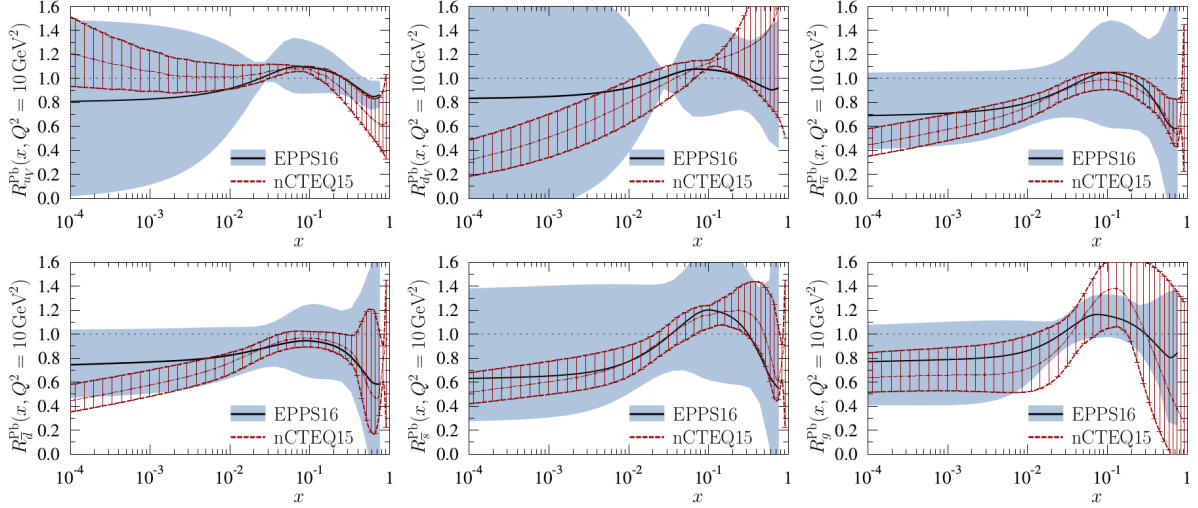


Figure 3.9: Comparison between the EPPS16 (black curve with blue band) and the nCTEQ15 (red curves with hatching) nuclear modifications performed at $Q^2 = 10 \text{ GeV}^2$. Figure taken from Ref. [158].

nPDF	EPS09	EPPS16	nCTEQ15
Order	NLO	NLO	NLO
Fit	nuclear modification	nuclear modification	nuclear PDF
Baseline PDF	CTEQ6	CT14	
Free parameters	15	20	17
Data points	929	1811	708
EMC DY dileptons in p-A	Yes	Yes	Yes
RHIC pions in d-A	Yes	Yes	Yes
SLAC l^\pm -A DIS	Yes	Yes	Yes
CHORUS ν -A DIS	No	Yes	No
RHIC DY in π -A	No	Yes	No
LHC dijets in pPb	No	Yes	No
LHC weak bosons in pPb	No	Yes	No

Table 3.2: Summary of the information of EPS09, EPPS16 and nCTEQ15 nuclear PDFs.

1740 region ($|y| < 2.5$). The results are in good agreement with NLO pQCD calculations with
 1741 and without nuclear PDF corrections. Moreover, the centrality dependence of the weak
 1742 boson yields is observed to scale with N_{coll} , within uncertainties. In the case of W boson,
 1743 the lepton charge asymmetry of W^\pm , defined as $(N_\ell^+ - N_\ell^-)/(N_\ell^+ + N_\ell^-)$, is found to be
 1744 different from the results in p-p collisions, but this is understood to be simply associated
 1745 to the different number of protons and neutrons in the Pb nuclei, the isospin effect. The

statistical precision of the results is not enough to provide significant constraints on the global fits to the PDFs.

Measurements from the ALICE collaboration on the production of Z bosons in Pb-Pb at $\sqrt{s_{NN}} = 5.20 \text{ TeV}$ complements the forward rapidity region ($2.5 < y < 4.0$). The ALICE results are in good agreement with model calculations including nuclear PDF corrections. On the contrary, the proton PDF calculations assuming only isospin effects deviates from the results by at most 3 standard deviations in the most central Pb-Pb collisions [164], starting to be sensitive to nuclear effects in the forward (low Bjorken-x) region.

p-Pb results. The ATLAS collaboration has measured the Z-boson production in p-Pb collisions at $\sqrt{s_{NN}} = 5.02 \text{ TeV}$. The Z-boson cross section as a function of the Z-boson rapidity determined in the centre-of-mass frame, is displayed in Figure 3.10. The results are better described by the PDF model calculations including nuclear modifications, although the free-proton PDF calculations are not excluded within the precision of the measurement.

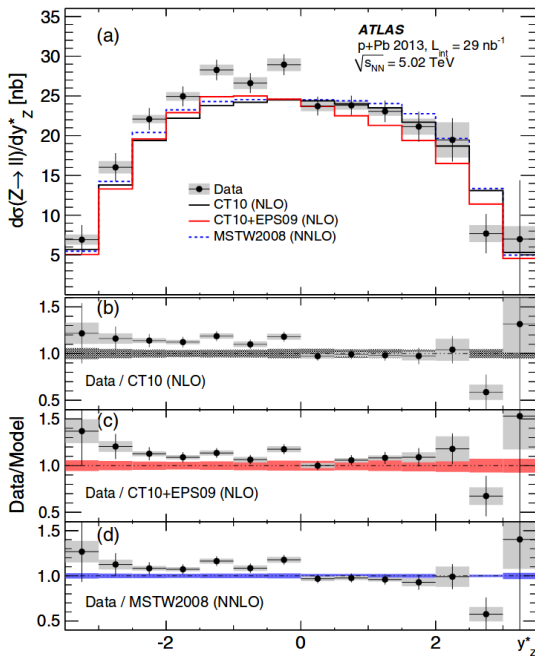


Figure 3.10: Distribution of the production cross section for $Z \rightarrow \mu^+ \mu^-$ measured as a function of the Z-boson rapidity measured in the centre-of-mass frame. Figure taken from Ref. [165].

The CMS and ALICE collaboration have published results on the production of W bosons in p-Pb collisions at $\sqrt{s_{NN}} = 5.02 \text{ TeV}$. The measurements of the W-boson

3.1. INTRODUCTION

1762 production cross section performed by the ALICE collaboration, as a function of the
 1763 lepton rapidity in the centre-of-mass frame, are shown in Figure 3.11. The ALICE results
 1764 are compared to NLO calculations using the CT10 proton PDF and NNLO calculations
 1765 using the FEWZ generator and the MSTW200 proton PDF, with and without EPS09
 1766 nuclear PDF corrections. The cross section results are found to be in good agreement with
 1767 the NLO model calculations while NNLO calculations without nuclear PDF modifications
 1768 slightly overestimate the measurement at forward lepton rapidity ($2.03 < |y_{\text{cms}}| < 3.53$).

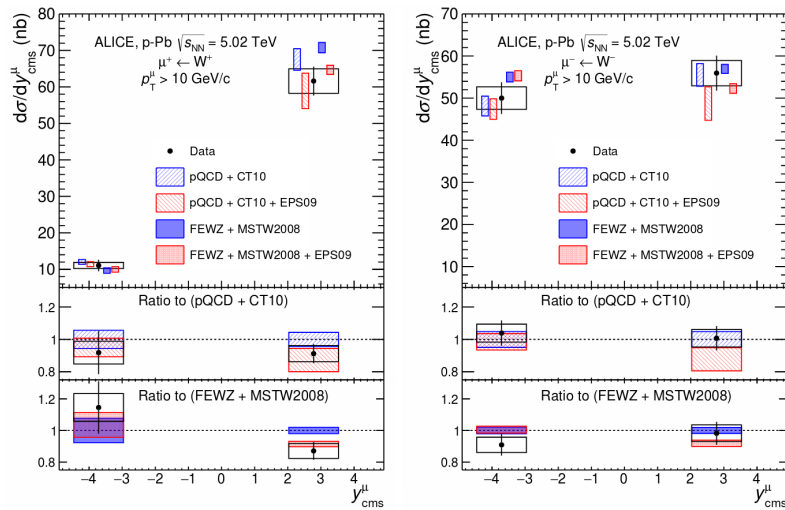


Figure 3.11: Distribution of the production cross section for $W^- \rightarrow \mu^- \bar{\nu}_\mu$ (left) and $W^+ \rightarrow \mu^+ \bar{\nu}_\mu$ (right) measured as a function of the muon rapidity in the centre-of-mass frame. Figure taken from Ref. [166].

1769 Finally, the W-boson measurements of CMS are performed in the muon and electron
 1770 decay channels as a function of the lepton pseudorapidity in the laboratory frame [167].
 1771 Figure 3.12 shows the measured cross sections for $W^- \rightarrow \ell^- \bar{\nu}_\ell$ (left) and $W^+ \rightarrow \ell^+ \nu_\ell$ (mid-
 1772 dle), and the lepton charge asymmetry (right), compared to the NLO pQCD calculations
 1773 using the CT10 proton PDF with and without EPS09 nuclear corrections. Both theoret-
 1774 ical calculations are found to be in good agreement with the measured cross sections
 1775 within uncertainties, except in the backward region ($\eta_{\text{lab}} < -1.0$) for W^- bosons, where a
 1776 small excess is seen in the results. The small deviation is also reflected in the measured
 1777 lepton charge asymmetry, where the model calculations overestimate the data in the
 1778 region $-2.0 < \eta_{\text{lab}} < -1.0$. It was suggested at the time that the small dis-agreement
 1779 between the PDF calculations and the data could be due to different flavour dependence
 1780 between the up and down quark PDFs [167].

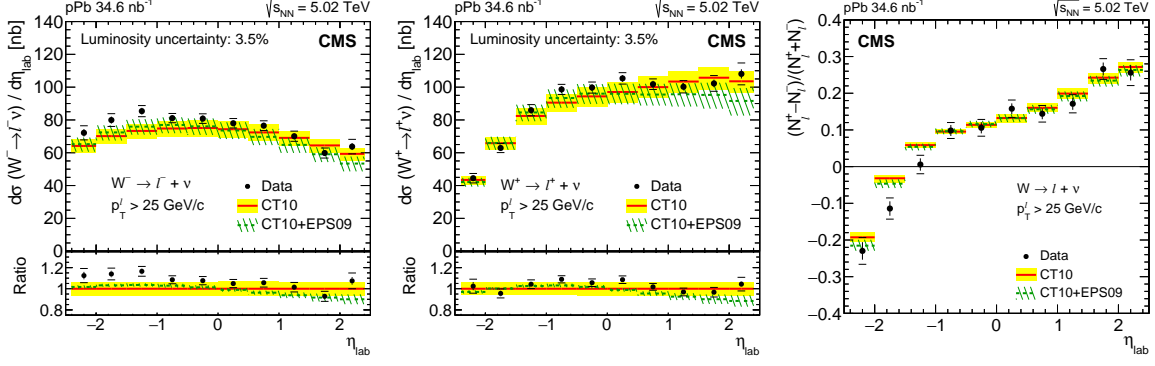


Figure 3.12: Distribution of the production cross section for $W^- \rightarrow \ell^- \bar{\nu}_\ell$ (left) and $W^+ \rightarrow \ell^+ \nu_\ell$ (middle), and the lepton charge asymmetry (right) measured as a function of the lepton pseudorapidity in the laboratory frame. The CT10 PDF calculations with EPS09 (green line) and without (red line) nuclear PDF corrections are included. The bottom panels present the ratio of the CT10+EPS09 (green line) and data (black points) normalised to the CT10 baseline. Figure taken from Ref. [167].

3.2 Analysis

In this section, the analysis of the W-boson production in p-Pb collisions at $\sqrt{s_{NN}} = 8.16$ TeV, is described. The measurement is performed in the $W^\pm \rightarrow \mu^\pm \nu_\mu$ decay channel using data recorded with the CMS detector and the signal event yields are extracted from the missing transverse momentum p_T^{miss} distributions. The analysis is currently in the final stage of the internal collaboration review and will be submitted to a peer-review journal in the near future.

The dataset used is introduced in Section 3.2.1, the NLO simulations for the signal and background processes are listed in Section 3.2.2, and the event selection is described in Section 3.2.3. The corrections for the simulated weak boson p_T and the p_T^{miss} are explained in Section 3.2.4 and Section 3.2.5, respectively. The measurement of the signal efficiency is presented in Section 3.2.6 and the extraction of the signal event yields is detailed in Section 3.2.7. The observables of the analysis are introduced in Section 3.2.8. In Section 3.2.9, the different sources of systematic uncertainties and the methods employed to estimate them are presented.

3.2.1 Dataset

The production of W bosons is measured in p-Pb collisions using data recorded by the CMS detector at the end of 2016. The dataset employed in this analysis is composed of

1799 events selected by the HLT trigger, requiring the presence of at least one identified muon
 1800 candidate with $p_T > 12 \text{ GeV}/c$. The data were reconstructed with CMSSW 8.0.30 and
 1801 thoroughly validated by the CMS collaboration. Only sections of the dataset, recorded
 1802 with all CMS subdetectors operating in optimal conditions, were processed. The total
 1803 integrated luminosity of the recorded data corresponds to 173.4 nb^{-1} , currently known
 1804 within 3.5% [168].

1805 The p-Pb data-taking period was divided in two parts, as explained in Section 2.1.5.
 1806 In the first part of the p-Pb run (labelled as Ppb), the proton beam was circulating in the
 1807 clockwise direction along the LHC ring, while in the second part (referred as pPb), the
 1808 proton beam was circulating counter-clockwise. The integrated luminosity recorded in
 1809 the Ppb and pPb runs was 62.6 nb^{-1} and 110.8 nb^{-1} , respectively.

1810 Since the LHC dipole magnets apply the same magnetic rigidity (i.e. momentum-
 1811 to-charge ratio) to both beams [169], the energy of the Pb beam is constrained by the
 1812 energy of the proton beam E_p , and the number of nucleons ($A_{\text{Pb}} = 208$) and electric
 1813 charge ($Z_{\text{Pb}} = 82$) of the Pb nucleus. During the entire p-Pb run, the energy of the proton
 1814 beam was 6.50 TeV and as a result, the energy per nucleon E_{Pb} of the Pb beam was then:

$$E_{\text{Pb}} = \frac{Z_{\text{Pb}}}{A_{\text{Pb}}} \times E_p = 2.56 \text{ TeV} \quad (3.17)$$

1815 In addition, the energy of the nucleon-nucleon collisions in the centre-of-mass (CM)
 1816 frame can be derived in this case using:

$$\sqrt{s_{\text{NN}}} = 2 \sqrt{\frac{Z_{\text{Pb}}}{A_{\text{Pb}}} \times E_p} = 8.16 \text{ TeV} \quad (3.18)$$

1817 Considering that the CMS detector is rapidity-symmetric with respect to the beam
 1818 orientation, the pPb and Ppb samples are merged in order to maximize the statistics of
 1819 the data. This is done by first flipping the sign of the pseudorapidity of particles from
 1820 the Ppb sample measured in the laboratory frame, and then combining them with the
 1821 events from the pPb sample. The combined samples corresponds to p-Pb collisions with
 1822 the proton always going toward positive pseudorapidity. From hereafter, all results in
 1823 this analysis are derived using the combined pPb sample.

1824 Due to the energy difference between the p-Pb colliding beams, the nucleon-pair CM
 1825 frame is not at rest with respect to the laboratory frame. Massless particles emitted in
 1826 the CM frame experience a constant longitudinal boost given by:

$$|\Delta\eta| = \frac{1}{2} \times \left| \ln \left(\frac{Z_{\text{Pb}}}{A_{\text{Pb}}} \right) \right| = 0.465 \quad (3.19)$$

1827 As a consequence, the pseudorapidity measured in the CM frame (η_{CM}) is derived
 1828 from the one determined in the laboratory frame (η_{lab}), in the following way:

$$\eta_{\text{CM}} = \eta_{\text{lab}} - 0.465 \quad (3.20)$$

1829 3.2.2 Next-to-leading order simulations

1830 Fully reconstructed Monte Carlo (MC) simulations are used to describe the W-boson
 1831 signal, and the top-quark and electroweak background processes. The MC samples were
 1832 generated at NLO using the PPositive Weight Hardest Emission Generator (POWHEG)
 1833 version 2 [170–172]. To account for QCD and electroweak theory corrections, the POWHEG-
 1834 BOX packages $W_{\text{ew}}\text{-BMMNP}$ [173] and $Z_{\text{ew}}\text{-BMMNPV}$ [174] were used to generate the
 1835 $p\bar{p} \rightarrow W \rightarrow \ell\nu_\ell$ and $p\bar{p} \rightarrow Z/\gamma^* \rightarrow \ell^+\ell^-$ processes, respectively. The $p\bar{p} \rightarrow t\bar{t}$ was generated
 1836 using the POWHEG-BOX package hvq [175], which is a heavy flavour quark generator at
 1837 NLO QCD.

1838 In order to simulate p-Pb collisions, I added to the POWHEG Fortran code a subroutine
 1839 that modifies the PDFs of one of the incoming particles (referred as the Pb nucleus) by
 1840 applying the EPPS16 nuclear correction factors derived for Pb^{82+} nuclei ² [158], since
 1841 the standard POWHEG framework only generates p-p collision events. In this case, the
 1842 POWHEG event generation starts by evaluating the PDFs associated to both incoming
 1843 particles (proton and Pb nucleus) using the NLO CT14 PDF set [150]. Afterwards, the
 1844 PDFs corresponding to the Pb nucleus are modified with my subroutine, following the
 1845 procedure defined in Ref. [158] and described in the following steps:

1846 1. The EPPS16 nuclear correction factors R are applied to the PDFs computed by
 1847 POWHEG, in the following way:

$$\begin{aligned} \hat{f}_p^d &= R_s^d f_p^{\bar{d}} + R_v^d (f_p^d - f_p^{\bar{d}}) & ; \quad \hat{f}_p^{\bar{d}} &= R_s^d f_p^{\bar{d}} \\ \hat{f}_p^u &= R_s^u f_p^{\bar{u}} + R_v^u (f_p^u - f_p^{\bar{u}}) & ; \quad \hat{f}_p^{\bar{u}} &= R_s^u f_p^{\bar{u}} \\ \hat{f}_p^x &= R_s^x f_p^x & ; \quad \hat{f}_p^{\bar{x}} &= R_s^x f_p^{\bar{x}} \quad \text{where } x = \{s, c, b\} \\ \hat{f}_p^g &= R_g^g f_p^g \end{aligned} \quad (3.21)$$

1848 where \hat{f}_p represent the PDFs of a proton bound in the Pb nucleus, f_p are the free
 1849 proton PDFs obtain with NLO CT14, and R_s^x , R_v^x and R_g^g are the EPPS16 nuclear
 1850 correction factors for sea quarks, valence quarks and gluons, accordingly.

²The EPPS16 nuclear correction factors for each nuclei can be found in <https://www.jyu.fi/science/en/physics/research/highenergy/urhic/npdfs/epps16-nuclear-pdfs>

- 1851 2. The bound neutron PDFs (\hat{f}_n) are then derived from the bound proton PDFs, by
 1852 interchanging the up and down (anti-)quark PDFs (isospin symmetry between
 1853 protons and neutrons), according to:

$$\begin{aligned}\hat{f}_n^d &= \hat{f}_p^u & ; \quad \hat{f}_n^u &= \hat{f}_p^d \\ \hat{f}_n^{\bar{d}} &= \hat{f}_p^{\bar{u}} & ; \quad \hat{f}_n^{\bar{u}} &= \hat{f}_p^{\bar{d}}\end{aligned}\tag{3.22}$$

1854 and assuming the same PDFs ($\hat{f}_n^i = \hat{f}_p^i$) for the other flavours.

- 1855 3. The bound proton and neutron PDFs are combined to form the Pb-nucleus PDFs
 1856 (f_{Pb}), taking into account the number of protons (Z_{Pb}) and neutrons ($N_{Pb} = A_{Pb} -$
 1857 Z_{Pb}) in the Pb nucleus, as done in:

$$\begin{aligned}f_{Pb}^d &= \left(\frac{Z_{Pb}}{A_{Pb}}\right) \hat{f}_p^d + \left(\frac{N_{Pb}}{A_{Pb}}\right) \hat{f}_n^d & ; \quad f_{Pb}^{\bar{d}} &= \left(\frac{Z_{Pb}}{A_{Pb}}\right) \hat{f}_p^{\bar{d}} + \left(\frac{N_{Pb}}{A_{Pb}}\right) \hat{f}_n^{\bar{d}} \\ f_{Pb}^u &= \left(\frac{Z_{Pb}}{A_{Pb}}\right) \hat{f}_p^u + \left(\frac{N_{Pb}}{A_{Pb}}\right) \hat{f}_n^u & ; \quad f_{Pb}^{\bar{u}} &= \left(\frac{Z_{Pb}}{A_{Pb}}\right) \hat{f}_p^{\bar{u}} + \left(\frac{N_{Pb}}{A_{Pb}}\right) \hat{f}_n^{\bar{u}} \\ f_{Pb}^i &= \hat{f}_p^i & \text{for other flavours}\end{aligned}\tag{3.23}$$

- 1858 4. The PDFs originally derived by POWHEG are then replaced with the modified PDFs
 1859 defined in Eq. (3.23), and the rest of the event generation is done with the standard
 1860 POWHEG framework with no further changes.

1861 The parton showering is performed by hadronizing the POWHEG events with PYTHIA
 1862 8.212 [176], using the CUETP8M1 underlying event (UE) tune [176, 177]. The full CMS
 1863 detector response is simulated in all MC samples, based on GEANT4 [178], considering
 1864 a realistic alignment and calibration of the beam spot and the different subdetectors
 1865 of CMS, tuned on data. The MC events are reconstructed with the standard CMS p-p
 1866 reconstruction software used during 2016 data taking.

1867 To consider a more realistic distribution of the underlying environment present in
 1868 p-Pb collisions, the MC signal events were embedded in a minimum bias (i.e. inelastic
 1869 hadronic interactions) sample generated with EPOS LHC [179], taking into account both
 1870 p-Pb boost directions. The EPOS LHC MC samples were tuned to reproduce the global
 1871 event properties of the p-Pb data such as the charged-hadron transverse momentum
 1872 spectrum and the particle multiplicity [180]. The list of simulated samples and the cross
 1873 sections used in this analysis are summarized in Table 3.3. The cross sections of the
 1874 electroweak processes corresponds to the POWHEG NLO cross sections scaled by A_{Pb} ,

1875 while the $t\bar{t}$ cross section is taken from the inclusive cross section measured in pPb
 1876 collisions at $\sqrt{s_{NN}} = 8.16 \text{ TeV}$ by the CMS collaboration [181].

Process	Cross section [nb]	Generated events
$p\text{Pb} \rightarrow W^+ \rightarrow \mu^+ \nu_\mu$	1214	982714
$p\text{pb} \rightarrow W^+ \rightarrow \mu^+ \nu_\mu$	1214	981874
$p\text{Pb} \rightarrow W^- \rightarrow \mu^- \bar{\nu}_\mu$	1083	995726
$p\text{pb} \rightarrow W^- \rightarrow \mu^- \bar{\nu}_\mu$	1083	998908
$p\text{Pb} \rightarrow W^+ \rightarrow \tau \nu_\tau$	1147	481125
$p\text{pb} \rightarrow W^+ \rightarrow \tau \bar{\nu}_\tau$	1147	500000
$p\text{Pb} \rightarrow W^- \rightarrow \tau \bar{\nu}_\tau$	1023	495450
$p\text{pb} \rightarrow W^- \rightarrow \tau \bar{\nu}_\tau$	1023	498092
$p\text{Pb} \rightarrow Z/\gamma^* \rightarrow \mu^+ \mu^-$	266	1000000
$p\text{pb} \rightarrow Z/\gamma^* \rightarrow \mu^+ \mu^-$	266	1000000
$p\text{pb} \rightarrow Z/\gamma^* \rightarrow \tau \bar{\tau}$	259	498444
$p\text{Pb} \rightarrow t\bar{t}$	45 ± 8	99578
$p\text{pb} \rightarrow t\bar{t}$	45 ± 8	100000

Table 3.3: Simulated NLO samples used for the W-boson measurement in p-Pb at 8.16 TeV. The listed cross sections are the POWHEG NLO cross sections scaled by $A_{\text{Pb}} = 208$, except for the $t\bar{t}$ production cross section which is taken from the CMS measurement in p-Pb at 8.16 TeV [181].

1877 The pPb and Pbp simulated samples are also combined in the same way as done for
 1878 data, but the generated events are weighed before merging the samples by applying a
 1879 global weight, according to their p-Pb boost direction, defined as:

$$w_{\text{MC}} = \frac{\sigma \times \mathcal{L}_{\text{data}}}{N_{\text{gen}}} \quad (3.24)$$

1880 where $\mathcal{L}_{\text{data}}$ corresponds to the integrated luminosity recorded in each proton-lead
 1881 run (110.8 nb^{-1} for pPb and 62.6 nb^{-1} for Pbp), σ is the cross section associated to the
 1882 simulated process (listed in Table 3.3) and N_{gen} is the total number of generated events.
 1883 The global weighing is applied to ensure that each MC sample is normalised to the
 1884 corresponding integrated luminosity of the data.

1885 3.2.3 Event selection

1886 The signal events, determined by the process $W \rightarrow \mu\nu_\mu$, are characterised by a high-
 1887 p_T muon and the presence of missing transverse momentum p_T^{miss} , originated from
 1888 the undetected neutrino. Events with similar characteristics can be produced by other

1889 background processes, such as semi-leptonic decays of hadrons formed within jets or
1890 dilepton decays of Z bosons. This section explain the different selections implemented to
1891 suppress the background while keeping the signal.

1892 **3.2.3.1 p-Pb global filter**

1893 In order to ensure that the samples are not contaminated by events not originating from
1894 the inelastic hadronic collisions, a standard p-Pb Global Event Filter (GEF) is applied.
1895 The different selections included in the p-Pb GEF are described below:

- 1896 • Primary vertex filter: requires the presence of a primary vertex reconstructed from
1897 at least two tracks, within a longitudinal (transverse) distance of 25 cm (2 cm) of
1898 the nominal interaction point. This selection reduces the contamination from non-
1899 collision backgrounds, such as cosmic-ray muons or accelerator-induced particles.
- 1900 • HF coincidence filter: requires at least one tower on each side of the interaction
1901 point in the Hadron-Forward calorimeter, with an energy deposit per tower of
1902 at least 3 GeV. This filter rejects events from electronic noise and beam-beam
1903 electromagnetic interactions.
- 1904 • Beam-scraping filter: requires at least 25% of tracks in the event to be high quality
1905 tracks. This requirement is used to further suppress the contribution from beam-
1906 related backgrounds, such as beam-gas interactions and beam-halo events.

1907 The impact of the GEF was checked both in data and simulation. Only 0.08% of
1908 events in data and 0.06% of events in the $W \rightarrow \mu\nu_\mu$ simulation, passing all analysis
1909 selections summarized in Section 3.2.3.5, were removed by the filter.

1910 **3.2.3.2 Trigger**

1911 The events used in this analysis were selected online with the HLT trigger HLT_PAL3Mu12.
1912 This trigger requires a fully reconstructed L3 muon with $p_T > 12$ GeV/c. The HLT trigger
1913 was seeded with the L1 trigger path L1_SingleMu7, which pass events with at least
1914 one L1 muon with $p_T > 7$ GeV/c. It is to be noted that only muons of p_T greater than
1915 25 GeV/c are considered in the offline analysis, and that this trigger is extremely efficient
1916 for those.

1917 A reconstructed muons is considered matched to the trigger, if it matches the L3
1918 muon that fired the trigger. The matching criteria between the reconstructed muon and
1919 the L3 muon requires:

$$\Delta R(\mu_{\text{reco}}, \mu_{\text{HLT}}) = \sqrt{(\eta_{\text{reco}}^\mu - \eta_{\text{HLT}}^\mu)^2 + (\phi_{\text{reco}}^\mu - \phi_{\text{HLT}}^\mu)^2} < 0.1 \quad (3.25)$$

3.2.3.3 Muon selection

Muon candidates are identified using a standard *tight* selection, optimised for muons with high p_T . The tight selection requires muon candidates to be reconstructed globally from hits in the muon stations and the tracker, be identified with the PF algorithm [111] and pass the following criteria:

- The muon track fit has at least a χ^2 per degree of freedom less than ten, ensuring a minimal fit quality.
- The muon track segments are matched to at least two muon stations, making the selection consistent with the muon trigger logic.
- The transverse impact parameter (longitudinal distance) of the muon track is consistent with the primary vertex within 2 mm (5 mm), to reduce the background from cosmic rays and muon decays in flight (e.g. from pion, kaon and heavy-flavour hadron decays).
- The muon track has at least one hit in the pixel detector to further suppress muons from decays in flight.
- The muon track includes hits in at least six inner-tracker layers to guarantee a good p_T measurement.

Apart from the *tight* identification criteria, muon candidates are also required to be isolated in order to reduce the proportion of muons coming from jets. Muons are considered isolated if the sum of the p_T of all PF-identified photons, charged hadrons and neutral hadrons, within a cone of $\Delta R(\mu, \text{PF}) < 0.3$, is less than 15% of the muon p_T^μ . The muon isolation variable is thus defined as:

$$I^\mu = \left(\sum_{\text{charged hadrons}}^{\Delta R < 0.3} p_T + \sum_{\text{neutral hadrons}}^{\Delta R < 0.3} p_T + \sum_{\text{photons}}^{\Delta R < 0.3} p_T \right) / p_T^\mu \quad (3.26)$$

Finally, muon candidates are required to have $p_T > 25 \text{ GeV}/c$ and be within $|\eta_{\text{lab}}| < 2.4$. If more than one muon is found with $p_T > 25 \text{ GeV}/c$ and passing the identification criteria in a given event, then the corresponding muon with the highest p_T is used. This happens in 3% of events in data but are later suppressed down to 0.001% of events with the $Z/\gamma^* \rightarrow \mu^+ \mu^-$ veto described in the next section.

1947 **3.2.3.4 $Z/\gamma^* \rightarrow \mu^+ \mu^-$ veto**

1948 A veto is applied to suppress the contribution from $Z/\gamma^* \rightarrow \mu^+ \mu^-$ background events. This
 1949 veto consists in removing events that contain at least two opposite-sign muons with
 1950 $p_T > 15 \text{ GeV}/c$, each passing the muon identification and isolation criteria.

1951 The probability that $Z/\gamma^* \rightarrow \mu^+ \mu^-$ events survive the veto is checked using simulation.
 1952 The denominator of the $Z/\gamma^* \rightarrow \mu^+ \mu^-$ veto efficiency is filled with muons passing the
 1953 signal selection criteria summarised in the next section, while the numerator is filled
 1954 with the same muons as long as the event pass the $Z/\gamma^* \rightarrow \mu^+ \mu^-$ veto. The simulated
 1955 survival probability is shown in Figure 3.13. As can be observed, most of the $Z/\gamma^* \rightarrow \mu^+ \mu^-$
 1956 events that survive the veto mainly contributes in the forward pseudorapidity region,
 1957 where one of the muons from the Z/γ^* -boson decay escapes the detector.

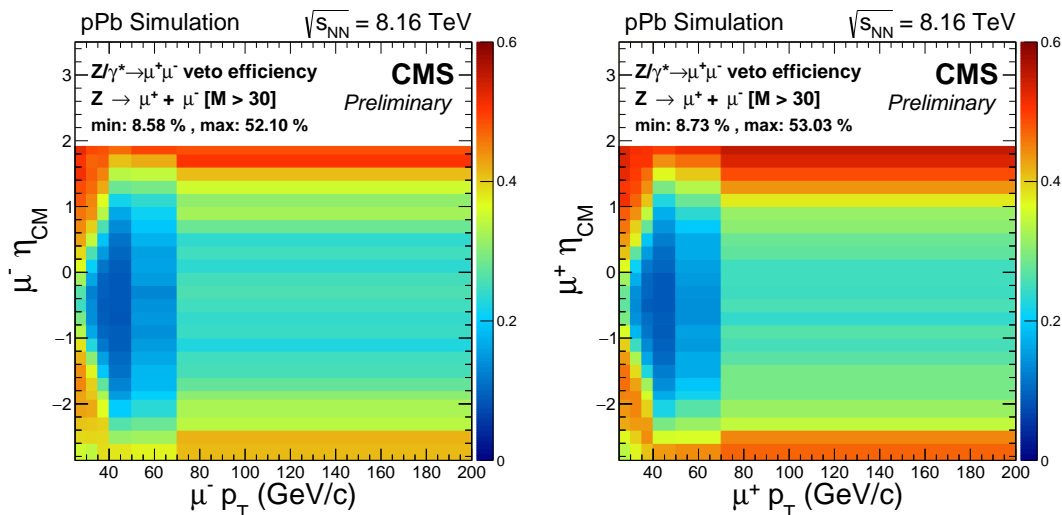


Figure 3.13: Survival probability of single muons from a $Z/\gamma^* \rightarrow \mu^+ \mu^-$ ($M > 30 \text{ GeV}/c^2$) simulation, as a function of the muon η_{CM}^μ and p_T^μ , separated in negative (left) and positive (right) charged muons. Muons are required to have $p_T > 25 \text{ GeV}/c$ and $|\eta| < 2.4$, match the trigger and pass the isolation and identification criteria.

1958 **3.2.3.5 Event selection summary**

1959 In summary, the signal selection consists of the detection of a high- p_T muon, passing the
 1960 identification criteria detailed in Section 3.2.3.3. The muon candidate is required to have
 1961 $p_T > 25 \text{ GeV}/c$, be isolated and match the trigger (see Section 3.2.3.2). The events entering
 1962 the signal region are also required to satisfy the p-Pb global event filter (Section 3.2.3.1)
 1963 and the $Z/\gamma^* \rightarrow \mu^+ \mu^-$ veto (Section 3.2.3.4).

1964 The other signature of a $W \rightarrow \mu\nu_\mu$ event is a high- p_T neutrino, estimated through the
 1965 p_T^{miss} . No explicit selection is applied on the missing transverse momentum. The p_T^{miss} is
 1966 directly used to extract the event yields by fitting the signal and background components.
 1967 Apart from the main signal sample, two more samples are used:

- 1968 • $Z \rightarrow \mu^+ \mu^-$ control sample: selects $Z \rightarrow \mu^+ \mu^-$ events by reverting the $Z/\gamma^* \rightarrow \mu^+ \mu^-$
 1969 veto and selecting $\mu^+ \mu^-$ pairs with invariant mass within the Z -boson mass window.
 1970 Used to derive corrections for the weak boson p_T (Section 3.2.4) and the p_T^{miss}
 1971 (Section 3.2.5).
- 1972 • QCD jet control sample: selects non-isolated muon events by reverting the muon
 1973 isolation cut. Used to determine the shape of the QCD jet background from data.

1974 The conditions used to define the signal and control regions of interest are illustrated
 1975 in Figure 3.14.

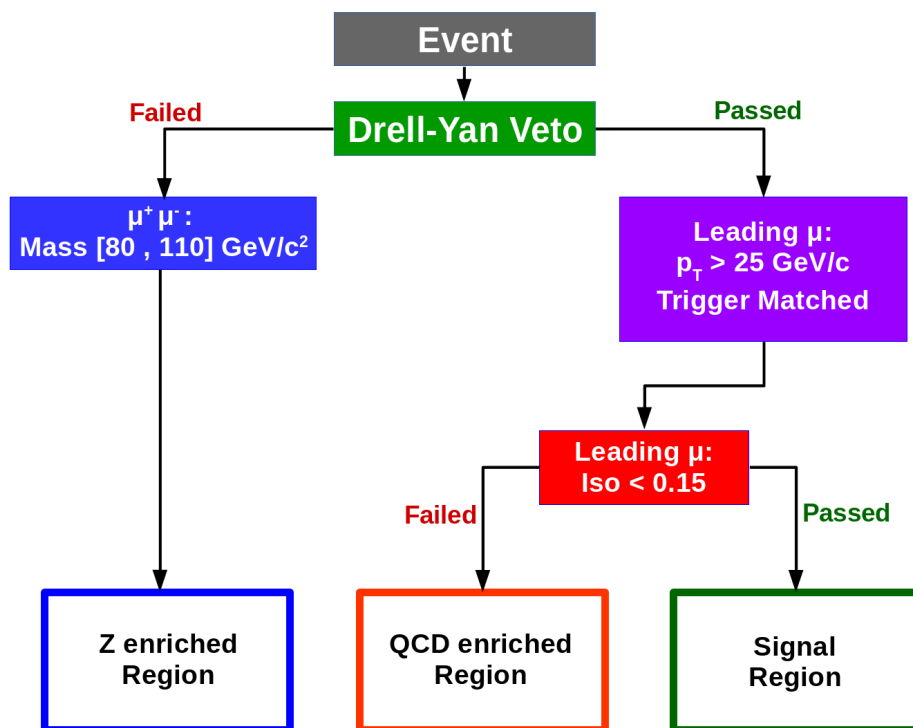


Figure 3.14: Flowchart illustrating the way the events are classified

1976 3.2.4 Correction for weak-boson transverse momentum

1977 In a p-Pb collision at high energies, the partons can be described as moving collinearly
 1978 with the proton or the Pb nucleus, contributing momentum only along the beam axis. As
 1979 a result, at leading order, W and Z bosons are produced with no transverse momentum.
 1980 Higher order processes, such as NLO or next-to-NLO, can radiate quarks and gluons
 1981 that recoil against the weak boson, which acquires transverse momentum in the process.

1982 Since the simulations were produced using the POWHEG NLO generator, the absence
 1983 of higher order contributions can lead to a mismodelling of the weak boson p_T , which can
 1984 then affect the p_T distribution of the boson decay products (e.g. muon and neutrino). To
 1985 check this, one can select $Z \rightarrow \mu^+ \mu^-$ events and compare the p_T distribution of Z boson
 1986 candidates from simulation and data.

1987 The p_T distribution of Z bosons has been measured in an on-going CMS analysis of
 1988 the Drell–Yan production in pPb collisions at 8.16 TeV³, which makes use of the same
 1989 data and electroweak NLO simulations presented in this chapter. As part of the DY
 1990 analysis, the measurement of the Z-boson p_T distribution in the dimuon mass region [60,
 1991 120] GeV/ c^2 was compared, after correcting for acceptance and efficiency, to the generated
 1992 one from POWHEG and found to disagree by up to 20%. To correct for the disagreement,
 1993 the ratio between the measured and simulated p_T -differential $Z \rightarrow \mu^+ \mu^-$ cross sections
 1994 was parametrised as a function of the Z-boson p_T , resulting in:

$$w^Z(p_T) = \frac{\left(\frac{d\sigma[Z \rightarrow \mu^+ \mu^-]}{dp_T}\right)^{\text{data}}}{\left(\frac{d\sigma[Z \rightarrow \mu^+ \mu^-]}{dp_T}\right)^{\text{MC}}} = \frac{1}{1.19 - 0.37 \times p_T^{-0.37}} \quad (3.27)$$

1995 and the generated Z-boson p_T distribution was then weighed per event using $w^Z(p_T)$.

1996 Considering that Z and W bosons have similar production mechanisms and masses,
 1997 $w^Z(p_T)$ is also used to weigh, on an event-by-event basis, the generated W-boson p_T
 1998 spectrum. The boson p_T weighing is applied to the POWHEG simulations of both signal
 1999 ($W \rightarrow \mu\nu_\mu$) and electroweak backgrounds ($W \rightarrow \tau\nu_\tau$, $Z/\gamma^* \rightarrow \mu^+ \mu^-$ and $Z/\gamma^* \rightarrow \tau\bar{\tau}$).

2000 The impact of the boson p_T weighing is checked on a W-boson enhanced sample in
 2001 data and simulation, made by applying a requirement on the transverse mass, defined
 2002 as $M_T = \sqrt{p_T^\mu \cdot p_T^{\text{miss}} \cdot (1 - \cos(\Delta\theta))}$, where $\Delta\theta$ is the azimuthal angle between the \vec{p}_T^{miss}
 2003 and muon \vec{p}_T^μ . The events of the W-boson enhanced sample are selected from the signal
 2004 region by requiring $M_T > 60$ GeV/ c , and the corresponding muon p_T distribution is then

³The details of the CMS Drell–Yan analysis can be checked in the private link <http://cms.cern.ch/iCMS/analysisadmin/cadilines?line=HIN-18-003&tp=an&id=2036&ancode=HIN-18-003>

2005 compared before and after applying the boson p_T weighing in Figure 3.15. The simulated
 2006 muon p_T distribution is observed to describe better the data in the high- p_T region
 2007 ($p_T^\mu \gtrsim 40$ GeV/c) after weighing the generated W-boson boson p_T distribution.

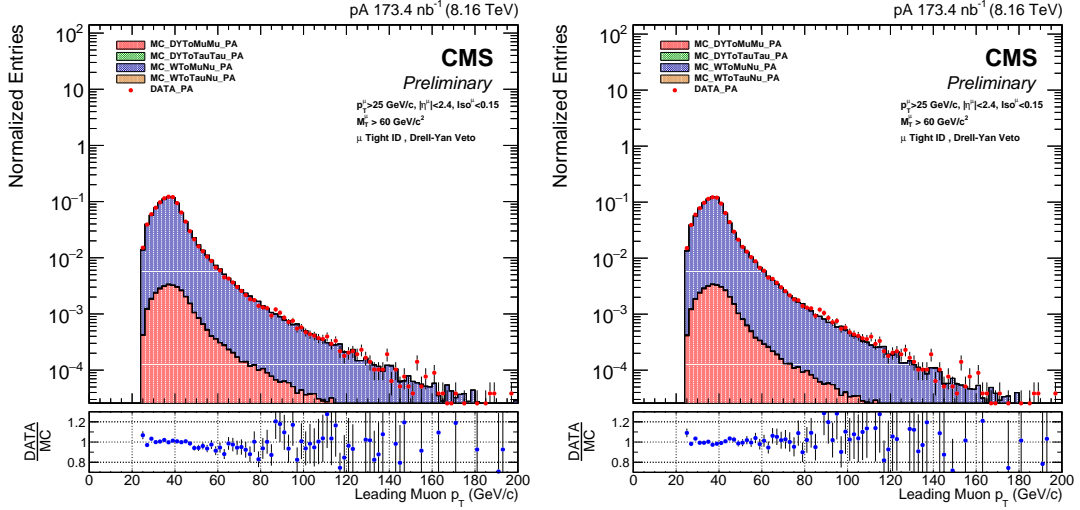


Figure 3.15: Muon p_T distribution extracted from the W-boson enhanced sample before (left) and after (right) applying the boson p_T weights. The red points correspond to data, while the blue and red filled areas correspond to events from the $W \rightarrow \mu\nu_\mu$ and $Z/\gamma^* \rightarrow \mu^+\mu^-$ simulations, respectively. The bottom panels shows the ratio of data over simulation.

3.2.5 Corrections for missing transverse momentum

2009 Since the W-boson analysis relies on p_T^{miss} distributions from simulations to extract the
 2010 signal, it is important that the simulated p_T^{miss} describes the data. To achieve this, the
 2011 p_T distribution of the reconstructed particles, including those recoiling against the weak
 2012 boson (referred as the recoil), have to be well modelled.

2013 The p_T^{miss} vector derived from $W \rightarrow \mu\nu_\mu$ events can be decomposed, according to
 2014 Eq. (2.5), in two parts: the p_T vector of the muon candidate (\vec{p}_T^μ) and the p_T vector of the
 2015 recoil (\vec{u}_T), as defined in:

$$\vec{p}_T^{\text{miss}} = -(\vec{u}_T + \vec{p}_T^\mu) \quad (3.28)$$

2016 The recoil \vec{u}_T is measured via the \vec{p}_T vectorial sum of all particles identified in an
 2017 event with the PF algorithm *excluding* the muon from the W-boson decay, as given by:

$$\vec{u}_T = \left(\sum_{\text{particles}} \vec{p}_T \right) - \vec{p}_T^\mu \quad (3.29)$$

2018 The recoil is a complex quantity that includes particles from the hard scattering
 2019 that balances the W-boson p_T and from the underlying event (e.g. spectator parton
 2020 interactions and multiple parton scatterings), as well as effects related to the detector
 2021 (e.g. electronic noise, p_T resolution, reconstruction efficiency and acceptance) and the
 2022 accelerator (e.g. beam-beam remnants). As a result, the recoil is difficult to simulate
 2023 precisely in p-Pb collisions and the mismodelling of the recoil u_T can affect the signal
 2024 extraction.

2025 To improve the modelling of the p_T^{miss} in the signal region, the p_T^{miss} is corrected in
 2026 two steps. First, the distribution of the simulated event activity measured as a function
 2027 of the total energy deposited in the HF calorimeter (hereafter referred as the HF energy)
 2028 is weighed to the level observed in data as detailed in Section 3.2.5.1. Afterwards, the
 2029 simulated recoil is calibrated following the procedure described in Section 3.2.5.2.

2030 3.2.5.1 Event activity weighing

2031 The muon isolation and the p_T^{miss} are computed by summing over particles produced in
 2032 the event. As a consequence, any disagreement in the modelling of the event activity (EA)
 2033 can impact the muon efficiency and the signal extraction. The disagreement between
 2034 data and the POWHEG simulations embedded in EPOS minimum bias events can be
 2035 caused by the presence of hard probes such as W bosons, which bias the event activity
 2036 towards higher particle multiplicity compared to minimum bias events.

2037 To check if the event activity is well modelled in the simulations, the distribution
 2038 of the number of tracks per event and the HF energy is compared between data and
 2039 simulation in a $Z \rightarrow \mu^+ \mu^-$ control sample. The $Z \rightarrow \mu^+ \mu^-$ events are selected by requiring
 2040 a $\mu^+ \mu^-$ pair within the invariant mass region $80 < M_{\mu^+ \mu^-} < 110$ GeV/ c^2 as detailed in
 2041 Section 3.2.3.5. The data-simulation comparisons are shown in Figure 3.16, and it is
 2042 observed that the simulated samples are indeed not able to reproduce the event activity
 2043 present in p-Pb data.

2044 The modelling of the event activity is improved using a set of weights determined
 2045 from the ratio of the number of $Z \rightarrow \mu^+ \mu^-$ events extracted from data and simulation in
 2046 different bins of HF energy (E_{HF}), as given by:

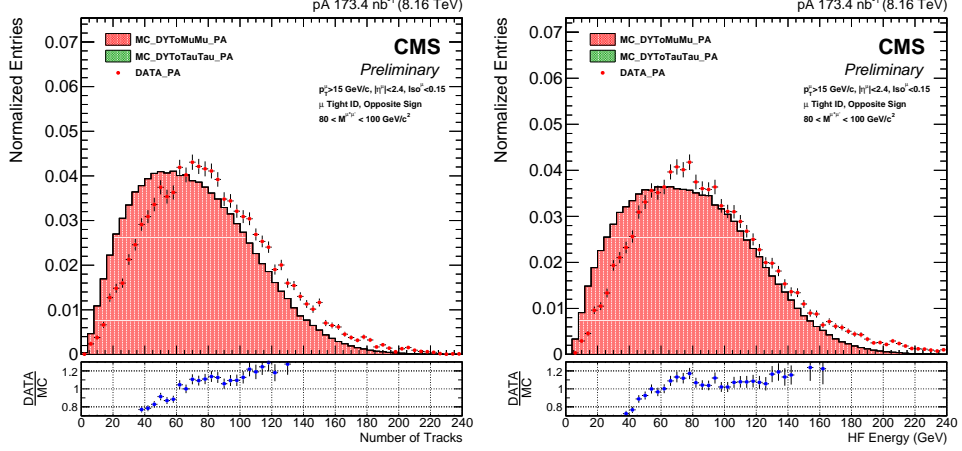


Figure 3.16: Distribution of the number of tracks per event (left) and the total energy deposited in the HF calorimeter (right) in $Z \rightarrow \mu^+ \mu^-$ events. The red points and filled area correspond to data and $Z/\gamma^* \rightarrow \mu^+ \mu^-$ simulation, respectively.

$$w^{\text{EA}}(E_{\text{HF}}) = \frac{N_{Z \rightarrow \mu^+ \mu^-}^{\text{data}}[E_{\text{HF}}]}{N_{Z \rightarrow \mu^+ \mu^-}^{\text{MC}}[E_{\text{HF}}]} \quad (3.30)$$

2047 The $w^{\text{EA}}(E_{\text{HF}})$ weights are used, event-by-event, to weigh the HF energy distribution
 2048 of the electroweak and $t\bar{t}$ simulations. Figure 3.17 shows that the HF energy weighing
 2049 improves the simulation-to-data agreement of the p_T^{miss} distribution of $Z \rightarrow \mu^+ \mu^-$ events.
 2050 The remaining level of disagreement in the p_T^{miss} is then corrected for by calibrating the
 2051 simulated recoil as explained in the next section.

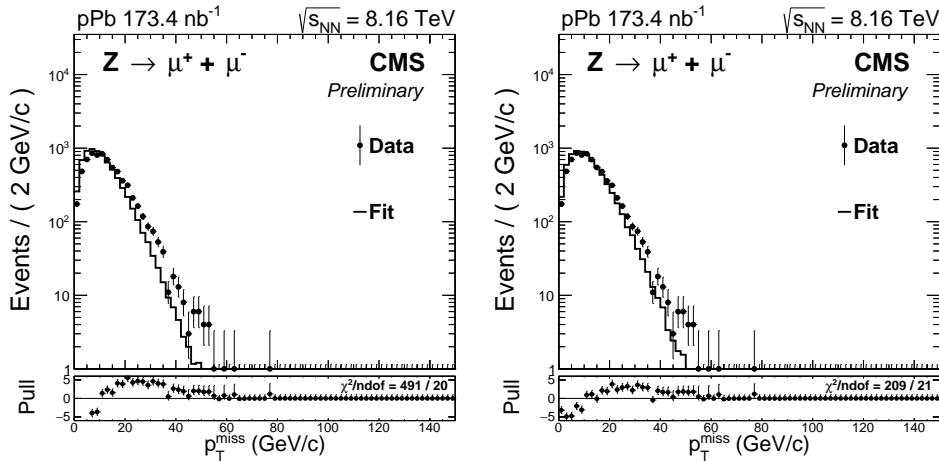


Figure 3.17: Comparison of the p_T^{miss} distribution in data and simulation for $Z \rightarrow \mu^+ \mu^-$ events before (left) and after (right) applying the HF energy weights.

2052 **3.2.5.2 Recoil calibration**

2053 The recoil calibration procedure starts by measuring the recoil in $Z \rightarrow \mu^+ \mu^-$ events in
 2054 data and simulation, and then parametrise, in each sample, the components of the recoil
 2055 \vec{u}_T with respect to the transverse momentum of the Z boson (q_T^Z). Afterwards, these
 2056 parametrisations are used to scale in each event the simulated \vec{u}_T components according
 2057 to the weak boson p_T , from each electroweak simulation, to match the average recoil
 2058 distribution measured in data.

2059 The $Z \rightarrow \mu^+ \mu^-$ control sample employed to extract the recoil calibration is the same
 2060 as the one used to derive the event activity weights described in the previous section. In
 2061 addition, the simulated HF energy and the generated Z -boson p_T distributions of the
 2062 control sample have been weighed accordingly.

2063 **Extraction of the recoil scale and resolution.** Since there are no neutrinos pro-
 2064 duced in the initial hard scattering of $Z \rightarrow \mu^+ \mu^-$ events, the p_T^{miss} spectrum can be
 2065 used to directly measure the p_T^{miss} resolution. Figure 3.18 compares the p_T^{miss} spectra
 2066 extracted from data and simulation in the $Z \rightarrow \mu^+ \mu^-$ control sample. It is observed that
 2067 the simulation does not properly describe the p_T^{miss} distribution measured in data.

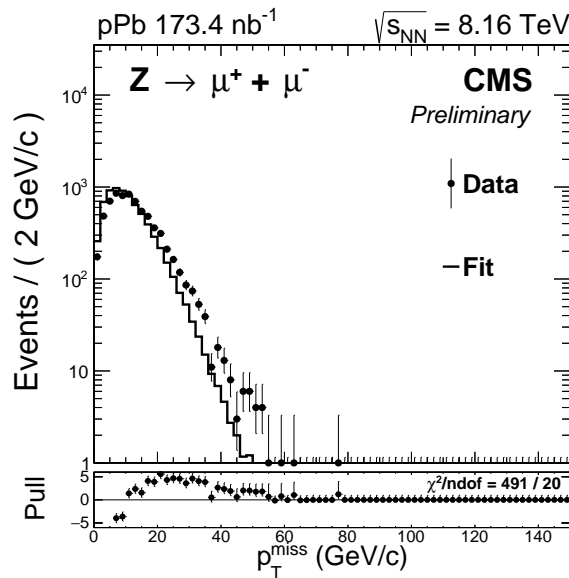


Figure 3.18: Distribution of the p_T^{miss} in data and simulation for $Z \rightarrow \mu^+ \mu^-$ selected events.

2068 In the case of $Z \rightarrow \mu^+ \mu^-$ events, the recoil \vec{u}_T is measured by *subtracting* the p_T vector
 2069 of the Z -boson candidate ($\vec{q}_T^Z = \vec{p}_T^{\mu^+} + \vec{p}_T^{\mu^-}$) from the \vec{p}_T^{miss} , according to:

$$\vec{u}_T = -\vec{p}_T^{\text{miss}} - \vec{q}_T^Z \quad (3.31)$$

2070 The recoil \vec{u}_T is then projected along the Z-boson \vec{q}_T^Z direction. The parallel and
 2071 perpendicular components of \vec{u}_T , with respect to the \vec{q}_T^Z , are labelled as u_{\parallel} and u_{\perp} ,
 2072 respectively. Figure 3.19 shows the components of the recoil in $Z \rightarrow \mu^+ \mu^-$ events.

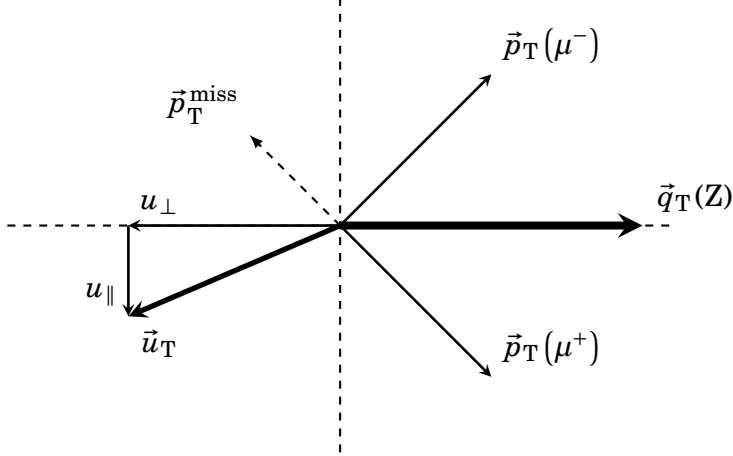


Figure 3.19: Definition and components of the recoil \vec{u}_T for $Z \rightarrow \mu^+ \mu^-$ events.

2073 The u_{\parallel} and u_{\perp} recoil components are evaluated event-by-event and sorted in 30 bins
 2074 of q_T^Z defined within the range $0 < q_T^Z < 140$ GeV/c. The distributions of u_{\parallel} and u_{\perp} from
 2075 data and simulation are fitted separately in each q_T^Z bin with a weighed sum of two
 2076 Gaussian functions, according to:

$$F(u_{\parallel}) = N_{\parallel} \cdot \left(f_{\parallel} \cdot \exp \left[\frac{(u_{\parallel} - \mu_{\parallel})^2}{2 \cdot \sigma_{\parallel,1}^2} \right] + (1 - f_{\parallel}) \cdot \exp \left[\frac{(u_{\parallel} - \mu_{\parallel})^2}{2 \cdot \sigma_{\parallel,2}^2} \right] \right) \quad (3.32)$$

$$F(u_{\perp}) = N_{\perp} \cdot \left(f_{\perp} \cdot \exp \left[\frac{(u_{\perp} - \mu_{\perp})^2}{2 \cdot \sigma_{\perp,1}^2} \right] + (1 - f_{\perp}) \cdot \exp \left[\frac{(u_{\perp} - \mu_{\perp})^2}{2 \cdot \sigma_{\perp,2}^2} \right] \right)$$

2077 where $N_{\parallel(\perp)}$ corresponds to the number of events in each q_T^Z bin, $f_{\parallel(\perp)}$ is the weight of
 2078 the Gaussian components, $\mu_{\parallel(\perp)}$ is the mean of the Gaussian functions, and $\sigma_{\parallel(\perp),1}$ and
 2079 $\sigma_{\parallel(\perp),2}$ are the corresponding Gaussian widths. The parameters f_{\parallel} and f_{\perp} are fixed to:
 2080 $f_{\parallel} = f_{\perp} = 0.70$ in data and $f_{\parallel} = f_{\perp} = 0.45$ in simulation, to obtain a better convergence of
 2081 the fits. The other parameters are left free.

2082 Examples of the distributions of the parallel and perpendicular recoil components are
 2083 shown in Figure 3.20 for data and simulation. Also, the fits performed with the weighed
 2084 combination of Gaussian functions and their pull distributions are presented.

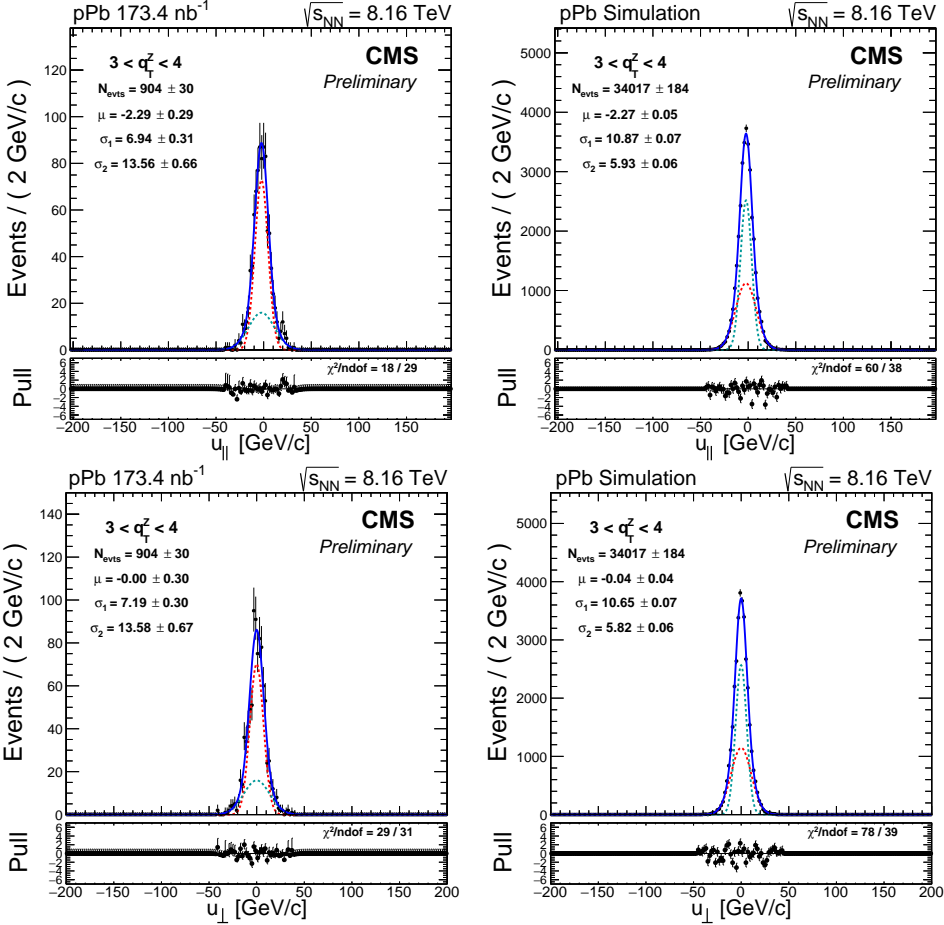


Figure 3.20: Distributions of the u_{\parallel} (top) and u_{\perp} (bottom) recoil components in data (left) and simulation (right). The fit function is based on a weighted sum of two Gaussian distributions as defined in Eq. (3.32). The plots correspond to the q_T^Z bin $[3, 4]$ GeV/c.

2085 **Parameterisation of the recoil scale.** The Gaussian mean parameter μ_{\parallel} of the
 2086 recoil parallel component is extracted in each q_T^Z bin by fitting the recoil u_{\perp} distribution
 2087 as shown in Figure 3.20. The profile of μ_{\parallel} as a function of q_T^Z is then fitted using the
 2088 following function:

$$\mu_{\parallel}(q_T^Z) = -\left(c_0 + c_1 q_T^Z\right) \left(\frac{1 + \text{Erf}\left[\alpha \cdot (q_T^Z)^{\beta}\right]}{2} \right) \quad (3.33)$$

2089 where c_0 , c_1 , α and β are free parameters, and $\text{Erf}(x)$ is the Gaussian error function.
 2090 These fits are shown in Figure 3.21, where the sign of μ_{\parallel} has been reversed to plot the
 2091 results in the positive y-axis. The slope c_1 and intercept c_0 parameters are found to be
 2092 $c_1 \approx 0.9$ and $c_0 < 1.0$ GeV/c, which means that the average u_{\parallel} is roughly 10% lower than

2093 q_T^Z and the contributions at $q_T^Z = 0$ are negligible. The distributions of the average u_{\parallel} for
 2094 data and simulation are observed to be in good agreement.

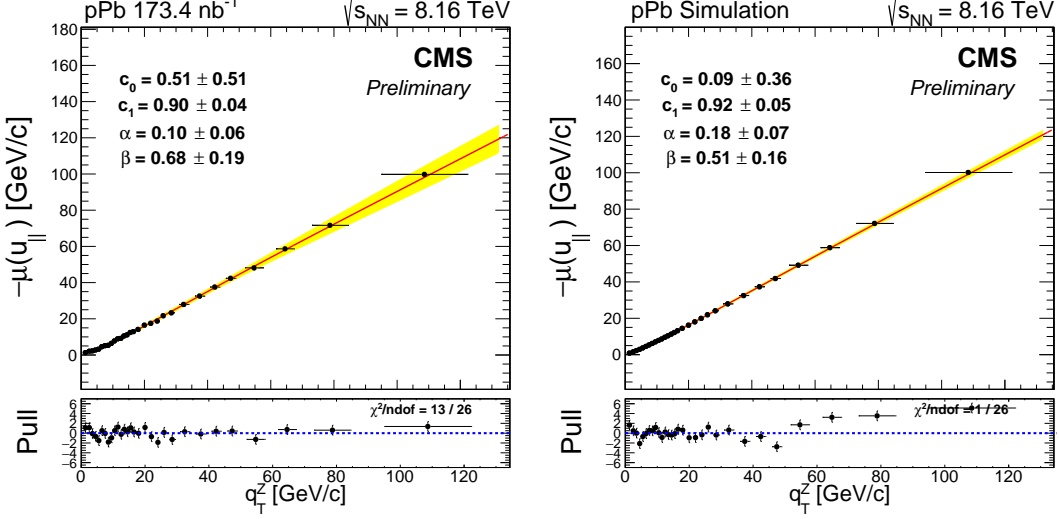


Figure 3.21: Fits of the profile of $-\mu_{\parallel}$ as a function of q_T^Z . The results are derived from $Z \rightarrow \mu^+ \mu^-$ events in data (left) and simulation (right). The yellow band represents the 68% error band of the fit.

2095 In the case of the perpendicular recoil component, the average u_{\perp} value should be
 2096 zero based on momentum conservation. To check this, the profile of the Gaussian mean
 2097 parameter μ_{\perp} as a function of q_T^Z is fitted in data and simulation with a constant function:

$$\mu_{\perp}(q_T^Z) = c_0 \quad (3.34)$$

2098 The outcome of the fits is shown in Figure 3.22. As expected, the μ_{\perp} is found to be
 2099 consistent with zero in simulation and data, showing that there is no bias that affects
 2100 the average value of the recoil component perpendicular to \vec{q}_T^Z . From now on, μ_{\perp} is fixed
 2101 to zero.

2102 **Parameterisation of the recoil resolution.** The two Gaussian width parameters
 2103 ($\sigma_{\parallel(\perp),1}$ and $\sigma_{\parallel(\perp),2}$) of the parallel (perpendicular) component of the recoil are also ex-
 2104 tracted from the recoil fits for each q_T^Z bin. The $\sigma_{\parallel(\perp),1}$ and $\sigma_{\parallel(\perp),2}$ parameters of u_{\parallel} (u_{\perp})
 2105 are parametrised as a function of q_T^Z using the following formula:

$$\sigma_{1,2}(q_T^Z) = \sqrt{s_0^2 + s_1^2 \cdot q_T^{\alpha}} \quad (3.35)$$

2106 where s_0 , s_1 and α are free parameters. The results of the fits to the σ_1 and σ_2
 2107 profiles as a function of q_T^Z are presented in Figure 3.23 for u_{\parallel} and in Figure 3.24 for u_{\perp} .

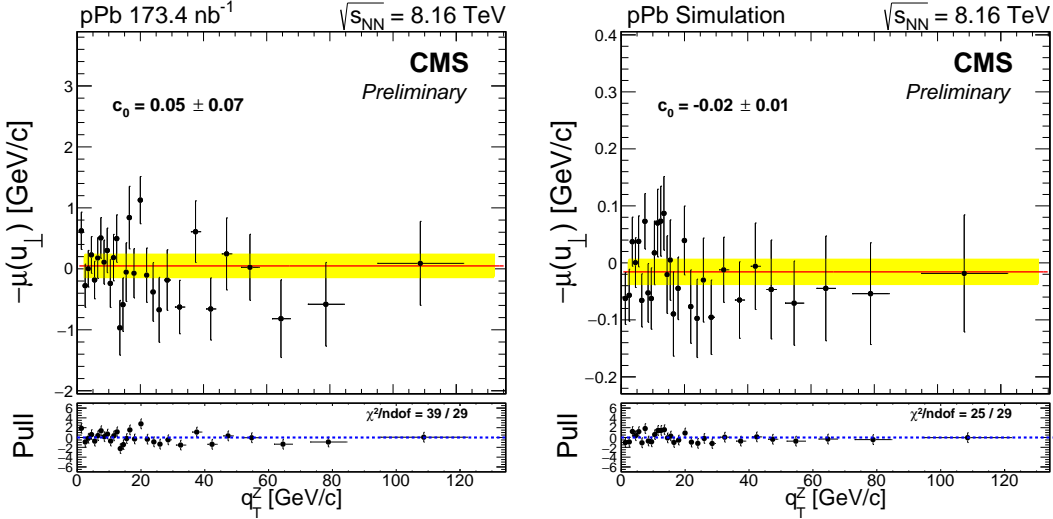


Figure 3.22: Fits of the profile of μ_{\perp} as a function of q_T^Z . The results are derived from $Z \rightarrow \mu^+ \mu^-$ events in data (left) and simulation (right). The yellow band represents the 68% error band of the fit.

2108 In addition, the profiles of the weighed average of the two Gaussian width parameters,
 2109 given by:

$$\begin{aligned}\sigma_{\perp} &= f_{\perp} \cdot \sigma_{\perp,1} + (1 - f_{\perp}) \cdot \sigma_{\perp,2} \\ \sigma_{\parallel} &= f_{\parallel} \cdot \sigma_{\parallel,1} + (1 - f_{\parallel}) \cdot \sigma_{\parallel,2}\end{aligned}\quad (3.36)$$

2110 are also fitted using Eq. (3.35) and the results are shown in Figure 3.24 and Fig-
 2111 ure 3.23.

2112 It is observed in Figure 3.23 and 3.24, that the recoil resolution increases with q_T^Z .
 2113 This is expected since high- p_T Z bosons are produced in association with several jets
 2114 from higher order processes, which contributes to the recoil resolution.

2115 Also, the parameter s_0 of the weighed average σ , which measure the recoil resolution
 2116 at $q_T^Z = 0$ GeV/c, is found to be larger in data than in simulation, which means that the
 2117 modelling of the contributions not originating from the hard scattering (e.g. underlying
 2118 events) are underestimated compared to data. In addition, the contributions to the recoil
 2119 resolution at high q_T^Z are also larger in data than in simulation.

2120 **Calibration of the simulated recoil.** The recoil corrections are applied to the fol-
 2121 lowing simulated processes: $W \rightarrow \mu\nu_{\mu}$, $Z/\gamma^* \rightarrow \mu^+ \mu^-$ and $W \rightarrow \tau\nu_{\tau}$. The simulated recoil
 2122 distribution is calibrated using the parametric equations obtained in the previous sec-

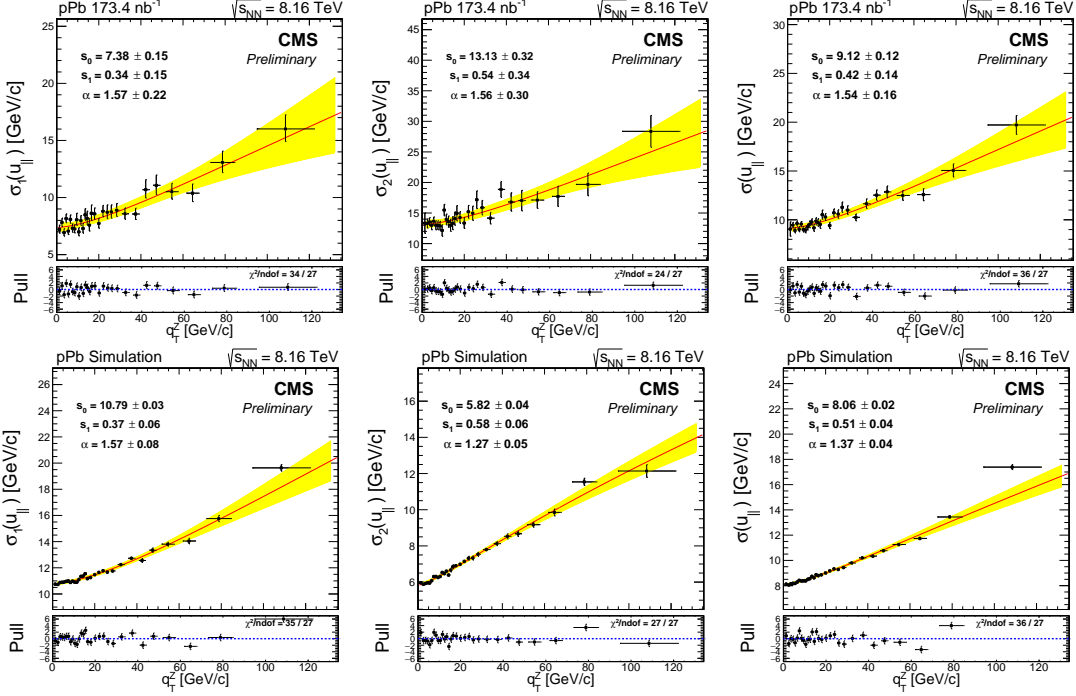


Figure 3.23: Fits to the profile of the $\sigma_{\parallel,1}$ (left), $\sigma_{\parallel,2}$ (middle) and weighed average σ_{\parallel} (right) values of the parallel recoil component as a function of q_T^Z . The results are derived from $Z \rightarrow \mu^+ \mu^-$ events in data (top) and simulation (bottom).

2123 tions for the Gaussian mean $\mu(q_T)$ and weighed-average width $\sigma(q_T)$. These parametric
2124 equations are summarised below:

- 2125 • Recoil parametric equations from data:

$$\begin{aligned} \mu_{\parallel}^{\text{data}}(q_T) &= (0.5 + 0.9 \cdot q_T) \left(\frac{1 + \text{Erf}[0.1 \cdot (q_T)^{0.7}]}{2} \right) \\ \sigma_{\parallel}^{\text{data}}(q_T) &= \sqrt{9.1^2 + 0.4^2 \cdot (q_T)^{1.5}} \\ \sigma_{\perp}^{\text{data}}(q_T) &= \sqrt{9.1^2 + 0.4^2 \cdot (q_T)^{1.3}} \end{aligned} \quad (3.37)$$

- 2126 • Recoil parametric equations from simulation:

$$\begin{aligned} \mu_{\parallel}^{\text{MC}}(q_T) &= (0.1 + 0.9 \cdot q_T) \left(\frac{1 + \text{Erf}[0.2 \cdot (q_T)^{0.5}]}{2} \right) \\ \sigma_{\parallel}^{\text{MC}}(q_T) &= \sqrt{8.1^2 + 0.5^2 \cdot (q_T)^{1.4}} \\ \sigma_{\perp}^{\text{MC}}(q_T) &= \sqrt{8.0^2 + 0.8^2 \cdot (q_T)^{0.9}} \end{aligned} \quad (3.38)$$

3.2. ANALYSIS

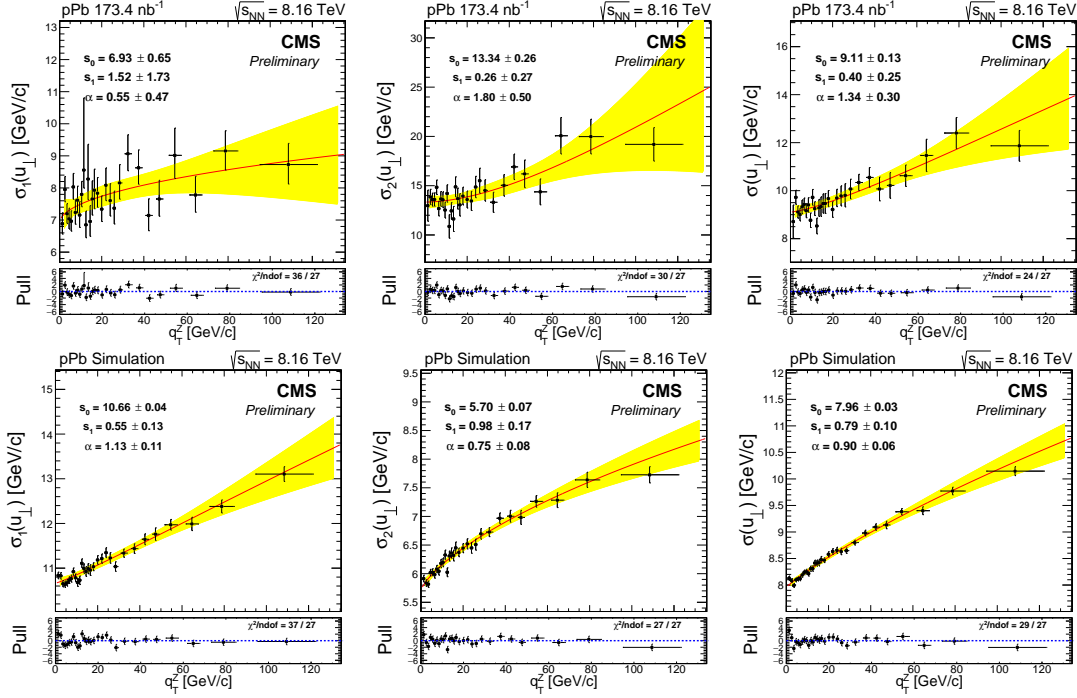


Figure 3.24: Fits for the $\sigma_{\perp,1}$ (left), $\sigma_{\perp,2}$ (middle) and weighed average σ_{\perp} (right) values of the recoil perpendicular component as a function of q_T . The results are derived from $Z \rightarrow \mu^+ \mu^-$ events in data (top) and simulation (bottom).

2127 The procedure to calibrate the simulated recoil starts by computing the p_T vector
 2128 of the boson (\vec{q}_T) and simulated recoil (\vec{u}_T^{MC}). The boson \vec{q}_T is determined using the
 2129 reconstructed muon information whenever possible, as described below:

- 2130 • $W \rightarrow \mu \nu_\mu$: \vec{q}_T is the \vec{p}_T sum of the reconstructed muon and generated neutrino.
 2131 • $W \rightarrow \tau \nu_\tau$: \vec{q}_T is the generated W boson p_T vector.
 2132 • $Z/\gamma^* \rightarrow \mu^+ \mu^-$: if one of the muons is not reconstructed, then \vec{q}_T is the \vec{p}_T sum of the
 2133 reconstructed muon and the generated-only muon, otherwise \vec{q}_T is equal to the \vec{p}_T
 2134 sum of both reconstructed muons (\vec{q}_T^{Z/γ^*}).

2135 The recoil \vec{u}_T^{MC} of the simulated event is derived by removing from the \vec{p}_T^{miss} , the
 2136 reconstructed muons from the decay of the weak boson. In other words, for $W \rightarrow \mu \nu_\mu$
 2137 events, $Z/\gamma^* \rightarrow \mu^+ \mu^-$ events with only one reconstructed muon ($Z/\gamma^* \rightarrow \mu$) and $W \rightarrow$
 2138 $\tau \nu_\tau$ events, the $\vec{u}_T^{MC} = -\vec{p}_T^{\text{miss}} - \vec{p}_T^\mu$, while for $Z/\gamma^* \rightarrow \mu^+ \mu^-$ events with both muons
 2139 reconstructed, the $\vec{u}_T^{MC} = -\vec{p}_T^{\text{miss}} - \vec{q}_T^{Z/\gamma^*}$.

Once the \vec{u}_T^{MC} and \vec{q}_T have been derived for a given event, the \vec{u}_T^{MC} is then separated in a component parallel (u_{\parallel}^{MC}) and perpendicular (u_{\perp}^{MC}) to the direction of \vec{q}_T . The simulated recoil components are then scaled event-by-event, according to:

$$\begin{aligned} u_{\parallel}^{\text{corr}} &= \left(u_{\parallel}^{MC} - \mu_{\parallel}^{MC}(q_T) \right) \cdot \left(\frac{\sigma_{\parallel}^{\text{data}}(q_T)}{\sigma_{\parallel}^{MC}(q_T)} \right) + \mu_{\parallel}^{\text{data}}(q_T) \\ u_{\perp}^{\text{corr}} &= u_{\perp}^{MC} \cdot \left(\frac{\mu_{\perp}^{\text{data}}(q_T)}{\sigma_{\perp}^{MC}(q_T)} \right) \end{aligned} \quad (3.39)$$

Afterwards, the corrected recoil \vec{u}_T^{corr} is propagated to the p_T^{miss} of the event, as follows:

- For $W \rightarrow \mu\nu_{\mu}$, $W \rightarrow \tau\nu_{\tau}$ and $Z/\gamma^* \rightarrow \mu$ events:

$$p_T^{\text{miss}} = |u_T^{\text{corr}} + \vec{p}_T^{\mu}| \quad (3.40)$$

- For fully reconstructed $Z/\gamma^* \rightarrow \mu^+ \mu^-$ events:

$$p_T^{\text{miss}} = |u_T^{\text{corr}} + \vec{q}_T^{Z/\gamma^*}| \quad (3.41)$$

As an alternative method used to determine the systematic uncertainty associated to the recoil calibration method, the simulated recoil components are smeared, instead of being scaled, by generating a random recoil component per event according to the following Gaussian distribution functions:

$$\begin{aligned} u_{\parallel}^{\text{corr}} &= \text{Gauss} \left(u_{\parallel} - \mu_{\parallel}^{MC}(q_T) + \mu_{\parallel}^{\text{data}}(q_T), \sqrt{\sigma_{\parallel}^{\text{data}}(q_T)^2 - \sigma_{\parallel}^{MC}(q_T)^2} \right) \\ u_{\perp}^{\text{corr}} &= \text{Gauss} \left(u_{\perp}, \sqrt{\sigma_{\perp}^{\text{data}}(q_T)^2 - \sigma_{\perp}^{MC}(q_T)^2} \right) \end{aligned} \quad (3.42)$$

Closure test. The recoil calibration is checked using the $Z \rightarrow \mu^+ \mu^-$ control sample. The p_T^{miss} spectrum from data and the corrected one from simulation are shown in Figure 3.25. As can be observed, the agreement between data and simulation is significantly improved after applying the recoil calibration using the scaling method.

Impact of the recoil calibration in the signal region. The p_T^{miss} distribution in the signal region is compared between data and the simulations. The fit to the data is performed following the signal extraction procedure described in Section 3.2.7. The recoil corrections are applied to the electroweak simulations using both the nominal

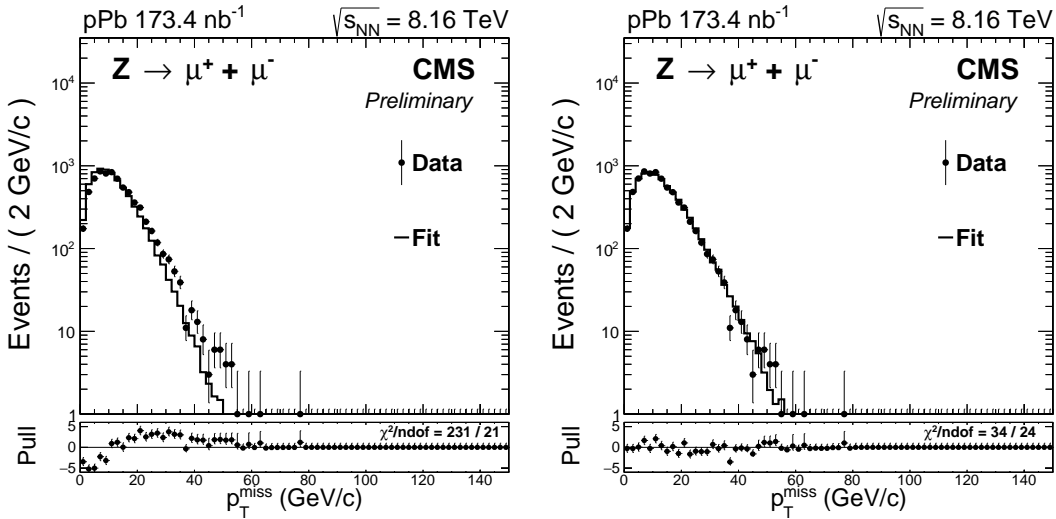


Figure 3.25: A comparison of the p_T^{miss} distribution from $Z \rightarrow \mu^+ \mu^-$ events between data and simulation, before (left) and after (right) calibrating the simulated recoil. The distributions of the simulated HF energy and generated Z-boson p_T have been weighed.

2159 scaling method and the alternative smearing method, and the results are shown in
 2160 Figure 3.26. Both the nominal and the alternative recoil calibrations improve significantly
 2161 the agreement between the p_T^{miss} distribution extracted from data and simulations.

2162 3.2.6 Signal efficiency

2163 The $W \rightarrow \mu\nu_\mu$ signal efficiency is defined as the probability for a muon with $p_T > 25$ GeV/ c
 2164 and $|\eta_{\text{lab}}^\mu| < 2.4$, to be reconstructed and pass all the analysis selection criteria. The signal
 2165 efficiency is obtained from simulation as detailed in Section 3.2.6.1 and then corrected
 2166 using data-to-MC efficiency ratios derived with the tag-and-probe method as explained
 2167 in Section 3.2.6.2.

2168 3.2.6.1 Simulated signal efficiency

2169 The signal efficiency is estimated using the $W \rightarrow \mu\nu_\mu$ simulations since they contain
 2170 the full history of the signal events, including the generation and reconstruction of the
 2171 particles. To improve the modelling of the event activity in p-Pb and the W-boson p_T
 2172 spectrum, the distribution of the generated W-boson p_T and simulated HF energy is
 2173 weighed per event as explained in Section 3.2.4 and Section 3.2.5.1, respectively.

2174 A reconstructed muon is considered an offline muon if it satisfies the signal selection
 2175 requirements. Among the selection criteria, an offline muon is required to satisfy the

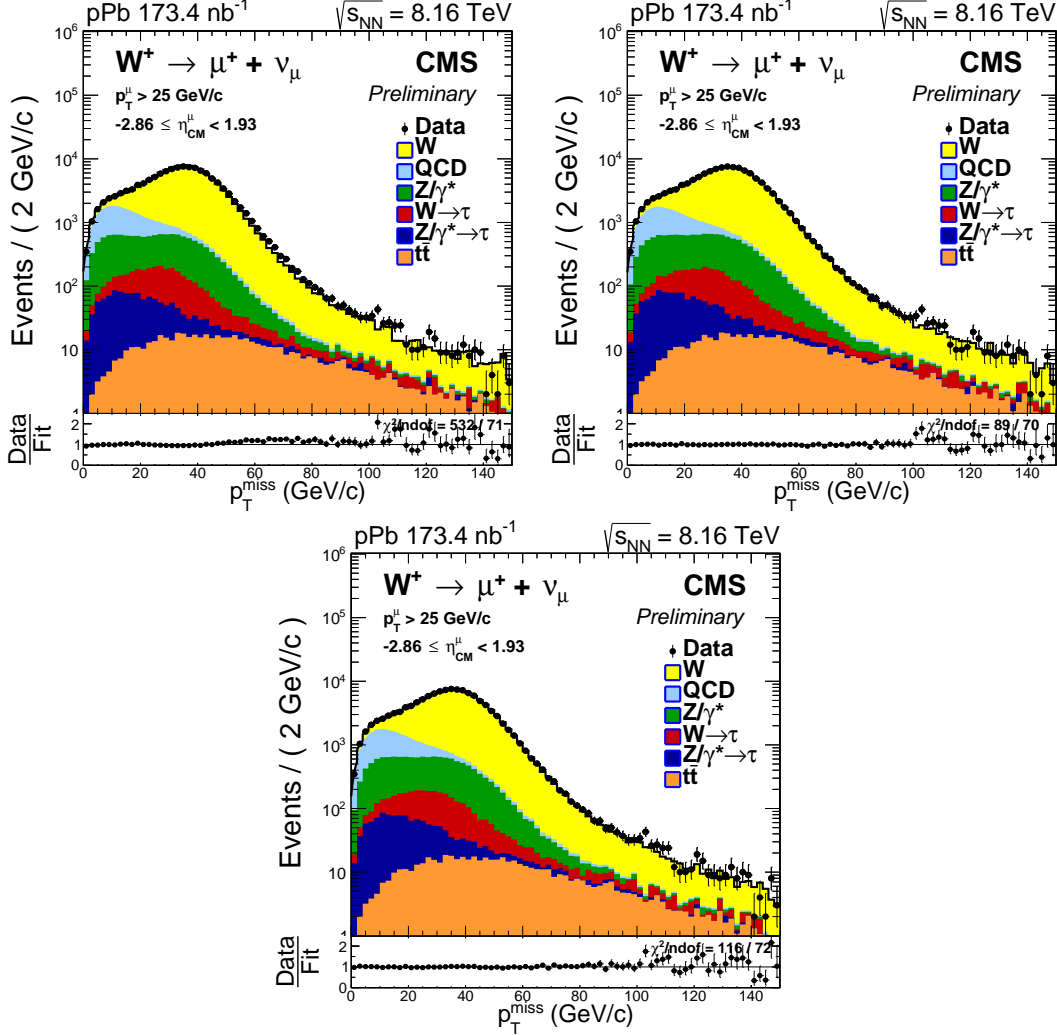


Figure 3.26: Comparison of the p_T^{miss} distribution in data and simulation for positive-charged muons in the η_{CM}^{μ} -inclusive signal region. The results are shown before (top-left) and after (top-right) applying the recoil calibrations using the nominal scaling method. The result using the alternative smearing method (bottom) is also presented. The distributions of the simulated HF energy and generated Z-boson p_T have been weighed.

isolation and identification criteria defined in Section 3.2.3.3, match the trigger, have $p_T^{\mu} > 25 \text{ GeV}/c$ and be within the CMS detector coverage $|\eta_{\text{lab}}^{\mu}| < 2.4$.

The signal efficiency of the simulated events is computed as the fraction of *generated* muons matched to an *offline* muon around a cone of $\Delta R = \sqrt{\Delta\eta^2 + \Delta\phi^2} < 0.05$. All generated muons are required to be within the analysis kinematic region ($p_T^{\mu} > 25 \text{ GeV}/c$ and $|\eta_{\text{lab}}| < 2.4$) and come from a W-boson decay. The signal efficiency of the pPb and Pbp

3.2. ANALYSIS

2182 $W \rightarrow \mu\nu_\mu$ simulations is derived as a function of the generated muon η_{lab}^μ , according to:

$$\epsilon_{\text{pPb(Pbp)}}^{\mu^\pm}(\eta_{\text{CM}}^\mu) = \left(\frac{N_{\text{off}}^{\mu^\pm}[\eta_{\text{lab}}^\mu]}{N_{\text{gen}, p_T > 25}^{\mu^\pm}[\eta_{\text{lab}}^\mu]} \right)_{\text{pPb(Pbp)}} \quad (3.43)$$

2183 where N_{off} and N_{gen} are the number of offline and generated muons, accordingly.
 2184 A comparison of the signal efficiencies from the pPb and Pbp simulations is shown in
 2185 Figure 3.27. A good agreement between the two samples is observed.

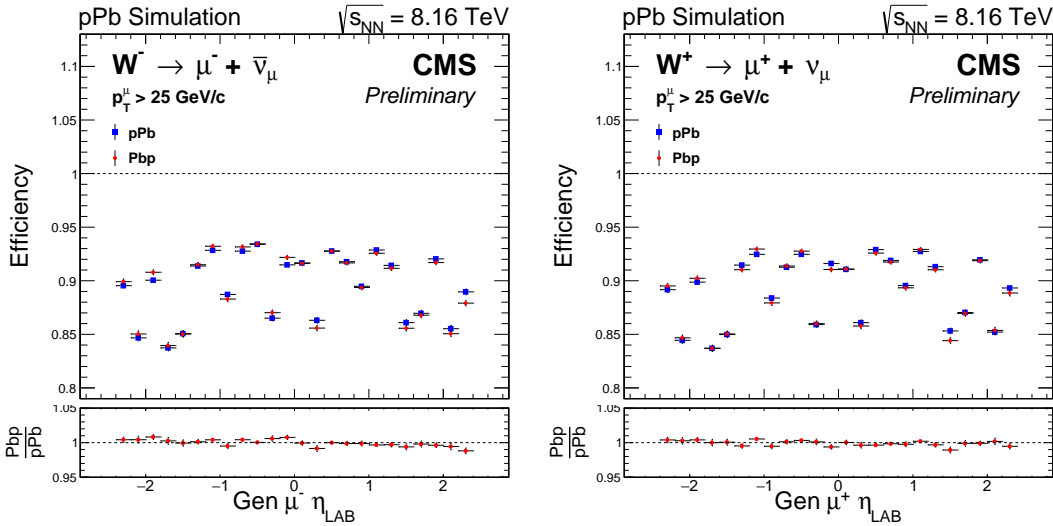


Figure 3.27: Comparison of the signal efficiency derived from the pPb and Pbp $W \rightarrow \mu\nu_\mu$ simulations as a function of the generated muon η_{lab} , separated in negative (left) and positive (right) charged muons. The distributions of the simulated HF energy and generated W-boson p_T have been weighed. The bottom panel shows the ratio of Pbp over pPb signal efficiencies.

2186 The signal efficiencies extracted from the pPb and Pbp $W \rightarrow \mu\nu_\mu$ simulations are then
 2187 combined in the centre-of-mass frame, and the final simulated signal efficiency $\epsilon_{\text{MC}}^{\mu^\pm}$ is
 2188 obtained as:

$$\epsilon_{\text{MC}}^{\mu^\pm}(\eta_{\text{CM}}^\mu) = \frac{\mathcal{L}_{\text{pPb}} \cdot \epsilon_{\text{pPb}}^{\mu^\pm}(\eta_{\text{CM}}^\mu) + \mathcal{L}_{\text{Pbp}} \cdot \epsilon_{\text{Pbp}}^{\mu^\pm}(\eta_{\text{CM}}^\mu)}{\mathcal{L}_{\text{pPb}} + \mathcal{L}_{\text{Pbp}}} \quad (3.44)$$

2189 where \mathcal{L}_{pPb} and \mathcal{L}_{Pbp} are the recorded integrated luminosity of each p-Pb run. The re-
 2190 sults of the $W \rightarrow \mu\nu_\mu$ efficiency, extracted from the simulations, are shown in Figure 3.28.

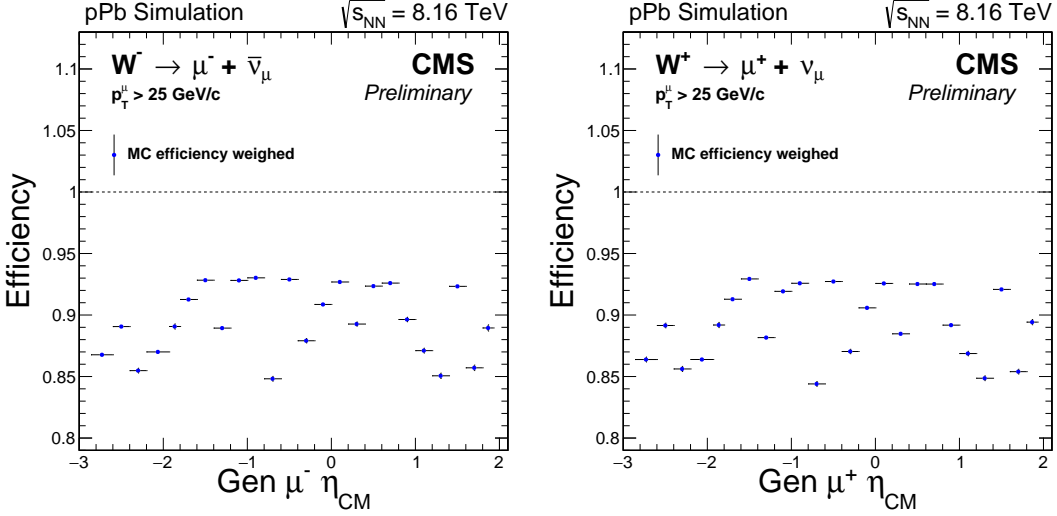


Figure 3.28: Simulated signal efficiency derived from the $W \rightarrow \mu\nu_\mu$ NLO simulations as a function of the generated muon η_{CM} , separated in negative (left) and positive (right) charged muons. The distributions of the simulated HF energy and generated W -boson p_T have been weighed.

3.2.6.2 Corrected signal efficiency

The simulation of the CMS detector is very precise but still far from fully describing all the detector conditions observed in real data. In order to compensate for the imperfections in the simulation, a set of data-to-MC corrections provided by the CMS heavy-ion (HIN) group are used to improve the estimation of the signal efficiency. These corrections are derived from the ratio of efficiencies measured in data and simulation using the tag-and-probe (TnP) method.

The tag-and-probe method is a data-driven technique widely used to compute efficiencies of physical objects, such as muons, produced from the decay of known mass resonances (e.g. Z bosons). The main advantage of the TnP method is that it can be applied to data and simulation, allowing to assess the differences between the two.

Definition of the tag-and-probe efficiencies. To study the different elements that enter in the reconstruction and selection of muons, the total muon efficiency is factorised in five different components, according to:

$$\epsilon^\mu = \epsilon_{\text{STA}} \cdot \epsilon_{\text{TRK}} \cdot \epsilon_{\text{ID}} \cdot \epsilon_{\text{Trig}} \cdot \epsilon_{\text{Iso}} \quad (3.45)$$

where each efficiency component is defined relative to the previous one, as described

2206 below:

- 2207 • ϵ_{STA} : represents the standalone-muon (STA) reconstruction efficiency. It is probed
2208 by tracker tracks and is derived by matching the probe to a standalone muon.
- 2209 • ϵ_{trk} : represents the global muon tracking efficiency. It is probed by standalone
2210 muons and is derived by matching the probe to a global muon.
- 2211 • ϵ_{ID} : represents the muon identification efficiency. It is probed by global muons and
2212 is determined by requiring that the probe satisfy the tight identification criteria
2213 defined in Section 3.2.3.3.
- 2214 • ϵ_{trig} : represents the muon trigger efficiency. It is probed by global muons passing
2215 the identification criteria, and it is determined by requiring that the probe is
2216 matched to the muon trigger.
- 2217 • ϵ_{iso} : represents the muon isolation efficiency. It is probed by global muons pass-
2218 ing the identification criteria and matched to the trigger, and it is computed by
2219 requiring that the probe pass the muon isolation requirement ($I^{\mu} < 0.15$).

2220 **Extraction of the tag-and-probe efficiencies.** For high- p_{T} muons ($p_{\text{T}} > 15 \text{ GeV}/c$),
2221 the dimuon decay of Z bosons is used to create a clean sample. In each event, a high-
2222 quality muon, called the *tag*, is combined with the *probe* of the efficiency being measured,
2223 to form a tag-probe pair within the Z-boson mass window. The tag and the probe are
2224 required to have $p_{\text{T}} > 15 \text{ GeV}/c$ and be inside the acceptance of CMS ($|\eta_{\text{lab}}| < 2.4$). In
2225 addition, the tag is also required to satisfy the muon isolation and identification criteria,
2226 and be matched to the trigger.

2227 The tag-probe pairs are separated into two samples depending on whether the
2228 probe pass the selection criteria under study. The efficiency is then determined by
2229 performing a simultaneous unbinned maximum likelihood fit to the tag-probe invariant
2230 mass distribution (m_{TP}) for failing and passing probes. The $Z \rightarrow \mu^+ \mu^-$ signal distributions
2231 are parametrised with a Voigt profile [182] and the background distributions with an
2232 exponential. The same procedure is performed for all efficiencies measured in data and
2233 simulation.

2234 As an example, the fits to the tag-probe invariant mass distribution for passing
2235 and failing probes, used to measure the STA reconstruction efficiency, are shown in
2236 Figure 3.29.

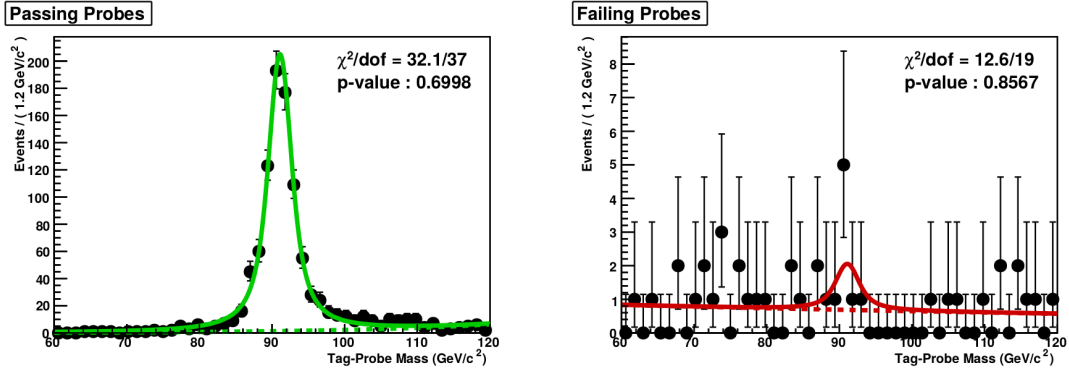


Figure 3.29: Fits to the tag-probe invariant mass distribution for passing (left) and failing (right) probes, used to measure the STA reconstruction efficiency. The results correspond to the probe kinematic region: $|\eta_{\text{lab}}| < 2.4$ and $50 < p_T < 80 \text{ GeV}/c$. Figures taken from the private Ref. [183].

Results of the tag-and-probe efficiencies. The STA reconstruction ϵ_{STA} and global muon tracking ϵ_{trk} efficiencies are found to be in very good agreement between data and simulation, and no correction is required for the simulated $W \rightarrow \mu\nu_\mu$ efficiency.

In the case of the muon identification ϵ_{ID} and isolation ϵ_{iso} efficiencies, the results obtained from simulation are observed to disagree with those from data, as shown in Figure 3.30. As a result, the efficiencies measured in data and simulation, as a function of the probed p_T , are fitted with: a linear function ($f_{\text{ID}}(p_T) = a \cdot p_T + b$) for muon identification and a displaced error function ($f_{\text{iso}}(p_T) = a \cdot \text{Erf}[(p_T - c)/b] + d$) for muon isolation. The fits to the efficiencies are performed in three regions of probe η_{lab} , corresponding to: $|\eta_{\text{lab}}^\mu| < 1.2$, $1.2 < |\eta_{\text{lab}}^\mu| < 2.1$ and $2.1 < |\eta_{\text{lab}}^\mu| < 2.4$. The ratios of the fitted functions extracted from the data and simulation efficiencies, for muon identification ($w_{\text{ID}} = f_{\text{ID}}^{\text{data}}/f_{\text{ID}}^{\text{MC}}$) and for muon isolation ($w_{\text{iso}} = f_{\text{iso}}^{\text{data}}/f_{\text{iso}}^{\text{MC}}$), are used as TnP corrections for the simulated $W \rightarrow \mu\nu_\mu$ efficiency.

The muon trigger efficiency ϵ_{trig} extracted from the simulation is seen to disagree with the results from data as a function of the probe η_{lab} , as presented in Figure 3.31. In this case, the ratio of the measured efficiency extracted from data and simulation ($w_{\text{trig}} = \epsilon_{\text{ID}}^{\text{data}}/\epsilon_{\text{ID}}^{\text{MC}}$), in each bin of probe η_{lab} , is used to correct the simulated $W \rightarrow \mu\nu_\mu$ efficiency.

Correction of the signal efficiency. The simulated signal efficiency is recomputed by weighing the offline muon yield per event using the TnP corrections provided by the CMS HIN group, for muon identification w_{ID} , trigger w_{trig} and isolation w_{iso} , according

3.2. ANALYSIS

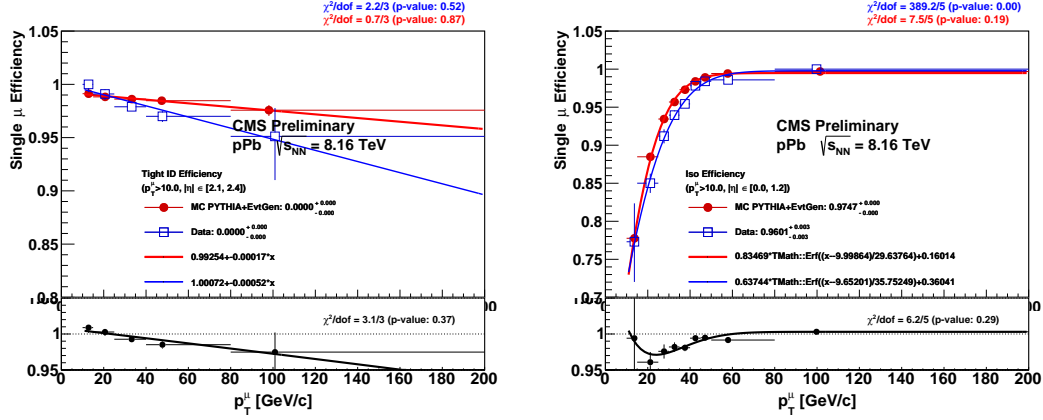


Figure 3.30: Muon identification (left) and isolation (right) efficiencies extracted from data (blue) and simulation (red) using the TnP method, as a function of the probe p_T . The bottom panels show the data-to-simulation efficiency ratio. The results of the fits to the efficiencies are also shown. Figures taken from the private Ref. [183].

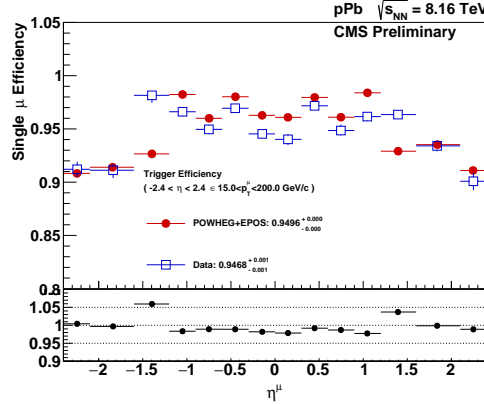


Figure 3.31: Muon trigger efficiency extracted from data (blue) and simulation (red) using the TnP method, as a function of the probe η_lab . The bottom panel shows the data-to-simulation efficiency ratio. Figure taken from the private Ref. [183].

2258 to:

$$\epsilon_{\text{corr}}^{\mu^\pm} = \frac{\left[\sum_{i=1}^{N_{\text{off}}^{\mu^\pm}} w_{\text{ID}}(p_T^\mu, |\eta_\text{lab}|) \cdot w_{\text{trig}}(\eta_\text{lab}) \cdot w_{\text{iso}}(p_T^\mu, |\eta_\text{lab}|) \right]}{N_{\text{gen}, p_T > 25}^{\mu^\pm}} \quad (3.46)$$

2259 where the TnP corrections are evaluated with the offline muon p_T and η_lab in each
2260 event, and the sum is performed over the simulated signal events.

2261 **Uncertainties of the tag-and-probe corrections.** The uncertainties associated to
2262 the TnP corrections are driven by the larger background and lower statistics present in
2263 data. As a result, only the uncertainties associated to the data efficiencies are propagated
2264 to the TnP corrections, while the simulation efficiencies are fixed. The statistical and
2265 systematic components of the TnP correction uncertainties are estimated by performing
2266 the following set of variations:

- 2267 • (A) Statistical uncertainty for muon ID and isolation: estimated by generating
2268 a hundred sets of TnP corrections using pseudo-experiments. For each pseudo-
2269 experiment, the data efficiency points are randomly varied based on a Gaussian
2270 distribution of width equal to the statistical uncertainty of the efficiency points.
2271 The varied data efficiencies are then refitted providing new TnP corrections.
- 2272 • (B) Statistical uncertainty for muon trigger: estimated with two sets of TnP correc-
2273 tions, determined by varying the data efficiency points up and down according to
2274 their statistical uncertainty.
- 2275 • (C) Systematic uncertainty of the efficiency extraction: derived by refitting the
2276 tag-probe invariant mass distributions after varying the signal and background
2277 functional forms, and by extending the range of the Z-boson mass window. These
2278 uncertainties are then propagated to the TnP corrections by varying the data
2279 efficiency points up and down by one standard deviation, producing two sets of TnP
2280 corrections.
- 2281 • (D) Systematic uncertainty of the efficiency parametrisation for muon ID and
2282 isolation: estimated by using the ratio of the efficiency points from data and
2283 simulation ($w = \epsilon^{\text{data}} / \epsilon^{\text{MC}}$), instead of the fitted efficiency curves.

2284 In addition, an uncertainty of 0.34% is included to account for the impact of the differ-
2285 ent level of event activity present in data and simulation. This is derived by comparing
2286 the simulated muon isolation efficiency before and after applying the HF energy weigh-
2287 ing. Moreover, an uncertainty of 0.6% is also added to account for possible mismodelling
2288 of the STA reconstruction efficiency, determined from the maximum difference between
2289 data and simulation.

2290 The uncertainties of the TnP corrections are propagated to the signal efficiency in
2291 two ways:

- For the hundred TnP corrections described in (A): the signal efficiency is recomputed with each of the TnP corrections and the RMS of the hundred signal efficiencies obtained is then taken as the uncertainty on the signal efficiency.
- For the up and down variations used in (B), (C) and (D): the uncertainty on the signal efficiency is determined from the maximum difference between the signal efficiency recomputed with the nominal and each of the varied TnP corrections.

The total uncertainty on the signal efficiency due to TnP corrections, is obtained by summing in quadrature the uncertainties from (A), (B), (C) and (D). The additional relative uncertainties of 0.34% and 0.6% are also included.

Results of the signal efficiency correction. The corrected signal efficiency is shown in Figure 3.32, including the uncertainties due to TnP correction.

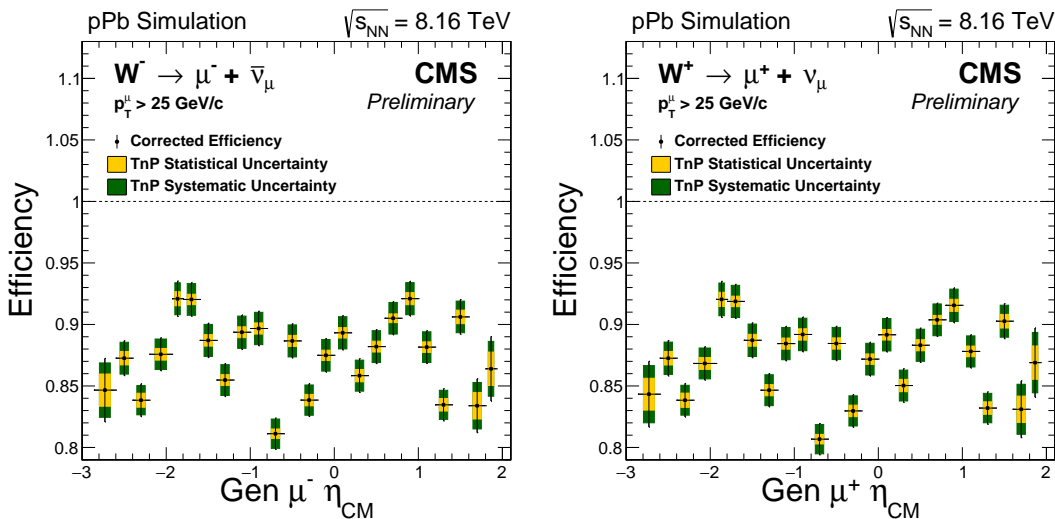


Figure 3.32: Corrected signal efficiency as a function of the generated muon η_{CM} , separated in negative (left) and positive (right) charged muons. The yellow and green boxes represents the uncertainty on the signal efficiency due to the TnP statistics and systematics, respectively.

The relative difference between the corrected and the simulated signal efficiencies ($(\epsilon_{corr} - \epsilon_{MC})/\epsilon_{MC}$), is presented in Table 3.4 as a function of the generated η_{CM} . The largest variation due to the TnP corrections is found to be 4.7%.

η_{CM}^μ Range	$\mu^- \frac{\epsilon_{corr} - \epsilon_{MC}}{\epsilon_{MC}} [\%]$	$\mu^+ \frac{\epsilon_{corr} - \epsilon_{MC}}{\epsilon_{MC}} [\%]$
-2.86 , -2.60	-2.4	-2.4
-2.60 , -2.40	-2.0	-2.1
-2.40 , -2.20	-1.9	-2.1
-2.20 , -1.93	0.7	0.5
-1.93 , -1.80	3.4	3.2
-1.80 , -1.60	0.8	0.6
-1.60 , -1.40	-4.4	-4.5
-1.40 , -1.20	-3.9	-4.0
-1.20 , -1.00	-3.7	-3.8
-1.00 , -0.80	-3.6	-3.7
-0.80 , -0.60	-4.4	-4.4
-0.60 , -0.40	-4.6	-4.6
-0.40 , -0.20	-4.6	-4.7
-0.20 , +0.00	-3.7	-3.8
+0.00 , +0.20	-3.6	-3.7
+0.20 , +0.40	-3.8	-3.9
+0.40 , +0.60	-4.5	-4.6
+0.60 , +0.80	-2.3	-2.3
+0.80 , +1.00	2.7	2.7
+1.00 , +1.20	1.2	1.1
+1.20 , +1.40	-1.9	-2.0
+1.40 , +1.60	-1.9	-2.0
+1.60 , +1.80	-2.7	-2.7
+1.80 , +1.93	-2.9	-2.8

Table 3.4: Relative difference between the corrected and simulated signal efficiencies as a function of the generated muon η_{CM} , separated in negative and positive charged muons.

3.2.7 Signal extraction

The signal and background event yields are extracted by fitting the p_T^{miss} distribution from data. The background events correspond to high- p_T muons that satisfy the signal selection criteria and are not produced from a direct decay of a W boson. A brief description of the background sources considered in this analysis is given below:

- QCD jet: constitute high- p_T muons produced from semi-leptonic decays of heavy-flavour hadrons formed within jets. Such muons are generally surrounded by a large hadronic activity and their contribution is significantly suppressed by selecting isolated muons ($I^\mu < 0.15$). However, muons from hadron decays can

sometimes pass the isolation criteria and thus, a small fraction of the QCD jet background remains in the signal region.

- $Z/\gamma^* \rightarrow \mu^+ \mu^-$: a high- p_T muon produced from a Z-boson decay or Drell–Yan. The contribution from this process is suppressed by applying the $Z/\gamma^* \rightarrow \mu^+ \mu^-$ veto, which excludes events containing at least one pair of well-identified isolated muons, each with $p_T > 15$ GeV/ c . The $Z/\gamma^* \rightarrow \mu^+ \mu^-$ events, in which one of the two muons is produced outside of the CMS coverage ($|\eta_{\text{lab}}| < 2.4$) or does not satisfy the muon selection criteria, survive the veto. Such events are expected to contribute more in the CMS endcap regions ($|\eta| > 2.0$), where one of the muons from the $Z/\gamma^* \rightarrow \mu^+ \mu^-$ decay escape the detector producing a large p_T^{miss} .
- $t\bar{t} \rightarrow \mu\nu_\mu + X$: a high- p_T muon from semi-leptonic decays of top (anti-)quarks. The inclusive cross section of top-quark pair production in pPb at $\sqrt{s_{\text{NN}}} = 8.16$ TeV, has been measured by the CMS collaboration to be $\sigma_{t\bar{t}} = 45 \pm 8$ nb $^{-1}$ [181]. The $t\bar{t}$ process is expected to have a very small impact in the signal region due its small inclusive cross section and its branching ratio (13.4%) to muons [19].
- $W \rightarrow \tau\nu_\tau \rightarrow \mu\nu_\mu + X$: consists of the leptonic decay of a W boson into a τ lepton, which then decays into a high- p_T muon.
- $Z/\gamma^* \rightarrow \tau\bar{\tau} \rightarrow \mu\nu_\mu + X$: corresponds to a ditau decay of a Z boson or virtual photon, where one of the τ leptons then decays into a high- p_T muon.

The largest source of background in the signal region correspond to QCD jets which represents approximately 18% of events in data. Among the electroweak background processes, the dominant one is the $Z/\gamma^* \rightarrow \mu^+ \mu^-$ background. The electroweak background amounts to roughly 12% of the events in the signal region, divided as: $Z/\gamma^* \rightarrow \mu^+ \mu^-$ (9%), $W \rightarrow \tau\nu_\tau$ (2%) and $Z/\gamma^* \rightarrow \tau\bar{\tau}$ (1%). The $t\bar{t}$ background contributes roughly 0.5% of events. Other electroweak processes such as double boson decays (WW, WZ and ZZ) have been checked to contribute less than 0.03%, so they are not considered.

The shape of the QCD jet background is modelled using a functional form derived from data as explained in Section 3.2.7.1 and the shapes of the signal, $t\bar{t}$ background and electroweak background are estimated using the p_T^{miss} distribution from simulations, as described in Section 3.2.7.2. Section 3.2.7.3 introduces the model used to extract the signal. The event yields obtained from the fits are presented in Section 3.2.7.4 and corrected for efficiency in Section 3.2.7.5.

3.2.7.1 Modelling of the QCD jet background

The QCD jet background cannot be simulated reliably in p-Pb collisions due to the imprecise knowledge of the production cross sections and nuclear modifications of hadrons, and the inaccurate modelling of the event activity. Thus, a data-driven approach is used to determine the QCD jet shape.

The overall procedure consist of the following steps: first parametrise the p_T^{miss} shape of the QCD jet background in a region dominated by non-isolated muons, then determine the dependence of the QCD jet functional form with respect to the muon isolation and finally extrapolate the QCD jet shape to low muon isolation values, namely in the signal region.

The shape of the QCD jet background is parametrised by a modified Rayleigh distribution, defined as:

$$f_{\text{QCD}}(p_T^{\text{miss}}) = p_T^{\text{miss}} \cdot \exp \left(-\frac{(p_T^{\text{miss}})^2}{2(\sigma_0 + \sigma_1 \cdot p_T^{\text{miss}} + \sigma_2 \cdot (p_T^{\text{miss}})^2)^2} \right) \quad (3.47)$$

where σ_0 , σ_1 , and σ_2 are free parameters extracted by performing an unbinned maximum-likelihood fit to the p_T^{miss} distribution in a control sample from data. The events in the control sample are selected by applying all signal selection requirements, except the muon isolation cut. The fits are performed separately for positive and negative charged muon events.

To derive the muon isolation dependence of the QCD jet background parameters, the p_T^{miss} spectrum in the control sample is fitted with the QCD jet functional form, in five bins of the muon isolation variable with the following boundaries: [0.4 , 0.5 , 0.6 , 0.7 , 0.8 , 0.9]. Lower muon isolation values ($I^\mu < 0.4$) are discarded, due to the large contamination from weak boson decays. The results of the QCD jet background fits, corresponding to the lowest and highest muon isolation regions, are shown in Figure 3.33.

The QCD background parameters σ_0 , σ_1 , and σ_2 , are extracted from the fits to the p_T^{miss} spectrum in each muon isolation bin, and their profile as a function of I^μ is observed to be well described by a linear function, given by:

$$\sigma_i(I^\mu) = \hat{\sigma}_i + s_i \cdot I^\mu \quad (3.48)$$

where $\hat{\sigma}_i$ and s_i are free parameters extracted separately for each QCD background parameter. The outcome of the linear fits is shown in Figure 3.34.

3.2. ANALYSIS

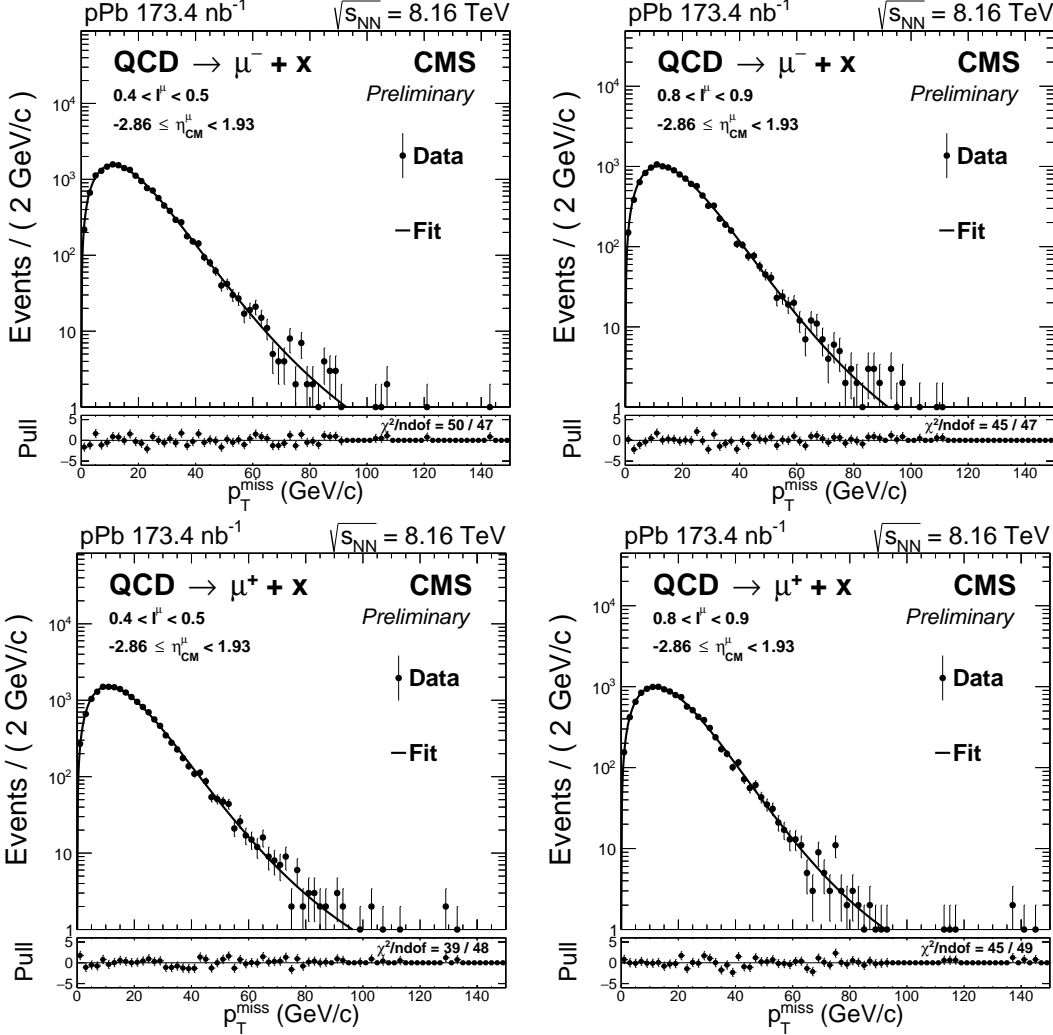


Figure 3.33: QCD jet background fits to the p_T^{miss} distribution in a control sample of non-isolated muon events corresponding to the muon isolation bins: $0.4 < I^\mu < 0.5$ (left) and $0.8 < I^\mu < 0.9$ (right). The results are shown for positive (top) and negative (bottom) charged muons separately.

2375 The σ_0 , σ_1 , and σ_2 parameters are extrapolated to the signal region (average muon
 2376 isolation of 0.03) using the parametrisation as a function of I^μ extracted from the linear
 2377 fits. The values of the QCD background parameters derived from the extrapolation are
 2378 presented in Table 3.5.

2379 The dependence of the extrapolated QCD jet shape on the muon η_{CM}^μ is checked by
 2380 splitting the control sample in different η_{CM}^μ bins, and then repeating the QCD jet shape
 2381 extraction procedure for each η_{CM}^μ bin. The results of the extrapolated values of σ_0 , σ_1 ,
 2382 and σ_2 , determined for each η_{CM}^μ bin, are compared in Figure 3.35 to the results obtained

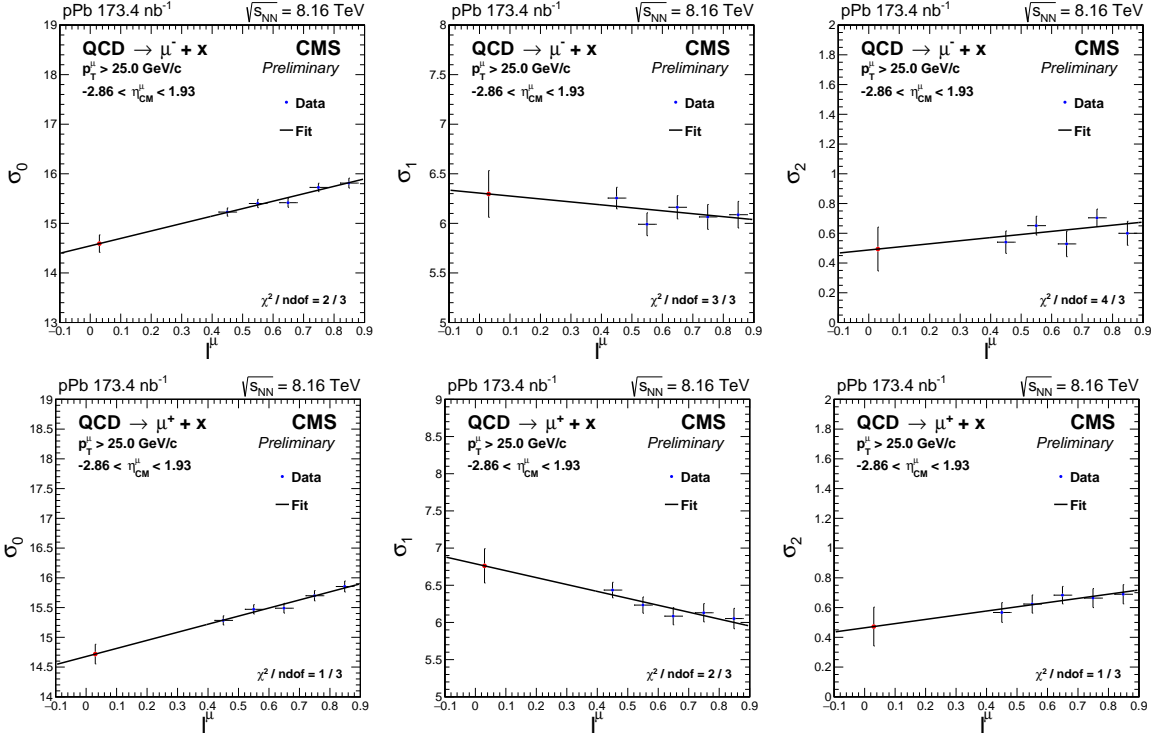


Figure 3.34: Linear fits to the profile of the QCD background parameters: σ_0 (left), σ_1 (middle) and σ_2 (right), with respect to the muon isolation variable I^μ . The results are shown for negative (top) and positive (bottom) charged muons in the η_{CM}^μ -inclusive range. The red points represent the value obtained by linearly extrapolating to $I^\mu = 0.03$.

Parameter	QCD jet $\rightarrow \mu^-$	QCD jet $\rightarrow \mu^+$
σ_0	14.6 ± 0.2	14.7 ± 0.2
σ_1	6.3 ± 0.2	6.8 ± 0.2
σ_2	0.5 ± 0.2	0.5 ± 0.1

Table 3.5: QCD background parameters extrapolated to $I^\mu = 0.03$. The results are presented for positive and negative charged muons in the η_{CM}^μ -inclusive range.

2383 in the η_{CM}^μ -inclusive range.

2384 It is observed that the σ_0 , σ_1 , and σ_2 parameters, extrapolated to low muon isolation,
 2385 do not vary significantly with respect to η_{CM}^μ and are found to be consistent with the
 2386 corresponding values obtained in the η_{CM}^μ -inclusive range. As a result, the extrapolated
 2387 parameters derived in the η_{CM}^μ -inclusive range for μ^+ and μ^- , are used to fix the QCD jet
 2388 background shape when fitting the signal.

3.2. ANALYSIS

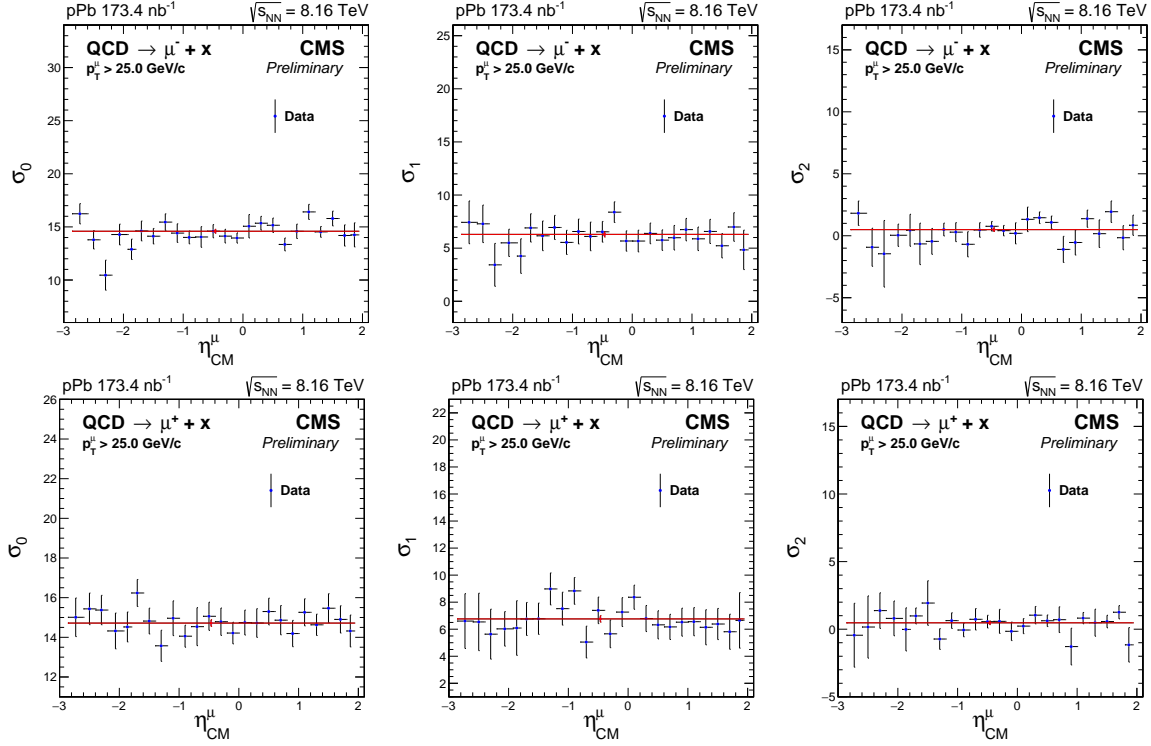


Figure 3.35: Muon η_{CM}^{μ} dependence of σ_0 (left), σ_1 (middle) and σ_2 (right) parameters extrapolated to $I^{\mu} = 0.03$. The results are shown for negative (top) and positive (bottom) charged muons. The red line corresponds to the QCD jet parameter extrapolated in the η_{CM}^{μ} -inclusive range.

2389 3.2.7.2 Modelling of the signal, $t\bar{t}$ and electroweak backgrounds

2390 The $p_{\text{T}}^{\text{miss}}$ distribution of the signal, as well as, the $t\bar{t}$ and electroweak background events,
 2391 are estimated using the corresponding POWHEG simulations mentioned in Section 3.2.2.
 2392 The simulated events for each process are required to satisfy the signal selection criteria
 2393 summarised in Section 3.2.3.5.

2394 In order to improve the description of the data, several corrections are applied to
 2395 the simulations. First, the simulated HF energy distribution is weighed as explained in
 2396 Section 3.2.5.1. Then, the generated weak boson p_{T} distribution from the $W \rightarrow \mu\nu_{\mu}$, $W \rightarrow$
 2397 $\tau\nu_{\tau}$, $Z/\gamma^* \rightarrow \mu^+\mu^-$ and $Z/\gamma^* \rightarrow \tau\bar{\tau}$ simulations, is weighed as described in Section 3.2.4
 2398 And finally, the recoil of $W \rightarrow \mu\nu_{\mu}$, $W \rightarrow \tau\nu_{\tau}$ and $Z/\gamma^* \rightarrow \mu^+\mu^-$ events is calibrated as
 2399 detailed in Section 3.2.5.2, improving the agreement of the $p_{\text{T}}^{\text{miss}}$ distribution between
 2400 data and simulation.

2401 Once the simulations have been corrected, the $p_{\text{T}}^{\text{miss}}$ shape of the signal, $t\bar{t}$ background
 2402 and electroweak background, is determined by building a template histogram of the

2403 simulated p_T^{miss} distribution (2 GeV/c bin width). These template histograms are then
 2404 used in the fitting procedure described in the next section.

2405 3.2.7.3 Fit model

2406 The number of $W \rightarrow \mu\nu_\mu$ signal events is obtained by performing an unbinned maximum-
 2407 likelihood fit of the observed p_T^{miss} distribution in different muon η_{CM}^μ regions. The fits
 2408 are done using a combination of template histograms and a functional form. The data
 2409 analysis framework RooFit v3.60 [184] is used to make the fits.

2410 The total fit model includes six contributions: the signal $W \rightarrow \mu\nu_\mu$ template (\mathcal{T}_W), the
 2411 electroweak background templates $Z/\gamma^* \rightarrow \mu^+\mu^-$ ($\mathcal{T}_{Z\mu}$), $W \rightarrow \tau\nu_\tau$ ($\mathcal{T}_{W\tau}$) and $Z/\gamma^* \rightarrow \tau\bar{\tau}$
 2412 ($\mathcal{T}_{Z\tau}$), the $t\bar{t}$ background template ($\mathcal{T}_{t\bar{t}}$), and the QCD jet background functional form
 2413 (\mathcal{F}_{QCD}). The model used to fit the data is:

$$N_W \cdot (\mathcal{T}_W + r_{Z\mu} \cdot \mathcal{T}_{Z\mu} + r_{W\tau} \cdot \mathcal{T}_{W\tau} + r_{Z\tau} \cdot \mathcal{T}_{Z\tau} + r_{t\bar{t}} \cdot \mathcal{T}_{t\bar{t}}) + N_{\text{QCD}} \cdot \mathcal{F}_{\text{QCD}} \quad (3.49)$$

2414 where N_W and N_{QCD} are the normalisation factors of the $W \rightarrow \mu\nu_\mu$ signal and QCD
 2415 jet background, $r_{t\bar{t}}$ represents the ratio of $t\bar{t}$ background events over the number of signal
 2416 events ($N_{t\bar{t}}/N_W$), and $r_{Z\mu}$, $r_{Z\tau}$ and $r_{W\tau}$ are the corresponding ratios for the $Z/\gamma^* \rightarrow \mu^+\mu^-$,
 2417 $Z/\gamma^* \rightarrow \tau\bar{\tau}$ and $W \rightarrow \tau\nu_\tau$ background processes, respectively.

2418 The shapes of the signal, $t\bar{t}$ background and electroweak background processes are
 2419 defined based on template histograms extracted from simulations. Being very small and
 2420 with a moderately discriminating shape, the electroweak and $t\bar{t}$ background components
 2421 cannot be directly and independently fitted on data. Instead, we take advantage that
 2422 their nuclear modification should be small and close to the one of the W -boson signal.
 2423 Thus, the ratios of $Z/\gamma^* \rightarrow \mu^+\mu^-$, $Z/\gamma^* \rightarrow \tau\bar{\tau}$, $W \rightarrow \tau\nu_\tau$ and $t\bar{t}$ events over the number of
 2424 $W \rightarrow \mu\nu_\mu$ events, are fixed to the results from simulations after having normalised all the
 2425 MC samples to the recorded integrated luminosity of data as detailed in Section 3.2.2
 2426 and applied all analysis corrections and selection criteria.

2427 The QCD jet background contribution is taken into account by means of a functional
 2428 form depending on three parameters. For the fits to the p_T^{miss} distribution in the signal
 2429 region, the σ_0 , σ_1 and σ_2 parameters are fixed to the extrapolated values mentioned in
 2430 Table 3.5, and the normalisation is left free.

2431 The p_T^{miss} distribution is fitted separately for $W^+ \rightarrow \mu^+\nu_\mu$ and $W^- \rightarrow \mu^-\bar{\nu}_\mu$ events.
 2432 Only the signal (N_W) and the QCD jet background (N_{QCD}) normalisation factors are left
 2433 free when fitting the signal region in data. The fits are done in the η_{CM}^μ -inclusive range
 2434 and in bins of muon η_{CM}^μ . The results of the fits performed in the η_{CM}^μ -inclusive range

2435 are shown in Figure 3.36 and those performed in the other muon η_{CM}^{μ} bins are presented
 2436 in Appendix A.

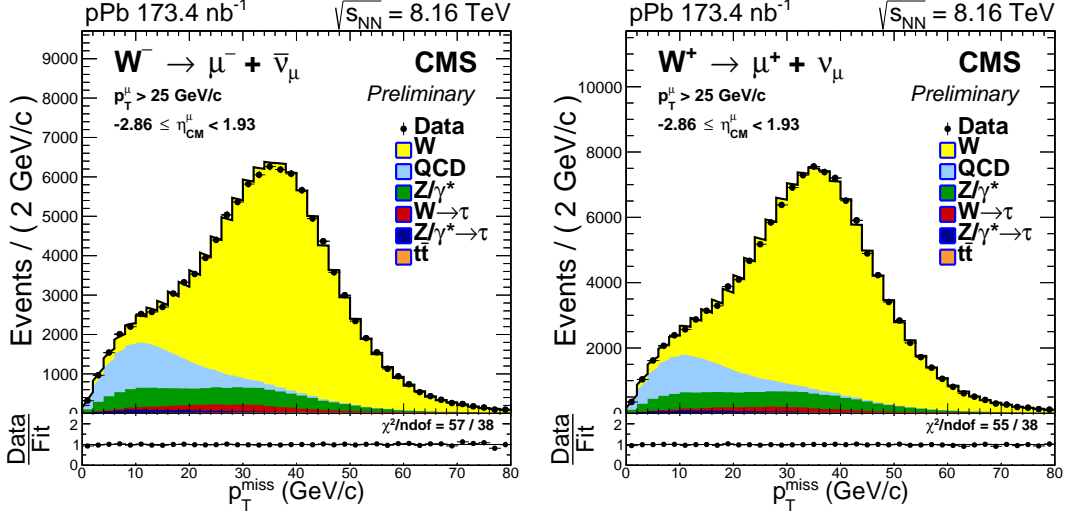


Figure 3.36: The p_T^{miss} distribution for $W^- \rightarrow \mu^- \bar{\nu}_\mu$ (left) and $W^+ \rightarrow \mu^+ \nu_\mu$ (right) events within the η_{CM}^{μ} -inclusive range, shown in linear scale. Unbinned fits to the data (black points) are performed with six contributions, stacked from top to bottom: $W \rightarrow \mu \nu_\mu$ (yellow), QCD jet (light blue), $Z/\gamma^* \rightarrow \mu^+ \mu^-$ (green), $W \rightarrow \tau \nu_\tau$ (red), $Z/\gamma^* \rightarrow \tau \bar{\tau}$ (dark blue) and $t\bar{t}$ (orange). The lower panel, on each figure, display the ratio of the measurements over the result of the fit. The χ^2 test value over the number of degrees of freedom is also shown.

2437 3.2.7.4 Extracted event yields

2438 The results of the fits to the data in each of the different muon η_{CM} bins are summarized
 2439 in Table 3.6 and Table 3.7 for $W^- \rightarrow \mu^- \bar{\nu}_\mu$ and $W^+ \rightarrow \mu^+ \nu_\mu$ events, respectively.

2440 3.2.7.5 Corrected event yields

2441 The signal event yields extracted from the fits are corrected by taking into account the
 2442 efficiency of the detector, according to:

$$N_{\mu}^{\pm}(\eta_{\text{CM}}^{\mu}) = \frac{N_{\mu,\text{raw}}^{\pm}(\eta_{\text{CM}}^{\mu})}{\epsilon_{\text{corr}}^{\pm}(\eta_{\text{CM}}^{\mu})} \quad (3.50)$$

2443 where $N_{\mu,\text{raw}}$ is the number of signal events extracted from the fits, N_{μ} is the number
 2444 of signal events after correcting for efficiency and $\epsilon_{\text{corr}}^{\pm}$ is the signal efficiency corrected

η_{CM}^{μ} Range	Total	Signal	$Z/\gamma^* \rightarrow \mu^+ \mu^-$	$W \rightarrow \tau \nu_{\tau}$	$Z/\gamma^* \rightarrow \tau \bar{\tau}$	$t\bar{t}$	QCD
-2.86 , -2.60	5210	4041 ± 65	560 ± 9	135 ± 2	45 ± 1	3.1 ± 0.1	427 ± 40
-2.60 , -2.40	4308	3395 ± 60	461 ± 8	102 ± 2	36 ± 1	4.0 ± 0.1	310 ± 37
-2.40 , -2.20	4273	3276 ± 59	449 ± 8	100 ± 2	36 ± 1	5.9 ± 0.1	407 ± 38
-2.20 , -1.93	6423	4920 ± 74	654 ± 10	156 ± 2	62 ± 1	12.9 ± 0.2	617 ± 48
-1.93 , -1.80	3140	2419 ± 52	303 ± 6	79 ± 2	28 ± 1	8.4 ± 0.2	302 ± 34
-1.80 , -1.60	4822	3672 ± 64	435 ± 8	117 ± 2	45 ± 1	15.2 ± 0.3	537 ± 43
-1.60 , -1.40	4727	3631 ± 64	390 ± 7	117 ± 2	39 ± 1	18.8 ± 0.3	533 ± 43
-1.40 , -1.20	4521	3590 ± 64	340 ± 6	109 ± 2	45 ± 1	21.6 ± 0.4	416 ± 40
-1.20 , -1.00	4626	3666 ± 65	306 ± 5	118 ± 2	48 ± 1	25.2 ± 0.4	463 ± 42
-1.00 , -0.80	4722	3762 ± 66	277 ± 5	119 ± 2	45 ± 1	32 ± 1	488 ± 43
-0.80 , -0.60	4198	3425 ± 63	238 ± 4	102 ± 2	46 ± 1	32 ± 1	355 ± 39
-0.60 , -0.40	4648	3738 ± 66	245 ± 4	119 ± 2	54 ± 1	35 ± 1	456 ± 43
-0.40 , -0.20	4344	3478 ± 64	226 ± 4	111 ± 2	50 ± 1	36 ± 1	443 ± 41
-0.20 , +0.00	4474	3510 ± 65	260 ± 5	113 ± 2	43 ± 1	39 ± 1	509 ± 43
+0.00 , +0.20	4643	3654 ± 65	309 ± 6	114 ± 2	47 ± 1	42 ± 1	477 ± 43
+0.20 , +0.40	4638	3533 ± 64	335 ± 6	111 ± 2	50 ± 1	42 ± 1	567 ± 44
+0.40 , +0.60	4718	3528 ± 63	390 ± 7	114 ± 2	46 ± 1	39 ± 1	601 ± 44
+0.60 , +0.80	4552	3375 ± 62	446 ± 8	103 ± 2	48 ± 1	37 ± 1	544 ± 43
+0.80 , +1.00	4637	3325 ± 61	489 ± 9	103 ± 2	43 ± 1	37 ± 1	640 ± 44
+1.00 , +1.20	4612	3265 ± 60	539 ± 10	105 ± 2	45 ± 1	29 ± 1	630 ± 44
+1.20 , +1.40	4053	2769 ± 55	517 ± 10	78 ± 2	38 ± 1	23.8 ± 0.5	627 ± 42
+1.40 , +1.60	4251	2917 ± 56	620 ± 12	96 ± 2	39 ± 1	21.5 ± 0.4	557 ± 42
+1.60 , +1.80	3844	2506 ± 51	611 ± 12	78 ± 2	35 ± 1	15.4 ± 0.3	599 ± 41
+1.80 , +1.93	2640	1719 ± 42	439 ± 11	54 ± 1	22 ± 1	9.6 ± 0.2	397 ± 33

Table 3.6: Event yields of $W^- \rightarrow \mu^- \bar{\nu}_{\mu}$ and background processes, extracted from the fits to the p_T^{miss} distribution in each muon η_{CM}^{μ} region. All analysis selection criteria are applied including the muon $p_T > 25$ GeV/c. All uncertainties shown are statistical only.

2445 with the TnP corrections. The statistical uncertainty of the corrected signal yields are
 2446 computed based on error propagation with:

$$\delta N_{\mu}^{\pm} = \frac{\delta N_{\mu, \text{raw}}^{\pm}(\eta_{\text{CM}}^{\mu})}{\epsilon_{\text{corr}}^{\pm}(\eta_{\text{CM}}^{\mu})} \quad (3.51)$$

2447 where $\delta N_{\mu, \text{raw}}^{\pm}$ is the uncertainty of the signal event yield determined from the fits
 2448 to the data. The results of the corrected signal event yields for each muon η_{CM}^{μ} range
 2449 are summarized in Table 3.8 and Table 3.9 for $W^- \rightarrow \mu^- \bar{\nu}_{\mu}$ and $W^+ \rightarrow \mu^+ \nu_{\mu}$ events,
 2450 accordingly.

η_{CM}^μ	Range	Total	Signal	$Z/\gamma^* \rightarrow \mu^+ \mu^-$	$W \rightarrow \tau \nu_\tau$	$Z/\gamma^* \rightarrow \tau \bar{\tau}$	$t\bar{t}$	QCD
-2.86 , -2.60		4465	3358 ± 59	583 ± 10	67 ± 1	44 ± 1	3.3 ± 0.1	409 ± 38
-2.60 , -2.40		4234	3247 ± 58	526 ± 9	65 ± 1	35 ± 1	4.2 ± 0.1	358 ± 36
-2.40 , -2.20		4377	3351 ± 60	500 ± 9	61 ± 1	36 ± 1	6.5 ± 0.1	423 ± 38
-2.20 , -1.93		6847	5257 ± 76	714 ± 10	101 ± 1	53 ± 1	14.3 ± 0.2	706 ± 49
-1.93 , -1.80		3592	2762 ± 55	385 ± 7	56 ± 1	29 ± 1	8.5 ± 0.2	400 ± 36
-1.80 , -1.60		5421	4299 ± 69	488 ± 8	94 ± 2	50 ± 1	16.0 ± 0.3	471 ± 43
-1.60 , -1.40		5343	4375 ± 70	446 ± 7	96 ± 2	45 ± 1	18.0 ± 0.3	364 ± 42
-1.40 , -1.20		5129	4182 ± 69	375 ± 6	98 ± 2	41 ± 1	23.4 ± 0.4	405 ± 43
-1.20 , -1.00		5382	4465 ± 72	339 ± 5	100 ± 2	53 ± 1	28.3 ± 0.5	395 ± 43
-1.00 , -0.80		5467	4485 ± 73	306 ± 5	100 ± 2	50 ± 1	32 ± 1	491 ± 45
-0.80 , -0.60		4738	3960 ± 68	244 ± 4	89 ± 2	42 ± 1	29 ± 1	373 ± 41
-0.60 , -0.40		5349	4435 ± 73	255 ± 4	99 ± 2	49 ± 1	38 ± 1	473 ± 45
-0.40 , -0.20		5027	4146 ± 70	238 ± 4	88 ± 1	46 ± 1	37 ± 1	468 ± 43
-0.20 , +0.00		5161	4269 ± 71	268 ± 4	99 ± 2	45 ± 1	39 ± 1	439 ± 43
+0.00 , +0.20		5473	4352 ± 72	308 ± 5	100 ± 2	52 ± 1	39 ± 1	621 ± 47
+0.20 , +0.40		5175	4179 ± 70	337 ± 6	99 ± 2	48 ± 1	37 ± 1	475 ± 44
+0.40 , +0.60		5482	4334 ± 71	399 ± 7	93 ± 2	43 ± 1	36 ± 1	576 ± 46
+0.60 , +0.80		5722	4469 ± 72	469 ± 8	99 ± 2	51 ± 1	38 ± 1	595 ± 47
+0.80 , +1.00		6061	4652 ± 72	561 ± 9	99 ± 2	48 ± 1	37 ± 1	664 ± 48
+1.00 , +1.20		5814	4404 ± 70	595 ± 9	102 ± 2	41 ± 1	33 ± 1	639 ± 47
+1.20 , +1.40		5365	4050 ± 67	570 ± 9	87 ± 1	35 ± 1	23.9 ± 0.4	596 ± 45
+1.40 , +1.60		5768	4308 ± 68	674 ± 11	92 ± 1	39 ± 1	21.5 ± 0.3	633 ± 46
+1.60 , +1.80		5320	3969 ± 65	662 ± 11	81 ± 1	34 ± 1	16.1 ± 0.3	557 ± 44
+1.80 , +1.93		3600	2654 ± 53	450 ± 9	63 ± 1	19.8 ± 0.4	9.3 ± 0.2	404 ± 36

Table 3.7: Event yields of $W^+ \rightarrow \mu^+ \nu_\mu$ and background processes, extracted from the fits to the p_T^{miss} distribution in each muon η_{CM}^μ region. All analysis selection criteria are applied including the muon $p_T > 25$ GeV/c. All uncertainties shown are statistical only.

3.2.8 Observables

The main motivation behind measuring the W-boson production in p-Pb collisions is to probe the nuclear modifications of the PDFs. To accomplish this, the efficiency-corrected $W \rightarrow \mu \nu_\mu$ event yields are combined to measure three kinds of observables: cross sections, muon charge asymmetry and forward-backward ratios.

W $\rightarrow \mu \nu_\mu$ cross sections. The $W^\pm \rightarrow \mu^\pm \nu_\mu$ differential cross sections are computed as a function of η_{CM}^μ , according to:

$$\frac{d\sigma(W^\pm \rightarrow \mu^\pm \nu_\mu)}{d\eta_{\text{CM}}^\mu}(\eta_{\text{CM}}^\mu) = \frac{N_\mu^\pm(\eta_{\text{CM}}^\mu)}{\mathcal{L} \cdot \Delta\eta_{\text{CM}}^\mu} \quad (3.52)$$

η_{CM}^μ Range	Extracted yield	Efficiency (%)	Corrected yield
-2.86 , -2.60	4041 ± 65	84.7 ± 0.2	4773 ± 77
-2.60 , -2.40	3395 ± 60	87.3 ± 0.2	3891 ± 69
-2.40 , -2.20	3276 ± 59	83.8 ± 0.2	3907 ± 71
-2.20 , -1.93	4920 ± 74	87.6 ± 0.2	5619 ± 84
-1.93 , -1.80	2419 ± 52	92.1 ± 0.2	2627 ± 56
-1.80 , -1.60	3672 ± 64	92.0 ± 0.1	3990 ± 70
-1.60 , -1.40	3631 ± 64	88.7 ± 0.2	4093 ± 72
-1.40 , -1.20	3590 ± 64	85.5 ± 0.2	4200 ± 75
-1.20 , -1.00	3666 ± 65	89.4 ± 0.2	4102 ± 73
-1.00 , -0.80	3762 ± 66	89.7 ± 0.2	4195 ± 74
-0.80 , -0.60	3425 ± 63	81.1 ± 0.2	4222 ± 78
-0.60 , -0.40	3738 ± 66	88.7 ± 0.2	4216 ± 75
-0.40 , -0.20	3478 ± 64	83.8 ± 0.2	4148 ± 76
-0.20 , +0.00	3510 ± 65	87.5 ± 0.2	4012 ± 74
+0.00 , +0.20	3654 ± 65	89.3 ± 0.2	4091 ± 73
+0.20 , +0.40	3533 ± 64	85.8 ± 0.2	4116 ± 74
+0.40 , +0.60	3528 ± 63	88.2 ± 0.2	4000 ± 72
+0.60 , +0.80	3375 ± 62	90.5 ± 0.2	3729 ± 68
+0.80 , +1.00	3325 ± 61	92.1 ± 0.2	3610 ± 66
+1.00 , +1.20	3265 ± 60	88.2 ± 0.2	3704 ± 68
+1.20 , +1.40	2769 ± 55	83.5 ± 0.2	3318 ± 65
+1.40 , +1.60	2917 ± 56	90.6 ± 0.2	3219 ± 61
+1.60 , +1.80	2506 ± 51	83.4 ± 0.2	3005 ± 61
+1.80 , +1.93	1719 ± 42	86.4 ± 0.3	1990 ± 48

Table 3.8: Corrected event yields of $W^- \rightarrow \mu^- \bar{\nu}_\mu$, given for each muon η_{CM}^μ bin. All analysis selection criteria are applied including the muon $p_T > 25$ GeV/c. The muon efficiency has been corrected by applying the tag-and-probe corrections, HF energy weights and vector boson p_T weights, event by event. All uncertainties shown are statistical only.

where $\mathcal{L} = 173.4 \pm 6.1$ nb $^{-1}$ is the recorded integrated luminosity, $\Delta\eta_{\text{CM}}^\mu$ is the width of the η_{CM}^μ range in which the measurement is performed and $N_\mu(\eta_{\text{CM}}^\mu)$ is the number of signal events after correcting for efficiency.

Muon charge asymmetry. The muon charge asymmetry measures the difference between the event yields of the $W^- \rightarrow \mu^- \bar{\nu}_\mu$ and $W^+ \rightarrow \mu^+ \nu_\mu$ processes, which is sensitive to the number of protons and neutrons in the nucleus (isospin effect), and to the flavour dependence of the nuclear modifications of the PDFs. It is defined in the following way:

η_{CM}^μ Range	Extracted yield	Efficiency (%)	Corrected yield
-2.86 , -2.60	3358 ± 59	84.3 ± 0.2	3982 ± 70
-2.60 , -2.40	3247 ± 58	87.3 ± 0.2	3721 ± 66
-2.40 , -2.20	3351 ± 60	83.8 ± 0.2	3997 ± 71
-2.20 , -1.93	5257 ± 76	86.8 ± 0.2	6055 ± 87
-1.93 , -1.80	2762 ± 55	92.0 ± 0.2	3001 ± 60
-1.80 , -1.60	4299 ± 69	91.9 ± 0.1	4679 ± 75
-1.60 , -1.40	4375 ± 70	88.7 ± 0.2	4931 ± 79
-1.40 , -1.20	4182 ± 69	84.7 ± 0.2	4940 ± 82
-1.20 , -1.00	4465 ± 72	88.4 ± 0.2	5049 ± 81
-1.00 , -0.80	4485 ± 73	89.2 ± 0.2	5029 ± 82
-0.80 , -0.60	3960 ± 68	80.7 ± 0.2	4908 ± 85
-0.60 , -0.40	4435 ± 73	88.5 ± 0.2	5015 ± 83
-0.40 , -0.20	4146 ± 70	83.0 ± 0.2	4996 ± 85
-0.20 , +0.00	4269 ± 71	87.2 ± 0.2	4897 ± 81
+0.00 , +0.20	4352 ± 72	89.2 ± 0.2	4881 ± 81
+0.20 , +0.40	4179 ± 70	85.0 ± 0.2	4915 ± 82
+0.40 , +0.60	4334 ± 71	88.3 ± 0.2	4908 ± 81
+0.60 , +0.80	4469 ± 72	90.4 ± 0.2	4944 ± 79
+0.80 , +1.00	4652 ± 72	91.6 ± 0.2	5081 ± 79
+1.00 , +1.20	4404 ± 70	87.8 ± 0.2	5016 ± 80
+1.20 , +1.40	4050 ± 67	83.2 ± 0.2	4867 ± 80
+1.40 , +1.60	4308 ± 68	90.3 ± 0.2	4773 ± 76
+1.60 , +1.80	3969 ± 65	83.1 ± 0.2	4776 ± 78
+1.80 , +1.93	2654 ± 53	86.9 ± 0.2	3054 ± 61

Table 3.9: Corrected event yields of $W^+ \rightarrow \mu^+ \nu_\mu$, given for each muon η_{CM}^μ . All analysis selection criteria are applied including the muon $p_T > 25$ GeV/c. The muon efficiency has been corrected by applying the tag-and-probe corrections, HF energy weights and vector boson p_T weights, event by event. All uncertainties shown are statistical only.

$$\mathcal{A}_\mu(\eta_{\text{CM}}^\mu) = \frac{N_\mu^+(\eta_{\text{CM}}^\mu) - N_\mu^-(\eta_{\text{CM}}^\mu)}{N_\mu^+(\eta_{\text{CM}}^\mu) + N_\mu^-(\eta_{\text{CM}}^\mu)} \quad (3.53)$$

where N_μ^- and N_μ^+ represents the efficiency-corrected number of $W^- \rightarrow \mu^- \bar{\nu}_\mu$ and $W^+ \rightarrow \mu^+ \nu_\mu$ events, respectively.

Forward-backward ratios. To probe the modification of the PDFs between different pseudorapidity regions, the signal event yields measured in the forward region ($\eta_{\text{CM}}^\mu > 0$) are combined with those measured in the backward region ($\eta_{\text{CM}}^\mu < 0$), to derive forward-

2470 backward ratios. These ratios are computed separately for $W^+ \rightarrow \mu^+ \nu_\mu$ and $W^- \rightarrow \mu^- \bar{\nu}_\mu$
 2471 events in the following way:

$$R_{FB}^\pm(\eta_{CM}^\mu) = \frac{N_\mu^\pm(+\eta_{CM}^\mu)}{N_\mu^\pm(-\eta_{CM}^\mu)} \quad (3.54)$$

2472 A forward-backward ratio is also derived for all $W \rightarrow \mu \nu_\mu$ events, by combining the
 2473 yields of the $W^- \rightarrow \mu^- \bar{\nu}_\mu$ and $W^+ \rightarrow \mu^+ \nu_\mu$ processes, according to:

$$R_{FB}(\eta_{CM}^\mu) = \frac{N_\mu^+ (+\eta_{CM}^\mu) + N_\mu^- (+\eta_{CM}^\mu)}{N_\mu^+ (-\eta_{CM}^\mu) + N_\mu^- (-\eta_{CM}^\mu)} \quad (3.55)$$

2474 3.2.9 Systematic uncertainties

2475 This section presents the different sources and the procedure employed to determine
 2476 the systematic uncertainties in the measurement of the W-boson production in p-Pb
 2477 collisions.

2478 3.2.9.1 Luminosity

2479 The recorded integrated luminosity of the 2016 p-Pb data sample is 173.4 nb^{-1} , and is
 2480 known with a precision of 3.5% [168]. Since the integrated luminosity cancels in forward-
 2481 backward ratios and in the muon charge asymmetry, it only affects the measurement of
 2482 the $W \rightarrow \mu \nu_\mu$ differential cross sections. In this case, this 3.5% systematic uncertainty is
 2483 global and the bin-to-bin correlations is 100%. This uncertainty is the dominant one on
 2484 the $W \rightarrow \mu \nu_\mu$ differential cross sections.

2485 3.2.9.2 Signal efficiency

2486 The dominant systematic uncertainty on the forward-backward ratios and muon charge
 2487 asymmetry are due to the estimation of the signal efficiency. Since the signal efficiencies
 2488 are computed from simulations and corrected using the TnP corrections, two sources
 2489 of systematic uncertainties are considered. The first one corresponds to the theoretical
 2490 modelling of the simulated signal, which takes into account the uncertainty on the
 2491 nuclear PDFs and the impact of the renormalisation and factorisation scales. The second
 2492 source corresponds to the TnP correction uncertainties, which derives from the $Z \rightarrow \mu^+ \mu^-$
 2493 control sample used to extract the TnP data efficiencies.

2494 **Theoretical modelling.** The NLO model used to generate the simulations can impact
2495 the measurement of the signal efficiencies. The main sources of theoretical uncertainties
2496 include the choice of the nuclear parton distribution function (EPPS16+CT14), and the
2497 renormalisation and factorisation scales.

2498 Since the PDFs are not calculable from first principles but are determined experi-
2499 mentally, in particular by the measurements reported here, the inclusion of any PDF
2500 introduces an additional systematic uncertainty. Thus, it is important to determine
2501 the impact of a change of PDF on the signal efficiencies. The procedure to derive the
2502 theoretical uncertainties of the PDF variations consist of reweighing the simulations
2503 event-by-event using weights derived from POWHEG after applying various PDF sets. The
2504 PDF sets are accessed through the LHAPDF6 [185] framework and consist of 56 CT14
2505 PDFs and 40 EPPS16 nuclear corrections. Once the simulations are reweighed with each
2506 PDF set, the efficiencies are recomputed and used to recalculate all the observables. The
2507 nPDF uncertainty is determined by combining the EPPS16+CT14 PDF variations of the
2508 observables using the Hessian approach, as recommended by the EPPS16 authors [158].

Moreover, the uncertainty due to the renormalisation (μ_R) and factorisation (μ_F)
scales is computed by varying these two scales in POWHEG using the following six
combinations:

$$(\mu_R/M_W, \mu_F/M_W) = [(0.5, 0.5), (1.0, 0.5), (0.5, 1.0), (1.0, 2.0), (2.0, 1.0), (2.0, 2.0)]$$

2509 The simulations are reweighed event by event using the POWHEG weights produced
2510 with each set of scales, then the efficiencies are recomputed and the observables are
2511 recalculated for each varied efficiency. The variations on the observables are combined
2512 by taking the envelope (i.e. the maximum variation in each η_{CM}^μ range).

2513 The systematic uncertainties from the PDF and scale variations are summed in
2514 quadrature, and amount to 0.1%. Thus, the theoretical uncertainties have negligible
2515 impact on the signal efficiencies.

2516 **Tag-and-probe correction.** The main source of systematic uncertainty in the mea-
2517 surement of the signal efficiency arises from the application of the TnP corrections. As
2518 mentioned in Section 3.2.6.2, the statistical and systematic uncertainties of the TnP
2519 corrections are derived from the muon identification, isolation and trigger efficiencies
2520 measured in data.

2521 It is crucial to consider the correlation between the different TnP uncertainties
2522 as a function of muon pseudorapidity and its charge, since they could cancel in the

2523 forward-backward ratios and muon charge asymmetry. The statistical TnP variations
2524 are uncorrelated between the different η_{lab} ranges in which they were derived. The sys-
2525 tematic TnP variations are considered to be fully correlated as a function of muon charge
2526 since the detector response is the same for muons and anti-muons, and uncorrelated
2527 between the different η_{CM} ranges (spanning different detectors).

2528 To compute the uncertainties, the muon charge asymmetry and the forward-backward
2529 ratios are recalculated for each efficiency derived by varying the TnP corrections. The TnP
2530 uncertainties are then determined by taking the difference between the value obtained
2531 with the varied TnP correction and its nominal value, combining the uncertainties as
2532 explained in Section 3.2.6.2. If the source of TnP correction is correlated in muon charge
2533 or pseudorapidity, the corresponding signal yields are varied at the same time. Moreover,
2534 for the W^\pm differential cross sections, the statistical and systematic TnP uncertainties
2535 are calculated by propagating the uncertainties on the corrected signal efficiency.

2536 The systematic uncertainty due to the TnP corrections amounts to 3.2% and the
2537 dominant TnP uncertainties are derived from the TnP systematic variations of the muon
2538 isolation (2.5%) and trigger (1.1%) components.

2539 3.2.9.3 QCD jet background

2540 The systematic uncertainty in the QCD jet background originates from the uncertainty
2541 in the modelling of the QCD jet p_T^{miss} distribution in the signal region. The nominal
2542 procedure consists in fixing the parameters of the modified Rayleigh distribution from
2543 the fits extrapolated from data as explained in Section 3.2.7.1. In order to estimate the
2544 uncertainty of the mismodelling of the QCD jet background shape, both the parameters
2545 and the functional form are varied.

2546 **QCD jet background parameters.** The first source of systematic uncertainty reflects
2547 the possible mismodelling of the QCD jet background shape due to the η_{CM}^μ dependence
2548 of the QCD background parameters. In order to check this, the parameters of the nominal
2549 QCD jet model are set free but constrained to be near their nominal values by using a
2550 Gaussian penalty. The width of the penalty Gaussian function is fixed, for a given QCD
2551 background parameter, to the root mean square (RMS) of the set of extrapolated results
2552 along all η_{CM}^μ ranges, shown in Figure 3.35. The RMS values used in the Gaussian
2553 penalty for the σ_0 , σ_1 and σ_2 parameters are presented in Table 3.10. The difference
2554 between the number of signal events extracted from the Gaussian-constrained fits and
2555 the nominal fits is taken as the systematic uncertainty, which is then propagated to all

observables. This source of uncertainty is considered to be fully uncorrelated since the p_T^{miss} distribution in each η_{CM}^μ range is fitted separately.

Parameter	RMS	
	$QCD \rightarrow \mu^-$	$QCD \rightarrow \mu^+$
σ_0	1.0	0.5
σ_1	0.9	0.9
σ_2	0.7	0.6

Table 3.10: The RMS of the set of QCD background parameters extrapolated along all η_{CM}^μ regions.

Another systematic variation consists of changing the muon isolation point used to extrapolate the QCD background parameters. In the nominal case, the isolation point of 0.03 is determined from the average muon isolation value in data within the signal region. As an alternative case, the muon isolation distribution is checked in a QCD PYTHIA simulated sample satisfying the signal selection criteria, and the average isolation value is determined to be approximately 0.08. As a result, the QCD background parameters are recomputed by extrapolating them to an isolation point of $I^\mu = 0.08$, and the fits are redone by fixing the QCD background parameters to the extrapolated values in the η_{CM}^μ -inclusive range as in the nominal case. The difference between the number of signal events extracted from the fits using the varied QCD background shape and the nominal results is taken as the systematic uncertainty. This uncertainty is propagated to all observables. The QCD background parameters extrapolated to $I^\mu = 0.08$ are listed in Table 3.11. Since the result in each η_{CM}^μ range varies independently, the uncertainty is considered to be fully uncorrelated.

Parameter	$QCD \rightarrow \mu^-$	$QCD \rightarrow \mu^+$
σ_0	14.67	14.79
σ_1	6.28	6.71
σ_2	0.50	0.49

Table 3.11: QCD shape parameters extrapolated to the average muon isolation point iso = 0.08.

The systematic uncertainty associated to the η_{CM}^μ dependence of the QCD background parameters amounts to 1.1%, while the uncertainty corresponding to the change of extrapolation point represents 0.2%.

2575 **QCD jet background functional form.** To assign a systematic uncertainty due to
2576 the assumed functional form for modelling the QCD jet background p_T^{miss} distribution,
2577 the shape of the QCD jet background is described using a different model. The alternative
2578 p_T^{miss} functional form employed, taken from Ref.[167], is given by:

$$f_{\text{QCD}}(p_T^{\text{miss}}) = (p_T^{\text{miss}} + x_0)^{\alpha} \cdot \exp\left(\beta \cdot \sqrt{p_T^{\text{miss}} + x_0}\right) \quad (3.56)$$

2579 The extrapolation procedure explained in Section 3.2.7.1 is redone using the alterna-
2580 tive model. All the fits are remade using the alternative QCD background functional form
2581 fixed to the parameters extrapolated in the η_{CM}^{μ} -inclusive range. The difference between
2582 the number of signal events measured using the alternative QCD background model and
2583 the nominal results is taken as the systematic uncertainty due to mismodelling of the
2584 QCD jet background shape. This systematic uncertainty is propagated to all observables
2585 and amounts to 0.6%. The bin-to-bin correlation is taken to be fully uncorrelated.

2586 3.2.9.4 Electroweak and $t\bar{t}$ backgrounds

2587 The $t\bar{t}$ background and the different sources of electroweak background are described
2588 using template histograms derived from simulations. The simulated samples are scaled
2589 to the recorded integrated luminosity of data using the NLO POWHEG cross sections for
2590 the electroweak processes and the CMS measured cross section for the $t\bar{t}$ production.
2591 Since for each these background sources, the ratio of background over signal events is
2592 fixed to simulation when performing the fits, a systematic uncertainty is assigned to each
2593 source by varying up and down their cross sections as explained below. The systematic
2594 uncertainty in each η_{CM}^{μ} range is derived by taking the maximum difference between
2595 the nominal and the up/down variations. The bin-to-bin correlations in muon charge and
2596 pseudorapidity are considered correlated since the total cross section is used to normalise
2597 all simulated events.

2598 **Z/ γ^* $\rightarrow \mu^+ \mu^-$ background.** The uncertainty on the ratio of Z/W total cross sections is
2599 estimated using the Monte Carlo for FeMtobarn processes (MCFM) program [186] at
2600 NLO with the CT14+EPPS16 nuclear PDFs. A relative uncertainty of 0.8% for Z/W^- and
2601 1.3% for Z/W^+ cross-section ratios is determined with MCFM taking into account the
2602 PDF uncertainties. Since the cross sections in the muon channel depend on the branching
2603 ratio associated to each process, their uncertainty has to also be taken into account.
2604 The values of the branching ratios correspond to $\text{BR}(Z \rightarrow \mu^+ \mu^-) = (3.366 \pm 0.007)\%$ and
2605 $\text{BR}(W \rightarrow \mu \nu_\mu) = (10.63 \pm 0.15)\%$ [19], which gives a relative uncertainty on the ratio of

2606 Z/W branching ratios of 1.4%. Summing in quadrature the MCFM uncertainties with the
 2607 ones derived from the branching ratios, one gets a total relative uncertainty for Z/W^+
 2608 of 1.6% and for Z/W^- of 1.9%. To be conservative the systematic variation is fixed to
 2609 2% overall. The systematic uncertainty is then determined by varying the $Z/\gamma^* \rightarrow \mu^+ \mu^-$
 2610 cross section by 2% up and down when performing the fits, yielding a change of 0.3% in
 2611 the measured $W \rightarrow \mu \nu_\mu$ cross sections.

2612 **$Z/\gamma^* \rightarrow \tau \bar{\tau}$ background.** The uncertainty on the ratio of $Z/\gamma^* \rightarrow \tau \bar{\tau}$ background over
 2613 signal events is considered to be the same as the 2% uncertainty determined for the
 2614 $Z/\gamma^* \rightarrow \mu^+ \mu^-$ background. Hence, the $Z/\gamma^* \rightarrow \tau \bar{\tau}$ cross section is varied by 2% up and
 2615 down when performing the fits. The impact of this systematic uncertainty is negligible
 2616 and modifies the $W \rightarrow \mu \nu_\mu$ cross sections by 0.01%.

2617 **$W \rightarrow \tau \nu_\tau$ background.** The values of the W-boson leptonic branching ratios correspond
 2618 to $\text{BR}(W \rightarrow \mu \nu_\mu) = (10.63 \pm 0.15)\%$ and $\text{BR}(W \rightarrow \tau \nu_\tau) = (11.38 \pm 0.21)\%$ [19], which gives a
 2619 relative uncertainty on the ratio of $W \rightarrow \tau \nu_\tau$ over $W \rightarrow \mu \nu_\mu$ cross sections of 2.3%. Thus,
 2620 the systematic uncertainty is estimated by varying the ratio of $W \rightarrow \tau \nu_\tau$ to signal events
 2621 up and down by $\pm 2.3\%$. The impact of this systematic uncertainty on the $W \rightarrow \mu \nu_\mu$ cross
 2622 sections is found to be 0.04%.

2623 **$t \bar{t}$ background.** The $t \bar{t}$ simulation is normalized using the CMS measured total cross
 2624 section $\sigma_{t \bar{t}} = 45 \pm 8 \text{ nb}^{-1}$ [181]. The systematic related to the $t \bar{t}$ background normalization
 2625 is computed by varying up and down the $t \bar{t}$ cross section by its measured relative
 2626 uncertainty ($\pm 18\%$). This systematic uncertainty amounts to 0.2%.

2627 3.2.9.5 Weak boson p_T

2628 The modelling of the weak boson p_T in the signal and electroweak background simula-
 2629 tions is corrected by weighing event-by-event the generated weak boson p_T distribution
 2630 following the procedure described in Section 3.2.4. To determine the impact of the
 2631 modelling of the weak boson p_T , the boson p_T corrections are removed and both the
 2632 efficiency and the fits to the p_T^{miss} distribution are remade. The systematic uncertainty is
 2633 determined in each η_{CM}^μ range from the difference between the nominal results and the
 2634 results obtained without weighing the generated boson p_T distribution. This uncertainty
 2635 amounts to 0.5% and it is considered to be correlated with respect to muon charge and
 2636 pseudorapidity.

3.2.9.6 Event activity

The modelling of the event activity present in p-Pb collisions is improved by weighing the distribution of the total HF energy, as explained in Section 3.2.5.1. The event activity is also correlated with other global variables, such as the number of tracks per event. Since the pseudorapidity coverage of the tracker ($|\eta| < 2.5$) and the HF calorimeter ($3.0 < |\eta| < 5.4$) is different, the HF energy and the track multiplicity are sensitive to different kinematic regions of the event activity. Thus, the systematic uncertainty on the modelling of the event activity is determined by weighing instead the distribution of the simulated track multiplicity following the same procedure as the one used for the HF energy. The fits to the p_T^{miss} distribution and the signal efficiency are recomputed after weighing the simulated track multiplicity distribution. The difference between the varied and nominal observables is assigned as the systematic uncertainty in each muon η_{CM}^μ range. This uncertainty is considered correlated in muon charge and pseudorapidity, and it amounts to 0.6%.

3.2.9.7 Recoil calibration

The uncertainties due to the recoil calibration are of different nature: statistical and systematic. The statistical component arises from the uncertainties associated to the recoil scale and resolution derived from the fits to the recoil distributions from data. The systematic components arise from the following sources:

- The recoil calibration method employed to correct the simulated p_T^{miss} distribution;
- The choice of functional form used to fit the recoil distributions in each q_T^Z range;
- The parametrisation of the q_T dependence of the recoil scale and resolution.

Statistical component. In order to estimate the uncertainty associated to the recoil resolution, the weighed average Gaussian widths of the perpendicular and parallel recoil components, defined in Eq. (3.36), are randomly smeared in each q_T^Z range using a Gaussian distribution centred on the parameter value and with a width equal to the parameter uncertainty. The q_T dependence is parametrised again using the nominal functions presented in Eq. (3.35). The procedure is repeated a hundred times, and the recoil calibrations are applied to the simulated p_T^{miss} distributions, redoing the measurements every time. The RMS of the number of signal events extracted from the fits using each variation of the recoil calibration, is used to determine the statistical

2668 uncertainty of the recoil calibration. This uncertainty is propagated to all observables
2669 and amounts to 0.09%. It is considered fully uncorrelated.

2670 **Systematic components.** The fit function used to parametrise the q_T dependence
2671 of the recoil scale and resolution, is varied in both data and simulation to determine
2672 the associated uncertainty. Instead of using the nominal functions for the Gaussian
2673 mean (Eq. (3.33)) and Gaussian widths (Eq. (3.35)), a second order polynomial is used to
2674 parametrise the Gaussian parameters with respect to q_T^Z . The varied recoil calibration
2675 is applied to the simulated p_T^{miss} distributions, which are then used to extract the
2676 signal from the data. The difference between the observables measured using the varied
2677 recoil calibration and the nominal observables, in each η_{CM}^μ , is assigned as a systematic
2678 uncertainty.

2679 The uncertainty on the shape of the recoil distributions in each q_T^Z range is estimated
2680 by varying the recoil fit model. Instead of using a sum of two Gaussian functions, the
2681 recoil distributions are parametrised with a sum of a Breit-Wigner and a Gaussian
2682 distribution, in both data and simulation (varied at the same time). The resulting
2683 q_T dependence of the recoil scale and resolution is determined following the nominal
2684 procedure and the measurements are performed again. The systematic uncertainty is
2685 determined as the variation between the observables derived with the varied recoil
2686 calibration and the nominal ones.

2687 Moreover, the uncertainty associated to the method used to apply the recoil calibration
2688 is determined by smearing the recoil distributions as described in Eq. (3.42), instead of
2689 scaling them as done in the nominal case. The difference between the varied and nominal
2690 observables in each η_{CM}^μ is assigned as a systematic uncertainty.

2691 The largest source of systematic uncertainty in this case is the one associated to
2692 the shape of the recoil distribution, which amounts to 0.3%. The uncertainty related
2693 to the recoil calibration represents 0.2%, while the uncertainty corresponding to the
2694 q_T dependence of the recoil scale and resolution is determined to be 0.06%. These
2695 uncertainties are considered correlated both in muon charge and pseudorapidity.

2696 **3.2.9.8 W-boson POWHEG BOX**

2697 The $W \rightarrow \mu\nu_\mu$ simulations were generated using the POWHEG-BOX package `W_ew-BMMNP` [173],
2698 in which electroweak NLO corrections are implemented. In order to asses the impact of
2699 these NLO corrections on the final results, the $W \rightarrow \mu\nu_\mu$ simulations were remade instead

2700 using the standard POWHEG-BOX package W [187], which does not include electroweak
 2701 NLO corrections, following the same procedure described in Section 3.2.2.

2702 To determine the systematic uncertainty, the signal efficiencies and the template
 2703 histograms for the signal were recomputed using the $W \rightarrow \mu\nu_\mu$ simulations without elec-
 2704 troweak NLO corrections. Then, the fits to the p_T^{miss} distribution in data were performed
 2705 again, and the difference between the observables measured using the varied signal
 2706 templates and the nominal results is assigned as a systematic uncertainty in each η_{CM}^μ
 2707 range. This uncertainty amounts to 0.9% and it is considered to be fully correlated.

2708 **3.2.9.9 Summary of systematic uncertainties**

2709 The largest systematic uncertainty for each category among all η_{CM}^μ ranges is sum-
 2710 marised in Table 3.12. The systematic uncertainties are shown for each observable, in-
 2711 cluding the $W \rightarrow \mu\nu_\mu$ cross sections, muon charge asymmetry and the forward-backward
 2712 ratios. The uncertainties presented for the cross sections are relative while those for the
 2713 forward-backward ratios and the muon charge asymmetry are absolute.

Systematic Variation	$\sigma(W^- \rightarrow \mu^-\bar{\nu}_\mu)$ [%]	$\sigma(W^+ \rightarrow \mu^+\nu_\mu)$ [%]	R_{FB}^-	R_{FB}^+	R_{FB}	\mathcal{A}_μ
Luminosity	3.5	3.5	0.000	0.000	0.000	0.000
Signal efficiency	3.0	3.2	0.026	0.037	0.030	0.011
QCD jet background	1.2	0.7	0.016	0.007	0.009	0.006
Electroweak and $t\bar{t}$ backgrounds	0.4	0.3	0.002	0.001	0.001	0.000
Weak boson p_T	0.5	0.4	0.001	0.001	0.001	0.001
Event activity	0.6	0.4	0.002	0.002	0.001	0.002
Recoil calibration	0.2	0.3	0.002	0.004	0.002	0.002
W-boson POWHEG-BOX	0.9	0.5	0.007	0.004	0.006	0.003
Total systematic uncertainty	4.8	4.8	0.030	0.038	0.031	0.013
Statistical uncertainty	2.4	2.0	0.026	0.029	0.019	0.015

Table 3.12: Maximum uncertainty of the measured observables determined for each category. The uncertainties of the $W \rightarrow \mu\nu_\mu$ differential cross sections are relative while for the forward-backward ratios and muon charge asymmetry are absolute.

2714 The uncertainties of the measurements are shown in Figure 3.37 as a function of
 2715 η_{CM}^μ . They are observed to be similar between the different η_{CM}^μ ranges, except for the
 2716 most backward and forward regions, which are driven by the systematic uncertainty
 2717 on the signal efficiency. It is also seen that the systematic uncertainties dominates on
 2718 the $W^\pm \rightarrow \mu^\pm\nu_\mu$ differential cross sections and the forward-backward ratios in all η_{CM}^μ
 2719 ranges. In the case of the muon charge asymmetry, most of the systematic uncertainties
 2720 are found to be suppressed due to the correlations in muon charge, and as a result, the
 2721 statistical uncertainties dominates in most of the η_{CM}^μ ranges.

3.2. ANALYSIS

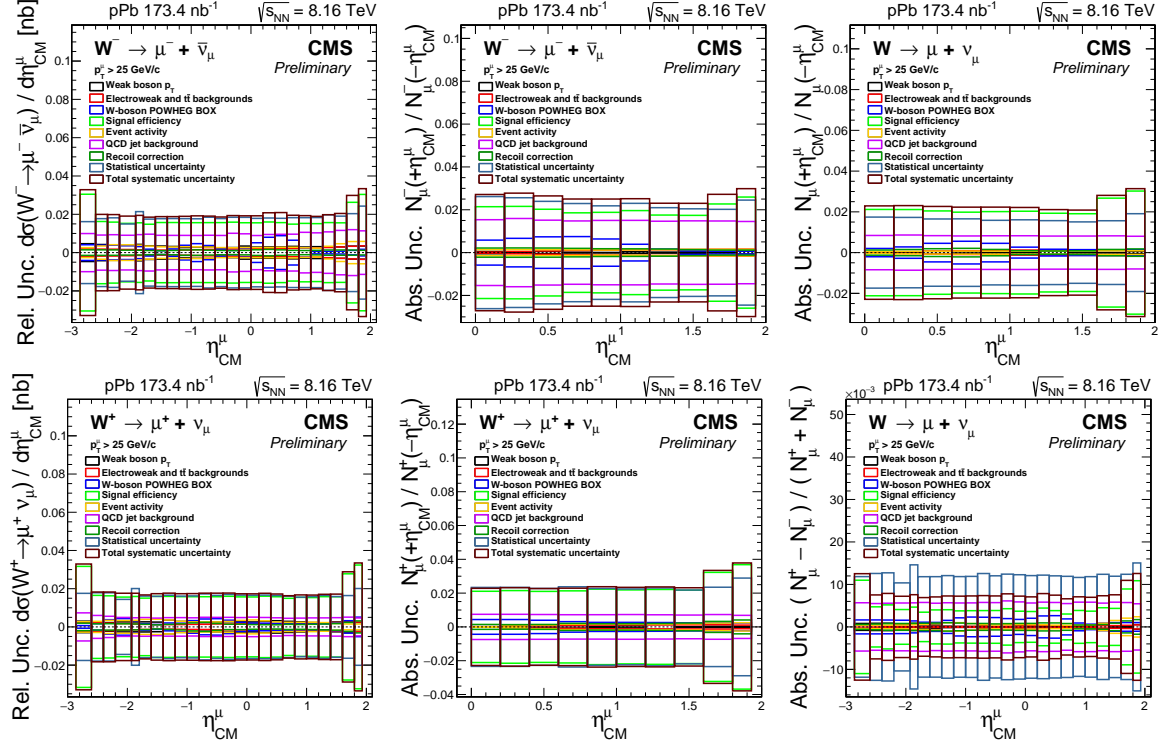


Figure 3.37: Uncertainty corresponding to each category as function of the muon η_{CM} . The plots are divided as: $W^- \rightarrow \mu^- \bar{\nu}_\mu$ (top-left) and $W^+ \rightarrow \mu^+ \nu_\mu$ (bottom-left) differential cross sections, $W^- \rightarrow \mu^- \bar{\nu}_\mu$ (top-middle) and $W^+ \rightarrow \mu^+ \nu_\mu$ (bottom-middle) forward-backward ratios, and finally the charge-summed forward-backward ratio (top-right) and muon charge asymmetry (bottom-right). The uncertainties of the cross sections are relative while for the forward-backward ratios and muon charge asymmetry are absolute. The global luminosity uncertainty of 3.5% is not included.

3.2.9.10 Covariance matrix

The covariance matrices of the $W \rightarrow \mu\nu_\mu$ differential cross sections, the forward-backward ratios and the muon charge asymmetry are computed by taking into account the measurements extracted in each η_{CM}^μ range. In the case of the $W^\pm \rightarrow \mu^\pm \nu_\mu$ differential cross sections and the $W^\pm \rightarrow \mu^\pm \nu_\mu$ forward-backward ratios, the matrices are made of 48x48 entries (24 muon η_{CM}^μ ranges times two muon charge measurements), while for the muon charge asymmetry and the charge-summed forward-backward ratio, only 24x24 entries are considered.

For a given (i,j) entry of the covariance matrix, the covariance is calculated as the uncertainty in bin i times the uncertainty in bin j. If the uncertainty is uncorrelated, the off-diagonal elements are set to zero. The total covariance matrix of each observable is

2733 determined by summing the covariance matrix of the statistical uncertainty together
2734 with the covariance matrices of all the systematic uncertainties.

2735 The covariance matrix of the statistical uncertainty corresponds to a fully diagonal
2736 matrix where each (i, i) element in the diagonal is the square of the statistical uncer-
2737 tainty of bin i. On the other hand, the covariance matrix of each systematic uncertainty
2738 is computed by taking into account the bin-to-bin correlations in muon charge and
2739 pseudorapidity.

2740 The total correlation matrix of each observable is derived from the total covariance
2741 matrix, using the following formula:

$$\text{corr}(i, j) = \frac{\text{cov}(i, j)}{\sqrt{\text{cov}(i, i) * \text{cov}(j, j)}} \quad (3.57)$$

2742 The corresponding correlation matrices are shown in Figure 3.38. The black lines
2743 are used to distinguish the different bins in muon charge, which are ordered in a given
2744 plot from top to bottom as: Minus-Minus, Minus-Plus, Plus-Minus and Plus-Plus. The
2745 large correlation observed in the $W \rightarrow \mu\nu_\mu$ differential cross sections arise from the
2746 luminosity uncertainty. On the other hand, the anti-correlation seen in the muon charge
2747 asymmetry derive from the TnP corrections for muon isolation and identification, which
2748 are applied as a function of $|\eta_{\text{lab}}|$ and thus, introduces correlations between the backward
2749 and forward pseudorapidity regions.

2750 3.3 Results

2751 This section presents the analysis results of the W-boson production in pPb collisions at
2752 $\sqrt{s_{\text{NN}}} = 8.16 \text{ TeV}$. The W-boson yields are extracted in the muon kinematic region defined
2753 by $p_T^\mu > 25 \text{ GeV}/c$ and $|\eta_{\text{lab}}^\mu| < 2.4$. The $W \rightarrow \mu\nu_\mu$ differential cross sections, the muon
2754 charge asymmetry, and the forward-backward ratios are measured as a function of muon
2755 η_{CM}^μ . The measurements are compared to PDF calculations with and without including
2756 nuclear modifications.

2757 3.3.1 W-boson production in p-Pb at 8.16 TeV

2758 The $W^\pm \rightarrow \mu^\pm \nu_\mu$ differential cross sections are derived using Eq. (3.52). The results of the
2759 differential cross sections of $W^+ \rightarrow \mu^+ \nu_\mu$ and $W^- \rightarrow \mu^- \bar{\nu}_\mu$ are shown as a function muon
2760 η_{CM}^μ in Figure 3.39. The vertical error bars represent the statistical uncertainties from
2761 the number of $W \rightarrow \mu\nu_\mu$ events measured in each η_{CM}^μ range, while the brackets show

3.3. RESULTS

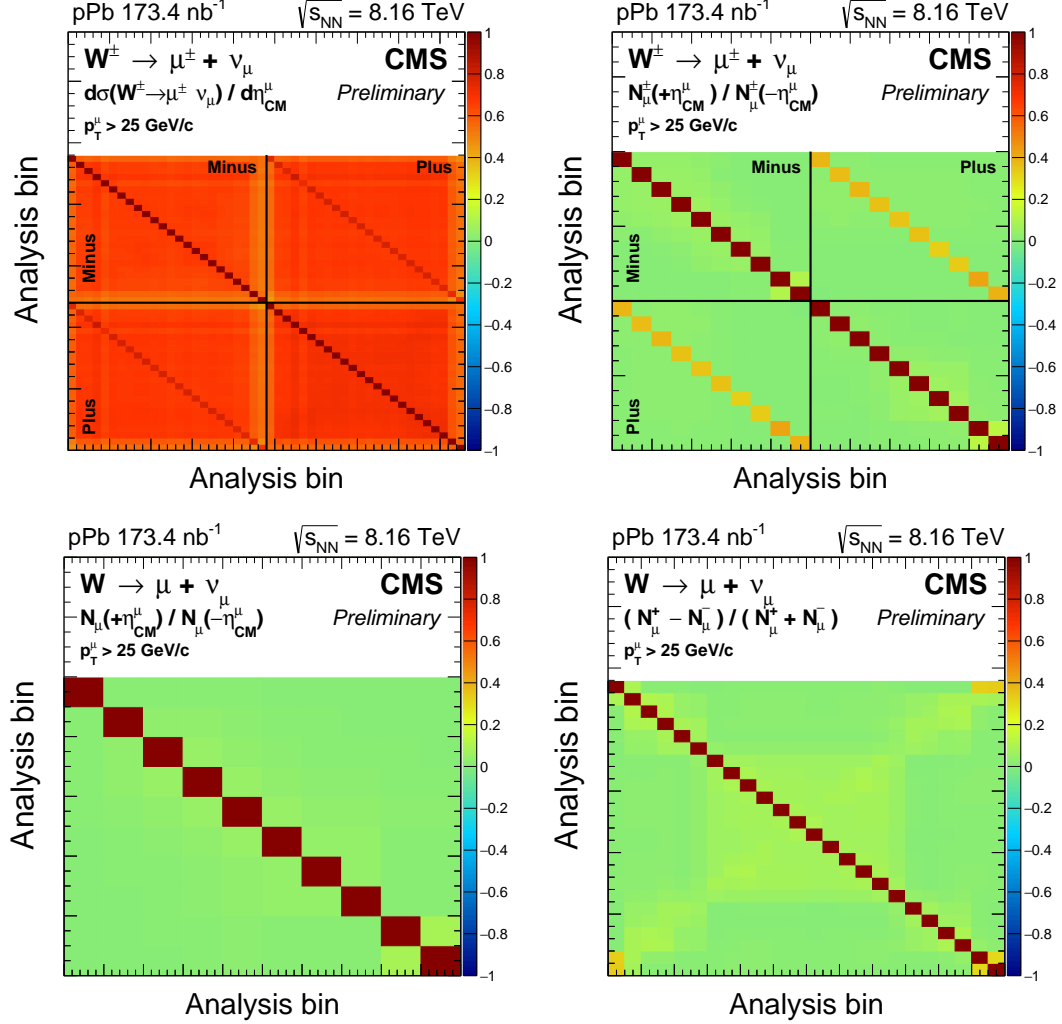


Figure 3.38: Correlation matrices for: W^\pm cross section (top-left) , $W^\pm R_{FB}$ (top-right) , charge-inclusive R_{FB} (bottom-left) , and charge asymmetry (bottom-right). The lines in the top plots are used to separate the different muon charge bins.

2762 the statistical and total systematic uncertainties summed in quadrature. The global
2763 integrated luminosity uncertainty of 3.5% [168] is not shown in the figures.

2764 The opposite trend seen between the $W^+ \rightarrow \mu^+ \nu_\mu$ and $W^- \rightarrow \mu^- \bar{\nu}_\mu$ differential cross
2765 sections as a function of η_{CM}^μ is expected from parity violation of the electroweak interac-
2766 tion. The W^+ bosons decay to a right-handed anti-muon boosted in the opposite direction,
2767 while the W^- bosons decay to a left-handed muon along the direction of the W^- boson.

2768 The muon charge asymmetry is determined from the efficiency-corrected signal event
2769 yields using Eq. (3.53). The measured muon charge asymmetry is shown in Figure 3.40
2770 as a function muon η_{CM}^μ .

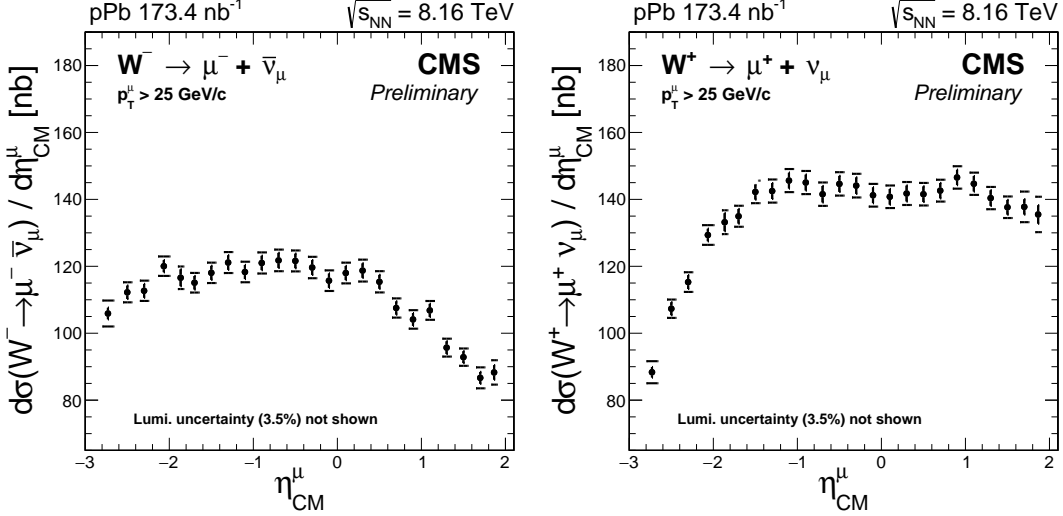


Figure 3.39: Differential production cross sections for $W^+ \rightarrow \mu^+ \nu_\mu$ (left) and $W^- \rightarrow \mu^- \bar{\nu}_\mu$ (right), as a function of the muon pseudorapidity in the center-of-mass frame. The brackets represent the statistical and systematic uncertainties summed in quadrature, while the error bars show the statistical uncertainties only. The global luminosity uncertainty of 3.5% [168] is not shown.

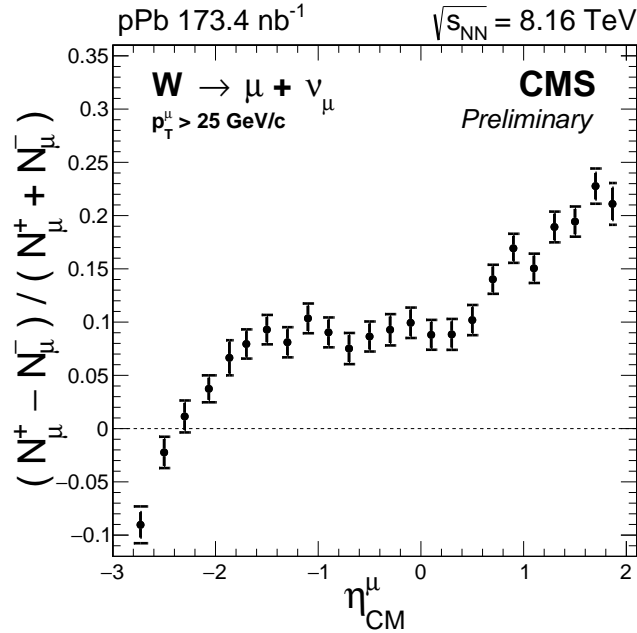


Figure 3.40: Muon charge asymmetry as a function of the muon pseudorapidity in the center-of-mass frame. The brackets represent the statistical and systematic uncertainties summed in quadrature, while the error bars show the statistical uncertainties only.

3.3. RESULTS

2771 The $W^+ \rightarrow \mu^+ \nu_\mu$ and $W^- \rightarrow \mu^- \bar{\nu}_\mu$ forward-backward ratios are computed using
 2772 Eq. (3.54), while the charge-summed forward-backward ratio is determined using Eq. (3.55).
 2773 As mentioned in Section 3.2.1, the forward region ($\eta_{CM}^\mu > 0$) is defined on the proton-going
 2774 direction while the backward region corresponds to the Pb-going direction. The results of
 2775 the muon forward-backward ratios are shown in Figure 3.41.

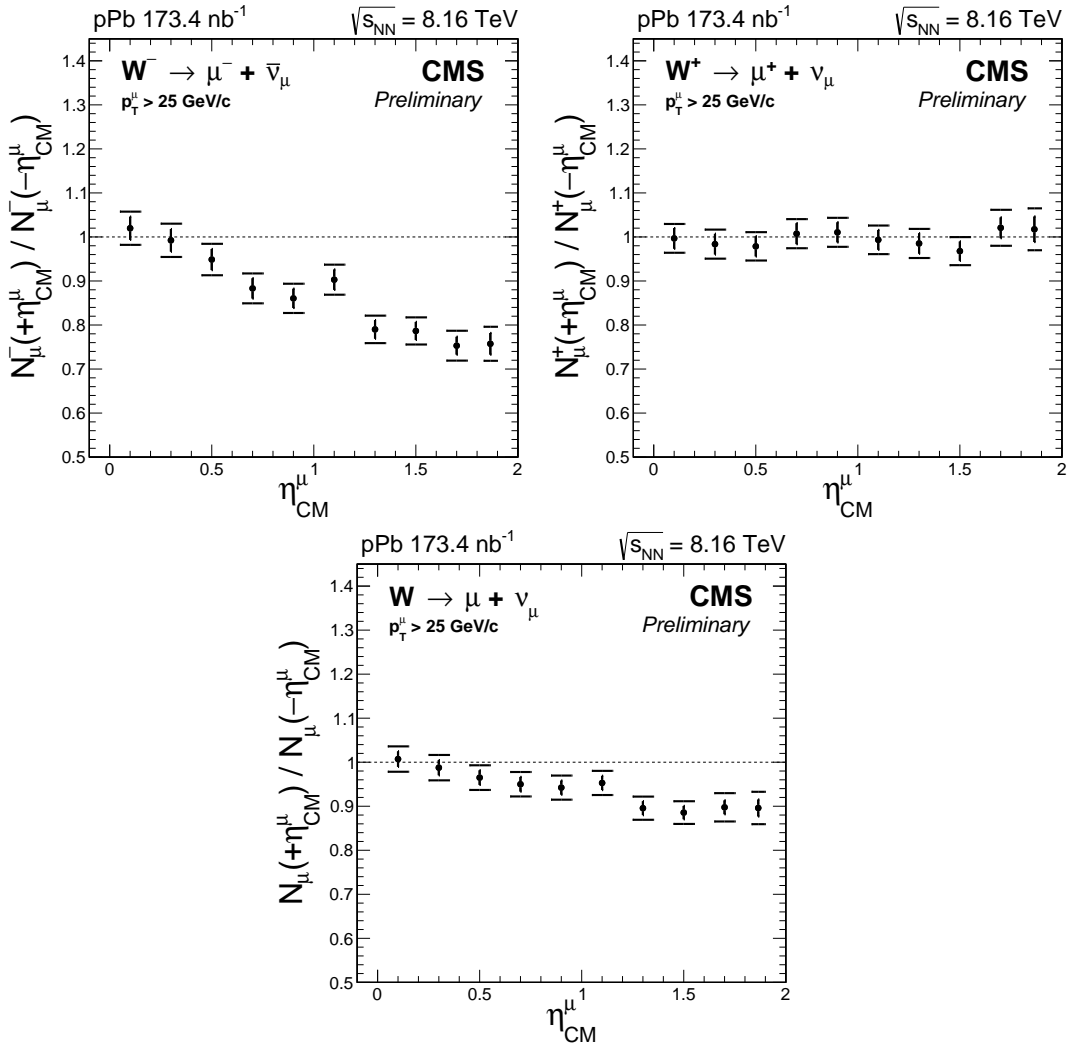


Figure 3.41: Forward-backward ratios, for the positive (top-left), negative (top-right) and all (bottom) charged muons. The brackets represent the statistical and systematic uncertainties summed in quadrature, while the error bars show the statistical uncertainties only.

3.3.2 Comparison with theoretical models

The measurements of the W-boson production in p-Pb collisions at 8.16 TeV are compared to three NLO PDF calculations. In all three PDF calculations, the isospin effect is taking into account for the Pb nucleus. A description of each PDF model is provided below:

- CT14: this model assumes no nuclear modifications and uses the NLO CT14 proton PDF for both the incoming proton and Pb-ion.
- CT14+EPPS16: this PDF model employs the CT14 PDF for the incoming proton and apply the EPPS16 nuclear corrections on the CT14 PDF for the incoming Pb-ion.
- CT14+nCTEQ15: this PDF model makes use of the CT14 PDF for the incoming proton and the nCTEQ15 nuclear PDF for the incoming Pb-ion.

The results of the PDF models are derived using the parton-level Monte Carlo program MCFM [186]. The comparison between the PDF calculations and the data are shown in Figure 3.42 for the $W \rightarrow \mu\nu_\mu$ differential cross sections, in Figure 3.43 for the muon charge asymmetry and in Figure 3.44 for the forward-backward ratios. In all figures, the results of the CT14 PDF model calculations are shown using continuous lines, while the CT14+EPPS16 and CT14+nCTEQ15, are shown with green and brown dashed lines, respectively.

As can be seen in Figure 3.42, the $W \rightarrow \mu\nu_\mu$ cross section measurements at forward rapidity favour the PDF calculations including nuclear modifications, while at backward rapidity all three PDF calculations are in good agreement with the data. Moreover, in the case of the muon charge asymmetry shown in Figure 3.43, the results of the theory calculations derived using the CT14 proton PDF only, and those including the EPPS16 nuclear modifications, are in good agreement with the measurements, while the nCTEQ15 nPDF calculations expect a slightly larger muon charge asymmetry in the most backward η_{CM}^μ range. Finally, from the ratios of the signal event yields at forward-over-backward η_{CM}^μ displayed in Figure 3.44, the nuclear PDF calculations describe much better the data compared to the free-nucleon PDF calculation.

In order to quantify the level of agreement between each PDF calculation and the measurements of the W-boson production in p-Pb collisions, a χ^2 test is performed according to:

3.3. RESULTS

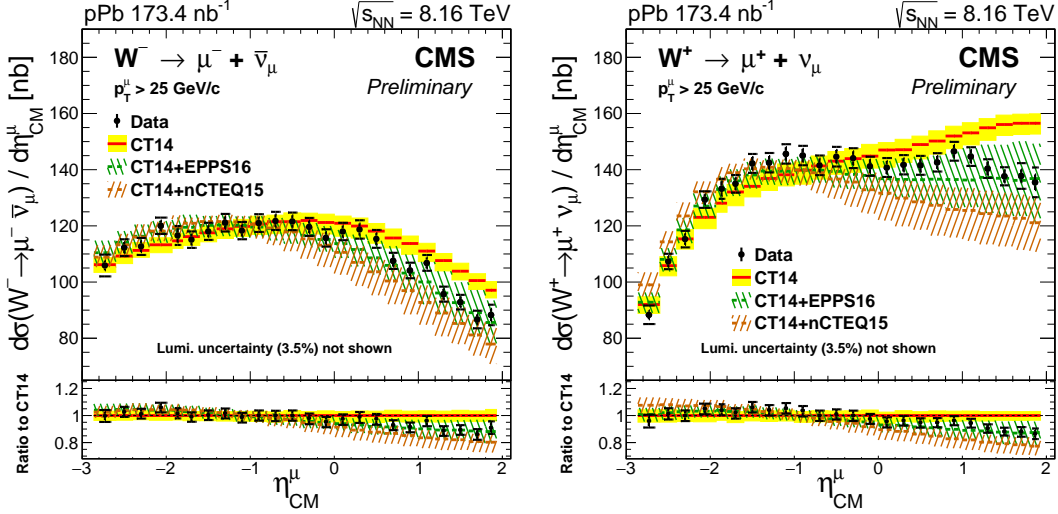


Figure 3.42: Differential cross sections for $W^+ \rightarrow \mu^+ \nu_\mu$ (left) and $W^- \rightarrow \mu^- \bar{\nu}_\mu$ (right), as a function of the muon η_μ^{CM} . Errors bars represent the statistical uncertainties, while the brackets represent the statistical and systematic uncertainties summed in quadrature. The global luminosity uncertainty of 3.5% is not displayed. Theoretical predictions with (CT14+EPPS16 shown in dashed green line and CT14+nCTEQ15 shown in dashed brown line) and without (CT14, solid red line) PDF nuclear modifications are also shown, with the uncertainty bands include the PDF uncertainties.

$$\chi^2 = \sum_i \sum_j \left[(t(i) - d(i)) \cdot (\text{COV}_{\text{data}} + \text{COV}_{\text{theory}})^{-1} [i, j] \cdot (t(j) - d(j)) \right] \quad (3.58)$$

where $t(i)$ is the value of the observable derived from the PDF calculation in bin i , $d(j)$ is the value of the observable measured in data in bin j , and $(\text{COV}_{\text{data}} + \text{COV}_{\text{theory}})^{-1}$ is the inverse of the sum of the covariance matrices extracted from the data and PDF calculations. This approach takes into account the bin-to-bin correlations in both muon charge and pseudorapidity.

The outcome of the χ^2 statistical test derived using the CT14 PDF, CT14+EPPS16 nPDF and CT14+nCTEQ15 nPDF calculations are summarized in Table 3.13. The results of the CT14 PDF calculations are significantly disfavoured by the measurements, while the PDF calculations including nuclear modifications are in good agreement. In addition, the measurements tend to favour the nPDF calculations of the CT14+EPPS16 model over the ones from the CT14+nCTEQ15 model.

Considering the smaller size of the uncertainties of the measurements compared to those from the PDF models, the measurements have the potential to constrain the parametrisations of the EPPS16 nuclear modifications and the nCTEQ15 nuclear PDFs.

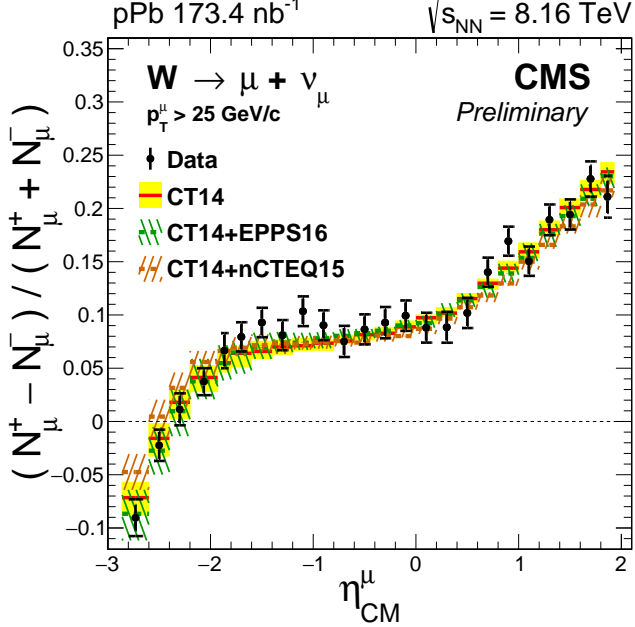


Figure 3.43: Muon charge asymmetry of $W \rightarrow \mu\nu_\mu$, given for each muon η_{CM}^μ range. Errors bars represent the statistical uncertainties, while the brackets represent the statistical and systematic uncertainties summed in quadrature. Theoretical predictions with (CT14+EPPS16 shown in dashed green line and CT14+nCTEQ15 shown in dashed brown line) and without (CT14, solid red line) PDF nuclear modifications are also shown, with the uncertainty bands. All theory uncertainty bands include the PDF uncertainties.

Observable	CT14			CT14+EPPS16			CT14+nCTEQ15		
	χ^2	ndf	Prob.(%)	χ^2	ndf	Prob.(%)	χ^2	ndf	Prob.(%)
$d\sigma(W^\pm \rightarrow \mu^\pm \nu_\mu)/d\eta_{CM}^\mu$	136	48	2×10^{-8}	32	48	96	40	48	79
$(N_\mu^+ - N_\mu^-)/(N_\mu^+ + N_\mu^-)$	23	24	54	18	24	80	29	24	23
$N_\mu^\pm(+\eta_{CM}^\mu)/N_\mu^\pm(-\eta_{CM}^\mu)$	98	20	3×10^{-10}	11	20	95	14	20	83
$N_\mu(+\eta_{CM}^\mu)/N_\mu(-\eta_{CM}^\mu)$	87	10	2×10^{-12}	3	10	99	5	10	90

Table 3.13: Results of the χ^2 statistical test between the measurements and the theory calculations from the CT14 PDF, CT14+EPPS16 nPDF and CT14+nCTEQ15 nPDF models. The value of the χ^2 , the number of degrees of freedom (ndf) and the χ^2 probability (Prob.), are presented for the $W^\pm \rightarrow \mu^\pm \nu_\mu$ differential cross sections, the muon charge asymmetry, the $W^\pm \rightarrow \mu^\pm \nu_\mu$ forward-backward ratios, and the charge-summed forward-backward ratio, respectively.

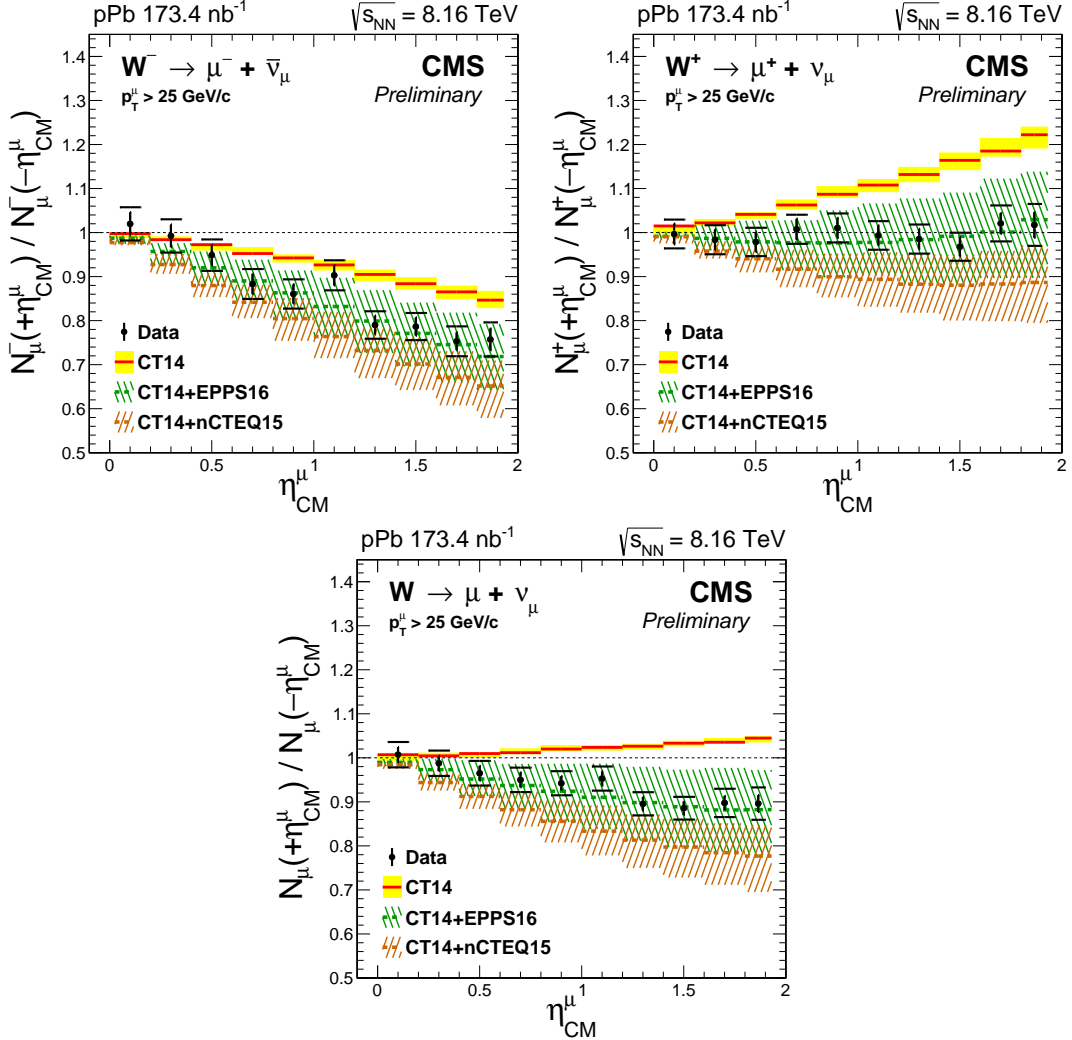


Figure 3.44: Forward-backward ratio of $W \rightarrow \mu\nu_{\mu}$, given for each muon η_{CM}^{μ} range separated in negative (top-left), positive (top-right) and all (bottom) charged muons. Errors bars represent the statistical uncertainties, while the brackets represent the statistical and systematic uncertainties summed in quadrature. Theoretical predictions with (CT14+EPPS16 shown in dashed green line and CT14+nCTEQ15 shown in dashed brown line) and without (CT14, solid red line) PDF nuclear modifications are also shown, with the uncertainty bands. All theory uncertainty bands include the PDF uncertainties.

2823 **CHARMONIUM PRODUCTION IN LEAD-LEAD COLLISIONS**

2824 This chapter reports the measurement of the production of J/ψ and $\psi(2S)$ mesons
2825 in lead-lead (Pb-Pb) collisions compared to p-p collisions at $\sqrt{s_{NN}} = 5.02\text{TeV}$. The
2826 physics of charmonia in heavy-ion collisions is briefly introduced in Section 4.1.
2827 The J/ψ and $\psi(2S)$ meson analyses are then described in detailed in Section 4.2. Sec-
2828 tion 4.3 presents the results of the prompt and nonprompt J/ψ -meson production, and
the nuclear modification of prompt $\psi(2S)$ mesons relative to J/ψ mesons.

2829 **4.1 Introduction**

2830 This section provides an introduction to the physics of charmonia in hadronic and heavy-
2831 ion collisions. The basic properties of charmonium states are detailed in Section 4.1.1,
2832 followed by a brief description of different models of charmonium hadroproduction in
2833 Section 4.1.2. A short overview of some nuclear matter effects that can impact the mea-
2834 surement of charmonium production in heavy-ion collisions are presented in Section 4.1.3,
2835 as well as the current understanding of their role in the past measurements.

2836 **4.1.1 Spectrum of charmonium states**

2837 Charmonia are bound states of a charm quark and anti-quark. They are part of the
2838 family of quarkonium mesons, briefly introduced in Section 1.2.4.4. The first observation
2839 of a charmonium state was published in 1974, by the collaborations lead by Burton

2840 Richter at SLAC [131] and Sam Ting at BNL [130]. Both experiments found a narrow
 2841 resonance in the e^+e^- and $\mu^+\mu^-$ decay channels with an invariant mass of $m \approx 3.1\text{ GeV}$,
 2842 which was named J by Sam Ting and ψ by Burton Richter, thus later referred as the J/ψ
 2843 meson.

2844 Following a non-relativistic approach, by solving the Schrödinger equation using a $c\bar{c}$
 2845 potential model as mentioned in Section 1.2.4.4, the charmonium states can be classified
 2846 according to the total spin S , orbital angular momentum L and total angular momentum
 2847 J of the $c\bar{c}$ system. Depending on the spin of the $c\bar{c}$ pair, charmonia can either be singlet
 2848 ($S = 0$) or triplet ($S = 1$). The charmonium states are typically labelled using the notation
 2849 $n^{2S+1}L_J$, where n is the principal quantum number. By convention, the charmonium
 2850 states with values $L = 0, 1, 2\dots$ are denoted as S, P, D In this notation, the J/ψ meson
 2851 ($n = 1, S = 1, J = 1$) represents the S-wave ground state 1^3S_1 , while the $\psi(2S)$ meson
 2852 ($n = 2, S = 1, J = 1$) corresponds to its first excited state 2^3S_1 . The mass of charmonium
 2853 states increases with n , being larger for higher excited states. Table 4.1 summarises the
 2854 mass and width of some charmonium states.

Charmonium state	$n^{2S+1}L_J$	Width [MeV/c^2]	Mass [MeV/c^2]
$\eta_c(1S)$	1^1S_0	32.1 ± 0.9	2983.9 ± 0.5
J/ψ	1^3S_1	0.0929 ± 0.0028	3096.900 ± 0.006
h_c	1^1P_1	0.70 ± 0.36	3525.38 ± 0.11
χ_{c0}	1^3P_0	10.5 ± 0.8	3414.71 ± 0.30
χ_{c1}	1^3P_1	0.88 ± 0.05	3510.67 ± 0.05
χ_{c2}	1^3P_2	2.00 ± 0.11	3556.17 ± 0.07
$\eta_c(2S)$	2^1S_0	$11.3^{+3.2}_{-2.9}$	3637.6 ± 1.2
$\psi(2S)$	2^3S_1	0.294 ± 0.008	3686.097 ± 0.010

Table 4.1: The width and mass of charmonium states below the $D\bar{D}$ -meson pair mass.
 Information taken from Ref. [19].

2855 The branching ratios for charmonium decays depend on the mass of the bound state.
 2856 On the one hand, charmonium states with masses above two times the D-meson mass
 2857 (m_D), that is $3.73\text{ GeV}/c^2$, preferentially decays to open-charm hadrons (i.e. with non-zero
 2858 charm quantum numbers, such as D mesons or charmed baryons), favoured by the Okuba-
 2859 Zweig-Iiluka (OZI) rule [188–190]. On the other hand, charmonium states with masses
 2860 below $2m_D$, decays radiatively (e.g. $\chi_c \rightarrow J/\psi + \gamma$) or hadronically (e.g. $\psi(2S) \rightarrow J/\psi + 2\pi$) to
 2861 lower mass charmonium states or light hadrons, and also electromagnetically to lepton
 2862 pairs. As a result, charmonium states below the $D\bar{D}$ threshold appear as mass peaks
 2863 in the dilepton invariant mass distribution, while those above do not. The different

2864 charmonium decays to lower mass charmonia are shown in Figure 4.1 and the main
 2865 branching ratios for decays of J/ψ and $\psi(2S)$ mesons are presented in Table 4.2.

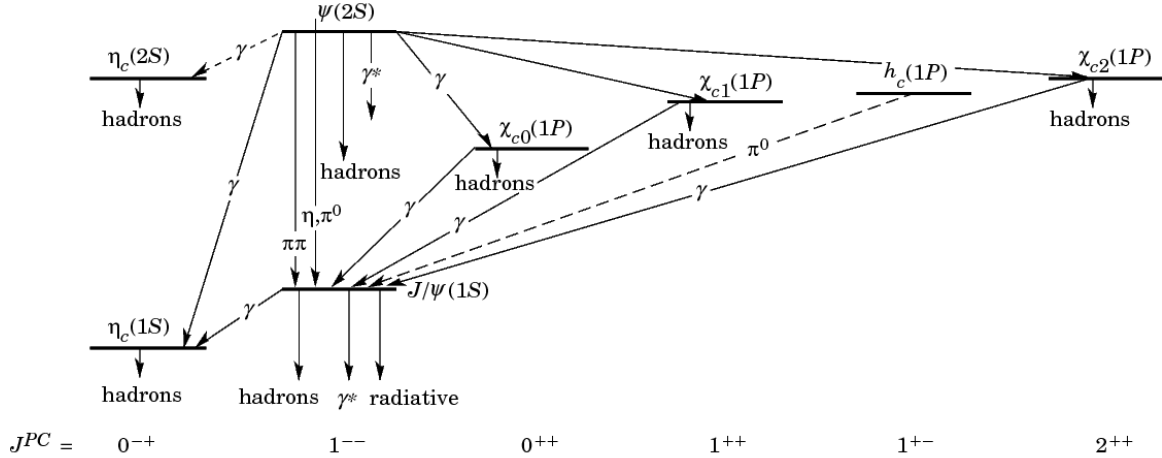


Figure 4.1: Illustration of the different charmonium decays to lower mass charmonium states. The dashed (solid) lines represent radiative (hadronic) decays. Figure taken from Ref. [191].

Charmonium	Branching ratio [%]		
	$\mu^+\mu^-$	e^+e^-	hadrons
J/ψ	5.961 ± 0.033	5.971 ± 0.032	87.7 ± 0.5
$\psi(2S)$	0.80 ± 0.06	0.793 ± 0.017	97.86 ± 0.13

Table 4.2: Branching ratios for decays of J/ψ and $\psi(2S)$ mesons. Information taken from Ref. [19].

2866 4.1.2 Hadroproduction of charmonia

2867 Charmonia can be produced from various sources including: the initial hard scattering
 2868 (direct), decays of higher mass charmonium states (feed-down), or weak decays of hadrons
 2869 containing bottom quarks. Directly produced charmonium states or those from feed-down
 2870 contributions are known as *prompt*, while charmonium states from b-hadron decays
 2871 are called *nonprompt*. A brief introduction to some of the models used to describe the
 2872 production of charmonia in hadron collisions are presented in the following sub-sections.

2873 **4.1.2.1 Colour singlet model**

2874 The Colour Singlet Model (CSM) was first proposed in 1975 by Einhorn and Ellis [192], to
2875 describe the hadroproduction of χ_c and η_c mesons. It assumes that the quantum numbers
2876 of the $c\bar{c}$ pairs do not change between its production and subsequent hadronisation into
2877 charmonia. As a consequence, the $c\bar{c}$ pair has the same angular momentum, spin and
2878 colour charge as the charmonium state it eventually forms and since all hadrons are
2879 colour singlets, the CSM requires the $c\bar{c}$ pair to be produced in a colour singlet state. The
2880 model also considers charmonia as non-relativistic bound states, neglecting the relative
2881 momentum of the charm quarks inside the charmonium [193]. Under these conditions,
2882 the probability that a colour-singlet $c\bar{c}$ pair becomes a charmonium state is proportional
2883 to the square of the $c\bar{c}$ wave function and its derivatives, evaluated at the origin in
2884 position space. The inclusive cross section of the production of a S-wave charmonium
2885 state Ψ in collisions of hadrons h_A and h_B , is given in the CSM by [194]:

$$\sigma^{\text{CSM}}[h_A h_B \rightarrow \Psi + X] = \sigma[h_A h_B \rightarrow c\bar{c}_{[1]} + X] \cdot |\psi_{c\bar{c}}(0)|^2 \quad (4.1)$$

2886 where $\sigma[h_A h_B \rightarrow c\bar{c}_{[1]} + X]$ is the hadroproduction cross section of a colour-singlet $c\bar{c}$
2887 pair, and $\psi_{c\bar{c}}$ is the corresponding $c\bar{c}$ wave function. The main advantage of the CSM is
2888 that it becomes fully predictive once the magnitudes of the $c\bar{c}$ wave functions are fixed,
2889 since it does not contain any other free parameters. The $|\psi_{c\bar{c}}(0)|^2$ can be determined from
2890 experimental measurements of charmonium decay widths or using potential models of
2891 the $c\bar{c}$ system [195].

2892 The CSM has been able to describe the bulk production of charmonia at RHIC [196],
2893 but it significantly underestimates the p_T -differential cross section of prompt charmonia
2894 measured in $p\bar{p}$ collisions at Tevatron [197]. Moreover, the model suffers from infrared
2895 divergences when extending the calculations to charmonium states with nonzero orbital
2896 angular momentum (e.g. χ_c meson) [198]. However, the inclusion of NLO and NNLO
2897 corrections in α_s improves the agreement with the experimental results [195].

2898 **4.1.2.2 Colour evaporation model**

2899 The Colour Evaporation Model (CEM) is an alternative model of charmonium production,
2900 introduced by Harald Fritz [199] and Francis Halzen [200] in 1977. Contrary to the
2901 CSM, the CEM allows the quantum states of the $c\bar{c}$ pair to change during its evolution.
2902 In the CEM, a charmonium state can be produced from any $c\bar{c}$ pair with an invariant
2903 mass between the threshold to create a charm-quark pair $2m_c$ and the one to produce

the lightest pair of open-charm hadrons $2m_D$ (i.e. D-meson pair). The CEM does not impose any constraints on the colour charge of the $c\bar{c}$ pair in order to form a charmonium state, and instead assumes that the colour state of the $c\bar{c}$ pair is neutralised via soft gluon interactions with the collision-induced medium after its production (this process is called colour evaporation). In addition, the interaction with the medium is assumed to randomise the spin and angular-momentum states of the $c\bar{c}$ pairs, making the CEM insensitive to the polarization of charmonia. The probability that $c\bar{c}$ pairs, with an invariant mass below $2m_D$, hadronise into a charmonium state is represented by a fraction F_ψ , which is assumed to be constant and universal (i.e. does not depend on the $c\bar{c}$ kinematics or the hard process) [198]. In the CEM, the hadronic cross section for the production of a charmonium state ψ is defined as:

$$\sigma^{\text{CEM}}[h_A h_B \rightarrow \psi + X] = F_\psi \int_{2m_c}^{2m_D} dm_{c\bar{c}} \frac{d\sigma[h_A h_B \rightarrow c\bar{c} + X]}{dm_{c\bar{c}}} \quad (4.2)$$

where $m_{c\bar{c}}$ is the invariant mass of the $c\bar{c}$ pair, and $\sigma[h_A h_B \rightarrow c\bar{c} + X]$ is the hadronic cross section of the production of $c\bar{c}$ pairs, averaged over all spin, angular-momentum and colour-charge states. The only free parameters of the CEM are the fractions F_ψ , which are constrained with experimental data. The description of the p_T distribution of charmonia requires to consider contributions from at least NLO, which includes $c\bar{c}$ -pair production associated with gluons or light (anti-)quarks [201].

The CEM has been successful at describing the overall hadronic production of charmonium states [202], but it fails to explain the differences observed between the hadroproduction and photoproduction measurements [198], and the relative production rates between the χ_{c1} and χ_{c2} states measured at Tevatron [203] and LHC [204]. Recent developments have lead to an improved version of the CEM [205], which attempts to describe the p_T -dependence of charmonium polarization by sorting the states based on their spin.

4.1.2.3 Nonrelativistic QCD

NonRelativistic QCD (NRQCD) is an effective quantum field theory formulated in 1992 by Geoffrey Bodwin, Eric Braaten and Peter Lepage [206], in an attempt to cure the infrared divergences present in the CSM calculations of P-wave charmonium states. The production and decay of charmonia involve large momentum scales, such as the charm-quark mass ($m_c = 1.29 \text{ GeV}/c^2$) or the parton momentum scales during the hard scattering, which are much larger than $\Lambda_{\text{QCD}} \approx 255 \text{ MeV}$. As a result, the α_s value

associated to the formation of $c\bar{c}$ pairs are small enough ($\alpha_s(m_c) \approx 0.25$) for perturbation theory to be applied. However, the hadronisation of $c\bar{c}$ pairs to charmonium states involves low-momentum processes which are inherently nonperturbative [198].

The NRQCD formalism makes use of perturbative calculation techniques by separating the high-momentum (short-distance) perturbative effects ($c\bar{c}$ -pair production) from the low-momentum (long-distance) nonperturbative effects (charmonium formation), in a process called factorisation. The NRQCD factorisation approach matches the derivations from full QCD at momentum scales less than $m_c v_c$, where v_c is the mean velocity of bound charm quarks in the charmonium CM frame. Since v_c is low for charmonia ($v_c^2 \approx 0.3$), the NRQCD calculations are simplified by applying nonrelativistic approximations [198]. The inclusive cross section for the production of a charmonium state ψ with $p_T \geq m_c$, from collisions of hadrons h_A and h_B , is determined in NRQCD by:

$$\sigma^{\text{NRQCD}} [h_A h_B \rightarrow \psi + X] = \sum_n \sigma [h_A h_B \rightarrow c\bar{c}_{[n]} + X] (\mu_\Lambda) \cdot \langle \mathcal{O}_n^\psi \rangle \quad (4.3)$$

where μ_Λ is an ultraviolet cutoff parameter. The nonperturbative coefficient $\langle \mathcal{O}_n^\psi \rangle$, called Long-Distance Matrix Element (LDME), is the vacuum expectation value of the NRQCD four-fermion operator \mathcal{O}_n^ψ and defines the probability for a $c\bar{c}$ pair in a given quantum state n to evolve into a charmonium state ψ . The LDMEs contain the nonperturbative components related to the hadronisation of the $c\bar{c}$ pairs into charmonia. These matrix elements are process independent and can be constrained by fitting experimental data [198]. Moreover, the perturbative coefficient $\sigma [h_A h_B \rightarrow c\bar{c}_{[n]} + X]$ represents the hadronic cross section for the production of $c\bar{c}$ pairs in a quantum state n and can be computed using pQCD. One important remark of NRQCD is that the $c\bar{c}$ pairs are not required to be produced with the same spin, angular momentum and colour charge as the charmonium states that they eventually hadronise to. As a consequence, the $c\bar{c}$ pairs can either be produced in a colour-singlet or colour-octet state [198]. Examples of Feynman diagrams involved in the production of J/ψ mesons from colour-singlet or colour-octet $c\bar{c}$ pairs are shown in Figure 4.2.

In practice, the sum over the quantum states shown in Eq. (4.3) is expanded in terms of v_c and α_s . The infinite number of independent matrix elements is then reduced to a finite set of LDMEs by truncating the sum up to a given order in v_c and making use of spin symmetry relations between charmonium states. At leading order in v_c , the S-wave charmonium multiplets (e.g. J/ψ and η_c) are described by four LDMEs (one colour singlet and three colour octet) [198], and the CSM can then be recovered by keeping only the colour-singlet term.

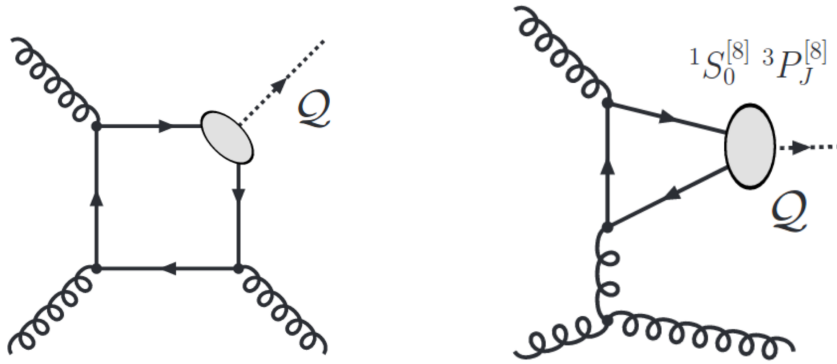


Figure 4.2: Illustration of a colour-singlet (left) and colour-octet (right) Feynman diagram, at leading order (α_s^3), that contributes to the production of quarkonium states. Diagrams taken from Ref. [207].

NRQCD has been very successful at describing the hadroproduction yield of charmonia at Tevatron, RHIC and LHC [208–211]. However, it fails to describe the J/ψ -meson polarization results in hadronic collisions at the Tevatron [212] and LHC [213]. In addition, recent measurements of prompt J/ψ mesons in jets produced in p-p collisions at $\sqrt{s} = 5.02 \text{ TeV}$ [214, 215], have shown significant deviations from the NRQCD calculations derived with the PYTHIA generator.

4.1.2.4 Charmonium production from b-hadron decays

The decay of b-hadrons constitute an important contribution to the production of charmonia. Bottom quarks are copiously produced at the LHC, mainly through the gluon fusion process ($g + g \rightarrow b + \bar{b} + X$). They hadronise to B mesons and b baryons (e.g. Λ_b and Σ_b baryons), which can then decay weakly into charmonia as shown in Figure 4.3. The branching ratios for inclusive decays of b hadrons (h_b) into charmonia, $BR(h_b \rightarrow \psi + X)$, has been determined by combining the measurements of b baryons and B mesons, performed at LHC, LEP, Tevatron and SppS, and are listed in Table 4.3.

The inclusive cross section of charmonium production from b-hadron decays in p-p collisions is described by:

$$\sigma[\text{pp} \rightarrow b + X \rightarrow \psi + X'] = \sum_{j=b \text{ hadrons}} \sigma[\text{pp} \rightarrow b + X] \otimes D(b \rightarrow h_b^j) \cdot BR(h_b^j \rightarrow \psi + X) \quad (4.4)$$

where $\sigma[\text{pp} \rightarrow b + X]$ is the total production cross section of bottom quarks in p-p collisions and $D(b \rightarrow h_b^j)$ is a fragmentation function (FF), which describes the probability that a bottom quark hadronises into a b hadron h_b^j with a fraction z of its momentum

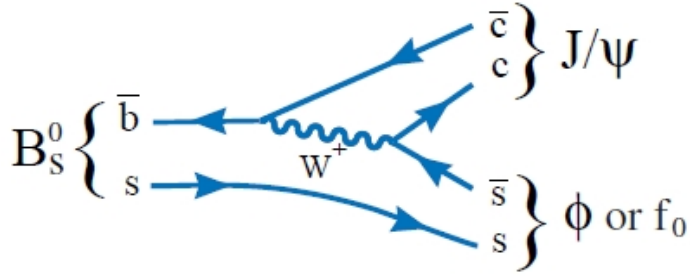


Figure 4.3: Feynman diagram of a B_s^0 decay to J/ψ meson. Diagram taken from Ref. [216].

Charmonium state	Branching ratio [%]
$\eta_c(1S)$	4.5 ± 1.9
J/ψ	1.16 ± 0.10
χ_{c0}	1.5 ± 0.6
χ_{c1}	1.4 ± 0.4
χ_{c2}	0.62 ± 0.29
$\psi(2S)$	0.286 ± 0.028

Table 4.3: Branching ratios for inclusive charmonium decays of b-hadron mixtures ($B^\pm/B^0/B_s^0/b$ -baryon) determined from measurements at LHC, LEP, Tevatron and SppS. Information taken from Ref. [19].

2987 ($p_{h_b} = z \cdot p_b$). The FFs are considered universal and can be extracted by fitting experi-
 2988 mental data. The bottom-quark fragmentation fractions for different b hadrons have
 2989 been measured at LEP and Tevatron, and the results are shown in Table 4.4.

b hadron	Fragmentation fraction [%]	
	$Z \rightarrow b\bar{b}$	$p\bar{p} \rightarrow b\bar{b} + X$
B^+	41.5 ± 0.8	32.4 ± 2.1
B^0	41.5 ± 0.8	32.4 ± 2.1
B_s^0	8.8 ± 1.3	10.1 ± 1.5
b baryons	8.9 ± 1.2	21.8 ± 4.7

Table 4.4: Fragmentation fractions of bottom quarks into b hadrons measured at Tevatron in $p\bar{p}$ collisions at $\sqrt{s} = 1.96$ TeV and at LEP in $Z \rightarrow b\bar{b}$ decays. Information taken from Ref. [19].

2990 4.1.3 Charmonia in heavy-ion collisions

2991 The observed yields of charmonia are modified in heavy-ion collisions by an interplay
 2992 of different effects that can take place in the initial or final state of the collision. The
 2993 effects that originates from the nuclear environment are often called cold nuclear matter
 2994 (CNM) effects, while those that are caused by the hot and dense medium formed in the
 2995 collision, the QGP, are known as hot nuclear matter (HNM) effects.

2996 4.1.3.1 Cold nuclear matter effects

2997 Understanding the impact of the cold nuclear matter effects is crucial to be able to char-
 2998 acterise the hot medium produced in heavy-ion collisions. The charmonium production
 2999 can be affected by several CNM effects, such as nuclear absorption, gluon shadowing,
 3000 energy loss and Cronin effect.

3001 **Nuclear absorption.** After the $c\bar{c}$ pairs are formed, they will then travel across the
 3002 nucleus. While crossing the nuclear medium, the $c\bar{c}$ pair may scatters with the target
 3003 nucleons. After successive interactions, the $c\bar{c}$ pair can end up breaking up and the charm
 3004 quarks then hadronise into open-charm mesons. This process is known as nuclear ab-
 3005 sorption. The probability that the $c\bar{c}$ pair survives the nuclear interactions is determined
 3006 using a Glauber model approach, given by [194]:

$$S_{\text{abs}} = \int d^2 b \int dz \cdot \rho_A(b, z) \cdot \exp \left[- \int_z^{\text{inf}} dz' \cdot \rho_A(b, z') \cdot \sigma_{\text{abs}}(z' - z) \right] \quad (4.5)$$

3007 where b is the impact parameter of the collision, ρ_A is the density profile of the
 3008 nucleus, z is the position of the $c\bar{c}$ pair production vertex along the beam direction, and
 3009 σ_{abs} is an effective cross section used to characterise the nuclear absorption.

3010 To determine the impact of the nuclear absorption on the production of charmonia,
 3011 it is useful to compare the collision time (τ_{coll}) to the typical time needed to form a
 3012 charmonium state (τ_ψ). The collision time is defined as the time it takes for two Lorentz-
 3013 contracted nuclei to cross, given by $\tau_{\text{coll}} = 2R/\gamma_{\text{CM}}$ [217], where $\gamma_{\text{CM}} = \sqrt{s_{\text{NN}}}/m_p$ is the
 3014 beam Lorentz γ factor in the CM frame, $m_p = 938 \text{ MeV}$ is the proton mass and R is the
 3015 radius of the nuclei ($\approx 6.62 \text{ fm}$ for a Pb nucleus [218]). Considering Pb-Pb collisions at
 3016 $\sqrt{s_{\text{NN}}} = 5.02 \text{ TeV}$, the collision time is less than $0.003 \text{ fm}/c$ which is much smaller than
 3017 the formation time of charmonia ($\tau_\psi \sim 0.4 \text{ fm}/c$) [194]. As a consequence, the charmonium
 3018 suppression due to nuclear absorption is expected to be negligible at the LHC.

3019 **Gluon shadowing.** At the LHC, the dominant production mode of $c\bar{c}$ pairs is the gluon
 3020 fusion process ($g+g \rightarrow \psi+X$), due to the large amount of gluons produced at high energies.
 3021 As a result, the charmonium production is sensitive to the nuclear modifications of the
 3022 gluon PDFs in heavy-ion collisions. The momentum fraction x of the two partons involved
 3023 depends, at leading order, on the charmonium mass m_ψ , the energy per nucleon $\sqrt{s_{NN}}$
 3024 and the charmonium rapidity y , according to $x = m_\psi \cdot e^{\pm y} / \sqrt{s_{NN}}$. In Pb-Pb collisions at
 3025 $\sqrt{s_{NN}} = 5.02$ TeV, the x -range probed by the production of charmonia in the CMS rapidity
 3026 coverage ($|y| < 2.4$) is $x < 10^{-2}$, which corresponds to the shadowing region. The EPPS16
 3027 and nCTEQ15 nuclear modifications of the gluon PDFs, evaluated at $Q = 3.16$ GeV, are
 3028 shown in Figure 4.4. The central value points to a depletion of the gluon nuclear PDFs
 3029 of the order of 20% at $x < 10^{-2}$, which should lead to a suppression of the charmonium
 3030 production. However, the nuclear PDFs are currently not constraint enough to provide
 3031 precise calculations of the impact of gluon shadowing at low x .

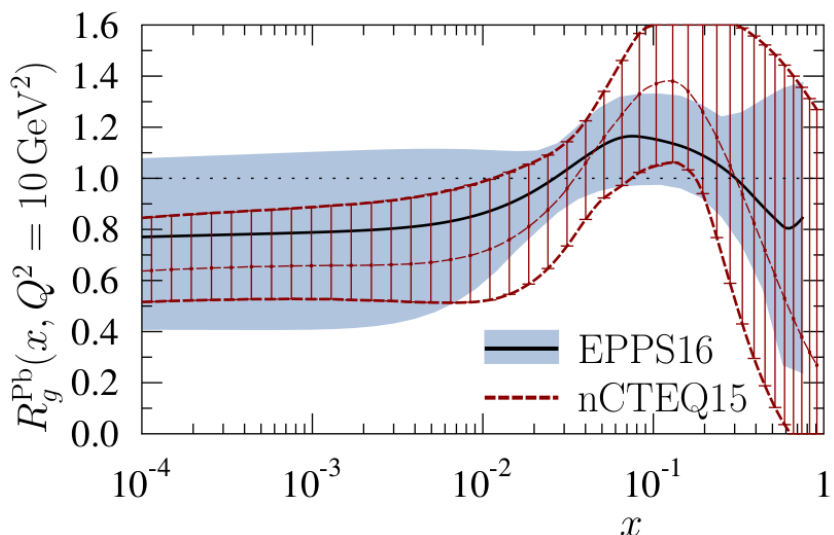


Figure 4.4: Gluon nuclear PDF modification factor determined with EPPS16 (black curve with blue band) and nCTEQ15 (red curves with hatching) nPDF calculations at $Q^2 = 10$ GeV 2 . Figure taken from Ref. [158].

3032 **Energy loss and Cronin effect.** When high-energy partons traverse the nuclear
 3033 medium, they lose energy through gluon radiation induced by multiple scatterings in
 3034 the target nucleus, before or after the hard interaction. It has been proposed by Arleo et
 3035 al [219–221], that if the formation time of the radiated gluon is much larger than the
 3036 size of the nucleus, the gluon radiation becomes coherent (i.e. the radiated gluon would

3037 see the nucleus as a whole), losing momentum along its direction. The coherent energy
3038 loss is proportional to the energy of the incident particle E and it effectively decreases
3039 the rapidity of the hard particle.

3040 Moreover, as high-energy partons undergo elastic scatterings in the nucleus, they
3041 gain transverse momentum in the process. As a consequence, the average partonic $\langle p_T^2 \rangle$
3042 (known as p_T -broadening) increases proportionally to the number of scattering centres
3043 encountered in the medium. These leads to an enhancement of the particle yields at
3044 intermediate p_T (< 10 GeVc). This effect was discovered in 1974 by Cronin et al, in
3045 proton-tungsten collisions [222], and it is known as the Cronin effect.

3046 The ALICE collaboration has measured the nuclear modification factor of J/ψ mesons
3047 in p -Pb collisions at $\sqrt{s_{NN}} = 5.02$ TeV [223]. The results are shown in Figure 4.5 as a
3048 function of p_T and compared to theory calculations including energy loss with (light
3049 green band) and without (dark green band) EPS09 nuclear PDFs. The theory calcula-
3050 tions considering energy loss and gluon shadowing are found to be consistent with the
3051 measurements at $p_T > 2$ GeV/c, while those with only energy loss effects overestimate the
3052 results in the central and forward rapidity regions. Regarding the low p_T and forward
3053 region, the theory calculations expect a larger suppression of J/ψ mesons than what is
3054 observed in the measurements.

3055 4.1.3.2 Hot nuclear matter effects

3056 Charmonia are considered important probes of the QGP since they are produced in the
3057 initial hard scattering and experience the full evolution of the medium. The presence
3058 of the deconfined medium is expected to dissociate the charmonium states through
3059 a process called colour-charge screening, which can occur sequentially depending on
3060 the medium temperature and the charmonium binding energies. In addition, the large
3061 abundance of charm quarks at the LHC can lead to a recombination of uncorrelated
3062 charm quarks, enhancing the charmonium yields.

3063 **Colour-charge screening.** In the presence of the QGP, the binding potential of char-
3064 monia is screened by the colour charges of the surrounding quarks in the medium.
3065 These mechanism was first proposed in 1986 by Matsui and Satz [75]. The colour-charge
3066 screening is described through a Debye screening radius $r_D(T) \propto 1/T$, which decreases
3067 for larger temperatures T of the medium. If the Debye screening radius becomes smaller
3068 than the radius of a given charmonium state, the charm quarks are no longer able

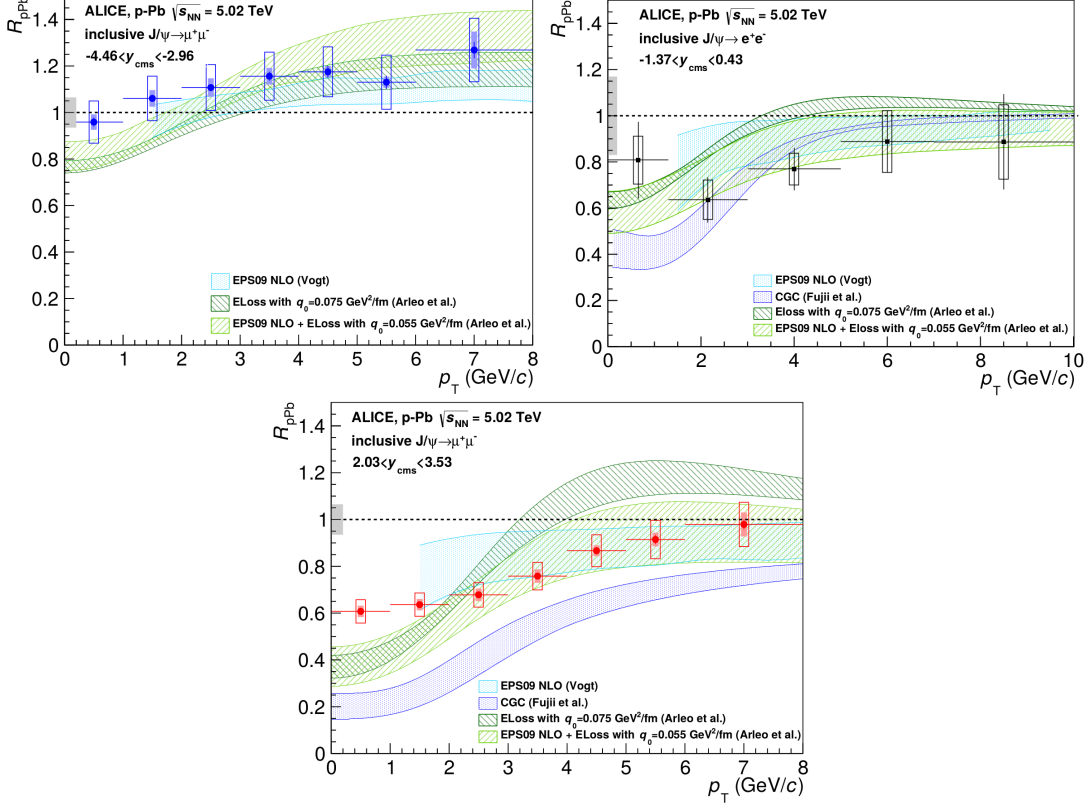


Figure 4.5: Nuclear modification factor of J/ψ mesons as a function of p_T in the backward (top-left), mid (top-right) and forward (bottom) rapidity regions. The bars (boxes) represent the statistical (systematic) uncertainties, while the gray box at unity indicate the size of the global uncertainty. The results are compared to nPDF (EPS09), energy loss (Arleo et al.), and gluon saturation (CGC) calculations. Figure taken from Ref. [223].

3069 to maintain the bound state and the $c\bar{c}$ pair dissociates. The $c\bar{c}$ binding potential $V_{c\bar{c}}$,
3070 including the colour-charge screening effect, can be expressed as:

$$V_{c\bar{c}}(r, T) = -\frac{a}{r} \exp \left[\frac{-r}{r_D(T)} \right] + b \cdot r_D(T) \left(1 - \exp \left[\frac{-r}{r_D(T)} \right] \right) \quad (4.6)$$

3071 where if $r_D \rightarrow \infty$ (i.e. no screening, $T = 0$), one recovers the Cornell potential shown
3072 in Eq. (1.17). On the other hand, if $r_D \rightarrow 0$, the $c\bar{c}$ binding potential becomes zero and
3073 the charm quarks are no longer confined. At the hadronisation stage, the deconfined
3074 charm quarks predominantly bind with light quarks, forming open-charm mesons and
3075 reducing the charmonium yields in the process.

3076 Since the charmonium radius increases for higher excited states, as shown in Ta-
3077 ble 4.5, it is expected that $\psi(2S)$ mesons will dissociate at lower medium temperatures
3078 compared to J/ψ mesons, leading to a sequential suppression pattern. These effect can be

3079 quantified by comparing the nuclear modification factor of $\psi(2S)$ mesons to the one of
 3080 J/ψ mesons.

Charmonium state	Binding energy [GeV]	Radius [fm]
J/ψ	0.64	0.25
$\chi_c(1P)$	0.20	0.36
$\psi(2S)$	0.05	0.45

Table 4.5: Binding energy and radius of J/ψ , $\chi_c(1P)$ and $\psi(2S)$ mesons. Information taken from Ref. [194].

3081 **Charmonium regeneration.** The charm-quark total cross section is large at the
 3082 LHC, leading to an abundant production of charm and anti-charm quarks (up to 100
 3083 $c\bar{c}$ pairs in a central collision), which may combine to produce a charmonium state.
 3084 This additional source of charmonium production is expected to enhance the nuclear
 3085 modification factor of charmonia. Since the thermal production of charm quarks (i.e.
 3086 produced in the medium) is negligible, due to their large mass, the recombined $c\bar{c}$ pairs
 3087 are mainly formed by charm quarks produced in the hard scattering. This recombination
 3088 mechanism, commonly known as charmonium regeneration, can be described using
 3089 a statistical model [224, 225], where the charm quarks are recombined during the
 3090 hadronisation stage. Alternatively, the regeneration of charmonia can also be described
 3091 using transport models [226], where the charmonium states are continuously dissociating
 3092 and regenerating throughout the evolution of the QGP. Since the uncorrelated charm
 3093 quarks are required to be close in phase space, to be able to form a charmonium state,
 3094 the regeneration mechanism mainly plays a role at low charmonium p_T and narrow
 3095 rapidities.

3096 4.1.3.3 Current understanding

3097 The suppression and regeneration of quarkonia, as a possible signature of the QGP, was
 3098 briefly discussed in Section 1.2.4.4. As was mentioned there, an anomalous suppression
 3099 of J/ψ and $\psi(2S)$ mesons in central collisions was already observed at SPS at $\sqrt{s_{NN}} =$
 3100 17.3 GeV [78, 227], which could not be explained considering only CNM effects. Later,
 3101 measurements performed at RHIC at $\sqrt{s_{NN}} = 200 \text{ GeV}$ [80] showed similar levels of J/ψ -
 3102 meson suppression at mid-rapidity and stronger suppression at forward rapidity. Two
 3103 explanations were proposed to describe the results at RHIC: the first one suggested that
 3104 contributions from regenerated J/ψ mesons could accommodate the agreement observed

3105 between RHIC and SPS, while the second one was able to describe the differences
3106 seen between forward and mid-rapidity taking into account nPDF effects and nuclear
3107 absorption.

3108 The production of J/ψ mesons has been measured at the LHC in Pb-Pb collisions at
3109 $\sqrt{s_{NN}} = 2.76\text{TeV}$. The general feature observed among the different LHC experiments
3110 is a strong suppression of charmonia ($R_{AA} << 1$) in central collisions consistent with
3111 colour-charge screening. In addition, the ALICE collaboration has reported a weaker
3112 suppression of J/ψ mesons in particular at low p_T compared to RHIC measurements [84],
3113 which has been attributed to J/ψ -meson regeneration. Measurements in p-Pb collisions
3114 have also been performed at the LHC, which are found to be consistent with calculations
3115 including nuclear modifications of the PDFs and/or energy loss. However, the exact
3116 contributions of the various hot and cold nuclear matter effects are difficult to asses,
3117 specially due to the large uncertainties on the gluon nuclear PDFs and the limited
3118 statistical precision of the data. As a result, more precise and differential measurements
3119 are needed, both to constrain the models and to disentangle the different contributions
3120 that play a role in heavy-ion collisions.

3121 As for bottomonia, measuring the excited states could bring important information.
3122 The CMS collaboration has reported the nuclear modification of $\psi(2S)$ mesons relative to
3123 J/ψ mesons in Pb-Pb collisions at $\sqrt{s_{NN}} = 2.76\text{TeV}$ [228]. The results of the double ratio
3124 of $\psi(2S)$ over J/ψ yields, $(N_{\psi(2S)}/N_{J/\psi})_{\text{Pb-Pb}}/(N_{\psi(2S)}/N_{J/\psi})_{\text{pp}}$, are presented as a function
3125 of $\langle N_{\text{part}} \rangle$ in Figure 4.6. The $\psi(2S)$ mesons are observed to be more suppressed than
3126 J/ψ mesons at high $p_T (> 6.5 \text{ GeV}/c)$ in the mid-rapidity region, consistent with the
3127 sequential suppression scenario. On the contrary, in the forward rapidity region and
3128 moderate p_T range ($3 < p_T < 30 \text{ GeV}/c$), the $\psi(2S)$ mesons are found to be less suppressed
3129 than J/ψ mesons in the most central Pb-Pb collisions, which was unexpected at the
3130 time and still not fully understood. However, a similar measurement performed by
3131 the ALICE collaboration in central Pb-Pb collisions [229], extending down to $p_T =$
3132 $0 \text{ GeV}/c$, points to a larger $\psi(2S)$ -meson suppression than for J/ψ mesons. Transport
3133 model calculations [230] have attempted to explain the results by arguing that $\psi(2S)$
3134 and J/ψ mesons are regenerated at different stages of the QGP evolution, leading to
3135 possible weaker suppression of $\psi(2S)$ relative to J/ψ mesons, depending on the region of
3136 phase space they are probed.

3137 The measurements of the charmonium production in Pb-Pb collisions at $\sqrt{s_{NN}} =$
3138 5.02TeV , presented in the following sections, benefits from a larger integrated luminosity
3139 ($\times 2$) and higher energy compared to the Pb-Pb measurements at $\sqrt{s_{NN}} = 2.76\text{TeV}$. This

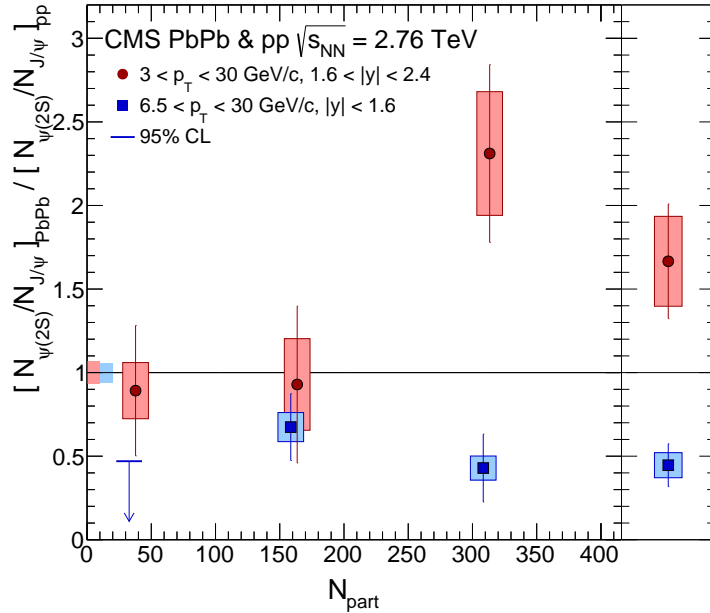


Figure 4.6: Double ratio of $\psi(2S)$ over J/ψ yields as a function of $\langle N_{\text{part}} \rangle$, in the mid-rapidity (blue squares) and forward rapidity (red circles) regions. The results integrated in centrality are shown at the rightmost edge. The bars (boxes) represents the statistical (systematic) uncertainties, while the boxes at unity indicate the uncertainties on the p-p measurements. Figure taken from Ref. [228].

3140 allows to extend the p_T reach of the measurements, increase the precision of the results
 3141 and perform more differential studies.

3142 4.2 Analysis

3143 In this section, two related analyses of the charmonium production in p-p and Pb-Pb
 3144 collisions at $\sqrt{s_{\text{NN}}} = 5.02 \text{ TeV}$, are described. The measurements are performed in the
 3145 $\mu^+ \mu^-$ decay channel using data recorded with the CMS detector. In both of the analy-
 3146 ses, I made significant contributions in the signal extraction, acceptance studies and
 3147 determination of the systematic uncertainties related to the fitting procedure.

3148 The first analysis [231] studies the modification of the prompt and nonprompt J/ψ
 3149 meson production in Pb-Pb compared to p-p collisions at the same energy. To accomplish
 3150 this, the nuclear modification factor of J/ψ mesons is measured in different collision
 3151 centrality bins, and J/ψ -meson p_T and rapidity (y) ranges. The second analysis [232]
 3152 probes the nuclear modification of $\psi(2S)$ mesons relative to J/ψ mesons, by measuring
 3153 the double ratio of $\psi(2S)$ over J/ψ yields in Pb-Pb relative to p-p collisions, defined as:

$$\rho^{\psi(2S)/J/\psi} = \frac{(N_{\psi(2S)}/N_{J/\psi})_{\text{PbPb}}}{(N_{\psi(2S)}/N_{J/\psi})_{\text{pp}}} \quad (4.7)$$

3154 One advantage of measuring the double ratio of charmonium yields is that the
3155 acceptance and efficiency of the two charmonium states cancels in the ratio due their
3156 similar masses and production mechanisms. For this reason, as well as the limited
3157 statistics of the $\psi(2S)$ mesons compared to J/ψ mesons, the second analysis was published
3158 first and relatively fast after the data was taken, while the first analysis was more
3159 elaborate and required more time to complete.

3160 The p-p and Pb-Pb datasets employed are introduced in Section 4.2.1, while the
3161 charmonium simulations are listed in Section 4.2.2 and the event selection is presented
3162 in Section 4.2.3. The procedure used to extract the prompt and nonprompt J/ψ -meson
3163 yields is explained in Section 4.2.4 and the extraction of the single ratios of $\psi(2S)$ over
3164 J/ψ meson yields is detailed in Section 4.2.5. The charmonium efficiency and acceptance
3165 are derived in Section 4.2.6. Section 4.2.7 and Section 4.2.8 report the systematic uncer-
3166 tainties associated to the measurement of the J/ψ -meson yields and the double ratio of
3167 charmonium yields, respectively.

3168 4.2.1 Dataset

3169 The measurement of the nuclear modification of $\psi(2S)$ and J/ψ mesons is performed
3170 using data recorded in 2015 by the CMS detector, in p-p and Pb-Pb collisions at $\sqrt{s_{\text{NN}}} =$
3171 5.02 TeV. The main datasets employed in the analyses, called *DoubleMu0* for p-p and
3172 *HIONiaDoubleMu0* for Pb-Pb, consist of events selected by the CMS trigger system,
3173 requiring the presence of at least two L1 muon candidates. An additional dataset selecting
3174 also L1 double muon events, referred as *HIONiaPeripheral30100*, is employed to measure
3175 the charmonium production in peripheral Pb-Pb collisions (centrality range 30 – 100%),
3176 since it accumulated more integrated luminosity than HIONiaDoubleMu0¹.

3177 The p-p and Pb-Pb datasets were reconstructed with CMSSW 7.5.8, making use of
3178 the standard p-p and heavy-ion specific reconstruction algorithms employed during the
3179 data-taking period, respectively. After a meticulous check of the quality of the data by
3180 the CMS collaboration, the content of the datasets were filtered excluding events in
3181 which the tracker or the muon system were not operating in proper conditions. The total
3182 integrated luminosity of the data samples is presented in Table 4.6.

¹The data rate of HIONiaDoubleMu0 was reduced during part of the Pb-Pb run because it exceeded the bandwidth threshold of the Tier-0 computing centre.

System	Primary dataset	Integrated luminosity
Pb-Pb	HIONiaDoubleMu0	$351 \mu b^{-1}$
Pb-Pb	HIONiaPeripheral30100	$464 \mu b^{-1}$
p-p	DoubleMu0	$28 pb^{-1}$

Table 4.6: Total integrated luminosity of each dataset used in the analysis of the charmonium nuclear modification in p-p and Pb-Pb collisions at $\sqrt{s_{NN}} = 5.02 \text{ TeV}$.

3183 4.2.2 Charmonium simulations

3184 The production of $\psi(2S)$ and J/ψ mesons is described using fully reconstructed Monte-
 3185 Carlo simulated samples. The simulations were made separately for charmonia produced
 3186 directly from the hard scattering (prompt J/ψ and $\psi(2S)$ mesons), and for J/ψ mesons
 3187 produced from the decay of b hadrons (nonprompt J/ψ mesons), for both p-p and Pb-Pb
 3188 collisions. The prompt $\psi(2S)$ and J/ψ events were generated with PYTHIA 8.209 [176],
 3189 which models the charmonium production using NRQCD. Regarding the nonprompt
 3190 J/ψ sample, the b hadrons ($B^\pm, B^0, \bar{B}^0, B_s^0, \bar{B}_s^0$ mesons) were decayed with the EVTGEN
 3191 v1.3 [233] package interfaced to PYTHIA 8.209. The CUETP8M1 underlying event PYTHIA
 3192 tune [177, 234] was used in all samples.

3193 Moreover, the underlying environment present in Pb-Pb collisions was first simulated
 3194 with HYDJET 1.9 [235] and then embedded to each PYTHIA signal event, by matching
 3195 the position of the simulated interaction vertex. The full CMS detector response was
 3196 simulated in all charmonium simulations, based on GEANT4 [178], and the p-p and Pb-Pb
 3197 simulated collision events were reconstructed with the corresponding reconstruction
 3198 algorithms used during 2015 data taking.

3199 In addition, the Pb-Pb simulations were produced in several ranges of charmonium
 3200 or B-meson p_T , in order to have similar statistics available in each p_T range. As a
 3201 result, w_{p_T} weights are used for each meson p_T range to combine the different Pb-Pb
 3202 simulations and form a continuous p_T spectrum.

3203 Finally, in order to match the centrality distribution of the signal simulations to what
 3204 is observed in data, each Pb-Pb event is weighed by the average N_{coll} corresponding
 3205 to the centrality range of the simulated collision. The differences between the data
 3206 and simulated centrality distributions are due to the fact that the signal events were
 3207 embedded into minimum bias HYDJET events equally distributed in centrality, while the
 3208 production of charmonium in data is biased towards more central collisions (i.e. scales
 3209 with N_{coll}). Thus, in summary, each Pb-Pb charmonium simulated event is weighed by:

$$w_{\text{MC}} = N^{gen} \frac{w_{p_T} \cdot N_{\text{coll}}}{\sum_{i=1}^{N^{gen}} (w_{p_T}^i \cdot N_{\text{coll}}^i)} \quad (4.8)$$

3210 where the weights are normalised so that their sum is effectively equal to the number
 3211 of generated events. The list of charmonium simulations are summarized in Table 4.7.

Process	Generator	Criteria	Acceptance	Events
$\text{PbPb} \rightarrow J/\psi \rightarrow \mu^+ \mu^-$	PYTHIA +HYDJET	$J/\psi p_T[0,3] \text{ GeV}/c$	2.5×10^{-1}	150659
		$J/\psi p_T[3,6] \text{ GeV}/c$	1.7×10^{-1}	3842575
		$J/\psi p_T[6,9] \text{ GeV}/c$	2.0×10^{-2}	2268977
		$J/\psi p_T[9,12] \text{ GeV}/c$	4.0×10^{-3}	168628
		$J/\psi p_T[12,15] \text{ GeV}/c$	1.2×10^{-3}	155793
		$J/\psi p_T[15,30] \text{ GeV}/c$	7.2×10^{-4}	104729
		$J/\psi p_T[30,\infty] \text{ GeV}/c$	3.3×10^{-5}	47059
		$\psi(2S) p_T[0,3] \text{ GeV}/c$	2.4×10^{-1}	96623
		$\psi(2S) p_T[3,6] \text{ GeV}/c$	2.1×10^{-1}	89880
		$\psi(2S) p_T[6,9] \text{ GeV}/c$	3.1×10^{-2}	98836
$\text{PbPb} \rightarrow \psi(2S) \rightarrow \mu^+ \mu^-$	PYTHIA +HYDJET	$\psi(2S) p_T[9,12] \text{ GeV}/c$	6.4×10^{-3}	102038
		$\psi(2S) p_T[12,15] \text{ GeV}/c$	2.0×10^{-3}	94370
		$\psi(2S) p_T[15,\infty] \text{ GeV}/c$	1.2×10^{-3}	49857
		$B p_T[0,3] \text{ GeV}/c$	2.7×10^{-1}	140257
		$B p_T[3,6] \text{ GeV}/c$	1.5×10^{-1}	5192754
		$B p_T[6,9] \text{ GeV}/c$	5.0×10^{-2}	1786414
$\text{PbPb} \rightarrow B \rightarrow J/\psi \rightarrow \mu^+ \mu^-$	EVTGEN +PYTHIA +HYDJET	$B p_T[9,12] \text{ GeV}/c$	1.0×10^{-3}	165143
		$B p_T[12,15] \text{ GeV}/c$	3.6×10^{-3}	141064
		$B p_T[15,30] \text{ GeV}/c$	2.1×10^{-3}	107742
		$B p_T[30,\infty] \text{ GeV}/c$	1.4×10^{-4}	41803
$\text{pp} \rightarrow J/\psi \rightarrow \mu^+ \mu^-$	PYTHIA		1.0	60830490
$\text{pp} \rightarrow \psi(2S) \rightarrow \mu^+ \mu^-$	PYTHIA		1.0	60830490
$\text{pp} \rightarrow B \rightarrow J/\psi \rightarrow \mu^+ \mu^-$	PYTHIA		1.0	69652510

Table 4.7: Simulations used in the analysis of the charmonium production in Pb-Pb and p-p collisions at 5.02 TeV.

3212 4.2.3 Event selection

3213 The charmonium candidates are reconstructed in the dimuon decay channel (i.e. $J/\psi \rightarrow$
 3214 $\mu^+ \mu^-$ and $\psi(2S) \rightarrow \mu^+ \mu^-$), by pairing opposite-charge muons. Since the J/ψ and $\psi(2S)$
 3215 masses are small ($m_{J/\psi} = 3.097 \text{ GeV}/c^2$ and $m_{\psi(2S)} = 3.686 \text{ GeV}/c^2$), the signal events are
 3216 dominated by the presence of low p_T muons ($\langle p_T^\mu \rangle \sim 1.6 \text{ GeV}/c$), contrary to the W-boson
 3217 analysis reported in Chapter 3. The selection used to identify the charmonium events is
 3218 detailed in this section.

3219 4.2.3.1 Minimum bias event selection

3220 The p-p and Pb-Pb minimum bias events are selected by applying a global event filter
 3221 (GEF) offline to suppress the background events not originating from the inelastic
 3222 hadronic scattering. The GEF for p-p collision events consists of the following filters:

- 3223 • Beam-Scraping filter: Requires at least 25% of tracks in the event to be high quality
 3224 tracks.
- 3225 • Primary Vertex filter: Requires a primary vertex reconstructed from at least two
 3226 tracks, within a longitudinal (transverse) distance of 25 cm (2 cm) of the IP.

3227 In the case of Pb-Pb collisions, since the projectiles are more charged (82 protons
 3228 per Pb ion), the background contribution from electromagnetic interactions between
 3229 Pb beams is significantly enhanced, and as a result a tighter event selection is applied
 3230 including the following filters:

- 3231 • HF coincidence filter: requires at least three towers on each side of the interaction
 3232 point in the HF calorimeter, with an energy deposit per tower of at least 3 GeV.
 3233 This filter rejects events from electronic noise and beam-beam electromagnetic
 3234 interactions.
- 3235 • Cluster compatibility filter: rejects beam-scraping events (i.e. muons produced
 3236 when the beam particles hit the LHC collimators), by requiring that the shape of
 3237 the silicon pixel clusters are compatible with tracks originating from the primary
 3238 vertex.

3239 and the Pb-Pb collision events are also required to contain at least one reconstructed
 3240 primary vertex as done for p-p data. The efficiency of the GEF in Pb-Pb minimum
 3241 bias events has been determined to be $99 \pm 2\%$. This efficiency can surpass 100% due

3242 to the remaining contamination of non-hadronic collisions in the sample. The number
3243 of Pb-Pb minimum bias events passing the GEF corresponds to $N_{\text{MB}} = 2.34 \times 10^9$ for
3244 HIONiaDoubleMu0 and $N_{\text{MB}} = 3.09 \times 10^9$ for HIONiaPeripheral30100.

3245 **4.2.3.2 Trigger**

3246 The events used in the analysis of the charmonium production in p-p and Pb-Pb collisions
3247 were selected by the trigger called HLT_HIL1DoubleMu0, which requires the presence
3248 of two L1 muons (with no muon p_T requirement) in coincidence with a bunch crossing
3249 identified by the BPTX detectors (to suppress contributions from cosmic-ray muons).

3250 In addition, events derived from the dimuon peripheral dataset HIONiaPeripheral-
3251 erial30100 were selected by the trigger HLT_HIL1DoubleMu0_2HF_Cent30100, which re-
3252 quires, in addition to the HLT_HIL1DoubleMu0 trigger conditions, a signal in coincidence
3253 on both sides of the HF detector and a total energy deposit in the HF calorimeters
3254 consistent with a collision centrality between 30% and 100%.

3255 To make sure that each muon employed in the analysis is associated to an online
3256 muon that fired the dimuon triggers, the reconstructed muons are required to be matched
3257 to the corresponding L1 muons within a η - ϕ cone defined as:

$$\Delta R(\mu_{\text{reco}}, \mu_{\text{L1}}) = \sqrt{(\eta_{\text{reco}} - \eta_{\text{L1}})^2 + (\phi_{\text{reco}} - \phi_{\text{L1}})^2} < 0.3 \quad (4.9)$$

3258 **4.2.3.3 Centrality determination in Pb-Pb collisions**

3259 The centrality percentiles of Pb-Pb collisions are derived by sampling the distribution of
3260 the total energy deposited in the HF calorimeters in bins of 0.5% of the total hadronic
3261 cross section. The HF energy distribution is determined in minimum-bias events (i.e.
3262 requiring at least one collision) passing the GEF. The yield as a function of the HF energy
3263 is then corrected for the efficiency of the minimum-bias trigger and the GEF selection.
3264 Figure 4.7 presents the distribution of the total HF energy in Pb-Pb collisions separated
3265 in centrality classes.

3266 Figure 4.8 shows the centrality distribution of the dimuon triggered Pb-Pb dataset.
3267 The selection of hard-probe processes, such as the production of charmonium states, bias
3268 the centrality distribution towards central collisions.

3269 The centrality percentiles are associated with the average geometrical quantities of
3270 the collision (e.g. N_{part} and T_{AA}) using a Glauber MC model as explained in Section 1.2.2.

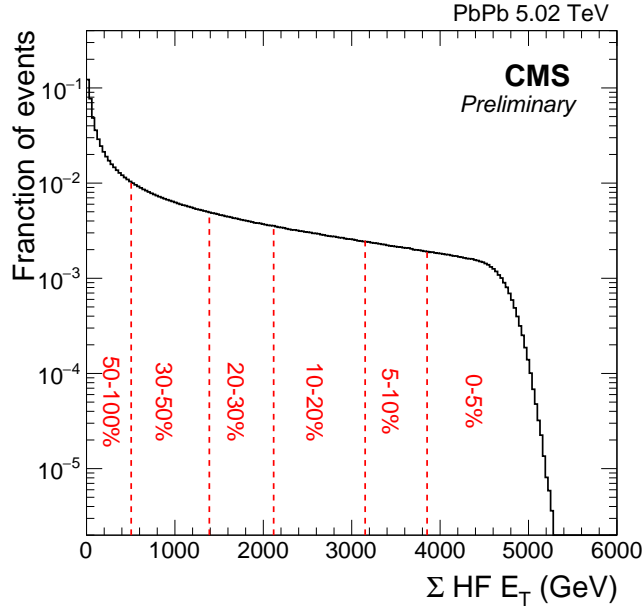


Figure 4.7: Distribution of the total energy deposited in the HF calorimeters in Pb-Pb collisions at 5.02 TeV, for minimum-bias events passing the GEF selection. The different centrality classes are shown. Figure taken from the private Ref. [236].

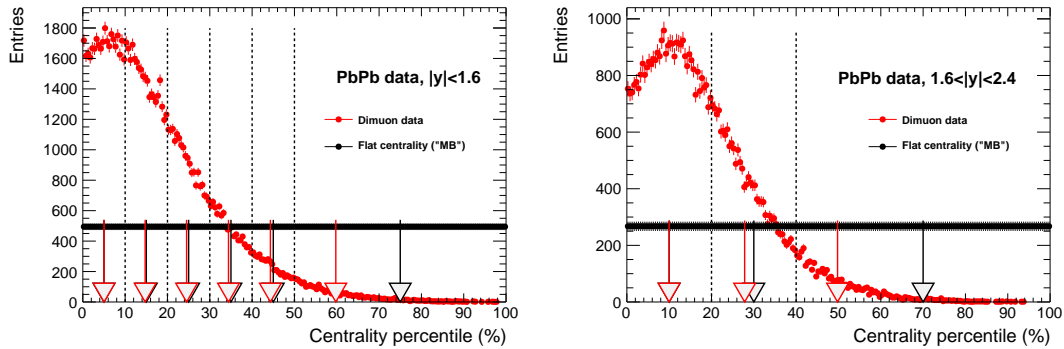


Figure 4.8: Centrality distribution of $\mu^+\mu^-$ events in Pb-Pb collisions passing the GEF cuts (red), with $2.2 < M_{\mu^+\mu^-} < 4.5 \text{ GeV}/c^2$, for $|y| < 1.6$ (left) and $1.6 < |y| < 2.4$ (right). The distribution of the minimum-bias sample, flat by definition, is shown in black. The limits of the centrality bins used for the $\psi(2S)$ analysis are shown as vertical dashed lines, with the most central (peripheral) range on the right (left). The average centrality in each centrality range is also shown as an arrow, in red and black for the dimuon and minimum-bias datasets, respectively.

3271 The centrality intervals used in Pb-Pb collisions and the corresponding average N_{part}
 3272 and T_{AA} values are presented in Table 4.8.

Centrality range [%]	$\langle T_{AA} \rangle$	$\langle N_{\text{part}} \rangle$
0 - 100	5.61+0.16–0.19	114.0+2.6–2.6
0 - 5	25.98+0.47–0.77	384.3+1.8–2.0
5 - 10	20.46+0.38–0.60	333.3+3.0–3.2
10 - 15	16.11+0.35–0.50	285.4+3.5–3.7
15 - 20	12.60+0.32–0.43	242.9+3.8–3.9
20 - 25	9.80+0.31–0.37	205.7+3.9–4.1
25 - 30	7.52+0.29–0.32	172.7+4.0–4.0
30 - 35	5.71+0.27–0.27	144.1+4.0–4.0
35 - 40	4.25+0.23–0.24	118.7+4.0–4.0
40 - 45	3.10+0.19–0.19	96.51+3.8–3.8
45 - 50	2.22+0.16–0.16	77.4+3.7–3.6
50 - 60	1.30+0.12–0.12	53.9+3.2–3.1
60 - 70	0.57+0.07–0.06	30.6+2.6–2.4
70 - 100	0.11+0.02–0.01	8.3+1.0–0.6
0 - 10	23.22+0.43–0.69	358.8+2.4–2.6
10 - 20	14.35+0.33–0.45	264.2+3.6–3.8
20 - 30	8.66+0.29–0.33	189.2+4.0–4.1
30 - 40	4.98+0.24–0.24	131.4+4.0–4.0
40 - 50	2.66+0.18–0.17	87.0+3.7–4.3
50 - 100	0.44+0.05–0.03	21.9+1.8–1.0
10 - 30	11.51+0.30–0.39	226.7+3.7–3.9
30 - 100	1.41+0.09–0.06	46.8+2.4–1.2
0 - 20	18.79+0.37–0.56	311.5+2.9–3.1
20 - 40	6.82+0.26–0.28	160.3+4.0–4.0
40 - 100	0.81+0.07–0.05	32.7+2.1–1.1

Table 4.8: Values of the centrality-integrated number of participants $\langle N_{\text{part}} \rangle$ and nuclear overlap factor $\langle T_{AA} \rangle$, determined in the different collision centrality ranges used in the analysis. Information taken from the private Ref. [236].

3273 4.2.3.4 Muon selection

3274 Muon candidates are identified using a *soft* selection. Contrary to the muon selection
 3275 criteria used in the W-boson analysis, which was optimised for high- p_T muons, the
 3276 *soft* selection has been designed to be highly efficient for muons with low transverse
 3277 momentum ($p_T < 10$ GeV/c). The *soft* selection requires muon candidates to pass the
 3278 following criteria:

- 3279 • The muon track is identified both by the tracker-muon and the global-muon algo-

3280 rithms.

- 3281 • The tracker track extrapolated to the muon system is matched with at least one
3282 muon segment within a distance less than 3σ along the x and y coordinates. Muon
3283 segments are excluded if they have a better match with other tracker tracks.
- 3284 • The muon track includes hits in more than five inner-tracker layers, ensuring a
3285 good p_T measurement.
- 3286 • The muon track has measurements in at least one pixel layer to suppress muons
3287 from decays in flight.
- 3288 • The transverse impact parameter (longitudinal distance) of the muon track is
3289 consistent with the primary vertex within 0.3 cm (20 cm), to reduce the background
3290 from cosmic-ray muons.

3291 **4.2.3.5 Muon kinematic cut**

3292 The single muon kinematic selection is optimised, using the J/ψ meson simulated samples,
3293 by requiring (in different muon $p_T - \eta$ bins) that the number of muon candidates passing
3294 the trigger, reconstruction and identification algorithms is more than 10% of the number
3295 of generated muons. The muon kinematic cuts are described in Eq. (4.10) and shown in
3296 Figure 4.9.

$$\begin{aligned}
 p_T^\mu &> 3.5 \text{ GeV}/c && \text{for } |\eta^\mu| < 1.2 \\
 p_T^\mu &> (5.77 - 1.89 \times |\eta^\mu|) \text{ GeV}/c && \text{for } 1.2 \leq |\eta^\mu| < 2.1 \\
 p_T^\mu &> 1.8 \text{ GeV}/c && \text{for } 2.1 \leq |\eta^\mu| < 2.4
 \end{aligned} \tag{4.10}$$

3297 **4.2.3.6 Charmonium selection**

3298 The $J/\psi \rightarrow \mu^+ \mu^-$ and $\psi(2S) \rightarrow \mu^+ \mu^-$ candidate selection consists of the detection of two
3299 low- p_T muons of opposite electric charge, each passing all identification criteria explained
3300 in Section 4.2.3.4, the kinematic cuts detailed in Section 4.2.3.5, and the trigger matching
3301 condition mentioned in Section 4.2.3.2. Moreover, each dimuon candidate is required to
3302 have a χ^2 probability larger than 1% that the two muons derive from a common vertex.

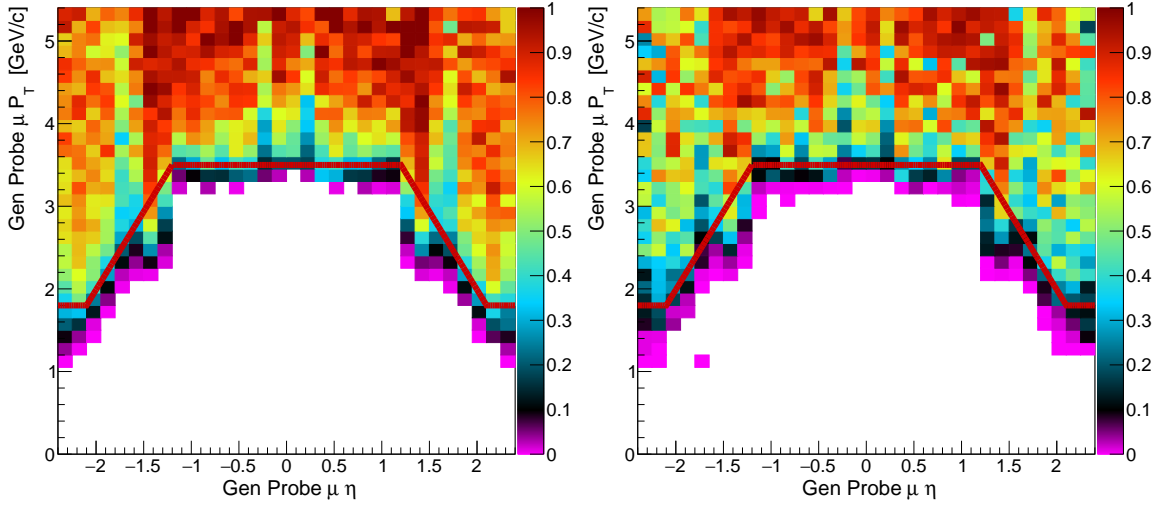


Figure 4.9: Distribution of the ratio of the number of reconstructed, identified and triggered muons over the number of generated muons, as a function of muon p_T and η . The results are derived from the prompt J/ψ simulations corresponding to p-p (left) and Pb-Pb (right) collisions. The red line represents the single muon kinematic cuts.

4.2.4 Extraction of prompt and nonprompt J/ψ mesons

This section describes the procedure used to extract the yields of prompt and nonprompt $J/\psi \rightarrow \mu^+ \mu^-$ candidates in p-p and Pb-Pb collision data. Considering the large lifetime of b hadrons ($\tau_B \sim 1.5$ ps), the prompt and nonprompt J/ψ mesons are distinguished by virtue of the pseudoproper-decay length $\ell_{J/\psi}$, determined from the displacement between the primary collision and secondary $\mu^+ \mu^-$ vertices, as detailed in Section 4.2.4.1.

The J/ψ -meson yields are extracted by performing a two-dimensional unbinned-maximum likelihood fit to the $\mu^+ \mu^-$ invariant mass ($m^{\mu\mu}$) and $\ell_{J/\psi}$ distributions (hereafter referred as 2D fit), performed with the RooFit framework [184]. The expression of the total functional form $F(m^{\mu\mu}, \ell_{J/\psi})$, used in the 2D fit, is defined as:

$$F(m^{\mu\mu}, \ell_{J/\psi}) = \sum_{i=J/\psi, \text{bkg}} N_i \cdot M_i(m^{\mu\mu}) \cdot D_i(\ell_{J/\psi}) \otimes R_i(\ell_{J/\psi}) \quad (4.11)$$

where \otimes represents a convolution with respect to the $\ell_{J/\psi}$ variable, $N_{J/\psi}$ is the number of inclusive J/ψ mesons (i.e. including prompt and nonprompt J/ψ mesons), N_{bkg} is the number of background dimuons, $R_{J/\psi}$ (R_{bkg}) represents the $\ell_{J/\psi}$ resolution of signal (background) dimuons, and M_i and D_i are the $m^{\mu\mu}$ and $\ell_{J/\psi}$ functional forms for each event source, respectively.

3318 The 2D fits are done in four rapidity intervals corresponding to 0-0.6, 0.6-1.2, 1.2-1.8
 3319 and 1.8-2.4. In the most forward rapidity region ($1.8 < |y^{\mu\mu}| < 2.4$), the J/ψ -meson yields
 3320 are extracted down to 3 GeV/c , while in the other rapidity regions ($|y^{\mu\mu}| < 1.8$) they
 3321 are extracted down to 6.5 GeV/c , reflecting the CMS detector acceptance. The signal
 3322 extraction is also performed in several centrality bins with the following boundaries: [0,
 3323 5, 10, 15, 20, 25, 30, 35, 40, 45, 50, 60, 70, 100%] at $|y^{\mu\mu}| < 2.4$ and [0, 10, 20, 30, 40, 50,
 3324 100%] in each of the rapidity intervals. The full set of analysis bins used in the J/ψ -meson
 3325 analysis is listed in Appendix B.

3326 Due to the complexity of the 2D functional form and the limited statistics to fully
 3327 constrain all its parameters at the same time, the 2D fits are performed in four sequential
 3328 steps:

- 3329 1. The $m^{\mu\mu}$ shape of the signal is parametrised using a weighed sum of two Crystal
 3330 Ball functions, while the background is described with a Chebyshev function
 3331 (Section 4.2.4.2). The $m^{\mu\mu}$ functional form is fitted on data and the corresponding
 3332 parameters are fixed in this step.
- 3333 2. The shape of the $\ell_{\text{J}/\psi}$ resolution is determined from data by fitting the $\ell_{\text{J}/\psi} < 0$
 3334 distribution with a weighed sum of three Gaussian distributions, taking into
 3335 account the $\ell_{\text{J}/\psi}$ uncertainty in each event (Section 4.2.4.3).
- 3336 3. The $\ell_{\text{J}/\psi}$ true lineshape of the nonprompt J/ψ mesons is parametrised with an expo-
 3337 nential function, while the nonprompt component of the background is parametrised
 3338 with a weighed sum of three exponential functions (Section 4.2.4.4). The $\ell_{\text{J}/\psi}$
 3339 functional form, derived by convolving the $\ell_{\text{J}/\psi}$ true lineshape with the $\ell_{\text{J}/\psi}$ resolution
 3340 model, is fitted on data and the parameters of the $\ell_{\text{J}/\psi}$ true lineshapes are con-
 3341 strained in this step.
- 3342 4. The $\ell_{\text{J}/\psi}$ and $m^{\mu\mu}$ distributions in data are fitted with the 2D functional form
 3343 $F(m^{\mu\mu}, \ell_{\text{J}/\psi})$ (Section 4.2.4.5), and the prompt and nonprompt J/ψ meson yields are
 3344 extracted (Section 4.2.4.6).

3345 A detailed description of each step is provided in Sections 4.2.4.2 to 4.2.4.5. An
 3346 example of the 2D fit results projected along the $m^{\mu\mu}$ and $\ell_{\text{J}/\psi}$ variables are shown in
 3347 Figure 4.10, extracted from Pb-Pb collision data.

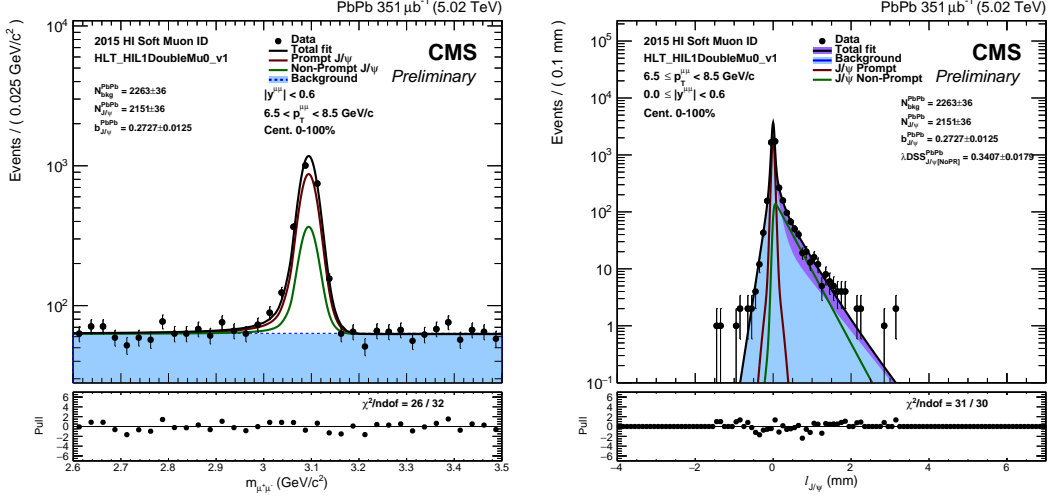


Figure 4.10: Results of the 2D fits performed on Pb-Pb data, projected onto the dimuon invariant mass (left) and pseudoproporper-decay length (right) variables.

4.2.4.1 Definition of pseudoproporper-decay length

The pseudoproporper-decay length $\ell_{J/\psi}$ of $\mu^+\mu^-$ candidates, used to estimate the b-hadron decay length, is defined as:

$$\ell_{J/\psi} = m_{J/\psi} \cdot \frac{\vec{p}^{\mu\mu} \cdot \vec{r}}{(p^{\mu\mu})^2} \quad (4.12)$$

where $m_{J/\psi} = 3.0969 \text{ GeV}/c^2$ is the mass of the J/ψ meson [19], $\vec{p}^{\mu\mu}$ is the dimuon momentum vector and \vec{r} is the displacement vector between the position of the primary collision vertex and the dimuon vertex.

The primary collision vertex is reconstructed by fitting the position, along the beam axis, of all tracks produced promptly within a radius of 5 cm from the interaction region, while the secondary $\mu^+\mu^-$ vertex is determined by extrapolating the position of closest approach between the two muon tracks. The vertex fit is performed using an adaptive vertex fitting algorithm [237, 238], which determines the best estimate of the vertex parameters, including its position and covariance matrix [239].

The uncertainty associated to the $\ell_{J/\psi}$ measurement, referred as σ_ℓ , is computed as:

$$\sigma_\ell = \sqrt{m_{J/\psi} \cdot \frac{\vec{p}^{\mu\mu} \cdot S \cdot \vec{p}^{\mu\mu}}{(p^{\mu\mu})^2}} \quad (4.13)$$

where S is the sum of the covariance matrices associated to the primary collision and $\mu^+\mu^-$ vertex fits. The pseudoproporper-decay length is measured in the CMS detector

3363 with a resolution of 35 μm , allowing to resolve the decay vertex of b hadrons.

3364 **4.2.4.2 Dimuon invariant mass parametrisation**

3365 The inclusive J/ψ meson and background yields are extracted by fitting the $m^{\mu\mu}$ distri-
 3366 bution in the dimuon invariant mass region $2.6 < m^{\mu\mu} < 3.5 \text{ GeV}/c^2$. The main source of
 3367 background in this mass region derives from pairs of uncorrelated muons produced from
 3368 leptonic decays of kaons and pions, and semi-leptonic decays of heavy-flavour hadrons.
 3369 These uncorrelated muon pairs are combined forming a continuous $m^{\mu\mu}$ distribution
 3370 (i.e. combinatorial background). On the contrary, the J/ψ mesons decay to correlated
 3371 muon pairs producing a narrow peak (i.e. resonance) in the $m^{\mu\mu}$ spectrum around
 3372 $m^{\mu\mu} \approx 3.09 \text{ GeV}/c^2$. As a consequence, different functional forms are used to model the
 3373 signal and background $m^{\mu\mu}$ shapes.

3374 **Parametrisation of the J/ψ -meson invariant mass shape.** The $m^{\mu\mu}$ distribution of
 3375 inclusive J/ψ mesons is modelled with a weighed sum of two Crystal Ball (CB) functions.
 3376 The Crystal Ball function consists of a Gaussian core and a power-law tail. The Gaussian
 3377 core is parametrised with a width σ_{CB} and a mean $m_{\text{J}/\psi}$, while the power-law tail
 3378 is parametrised by an exponent $n_{\text{J}/\psi}$ that accounts for energy loss due to final-state
 3379 photon radiation and a parameter $\alpha_{\text{J}/\psi}$ that determines the transition point between the
 3380 Gaussian and the power-law functions, as defined in:

$$\text{CB}(m) = \begin{cases} \frac{1}{\sqrt{2\pi}\sigma_{\text{CB}}} \exp\left[-\frac{1}{2}\left(\frac{m-m_{\text{J}/\psi}}{\sigma_{\text{CB}}}\right)^2\right], & \text{if } \left(\frac{m-m_{\text{J}/\psi}}{\sigma_{\text{CB}}}\right) > -\alpha_{\text{J}/\psi} \\ \frac{1}{\sqrt{2\pi}\sigma_{\text{CB}}} \exp\left[-\frac{|\alpha_{\text{J}/\psi}|^2}{2}\right] \left(\frac{n_{\text{J}/\psi}}{|\alpha_{\text{J}/\psi}|}\right)^{n_{\text{J}/\psi}} \left(\frac{n_{\text{J}/\psi}}{|\alpha_{\text{J}/\psi}|} - |\alpha_{\text{J}/\psi}| - \frac{m-m_{\text{J}/\psi}}{\sigma_{\text{CB}}}\right)^{-n_{\text{J}/\psi}}, & \text{if } \left(\frac{m-m_{\text{J}/\psi}}{\sigma_{\text{CB}}}\right) \leq -\alpha_{\text{J}/\psi} \end{cases} \quad (4.14)$$

3381 The total $m^{\mu\mu}$ functional form of the signal is then given by:

$$M_{\text{J}/\psi}(m^{\mu\mu}) = f_{\text{J}/\psi} \cdot \text{CB}_1(m^{\mu\mu}) + (1 - f_{\text{J}/\psi}) \cdot \text{CB}_2(m^{\mu\mu}) \quad (4.15)$$

3382 where the two Crystal Ball functions are defined with common mean $m_{\text{J}/\psi}$ and tail
 3383 parameters $\alpha_{\text{J}/\psi}$ and $n_{\text{J}/\psi}$, and the two CB widths are constrained such that $\sigma_{\text{CB},2} \geq \sigma_{\text{CB},1}$.

3384 The Crystal Ball parameters are optimised by fitting the prompt J/ψ -meson simu-
 3385 lations. On the one hand, the parameters are found to be consistent within different
 3386 collision systems and also as a function of collision centrality and dimuon p_{T} . On the

other hand, the fits performed in the inclusive dimuon rapidity region ($|y^{\mu\mu}| < 2.4$) are different from those done in differential $y^{\mu\mu}$ regions. As a result, different sets of parameters are used for the differential and integrated rapidity regions, extracted from the p-p and Pb-Pb prompt J/ψ -meson simulations. The set of parameters for the differential rapidity regions are determined from the corresponding rapidity-averaged values.

When fitting the $m^{\mu\mu}$ distribution in p-p and Pb-Pb collision data, the tail parameters $\alpha_{J/\psi}$ and $n_{J/\psi}$ are fixed to the values extracted from simulation, while the ratio of CB widths ($\sigma_{CB,2}/\sigma_{CB,1}$) is also fixed to simulation only when fitting the Pb-Pb data. This is done because the data samples do not provide sufficient constraining power to reliably estimate the CB tail parameters. The set of parameters left free in both p-p and Pb-Pb data fits are $f_{J/\psi}$, $m_{J/\psi}$ and $\sigma_{CB,1}$, while $\sigma_{CB,2}$ is left free only in the p-p data fits. The signal shape parameters extracted from simulations are summarised in Table 4.9.

Rapidity region	$f_{J/\psi}$	$\alpha_{J/\psi}$	$n_{J/\psi}$	$\sigma_{CB,2}/\sigma_{CB,1}$
Differential	0.78	2.10	1.35	1.68
$ y < 2.4$	0.58	1.94	1.64	2.06

Table 4.9: Parameters extracted from the prompt J/ψ -meson simulation and used to constrain the double Crystal Ball functions in each differential and integrated rapidity region. The parameters fixed to simulation in both Pb-Pb and p-p data fits are shown in bold blue colour, while those fixed to simulation only on Pb-Pb data are displayed in bold red colour. The $f_{J/\psi}$ values from simulation are only used to initialise them in the data fits.

Parametrisation of the background invariant mass shape. The $m^{\mu\mu}$ distribution of background dimuons is described with a Chebyshev function of order N , defined as:

$$M_{\text{bkg}}^N(m^{\mu\mu}) = \sum_{i=0}^N c_i T_i(m^{\mu\mu}) \quad (4.16)$$

where T_i is a Chebyshev polynomial of order i and c_i is the corresponding fit parameter. The Chebyshev polynomials are determined using the following recurrence relation [240]:

$$T_0(m) = 1 \quad ; \quad T_1(m) = m \quad ; \quad T_{i+1}(m) = 2mT_i(m) - T_{i-1}(m) \quad (4.17)$$

The main advantage of using a Chebyshev function is that the fit parameters c_i are fully uncorrelated between them, improving the convergence of the dimuon invariant mass fits. The order of the background $m^{\mu\mu}$ model is varied between 0 and 6, and the

best order for each analysis bin is chosen by performing a Log-Likelihood Ratio (LLR) test. The LLR test compares the resulting minimised Negative Log-Likelihood (NLL) of a Chebyshev fit of order N to the NLL of a Chebyshev fit of order $N + 1$ and $N + 2$ (two subsequent orders are needed to account for the change between odd and even polynomials).

The difference between the NLL values derived from the fits using a Chebyshev polynomial of order N and $M > N$, is proportional to a χ^2 distribution with $2(M - N)$ number of degrees of freedom, in particular:

$$\chi^2_{N \rightarrow N+1} = 2 \cdot (\text{NLL}_N - \text{NLL}_{N+1}) \quad ; \quad \chi^2_{N \rightarrow N+2} = 2 \cdot (\text{NLL}_N - \text{NLL}_{N+2}) \quad (4.18)$$

For a given Chebyshev function of order N , the next order is considered to fit the data significantly better if the χ^2 probabilities associated to the $N + 1$ or $N + 2$ orders are less than 5%. Thus, if in a given analysis bin, the next order does not significantly improve the quality of the fit, then the current order of the Chebyshev function is chosen. As an example, Table 4.10 summarise the results of the LLR test performed in Pb-Pb data for dimuons within $0.6 < |y^{\mu\mu}| < 1.2$ and $9.5 \leq p_T^{\mu\mu} < 11$ GeV/c, which in this case the first order is chosen since $p(\chi^2_{1 \rightarrow 2}, 2)$ and $p(\chi^2_{1 \rightarrow 3}, 4)$ are larger than 5%.

M	NLL	$p(N = 0)$	$p(N = 1)$	$p(N = 2)$	$p(N = 3)$	$p(N = 4)$
0	-28534.76					
1	-28537.94	4.2%				
2	-28538.08	15.6%	86.8%			
3	-28538.44	28.9%	90.9%	69.8%		
4	-28538.82	42.3%	94.1%	83.3%	68.8%	
5	-28538.93	59.7%	98.2%	94.6%	91.4%	89.4%
6	-28539.40	67.9%	98.3%	95.5%	92.7%	88.2%

Table 4.10: Results of the LLR test used to determine the order of the Chebyshev function for the background $\mu^+ \mu^-$ invariant mass fitted in Pb-Pb data within $0.6 < |y^{\mu\mu}| < 1.2$ and $9.5 \leq p_T^{\mu\mu} < 11$ GeV/c. The LLR test results of which the χ^2 probability determined for two consecutive orders ($M = N + 1$ and $M = N + 2$) are higher than 5% are highlighted in bold.

Another example is given in Figure 4.11, where the fits to the dimuon invariant mass distribution in Pb-Pb and p-p collision data have been performed using a first order and second order Chebyshev function, respectively. Among all the analysis bins, the orders of the Chebyshev function selected by the LLR tests are no larger than first order in Pb-Pb fits and third order in p-p fits.

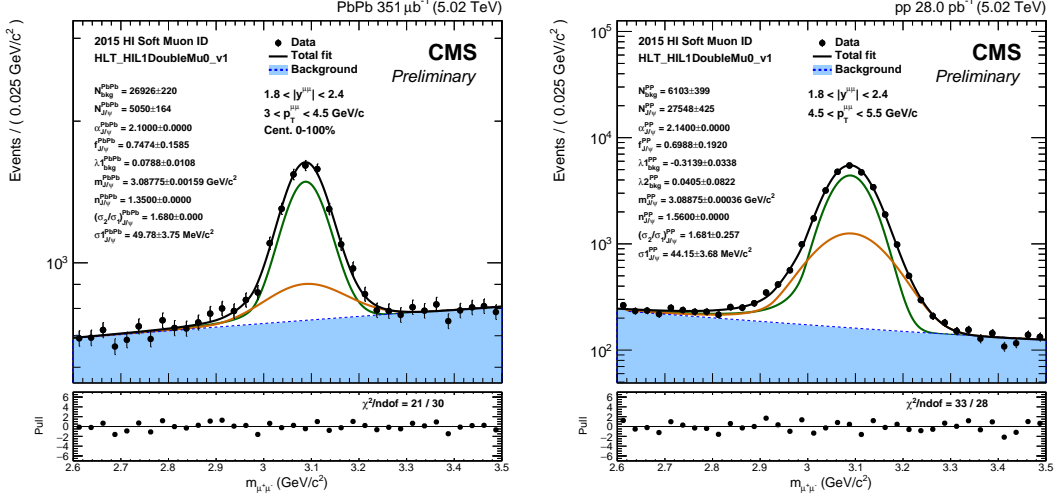


Figure 4.11: Results of the fits to the $\mu^+ \mu^-$ invariant mass distribution in Pb-Pb (left) and p-p (right) data. The black line represents the total fit model while the blue filled area represents the fitted background shape.

4.2.4.3 Pseudoproper-decay length resolution

The $\ell_{J/\psi}$ resolution depends on the measurement of the dimuon momentum and its vertex position, and as a result, it is affected by the $\ell_{J/\psi}$ uncertainty (σ_ℓ) of each event. In addition, since the σ_ℓ depends on the p_T and rapidity of dimuon candidates, the σ_ℓ distribution may differ between background and signal dimuons. In order to take into account the $\ell_{J/\psi}$ uncertainty in each event, the $\ell_{J/\psi}$ resolution of signal and background dimuons is modelled with:

$$R_{J/\psi(\text{bkg})}(\ell_{J/\psi}) = \int d\sigma_\ell R(\ell_{J/\psi}|\sigma_\ell) \cdot \mathcal{P}_{J/\psi(\text{bkg})}(\sigma_\ell) \quad (4.19)$$

where $R(\ell_{J/\psi}|\sigma_\ell)$ is the functional form of the $\ell_{J/\psi}$ resolution depending on σ_ℓ , and $\mathcal{P}_{J/\psi(\text{bkg})}(\sigma_\ell)$ represents the signal (background) σ_ℓ distribution.

Using this approach, the $\ell_{J/\psi}$ resolution is adjusted for each event to the measured $\ell_{J/\psi}$ uncertainty weighed by the corresponding σ_ℓ distribution for signal and background dimuons. The parametrisation of the $\ell_{J/\psi}$ resolution and the determination of the σ_ℓ distributions are detailed as follows.

Extraction of the σ_ℓ distribution. The distribution of σ_ℓ is described using a template histogram determined from data. The corresponding σ_ℓ distributions for signal and background dimuons are extracted using the statistical technique called *sPlot* [241].

3443 The *sPlot* technique can be applied to a multivariate data sample made of a com-
 3444 bination of several sources of events (e.g. signal and background), where each event is
 3445 described by a set of variables divided in two categories. The first category consists of
 3446 discriminating variables whose distributions are known for each source of events, while
 3447 the second category corresponds to a set of variables, called control variables, whose
 3448 distributions for some sources are unknown. The *sPlot* technique allows to reconstruct
 3449 the distribution of the control variables for each source, by weighing the events with the
 3450 so-called *sWeights*, computed with the information of the discriminating variables.

3451 In the J/ψ meson analysis, the $\mu^+ \mu^-$ invariant mass is used as discriminating variable
 3452 in order to determine the signal and background distributions of σ_ℓ . The corresponding
 3453 *sWeights* are derived using the $m^{\mu\mu}$ functional forms of each source ($M_{J/\psi}$ and M_{bkg}),
 3454 obtained in Section 4.2.4.2, in the following way:

$${}_s\mathcal{W}_i(m^{\mu\mu}) = \frac{\sum_{j=\{\text{J}/\psi, \text{bkg}\}} V_{i,j} \cdot M_j(m^{\mu\mu})}{\sum_{j=\{\text{J}/\psi, \text{bkg}\}} N_j \cdot M_j(m^{\mu\mu})} , \quad \text{for } i = \text{J}/\psi, \text{bkg} \quad (4.20)$$

3455 where N_j is the number of dimuon events from source j , and $V_{i,j}$ is the element of
 3456 the covariance matrix associated to the i^{th} and j^{th} source ($i, j = J/\psi$ and background).
 3457 The covariance matrix of each source is computed by inverting the following matrix:

$$V_{i,j}^{-1} = \frac{M_i(m_{\mu\mu}) \cdot M_j(m_{\mu\mu})}{\sum_{i=\{\text{J}/\psi, \text{bkg}\}} N_i \cdot M_i(m_{\mu\mu})} \quad (4.21)$$

3458 Once determined, the ${}_s\mathcal{W}_{J/\psi}$ and ${}_s\mathcal{W}_{\text{bkg}}$ weights are then applied to each event to
 3459 create a signal-like and a background-like dataset. Each dataset is subsequently projected
 3460 onto the σ_ℓ variable, to extract the signal and background σ_ℓ distributions and form σ_ℓ
 3461 template histograms for each source. An example of a σ_ℓ distribution in p-p and Pb-Pb
 3462 collision data is presented in Figure 4.12.

3463 **Parametrisation of the $\ell_{J/\psi}$ resolution.** The $\ell_{J/\psi}$ resolution is parametrised in data
 3464 from the negative tail of the $\ell_{J/\psi}$ signal distribution, which is due to resolution. Since
 3465 both signal and background dimuons can have negative $\ell_{J/\psi}$ values, the contribution from
 3466 each source is separated using the *sPlot* technique, as was done for the σ_ℓ distribution in
 3467 the previous part. The resulting $\ell_{J/\psi} < 0$ distribution, derived from the *sPlot* signal-like
 3468 dataset, is then fitted with a weighed sum of three Gaussian functions, defined as:

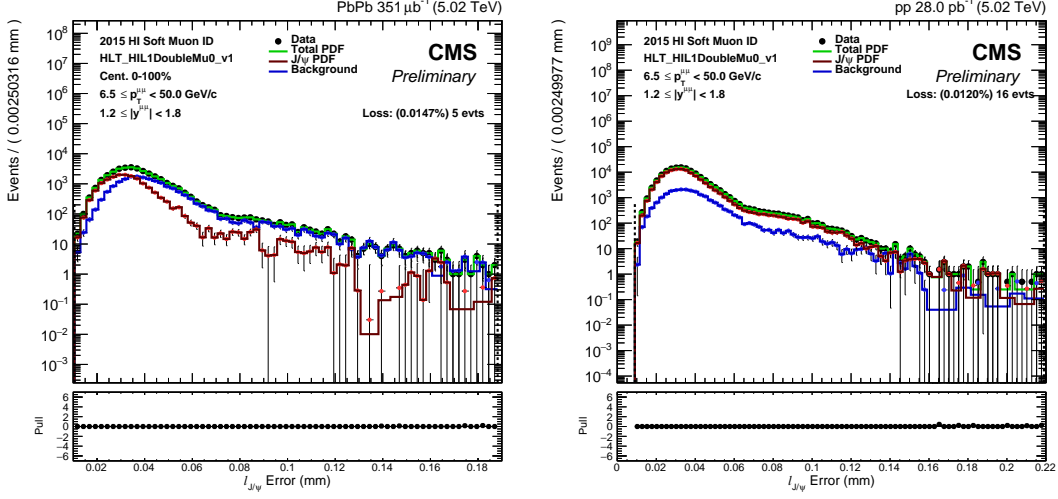


Figure 4.12: Distributions of the σ_ℓ for signal (red line), background (blue line) and all (green line) dimuons, extracted from Pb-Pb (left) and p-p (right) data. The dashed lines represents the σ_ℓ range used to extract the template histograms. The bottom panel shows the ratio between the data and the total template histogram extracted using the sPlot technique.

$$R(\ell_{J/\psi}|\sigma_\ell) = \frac{f_1^r}{s_1^r \sigma_\ell \sqrt{2\pi}} \exp \left[\frac{1}{2} \left(\frac{\ell_{J/\psi}}{s_1^r \sigma_\ell} \right)^2 \right] + (1-f_1^r) \left[\frac{f_2^r}{s_2^r \sigma_\ell \sqrt{2\pi}} \exp \left[\frac{1}{2} \left(\frac{\ell_{J/\psi}}{s_2^r \sigma_\ell} \right)^2 \right] + \frac{(1-f_2^r)}{s_3^r \sigma_\ell \sqrt{2\pi}} \exp \left[\frac{1}{2} \left(\frac{\ell_{J/\psi}}{s_3^r \sigma_\ell} \right)^2 \right] \right] \quad (4.22)$$

where s^r are scale factors that account for deviations from the measured $\ell_{J/\psi}$ uncertainties, and f^r are the weights of the Gaussian components. The s^r and f^r parameters are left free in the fits to the data. The Gaussian mean values have been checked to be consistent with zero, and are fixed to zero in the fits. The scale factors s_i^r are constrained such that $s_3^r \geq s_2^r \geq s_1^r$.

Two examples of $\ell_{J/\psi}$ resolution fits for p-p and Pb-Pb data are given in Figure 4.13 plotted as a function of $\ell_{J/\psi}/\sigma_\ell$.

4.2.4.4 Pseudoproper-decay length parametrisation

The $\ell_{J/\psi}$ distribution of $J/\psi \rightarrow \mu^+ \mu^-$ events is separated in two components: prompt and nonprompt J/ψ mesons. In the case of background dimuons, the description of the $\ell_{J/\psi}$ distribution is also separated in a prompt and nonprompt component. On the one

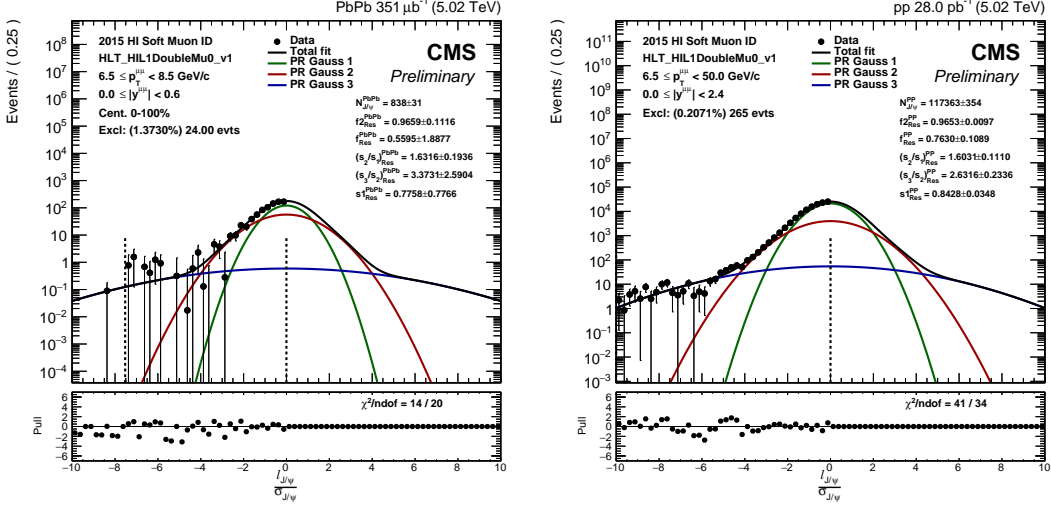


Figure 4.13: Results of the $\ell_{J/\psi}$ resolution fits for signal dimuons in data. The results are presented as a function of $\ell_{J/\psi}/\sigma_\ell$ and the dashed lines represent the fitted range.

hand, the prompt background component represents $\mu^+ \mu^-$ pairs from background events whose dimuon vertex is consistent with the primary collision vertex, such as low mass Drell-Yan events. On the other hand, the nonprompt background component are made of uncorrelated muons faking a displaced vertex.

Parametrisation of the $\ell_{J/\psi}$ true lineshape of J/ψ mesons. The $\ell_{J/\psi}$ true lineshape of prompt J/ψ mesons is described with a Dirac delta function ($\delta(\ell_{J/\psi})$) and the one for nonprompt J/ψ mesons is modelled with an exponential function. The signal $\ell_{J/\psi}$ true functional form is then given by:

$$D_{J/\psi}(\ell_{J/\psi}) = b_{J/\psi} \cdot \exp(-|\lambda_B| \cdot \ell_{J/\psi}) + (1 - b_{J/\psi}) \cdot \delta(\ell_{J/\psi}) \quad (4.23)$$

where $b_{J/\psi}$ is the fraction of nonprompt J/ψ mesons and λ_B represents the average decay length of b hadrons. The λ_B parameter is initialised, when performing the 2D fits on data, to the value obtained by fitting the generated $\ell_{J/\psi}$ distribution of the nonprompt J/ψ simulation.

Examples of fits to the generated $\ell_{J/\psi}$ distribution of nonprompt J/ψ simulations are shown in Figure 4.14 for Pb-Pb and p-p data (the λ_B parameter is labelled in the plots as λ_{DSS} ²).

²The initial DSS stands for Decays on Single Side

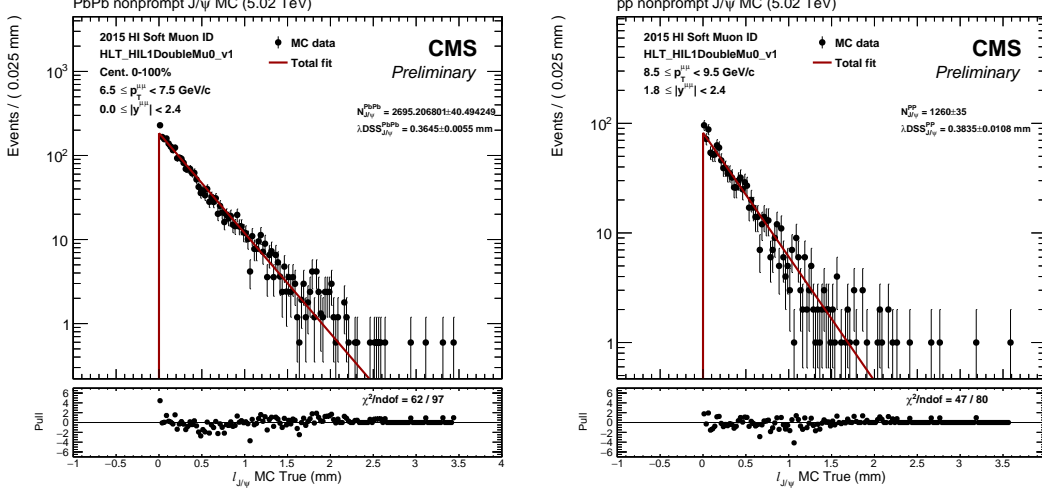


Figure 4.14: Fits to the $\ell_{J/\psi}$ distribution of generated nonprompt $J/\psi \rightarrow \mu^+ \mu^-$ events in Pb-Pb (left) and p-p (right) simulations. The fitted value for $\lambda_B = \lambda_{\text{DSS}}$ is shown.

Parametrisation of the background $\ell_{J/\psi}$ true lineshape. The nonprompt component of the background $\ell_{J/\psi}$ true lineshape is described with a weighed sum of three exponential functions, while the prompt component is described with a Dirac delta function. The full background $\ell_{J/\psi}$ true model is defined as:

$$D_{\text{bkg}}(\ell_{J/\psi}) = b_{\text{bkg}} \cdot \{f_{\text{DL}} [f_{\text{SS}} \cdot \exp(-|\lambda_{\text{SS}}| \ell_{J/\psi}) + (1 - f_{\text{SS}}) \cdot \exp(|\lambda_F| \cdot \ell_{J/\psi})] \\ + (1 - f_{\text{DL}}) \cdot \exp(-|\lambda_{\text{DS}}| |\ell_{J/\psi}|)\} \\ + (1 - b_{\text{bkg}}) \cdot \delta(\ell_{J/\psi}) \quad (4.24)$$

where b_{bkg} is the fraction of nonprompt background dimuons, f_{DL} and f_{SS} are the weights of the exponential functions, and λ_{SS} , λ_F and λ_{DS} are the exponential parameters associated to the single sided ($\ell_{J/\psi} > 0$), flipped ($\ell_{J/\psi} < 0$) and double sided (symmetric $\ell_{J/\psi}$) exponential decay models, respectively.

The $\ell_{J/\psi}$ true lineshape of the background is parametrised in data by fitting the $\ell_{J/\psi}$ distribution of the background-like data sample derived with the *sPlot* technique. The model used to fit the data is given by:

$$F_{\text{bkg}}(\ell_{J/\psi}) = N_{\text{bkg}} \cdot D_{\text{bkg}}(\ell_{J/\psi}) \otimes R_{\text{bkg}}(\ell_{J/\psi}) \quad (4.25)$$

where the $\ell_{J/\psi}$ resolution parameters have been fixed to data as detailed in Section 4.2.4.3, and only the N_{bkg} and the D_{bkg} parameters (λ , f and b_{bkg}) are left free.

4.2. ANALYSIS

3508 Examples of fits to the $\ell_{J/\psi}$ distribution of background dimuons are shown in Figure 4.15
 3509 for p-p and Pb-Pb data.

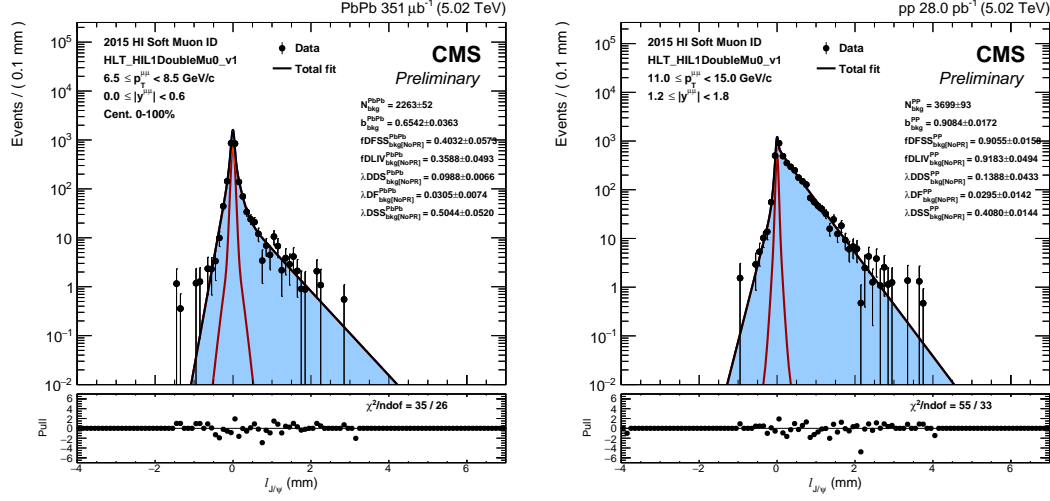


Figure 4.15: Fits to the $\ell_{J/\psi}$ distribution of background events in Pb-Pb (left) and p-p (right) collision data.

4.2.4.5 Two-dimensional fit to the $m^{\mu\mu}$ and $\ell_{J/\psi}$ distributions

3510 The 2D fits to the $m^{\mu\mu}$ and $\ell_{J/\psi}$ distributions represents the last step in the procedure
 3511 to extract the J/ψ -meson yields. The parameters used in the 2D fit model are fixed as
 3512 explained in the previous sections, except for the average decay length of b hadrons λ_B ,
 3513 the fraction of nonprompt J/ψ -mesons $b_{J/\psi}$, the inclusive J/ψ -meson yield $N_{J/\psi}$, and the
 3514 background yield N_{bkg} . Figure 4.10 shows an example of 2D fit extracted from Pb-Pb
 3515 collision data.
 3516

4.2.4.6 Prompt and nonprompt J/ψ meson yields

3517 Finally, the yields of the prompt ($N_{J/\psi}^P$) and nonprompt ($N_{J/\psi}^{\text{NP}}$) J/ψ mesons are simply
 3518 derived from the number of inclusive J/ψ mesons $N_{J/\psi}$ and the fraction of nonprompt J/ψ
 3519 mesons $b_{J/\psi}$, according to:
 3520

$$N_{J/\psi}^P = (1 - b_{J/\psi}) \cdot N_{J/\psi} \quad (4.26)$$

$$N_{J/\psi}^{\text{NP}} = b_{J/\psi} \cdot N_{J/\psi}$$

3521 and the corresponding statistical uncertainty are computed using error propagation
3522 and taking into account the correlation between $b_{J/\psi}$ and $N_{J/\psi}$, determined from the 2D
3523 fits.

3524 **4.2.5 Extraction of prompt $\psi(2S)$ / J/ψ ratio**

3525 This section explain the steps followed to measure the ratio of prompt $\psi(2S)$ over J/ψ
3526 meson yields, in p-p and Pb-Pb collisions. In this case, due to the low amount of $\psi(2S)$
3527 mesons present in Pb-Pb collisions, it is not possible to perform a 2D fit to the $m^{\mu\mu}$ and
3528 $\ell_{J/\psi}$ distributions, and an alternative procedure is used instead to measure the prompt
3529 charmonium yields.

3530 In order to extract the yields of prompt charmonia, the dimuons are required to pass
3531 a $\ell_{J/\psi}$ selection that rejects dimuons with $\ell_{J/\psi}$ values above a given threshold. The $\ell_{J/\psi}$
3532 selection threshold is optimized using simulations as detailed in Section 4.2.5.1, keeping
3533 90% of prompt charmonia while rejecting more than 80% of nonprompt charmonia. Then,
3534 the $\psi(2S)$ -to- J/ψ yields ratio is extracted from data by fitting the $m^{\mu\mu}$ distribution of
3535 dimuons passing the $\ell_{J/\psi}$ selection, as explained in Section 4.2.5.2. And finally, the ratio
3536 of prompt $\psi(2S)$ over J/ψ meson yields is determined by subtracting the remaining
3537 nonprompt charmonia passing the $\ell_{J/\psi}$ selection, as described in Section 4.2.5.3.

3538 Due to the more limited $\psi(2S)$ -meson statistics, the extraction of the ratios of $\psi(2S)$
3539 over J/ψ meson yields is performed in wider bins compared to the J/ψ -meson analysis. In
3540 this case, the fits are performed in two kinematic regions: mid-rapidity ($0 < |y^{\mu\mu}| < 1.6$,
3541 $p_T^{\mu\mu} > 6.5$ GeV/c) and forward rapidity ($1.6 < |y^{\mu\mu}| < 2.4$, $p_T^{\mu\mu} > 3$ GeV/c). The lower $p_T^{\mu\mu}$
3542 thresholds in each rapidity region reflects the acceptance of the detector. The measure-
3543 ments are also extracted in different $p_T^{\mu\mu}$ intervals with boundaries: [6.5, 9, 12, 15, 20,
3544 30] GeV/c at mid-rapidity and [3, 6.5, 12, 30] GeV/c at forward rapidity, and in different
3545 centrality bins corresponding to: 0-10, 10-20, 20-30, 30-40, 40-50 and 50-100% at mid-
3546 rapidity, and 0-20, 20-40 and 40-100% at forward rapidity. The analysis bins used in the
3547 $\psi(2S)$ -to- J/ψ double ratio analysis are summarised in Table B.4.

3548 **4.2.5.1 Definition of the $\ell_{J/\psi}$ selection for prompt charmonia**

3549 The threshold of the $\ell_{J/\psi}$ selection is tuned using prompt J/ψ simulations, by requiring
3550 that the fraction of prompt J/ψ mesons that pass the selection is 90%, in each analysis
3551 bin. The simulated $\ell_{J/\psi}$ distributions of prompt and nonprompt signal dimuons in the

4.2. ANALYSIS

forward rapidity region, and the corresponding $\ell_{J/\psi}$ selection threshold, are shown in Figure 4.16.

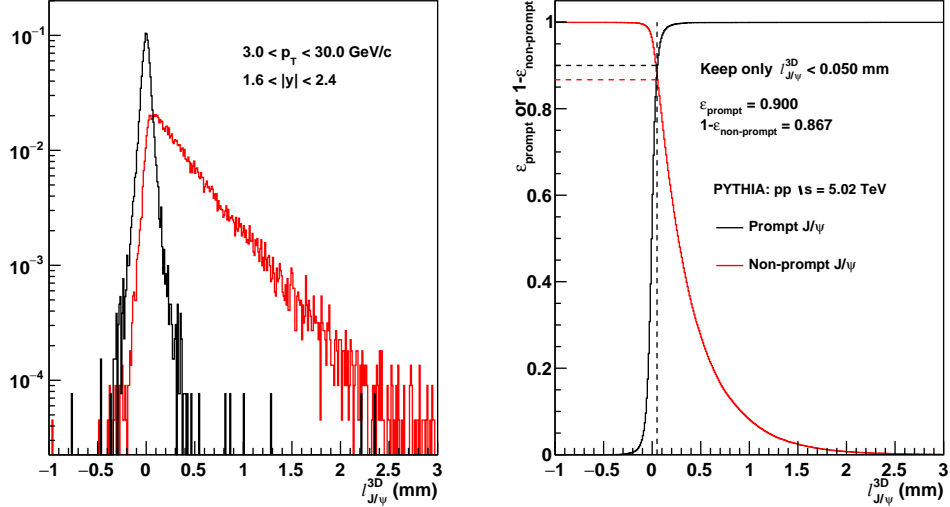


Figure 4.16: Distribution of $\ell_{J/\psi}$ (left) in the p-p simulations of prompt and nonprompt J/ψ mesons, and an illustration (right) of the way the $\ell_{J/\psi}$ selection threshold is chosen. The results corresponds to the mid-rapidity region $|y^{\mu\mu}| < 1.6$.

The $\ell_{J/\psi}$ selection thresholds extracted from the simulations are found to be consistent between the different collision systems and centrality bins, but they vary between different dimuon p_T and rapidity regions. As a result, the thresholds are extracted in several $p_T^{\mu\mu}$ regions at mid- and forward rapidity. Then, the profile of the $\ell_{J/\psi}$ selection thresholds (l_P) with respect of $p_T^{\mu\mu}$ is fitted separately for each rapidity region, with the following function:

$$l_P(p_T^{\mu\mu}) = a + \frac{b}{p_T^{\mu\mu}} \quad (4.27)$$

where a and b are free parameters. Figure 4.17 displays the fit results of the l_P profile as a function of $p_T^{\mu\mu}$ in the two rapidity regions. The $\ell_{J/\psi}$ selection, derived from the fits as a function of $p_T^{\mu\mu}$, is summarised in:

$$\ell_{J/\psi} < \begin{cases} 0.012 + (0.23/p_T^{\mu\mu}), & \text{if } |y^{\mu\mu}| \leq 1.6 \\ 0.014 + (0.28/p_T^{\mu\mu}), & \text{if } |y^{\mu\mu}| > 1.6 \end{cases} \quad (4.28)$$

3563

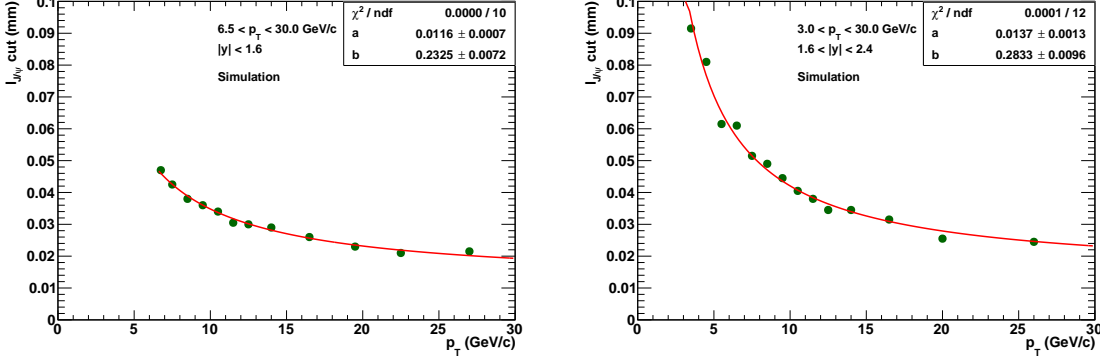


Figure 4.17: Profile of the $\ell_{J/\psi}$ selection thresholds (green points) with respect to $p_T^{\mu\mu}$, extracted from the J/ψ simulations in the mid-rapidity (left) and forward rapidity (right) regions. The fitted functions (red lines) are also displayed and the values of their parameters are shown in the box.

3564 The efficiencies of passing the $\ell_{J/\psi}$ selection, as a function of $p_T^{\mu\mu}$, are presented in
 3565 Figure 4.18. By construction, the $\ell_{J/\psi}$ selection efficiencies of prompt J/ψ mesons are close
 3566 to 90%, while it is observed to be more efficient for prompt $\psi(2S)$ mesons, due to the
 3567 slightly higher momentum of the muons. However, the difference between the prompt
 3568 J/ψ and $\psi(2S)$ efficiencies are found to be the same in p-p and Pb-Pb simulations. The
 3569 efficiency for nonprompt J/ψ mesons, leading to a contamination from this component, is
 3570 seen to increase when going towards lower $p_T^{\mu\mu}$ values reaching up to 20%. These efficien-
 3571 cies are used in Section 4.2.5.3 to subtract the nonprompt charmonium contamination
 3572 from the measured ratios of $\psi(2S)$ over J/ψ mesons.

3573 4.2.5.2 Fits to the dimuon invariant mass distribution

3574 The ratio of $\psi(2S)$ over J/ψ meson yields is extracted separately in p-p and Pb-Pb colli-
 3575 sions by performing an unbinned maximum-likelihood fit to the $m^{\mu\mu}$ distribution within
 3576 the region $2.2 < m_{\mu^+\mu^-} < 4.5 \text{ GeV}/c^2$. The total fit model used is defined as:

$$F(m^{\mu\mu}) = N_{J/\psi} \cdot [M_{J/\psi}(m^{\mu\mu}) + R_\psi \cdot M_{\psi(2S)}(m^{\mu\mu})] + N_{\text{bkg}} \cdot M_{\text{bkg}}(m^{\mu\mu}) \quad (4.29)$$

3577 where R_ψ is the $\psi(2S)$ -to- J/ψ yields ratio, $N_{J/\psi}$ (N_{bkg}) is the number of J/ψ meson
 3578 (background) events, and M_i represents the $m^{\mu\mu}$ functional form for each source of
 3579 events.

3580 The parametrisation of the signal and background $m^{\mu\mu}$ distributions follows the same
 3581 strategy used in Section 4.2.4.2. The shapes of J/ψ and $\psi(2S)$ mesons are described using

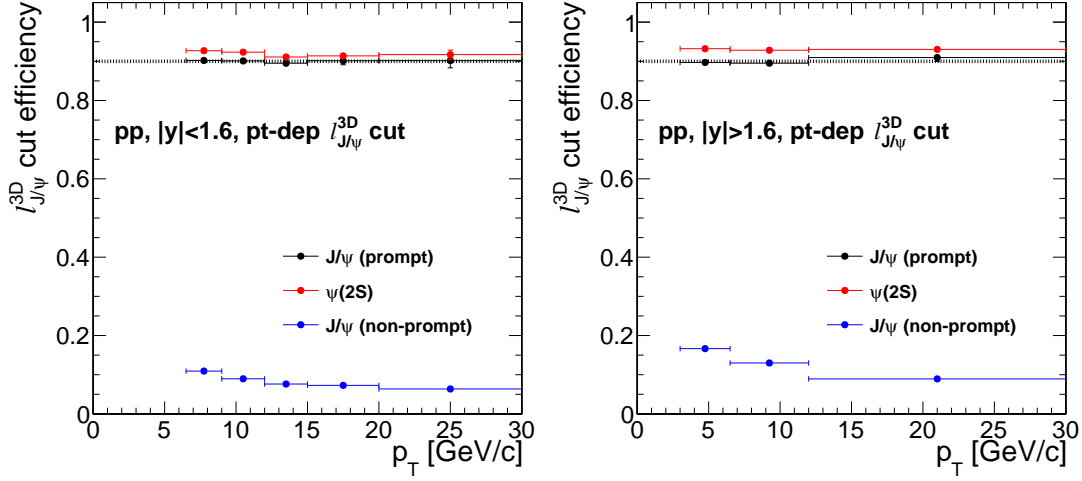


Figure 4.18: Efficiency of passing the $\ell_{J/\psi}$ selection as a function of $p_T^{\mu\mu}$ for prompt J/ψ (black points), prompt $\psi(2S)$ (red points) and nonprompt J/ψ (blue points) mesons. The results are extracted from p-p simulations in the mid-rapidity (left) and forward rapidity (right) regions.

3582 a weighed sum of two Crystall Ball functions with common mean. Since the statistics
 3583 in data is not enough to reliable fit the $\psi(2S)$ mass peak, the $\psi(2S)$ CB parameters
 3584 are constrain to the J/ψ ones. The following criteria are used to constrain the $\psi(2S)$ CB
 3585 parameters when performing the data fits:

- 3586 • The common tail parameters are taken to be the same between the J/ψ and $\psi(2S)$
 3587 CB functions ($\alpha_{\psi(2S)} = \alpha_{J/\psi}$, $n_{\psi(2S)} = n_{J/\psi}$).
- 3588 • The weight of the $\psi(2S)$ CB components is fixed to the J/ψ CB weight ($f_{\psi(2S)} = f_{J/\psi}$).
- 3589 • The $\psi(2S)$ CB mean parameter is fixed to the J/ψ CB mean multiplied by the mass
 3590 ratio of $\psi(2S)$ over J/ψ mesons ($m_{\psi(2S)}/m_{J/\psi} = 1.1902$) [19].
- 3591 • The two width parameters of the $\psi(2S)$ CB function are fixed to the corresponding
 3592 J/ψ CB widths scaled by the $\psi(2S)$ to J/ψ mass ratio ($\sigma_{CB,i}^{\psi(2S)} = (m_{\psi(2S)}/m_{J/\psi}) \cdot \sigma_{CB,i}^{J/\psi}$).

3593 The J/ψ CB parameters are tuned using the prompt J/ψ simulations after applying
 3594 the $\ell_{J/\psi}$ selection defined in the previous section. The parameter values extracted from
 3595 the p-p and Pb-Pb simulations are found to be in good agreement, and thus, the results
 3596 obtained from the p-p simulation are used. The nominal values of the CB parameters
 3597 are presented in Table 4.11, where those that appear in bold are fixed when performing
 3598 the fits to $m^{\mu\mu}$ distribution in data. The parameters that are left free in the data fits are:

the weight of the CB components $f_{J/\psi}$, the mean parameter $m_{J/\psi}$, the width parameter $\sigma_{CB,1}^{J/\psi}$, the number of J/ψ mesons $N_{J/\psi}$, and the ratio of $\psi(2S)$ over J/ψ meson yields R_ψ . When fitting the p-p data, the width parameter $\sigma_{CB,2}$ is also left free.

$y^{\mu\mu}$	$p_T^{\mu\mu}$ [GeV/c]	$f_{J/\psi}$	$\alpha_{J/\psi}$	$n_{J/\psi}$	$\sigma_{CB,2}/\sigma_{CB,1}$
0–1.6	6.5–30.0	0.71	1.87	1.76	1.94
1.6–2.4	3.0–30.0	0.82	2.18	1.46	1.79

Table 4.11: Parameters extracted for the double Crystal Ball function from the prompt J/ψ -meson p-p simulation after applying the $\ell_{J/\psi}$ selection. The values shown correspond to the p_T -centrality integrated fits. The CB parameters fixed to simulation when performing the data fits are shown in bold font.

In the case of the background, the $m^{\mu\mu}$ shape is modelled using a Chebyshev function of order N , where the order for each analysis bin is defined using a LLR test as performed in Section 4.2.4.2. The selected background Chebyshev functions are of first or second order.

The results of the fits to the $m^{\mu\mu}$ distribution in Pb-Pb and p-p collisions, performed in the p_T -centrality-inclusive region at mid-rapidity after applying the $\ell_{J/\psi}$ selection, are shown in Figure 4.19.

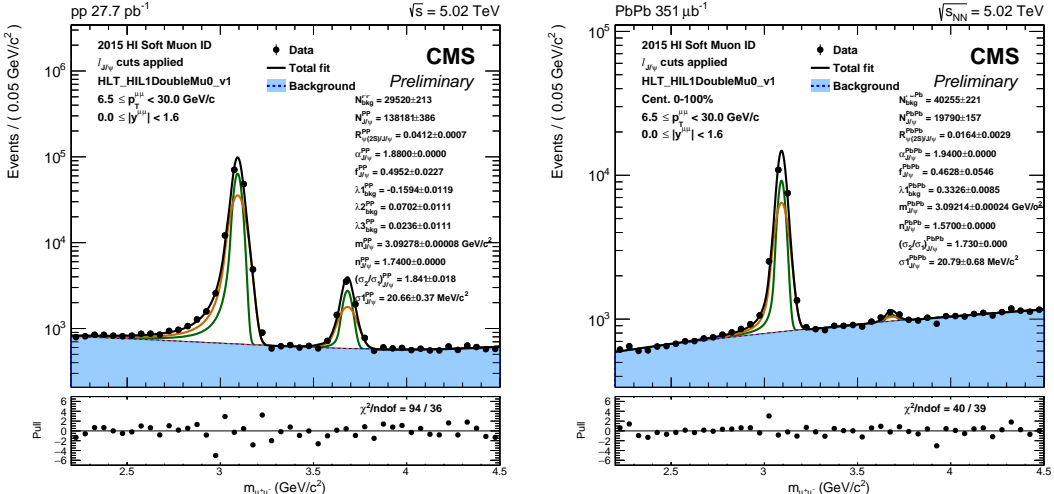


Figure 4.19: Fits to the $m^{\mu\mu}$ distribution in p-p (left) and Pb-Pb (right) collisions. The results correspond to dimuon events derived in p_T -centrality-inclusive region at mid-rapidity after applying the $\ell_{J/\psi}$ selection. The black line represents the total fit model while the blue filled area represents the fitted background shape.

3609 **4.2.5.3 Correction for nonprompt charmonium contamination**

3610 Since the main goal of the analysis is to measure the ratio of prompt $\psi(2S)$ over J/ψ
 3611 meson yields, it is important to correct for the amount of nonprompt charmonia that
 3612 remains after selecting dimuons with low $\ell_{J/\psi}$, even though they represent a small
 3613 fraction of the sample. In order to do this, four categories of events are considered as
 3614 illustrated in Figure 4.20, which are:

- 3615 • (A): Prompt charmonia passing the $\ell_{J/\psi}$ selection.
 3616 • (B): Nonprompt charmonia passing the $\ell_{J/\psi}$ selection.
 3617 • (C): Prompt charmonia failing the $\ell_{J/\psi}$ selection.
 3618 • (D): Nonprompt charmonia failing the $\ell_{J/\psi}$ selection.

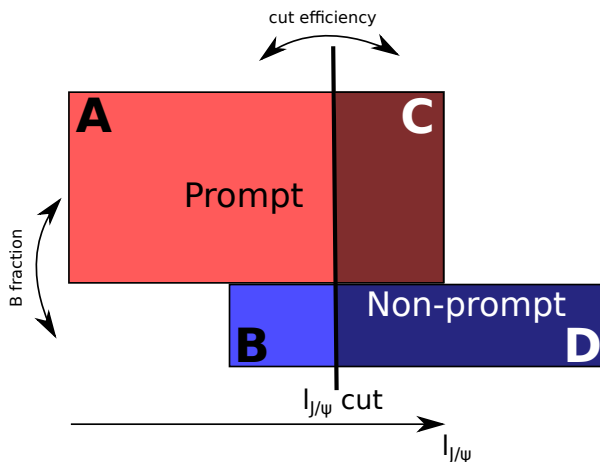


Figure 4.20: Definition of the different categories of events considered for the subtraction of nonprompt charmonia.

3619 Based on the categories presented in Figure 4.20, the objective is to extract the
 3620 number of *prompt* ψ ($\psi(2S)$ or J/ψ) mesons defined in the region $A + C$. The number
 3621 of charmonia in the region $A + B$ (labelled as *pass*) is extracted from the $m^{\mu\mu}$ fits after
 3622 selecting dimuons passing the $\ell_{J/\psi}$ selection. Furthermore, the charmonium yields in the
 3623 region $C + D$ (referred as *fail*) are simply measured by inverting the $\ell_{J/\psi}$ selection (i.e.
 3624 selecting dimuons with high $\ell_{J/\psi}$) and redoing the fits to the $m^{\mu\mu}$ spectrum following the
 3625 same procedure used in the previous section.

3626 Using the $\ell_{J/\psi}$ selection efficiencies estimated from the prompt (ϵ_ψ^P) and nonprompt
 3627 (ϵ_ψ^{NP}) charmonium simulations, and the charmonium yields extracted from the $m^{\mu\mu}$ fits

3628 after applying the $\ell_{J/\psi}$ selection (N_ψ^{pass}) and inverting it (N_ψ^{fail}), one can derived the
 3629 following equation:

$$N_\psi^{\text{pass}} = \left[\epsilon_\psi^P \cdot f_\psi^P + \epsilon_\psi^{\text{NP}} \cdot (1 - f_\psi^P) \right] \cdot N_\psi^{\text{tot}} \quad (4.30)$$

3630 where f_ψ^P is the fraction of prompt charmonia and N_ψ^{tot} is the total amount of ψ
 3631 mesons (i.e. $N_\psi^{\text{tot}} = N_\psi^{\text{pass}} + N_\psi^{\text{fail}}$). One can then deduce from Eq. (4.30) the number of
 3632 prompt charmonia, given by:

$$N_\psi^P = f_\psi^P \cdot N_\psi^{\text{tot}} = \frac{N_\psi^{\text{pass}} - \epsilon_\psi^{\text{NP}} \cdot N_\psi^{\text{tot}}}{\epsilon_\psi^P - \epsilon_\psi^{\text{NP}}} \quad (4.31)$$

3633 The ratios of prompt $\psi(2S)$ over J/ψ meson yields are then determined for p-p and
 3634 Pb-Pb collisions, according to:

$$R_\psi^P = \frac{N_{\psi(2S)}^P}{N_{J/\psi}^P} \quad (4.32)$$

3635 The largest relative difference between the ratios of charmonium yields extracted
 3636 from the $m^{\mu\mu}$ distribution of dimuons passing the $\ell_{J/\psi}$ selection (R_ψ^{pass}) and the ratios of
 3637 prompt charmonium yields (R_ψ^P), is found to be 6% for p-p data and 18% for Pb-Pb data.
 3638 Regarding the double ratio, the largest relative difference is 16%.

3639 4.2.6 Charmonium acceptance and efficiency

3640 This section presents the standard procedure used to estimate the charmonium ac-
 3641 ceptance and efficiency based on simulations. In order to improve the modelling of
 3642 the p_T and rapidity spectra of charmonia, the kinematic distribution of the simulated
 3643 dimuons are weighed as explained in Section 4.2.6.1. Afterwards, the J/ψ meson accep-
 3644 tance and efficiency are determined from simulations as described in Section 4.2.6.2
 3645 and Section 4.2.6.3, respectively. Then, the J/ψ meson efficiency is corrected using data-
 3646 to-simulation efficiency ratios derived with the tag-and-probe method as detailed in
 3647 Section 4.2.6.4. Finally, the double ratio of prompt $\psi(2S)$ over J/ψ meson efficiencies in
 3648 Pb-Pb relative to p-p collisions are checked to be consistent with unity in Section 4.2.6.5.

3649 4.2.6.1 Correction for charmonium p_T and rapidity

3650 The detector acceptance and efficiency depends on the p_T and rapidity distributions of the
 3651 detected particles. In order to derive reliable estimations from charmonium simulations,

3652 it is important to ensure that the kinematic distributions of charmonia are as close as
 3653 possible to that of real data.

3654 To accomplish this, a weight is assigned to each simulated dimuon according to
 3655 their $y^{\mu\mu}$ and $p_T^{\mu\mu}$. This weight is obtained from the ratio of the J/ψ -meson p_T spectrum
 3656 measured in data over the one derived from simulation, in the different rapidity regions
 3657 used in the J/ψ -meson analysis. The number of observed prompt and nonprompt J/ψ
 3658 mesons extracted from the 2D fits to the $m^{\mu\mu}$ and $\ell_{J/\psi}$ distributions in data, described
 3659 in Section 4.2.4, are compared to the corresponding ones measured in the prompt and
 3660 nonprompt $J/\psi \rightarrow \mu^+ \mu^-$ simulations, respectively. The $p_T^{\mu\mu}$ distributions in each rapidity
 3661 region are normalised to the number of observed J/ψ mesons (prompt or nonprompt)
 3662 in the inclusive region ($|y^{\mu\mu}| < 2.4$ and $3.0 < p_T^{\mu\mu} < 50$ GeV/c). The J/ψ -meson kinematic
 3663 weights are then defined as:

$$w^{J/\psi}(p_T^{\mu\mu}, y^{\mu\mu}) = \frac{\frac{1}{N_{\text{data}}^{\mu\mu}} \frac{d^2 N_{\text{data}}^{\mu\mu}}{dp_T^{\mu\mu} dy^{\mu\mu}}(p_T^{\mu\mu}, y^{\mu\mu})}{\frac{1}{N_{\text{MC}}^{\mu\mu}} \frac{d^2 N_{\text{MC}}^{\mu\mu}}{dp_T^{\mu\mu} dy^{\mu\mu}}(p_T^{\mu\mu}, y^{\mu\mu})} \quad (4.33)$$

3664 where $N_{\text{data}}^{\mu\mu}$ and $N_{\text{MC}}^{\mu\mu}$ are the number of J/ψ mesons measured in the inclusive region
 3665 in data and simulation, respectively. The J/ψ -meson kinematic weights determined as a
 3666 function of $p_T^{\mu\mu}$, in the mid-rapidity region, are presented in Figure 4.21. They are found
 3667 to vary between 0.4 and 1.6 depending on $p_T^{\mu\mu}$ and $y^{\mu\mu}$.

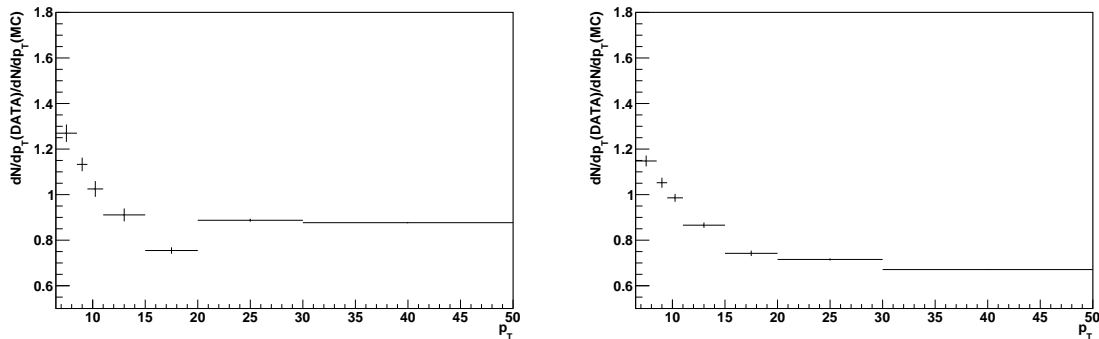


Figure 4.21: Data-to-simulation ratios of the prompt J/ψ -meson p_T distribution measured in the $|y^{\mu\mu}| < 0.6$ rapidity region, in Pb-Pb (left) and p-p (right) collisions.

3668 4.2.6.2 Acceptance of J/ψ mesons

3669 The J/ψ -meson acceptance is estimated using the p-p simulations. It is defined as the
 3670 fraction of generated $\mu^+ \mu^-$ pairs from J/ψ -meson decays, with each muon satisfying the

kinematic selection (labelled as *in CMS*) listed in Section 4.2.3.5. The modelling of the p_T and rapidity of prompt and nonprompt J/ψ mesons is improved by weighing each generated dimuon, based on their $p_T^{\mu\mu}$ and $y^{\mu\mu}$ values, using the J/ψ -meson kinematic weights $w^{J/\psi}$ defined in the previous section. The J/ψ -meson acceptance ($\mathcal{A}_{J/\psi}$) is determined as a function of the generated dimuon p_T and rapidity, according to:

$$\mathcal{A}_{J/\psi}(p_T^{\mu\mu}, y^{\mu\mu}) = \frac{N_{\text{gen},\mu \text{ in CMS}}^{J/\psi \rightarrow \mu^+ \mu^-}(p_T^{\mu\mu}, y^{\mu\mu})}{N_{\text{gen}}^{J/\psi \rightarrow \mu^+ \mu^-}(p_T^{\mu\mu}, y^{\mu\mu})} \quad (4.34)$$

where $N_{\text{gen}}^{J/\psi \rightarrow \mu^+ \mu^-}(p_T^{\mu\mu}, y^{\mu\mu})$ is the number of generated dimuons in a given $p_T^{\mu\mu}$ and $y^{\mu\mu}$ range, and $N_{\text{gen},\mu \text{ in CMS}}^{J/\psi \rightarrow \mu^+ \mu^-}(p_T^{\mu\mu}, y^{\mu\mu})$ represents the number of those satisfying the muon kinematic selection.

The J/ψ -meson acceptance derived from the prompt J/ψ simulations is presented in Figure 4.22. The trend observed as a function of dimuon p_T and rapidity is caused by the CMS muon kinematic coverage. J/ψ mesons produced in the forward region or at higher p_T are more likely to decay to muons that reach the CMS muon stations than those produced at mid-rapidity or lower p_T .

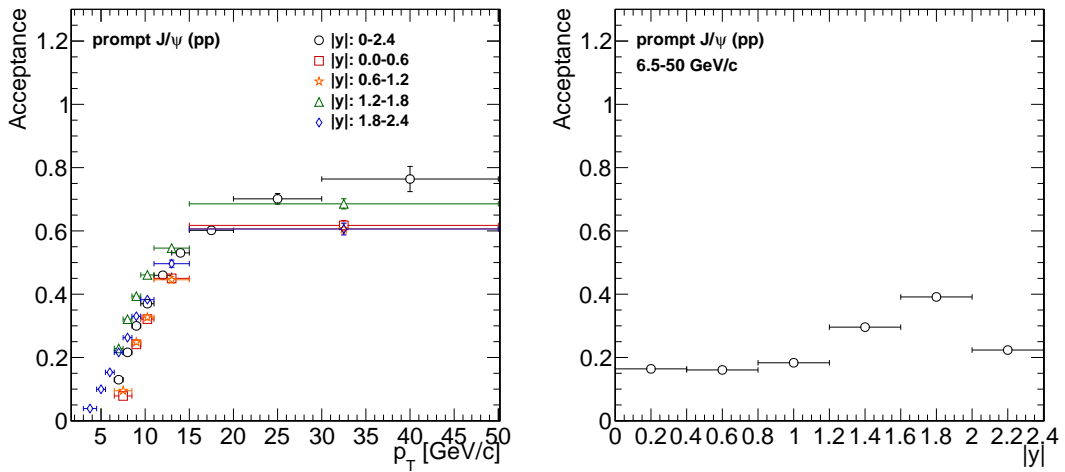


Figure 4.22: Acceptance of prompt J/ψ mesons, estimated from simulations, as a function of $p_T^{\mu\mu}$ (left) and $y^{\mu\mu}$ (right). The error bars represent the statistical uncertainties.

4.2.6.3 Efficiency of J/ψ mesons

The $J/\psi \rightarrow \mu^+ \mu^-$ simulations are used to measure the efficiency of prompt and nonprompt J/ψ mesons, in p-p and Pb-Pb collisions. In this case, a reconstructed $\mu^+ \mu^-$ pair is

3687 considered to be an offline dimuon if it satisfies the charmonium selection requirements
 3688 detailed in Sections 4.2.3.4 to 4.2.3.6. Among these selection criteria, each reconstructed
 3689 muon is required to satisfy the muon kinematic selection and identification criteria, and
 3690 match the trigger. Also, the two muon tracks of the offline dimuon are required to derive
 3691 from a common vertex with χ^2 probability larger than 1%.

3692 The J/ψ -meson efficiency is defined as the fraction of generated $\mu^+ \mu^-$ pairs in the ac-
 3693 ceptance that can be matched to an offline dimuon, with each generated muon satisfying
 3694 the kinematic selection. The matching between a generated and an offline $\mu^+ \mu^-$ pair is
 3695 performed by requiring that each generated and reconstructed muon of same charge are
 3696 within $\Delta R(\mu_{\text{gen}}, \mu_{\text{reco}}) < 0.03$. The p_T and rapidity spectra of the offline and generated
 3697 dimuons are weighed per event with the $w^{J/\psi}$ kinematic weights, as was done in the
 3698 previous section. The J/ψ -meson efficiency ($\epsilon_{J/\psi}$) is computed as a function of the dimuon
 3699 p_T and rapidity, according to:

$$\epsilon_{J/\psi}(p_T^{\mu\mu}, y^{\mu\mu}) = \frac{N_{\text{offline}}^{J/\psi \rightarrow \mu^+ \mu^-}(p_T^{\mu\mu}, y^{\mu\mu})}{N_{\text{gen}, \mu \text{ in CMS}}^{J/\psi \rightarrow \mu^+ \mu^-}(p_T^{\mu\mu}, y^{\mu\mu})} \quad (4.35)$$

3700 where $N_{\text{offline}}^{J/\psi \rightarrow \mu^+ \mu^-}$ and $N_{\text{gen}, \mu \text{ in CMS}}^{J/\psi \rightarrow \mu^+ \mu^-}$ are the number of offline and generated pairs of
 3701 muons within the kinematic acceptance of the analysis, accordingly.

3702 4.2.6.4 Efficiency of J/ψ mesons corrected with the tag-and-probe method

3703 In order to take into account possible discrepancies between the muon efficiencies in
 3704 simulation and those in data, the J/ψ -meson efficiencies are corrected with a set of
 3705 data-to-simulation corrections provided by the CMS HIN group and derived using the
 3706 tag-and-probe method. This collective work, to which I only participated marginally, is
 3707 documented in an internal analysis note [242].

3708 The TnP corrections for Pb-Pb and p-p efficiencies are computed following a procedure
 3709 similar to the one used for p-Pb collisions, which is described in detail in Section 3.2.6.2.
 3710 The main difference is that it addresses lower muon momentum. To provide these
 3711 muons, a sample of J/ψ mesons is used instead of Z bosons. Thus, the TnP corrections
 3712 are extracted from the prompt $J/\psi \rightarrow \mu^+ \mu^-$ simulations and from a data sample of
 3713 single muon events selected with the HLT trigger. The TnP method is used to measure
 3714 the standalone-muon reconstruction, tracking, identification and trigger efficiencies in
 3715 data and simulation. Apart from the different muon identification and trigger criteria,
 3716 these TnP efficiencies are probed in the same way as done for p-Pb collisions. The TnP

efficiencies are extracted by fitting the tag-probe invariant mass distribution, within the J/ψ mass region ($2.6 < m^{\mu\mu} < 3.5 \text{ GeV}/c^2$), for probes passing and failing the criteria of each efficiency under study.

After comparing the TnP efficiencies extracted from data and simulation, it is found that the muon simulated efficiencies for standalone-muon reconstruction, tracking and identification, are in good agreement with the data efficiencies. However, the trigger efficiencies are observed to disagree between simulation and data both in p-p and Pb-Pb collisions, as shown in Figure 4.23. As a result, only the simulated trigger efficiency requires a correction.

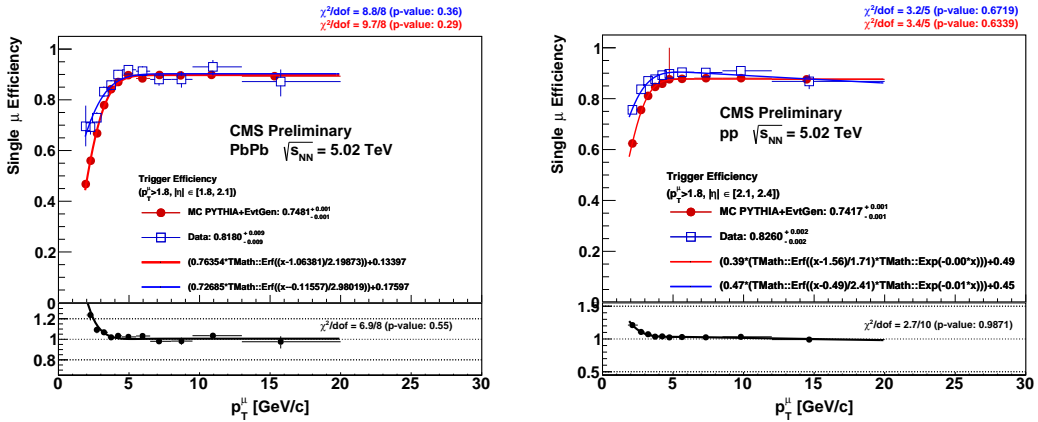


Figure 4.23: Muon trigger efficiencies as a function of the probe p_T . The efficiencies are extracted, using the TnP method, from data (blue) and simulation (red) in Pb-Pb collisions at $1.8 < |\eta^\mu| < 2.1$ (left) and p-p collisions at $2.1 < |\eta^\mu| < 2.4$ (right). The bottom panels show the data-to-simulation efficiency ratio. The results of the fits to the efficiencies are also shown. Figures taken from the private Ref. [242].

The muon trigger efficiencies are measured with respect to the probe p_T , in four $|\eta|$ regions with boundaries: $[0.0, 1.2, 1.8, 2.1, 2.4]$. The p_T dependence in each $|\eta|$ region is parametrised with a function of the form $f_{\text{trig}}(p_T) = c_1 \cdot \text{Erf}[(p_T - c_2)/c_3] \cdot \exp[c_4 \cdot p_T] + c_5$, where Erf is the error function and c_i are free parameters. The TnP-correction weight for the trigger efficiency is then derived from the ratio of the fitted functions, extracted from data and simulation, as a function of probe p_T in each $|\eta|$ region, given by:

$$w_{\text{trig}}(p_T, |\eta|) = \left[\frac{f_{\text{trig}}^{\text{data}}(p_T)}{f_{\text{trig}}^{\text{MC}}(p_T)} \right] (|\eta|) \quad (4.36)$$

To apply the TnP corrections, the J/ψ -meson efficiency is recomputed by weighing each offline dimuon with the TnP-correction weights for each muon to trigger, according

3734 to:

$$\epsilon_{J/\psi} = \frac{\left[N_{\text{offline}}^{J/\psi \rightarrow \mu^+ \mu^-} \sum_{i=1}^{N_{\text{offline}}^{J/\psi \rightarrow \mu^+ \mu^-}} w_{\text{trig}}(p_T^{\mu,+}, |\eta^{\mu,+}|) \cdot w_{\text{trig}}(p_T^{\mu,-}, |\eta^{\mu,-}|) \right]}{N_{\text{gen},\mu \text{ in CMS}}^{J/\psi \rightarrow \mu^+ \mu^-}} \quad (4.37)$$

3735 where $p_T^{\mu,+(\mu,-)}$ is the transverse momentum of positive (negative) charged muons, and
 3736 $\eta^{\mu,+(\mu,-)}$ is the corresponding pseudorapidity. The TnP corrections increase the J/ψ -meson
 3737 efficiency by 35% at $3 < p_T^{\mu\mu} < 6.5$ GeV/c, while the range of variation at $p_T^{\mu\mu} > 10$ GeV/c is
 3738 less than 4%. The corrected J/ψ -meson efficiencies are shown for p-p and Pb-Pb simulated
 3739 events in Figure 4.24 and Figure 4.25, respectively.

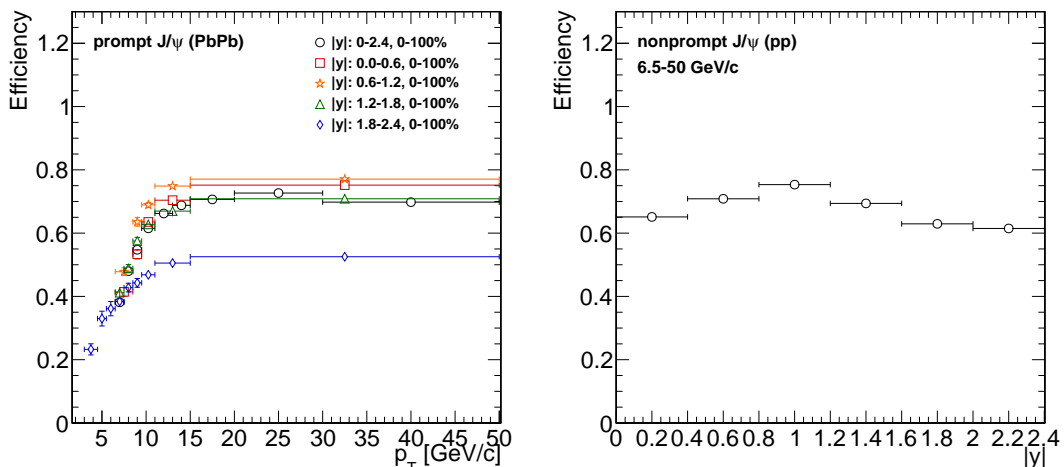


Figure 4.24: Corrected efficiencies of prompt J/ψ mesons measured in p-p collisions, as a function of $p_T^{\mu\mu}$ (left) and rapidity (right) in different rapidity regions. The error bars represent statistical uncertainties.

3740 **4.2.6.5 Double ratio of prompt $\psi(2S)/J/\psi$ efficiencies**

3741 Since the prompt $\psi(2S)$ and J/ψ mesons have similar masses and production mechanisms,
 3742 it is expected that their efficiencies cancel at first order when measuring the double
 3743 ratio of prompt charmonium yields in Pb-Pb relative to p-p collisions. In order to check
 3744 this, the efficiency of $\psi(2S)$ mesons ($\epsilon_{\psi(2S)}$) is estimated from the prompt $\psi(2S) \rightarrow \mu^+ \mu^-$
 3745 simulation, following the same procedure used to determine the J/ψ meson efficiency,
 3746 described in the previous sections.

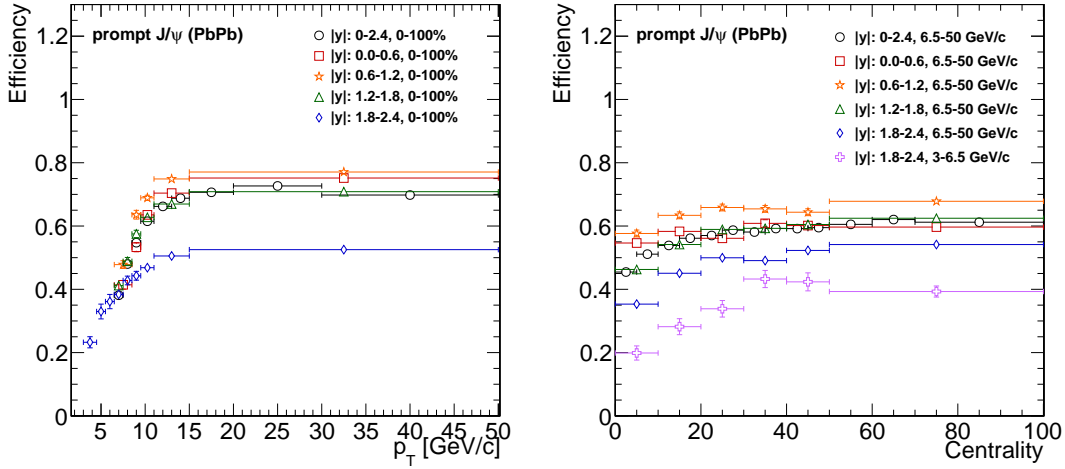


Figure 4.25: Corrected efficiencies of prompt J/ψ mesons measured in Pb-Pb collisions, as a function of $p_T^{\mu\mu}$ (left) and centrality (right), in different rapidity regions. The error bars represent statistical uncertainties.

3747 The prompt $\psi(2S)$ and J/ψ meson efficiencies are computed in p-p and Pb-Pb collisions,
 3748 including the $\ell_{J/\psi}$ selection defined in Section 4.2.5, and the double ratio of prompt
 3749 charmonium efficiencies is then computed as:

$$\chi^{\psi(2S)/J/\psi} = \frac{\left(\epsilon_{\psi(2S)} / \epsilon_{J/\psi}\right)_{\text{PbPb}}}{\left(\epsilon_{\psi(2S)} / \epsilon_{J/\psi}\right)_{\text{pp}}} \quad (4.38)$$

3750 The results of the double ratio of prompt charmonium efficiencies are presented in
 3751 Figure 4.26. It is observed that the $\chi^{\psi(2S)/J/\psi}$ is consistent with unity overall as expected.
 3752 Thus, the measurements of the double ratio of prompt charmonium yields do not require
 3753 to be corrected for detector efficiency, and the difference with respect to unity is assigned
 3754 as a systematic uncertainty as detailed in Section 4.2.8.2.

3755 4.2.7 Systematic uncertainties of J/ψ -meson yields

3756 This section describes the procedure used to derive the systematic uncertainties associ-
 3757 ated to the measurement of the prompt and nonprompt J/ψ -meson yields. The different
 3758 sources of systematic uncertainties arise from: the parametrisation of the dimuon in-
 3759 variant mass and pseudoproper-decay length distributions used to extract the signal,
 3760 and the estimation of the efficiency of J/ψ mesons. In this case, the leading systematic
 3761 uncertainty of the J/ψ -meson measurements in p-p and Pb-Pb collisions correspond to the

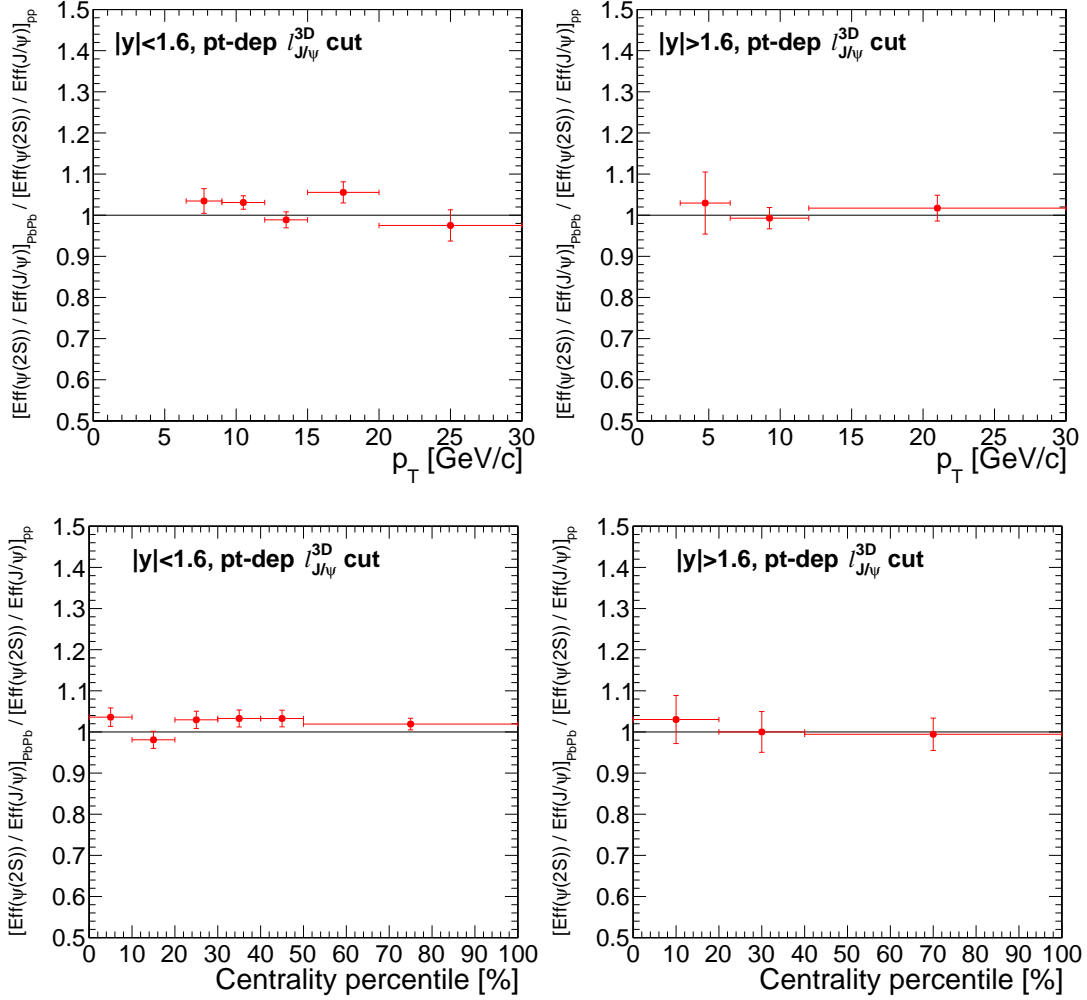


Figure 4.26: Double ratios of prompt charmonium efficiencies as a function of $p_T^{\mu\mu}$ (top) and centrality (bottom), in the rapidity regions: $|y^{\mu\mu}| < 1.6$ (left) and $|y^{\mu\mu}| > 1.6$ (right). The error bars represent statistical uncertainties.

3762 TnP efficiency corrections and the $\ell_{J/\psi}$ parametrisation, respectively. When describing
 3763 each systematic source, the corresponding largest relative uncertainty is mentioned.

3764 4.2.7.1 Uncertainty on the dimuon invariant mass parametrisation

3765 The uncertainty associated to the modelling of the $m^{\mu\mu}$ distribution arise from the
 3766 parametrisation of the signal and background invariant mass shape. It is determined by
 3767 varying the different components of the $m^{\mu\mu}$ functional form and redoing the 2D data
 3768 fits, while using the nominal $\ell_{J/\psi}$ functional form.

3769 **Parametrisation of the J/ψ -meson invariant mass distribution.** In order to esti-
3770 mate the systematic uncertainty associated to the choice of the J/ψ -meson invariant mass
3771 shape, two variations are performed:

- 3772 • **Variation of the J/ψ -meson invariant mass parameters:** the parameters fixed
3773 to simulation (i.e. the tail parameters $\alpha_{J/\psi}$ and $n_{J/\psi}$, and the ratio of CB widths) are
3774 released and the data fits are repeated. To improve the convergence of the fits, a set
3775 of Gaussian penalty functions, centred in the nominal value of the corresponding
3776 parameters, are added to constrain their range of variation.

3777 The range of variation of $\alpha_{J/\psi}$, $n_{J/\psi}$ and the ratio of CB widths is determined from
3778 data by redoing the $m^{\mu\mu}$ fits, leaving only one parameter free at the time while
3779 the other parameters are fixed to their nominal values. The RMS of the difference
3780 between the parameter value extracted from the data fit and the nominal one is
3781 computed including the results from different $p_T^{\mu\mu}$ and centrality intervals within
3782 each rapidity region, and the largest RMS obtained among the different rapidity
3783 regions is taken as the width of the corresponding Gaussian penalty function. The
3784 RMS is defined here as:

$$\text{RMS} = \sqrt{\frac{1}{\sum_i 1/(\sigma_{\text{data}}^i)^2} \cdot \sum_i \frac{(\text{par}_{\text{MC}} - \text{par}_{\text{data}}^i)^2}{(\sigma_{\text{data}}^i)^2}} \quad (4.39)$$

3785 where the sum runs over different p_T and centrality bins in the same rapidity
3786 region, $\text{par}_{\text{data}}^i$ and σ_{data}^i is the value and uncertainty of the parameter extracted
3787 from the data fit in a given analysis bin i , respectively, and par_{MC} is the correspond-
3788 ing nominal value derived from simulation. The width of the Gaussian penalty
3789 functions of each CB parameter is presented, relative to the nominal parameter
3790 value, in Table 4.12.

System	$\alpha_{J/\psi}$ [%]	$n_{J/\psi}$ [%]	$\sigma_{\text{CB},2}/\sigma_{\text{CB},1}$ [%]
p-p	16	21	
Pb-Pb	21	54	30

Table 4.12: Relative width used in the Gaussian penalty functions for the tail parameters $\alpha_{J/\psi}$ and n , and the ratio of CB widths. The Gaussian width is shown relative to the nominal parameter value.

3791 The systematic uncertainty associated to the determination of the signal mass
3792 parameters from simulations is then estimated by performing the data fits with

3793 the Gaussian penalty functions, and the difference between the varied J/ψ -meson
 3794 yields and the nominal results is taken as the uncertainty.

- 3795 • **Variation of the J/ψ -meson invariant mass model:** the functional form of
 3796 the signal invariant mass shape is changed from the nominal double Crystal
 3797 Ball function to a Crystal Ball plus a Gaussian function (with common mean
 3798 parameters), defined as:

$$M_{J/\psi}(m_{\mu^+\mu^-}) = f_{J/\psi} \cdot \text{CB}(m^{\mu\mu}) + (1 - f_{J/\psi}) \cdot \text{Gauss}(m^{\mu\mu}) \quad (4.40)$$

3799 As in the nominal case, the parameters of the alternative signal $m^{\mu\mu}$ model are
 3800 tuned from fits to the J/ψ -meson simulations, and the tail parameters $\alpha_{J/\psi}$ and $n_{J/\psi}$
 3801 are fixed to simulation in both p-p and Pb-Pb data fits, while the ratio of CB over
 3802 Gaussian widths ($\sigma_{\text{CB}}/\sigma_{\text{G}}$) is fixed only in the Pb-Pb data fits.

- 3803 • The systematic uncertainty on the signal shape parametrisation is then determined
 3804 from the quadratic sum of the uncertainties obtained from varying the invariant mass
 3805 parameters and the shape model. The corresponding uncertainty for prompt and non-
 3806 prompt J/ψ mesons amounts to 1.2% (2.7%) and 2.4% (2.7%), in p-p (Pb-Pb) collisions,
 3807 respectively.

3808 **Parametrisation of the background invariant mass shape.** In the case of the
 3809 background invariant mass parametrisation, three variations are performed to derive
 3810 the corresponding systematic uncertainty, given by:

- 3811 • **Variation of the LLR test threshold:** the χ^2 probability threshold is increased
 3812 from the nominal value (5%) to 10% and reduced to 2.5%, and the LLR tests are
 3813 repeated for each threshold. The background models selected from each LLR test
 3814 are then used to redo the 2D fits.
- 3815 • **Variation of the dimuon invariant mass fitting range:** the range of the $m^{\mu\mu}$
 3816 distribution used in the 2D fits is changed from 2.6-3.5 GeV/c^2 to 2.6-3.4 GeV/c^2 .
 3817 The 2D fits are then remade using the same orders of Chebyshev functions as used
 3818 in the nominal fits.
- 3819 • **Variation of the background invariant mass model:** the background $m^{\mu\mu}$
 3820 functional form is changed from the nominal Chebyshev function to an exponential
 3821 of a Chebyshev function, defined as:

$$M_{\text{bkg}}^N(m^{\mu\mu}) = \exp \left[\sum_{i=0}^N c_i T_i(m^{\mu\mu}) \right] \quad (4.41)$$

where T are Chebyshev polynomials and c are free parameters. As in the nominal analysis, the $m^{\mu\mu}$ distribution in data is fitted using the alternative background model with orders between 0 and 6, and the LLR test is employed with a 5% threshold to decide the best order in each analysis bin.

The uncertainty associated to each systematic variation is determined by computing the deviation of the measured prompt and nonprompt J/ψ -meson yields from the nominal results. In the case of the two variations done for the LLR test threshold, the maximum deviation between the two variations is taken for each J/ψ -meson yield. The systematic uncertainties of the different sources are combined by adding them in quadrature. The combined uncertainty amounts to 0.6% (3.0%) for prompt J/ψ mesons and 1.6% (2.9%) for nonprompt J/ψ mesons, in p-p (Pb-Pb) collisions.

4.2.7.2 Uncertainty on the pseudoproper-decay length parametrisation

The different systematic variations performed for the pseudoproper-decay length parametrisation are summarised as follows:

1. Modelling of the σ_ℓ distribution: replace the nominal signal and background σ_ℓ templates in the 2D fits with the template of the total σ_ℓ distribution.
2. Parametrisation of the $\ell_{J/\psi}$ resolution: parametrise the $\ell_{J/\psi}$ resolution model using the simulated sample of prompt J/ψ mesons instead of data.
3. Parametrisation of the nonprompt J/ψ -meson $\ell_{J/\psi}$ shape: replace the exponential $\ell_{J/\psi}$ model used to describe nonprompt J/ψ mesons in the 2D fits with a template of the $\ell_{J/\psi}$ distribution derived from simulation.
4. Parametrisation of the background $\ell_{J/\psi}$ shape: use a template of the $\ell_{J/\psi}$ distribution from the background-like dataset derived with $sPlot$, instead of a functional form.

The method and result of these four sources are detailed below, and the resulting uncertainties are summed in quadrature with the other systematic sources.

3847 **Modelling of the σ_ℓ distribution.** To estimate the uncertainty associated to the use
 3848 of the signal and background σ_ℓ template histograms, derived from the *sPlot* background-
 3849 and signal-like datasets, the template histograms of the signal and background are made
 3850 instead using the full σ_ℓ distribution and the 2D fits are remade. The difference between
 3851 the varied and nominal J/ψ meson yields is taken as the systematic uncertainty, which
 3852 amounts to 0.6% (6.3%) for prompt J/ψ mesons and 2.1% (4.2%) for nonprompt J/ψ mesons,
 3853 in p-p (Pb-Pb) collisions.

3854 **Parametrisation of the $\ell_{J/\psi}$ resolution.** The systematic uncertainty due to the
 3855 parametrisation of the $\ell_{J/\psi}$ resolution is estimated by extracting the $\ell_{J/\psi}$ resolution
 3856 parameters from J/ψ -meson simulations instead of the data. The $\ell_{J/\psi}$ resolution parame-
 3857 ters are extracted from simulated samples of prompt J/ψ mesons by fitting the nominal
 3858 $\ell_{J/\psi}$ resolution model (weighed sum of three Gaussians) to the simulated $\ell_{J/\psi}$ distribu-
 3859 tion. The varied $\ell_{J/\psi}$ resolution parameters are then used to remake the 2D fits and the
 3860 uncertainty is derived from the difference between the varied J/ψ -meson yields and the
 3861 nominal ones. This systematic uncertainty amounts in p-p (Pb-Pb) collisions to 1.5%
 3862 (4.7%) for prompt J/ψ mesons and 5.3% (9.6%) for nonprompt J/ψ mesons.

3863 **Parametrisation of the nonprompt J/ψ -meson $\ell_{J/\psi}$ shape.** The systematic uncer-
 3864 tainty associated to the modelling of the $\ell_{J/\psi}$ distribution of nonprompt J/ψ mesons is
 3865 computed by replacing the nominal signal functional form (convolution of exponential
 3866 decay with $\ell_{J/\psi}$ resolution model) with an unbinned template of the reconstructed $\ell_{J/\psi}$
 3867 distribution derived from simulation of nonprompt J/ψ mesons. The $\ell_{J/\psi}$ templates are
 3868 made using a kernel estimation technique [243], implemented in the RooFit framework,
 3869 which parametrise the distribution of a given variable by superimposing a Gaussian
 3870 function to each data point. The uncertainty is then determined from the difference be-
 3871 tween the varied signal yields and the nominal results, and reaches up to 0.8% (3.4%) for
 3872 prompt J/ψ mesons and 2.1% (12.1%) for nonprompt J/ψ mesons, in p-p (Pb-Pb) collisions.

3873 **Parametrisation of the background $\ell_{J/\psi}$ shape.** The systematic uncertainty re-
 3874 lated to the choice of background $\ell_{J/\psi}$ model is determined by replacing the nominal
 3875 background functional form (three exponential decay functions convolved with the $\ell_{J/\psi}$
 3876 resolution model) with an unbinned template. The template is built from the $\ell_{J/\psi}$ distri-
 3877 bution of the *sPlot* background-like dataset employed in Section 4.2.4.4, using the RooFit
 3878 kernel estimation technique. This uncertainty contributes in p-p (Pb-Pb) collisions up to
 3879 0.5% (10%) for prompt J/ψ mesons and 1.2% (22.3%) for nonprompt J/ψ mesons.

4.2.7.3 Uncertainty on the J/ψ -meson efficiency

There are two main sources of systematics that affects the measurement of the J/ψ -meson efficiencies: the TnP-correction weights used to correct the simulated efficiencies and the charmonium $p_T^{\mu\mu}$ - $y^{\mu\mu}$ weights applied to improve the modelling of the J/ψ -meson p_T and rapidity. Among these two, the largest uncertainty is obtained from the TnP corrections, which is dominated by the uncertainty on the extraction of the standalone-muon reconstruction efficiency in data.

Tag-and-probe correction. The uncertainty associated to the TnP correction derives from the measurement of the TnP data efficiency of muon identification, trigger, tracking and standalone-muon reconstruction.

Regarding the tracking efficiency, an overall systematic uncertainty is determined from the largest difference found between data and simulation, which corresponds to a relative uncertainty on the J/ψ -meson yields measured in p-p and Pb-Pb collisions of 1.0% and 2.4%, respectively. On the other hand, for the standalone-muon reconstruction, trigger and muon identification, the uncertainties of the TnP-correction weights are separated in a statistical and systematic component. The statistical component of the TnP-correction uncertainty is evaluated by producing a hundred sets of TnP-correction weights, where each point is randomly generated using a Gaussian distribution spread according to its statistical uncertainty. The hundred sets of TnP-correction weights are then used to recompute the J/ψ -meson efficiencies and the corresponding systematic uncertainty is estimated by computing the RMS of the hundred variations of the prompt and nonprompt J/ψ -meson efficiencies. The systematic component of the TnP-correction uncertainty is propagated using two sets of TnP-correction weights generated by shifting all points up and down, according to the systematic uncertainty of each point (derived by varying the settings of the TnP invariant mass fits). The J/ψ -meson efficiencies are then corrected with each set of TnP-correction weights and the maximum deviation of the two varied efficiencies with respect to the nominal one is taken as the systematic uncertainty on the efficiency of prompt and nonprompt J/ψ mesons.

The statistical component of the TnP uncertainty represents 1.5% (4.6%) for the p-p (Pb-Pb) efficiencies. Regarding the systematic components of the TnP uncertainty, the largest uncertainty is obtained from the standalone-muon reconstruction efficiency, which corresponds to 9.6%, while the TnP-correction uncertainties associated to the trigger and muon identification efficiencies in p-p (Pb-Pb) collisions amounts to 0.5% (5.2%) and to 1.1% (3.3%), respectively.

3914 **Charmonium transverse momentum and rapidity weighing.** The simulated sam-
 3915 ples of J/ψ mesons are weighed as a function of dimuon p_{T} and rapidity, to match the
 3916 p_{T} spectrum of prompt and nonprompt J/ψ mesons observed in data in four rapidity
 3917 regions. In order to estimate the uncertainty of the weighing procedure, a hundred
 3918 sets of weights are randomly generated using a Gaussian distribution for each $p_{\text{T}}^{\mu\mu}$ - $y^{\mu\mu}$
 3919 interval, where the Gaussian width is fixed to the uncertainty of the corresponding
 3920 dimuon kinematic weight. The simulations are reweighed with each set of generated
 3921 dimuon kinematic weights and then used to recompute the efficiencies of prompt and
 3922 nonprompt J/ψ mesons. The corresponding systematic uncertainty is then determined
 3923 from the RMS of the hundred varied efficiencies compared to the nominal efficiency for
 3924 prompt and nonprompt J/ψ mesons. In this case, the largest relative uncertainty on the
 3925 p-p (Pb-Pb) J/ψ -meson efficiencies corresponds to 0.2% (1.8%).

3926 4.2.8 Systematic uncertainties on the $\psi(2\text{S})/\text{J}/\psi$ ratio

3927 This section is dedicated to the systematic uncertainties that contributes in the measure-
 3928 ment of the $(N_{\psi(2\text{S})}/N_{\text{J}/\psi})_{\text{PbPb}}/(N_{\psi(2\text{S})}/N_{\text{J}/\psi})_{\text{pp}}$ double ratio. Three sources of systematics
 3929 are accounted for: the parametrisation of the dimuon invariant mass used in the signal
 3930 extraction, the degree of cancellation of the charmonium efficiencies in the double ratio
 3931 and the subtraction of the nonprompt charmonium component.

3932 4.2.8.1 Uncertainty on the dimuon invariant mass parametrisation

3933 A large part of the method used to determine the uncertainty on the signal and back-
 3934 ground $m^{\mu\mu}$ shape parametrisation is common to the one used for the prompt and
 3935 nonprompt J/ψ meson yields, presented in Section 4.2.7.1. Indeed, the $\psi(2\text{S})$ -to- J/ψ dou-
 3936 ble ratio analysis was performed first and was less demanding in terms of systematic
 3937 uncertainties, due to the limited $\psi(2\text{S})$ statistics. However, it served as a basis for the
 3938 J/ψ -meson yield analysis and all the sources considered here were kept.

3939 The functional forms of the J/ψ -meson, $\psi(2\text{S})$ -meson and background invariant mass
 3940 shape are varied accordingly and the fits to data are remade. The nominal background
 3941 shape is used when varying the signal functional form and vice versa. The variations
 3942 performed on the signal functional forms includes:

- 3943 • varying the CB parameters fixed to simulation ($\alpha_{\text{J}/\psi}$, $n_{\text{J}/\psi}$ and $\sigma_{\text{CB},2}/\sigma_{\text{CB},1}$) in the
 3944 following way:

- 3945 1. setting $\alpha_{J/\psi}$ free while keeping $n_{J/\psi}$ (and $\sigma_{CB,2}/\sigma_{CB,1}$ in PbPb fits) fixed to
3946 simulation;
3947 2. setting $n_{J/\psi}$ free while keeping $\alpha_{J/\psi}$ fixed (only done for pp data since the PbPb
3948 data fits did not converge);
3949 3. fixing the CB parameters to their corresponding values derived from the
3950 prompt $\psi(2S)$ -meson simulation, instead of the J/ψ -meson simulation.
3951 • changing the signal shape model by using a Gaussian plus a Crystal Ball function
3952 (with common mean), instead of the nominal double Crystal Ball function. The
3953 alternative model parameters are tuned and fixed in the same way as done for the
3954 nominal model;

3955 In the case of the background functional form, the following variations are done:

- 3956 • the fitted dimuon invariant mass range is changed to 2.2-4.2 GeV/c^2 , instead of
3957 2.2-4.5 GeV/c^2 ;
3958 • the background shape model is changed to an exponential of a Chebyshev function,
3959 instead of the nominal Chebyshev function. The LLR tests are remade to determine
3960 the best order of the exponent in each analysis bin;
3961 • the LLR test selection criteria is changed by varying the χ^2 -probability threshold
3962 to 10% and 2.5%, instead of nominal 5%.

3963 The difference between the $(N_{\psi(2S)}/N_{J/\psi})$ ratio extracted from the varied data fits and
3964 the nominal results defines the uncertainty on the single ratio of charmonium yields.

3965 In the case of the two LLR test variations, the largest difference in the single ratios is
3966 considered. This procedure is performed separately for p-p and Pb-Pb collisions, and the
3967 corresponding uncertainties on the single ratios are then propagated to the double ratio.

3968 The uncertainties derived from each of the signal and background model variations
3969 are summed in quadrature. The largest relative uncertainty on the $(N_{\psi(2S)}/N_{J/\psi})$ ra-
3970 tio, measured in p-p (Pb-Pb) collisions, corresponds to 1.9% (18.5%) from the signal
3971 parametrisation and 5.3% (37.3%) from the background parametrisation.

3972 4.2.8.2 Uncertainty on the cancellation of the double ratio of efficiencies

3973 The cancellation of the double ratio of $\psi(2S)$ over J/ψ meson efficiencies is verified up to
3974 a finite degree of precision determined by the statistical precision of the simulations and

3975 the modelling of the charmonium kinematic spectra. In this case, the following sources
 3976 of systematic uncertainties are taken into account:

- 3977 • the statistical uncertainty of the double ratio of efficiencies extracted from the
 3978 simulated samples (i.e. the error bars in Figure 4.26);
- 3979 • the difference between unity and the value of the double ratio of efficiencies
 3980 computed after weighing per-event the simulated dimuon p_T spectrum to the
 3981 corresponding charmonium p_T distribution observed in data (the charmonium p_T
 3982 spectrum in data is extracted from the nominal fits);
- 3983 • the spread of the double ratio of efficiencies determined with MC studies, consider-
 3984 ing the range of p_T spectra compatible with the Pb-Pb and p-p data. This is done
 3985 by generating a hundred random p_T distributions of the charmonium p_T spectrum
 3986 extracted from the nominal data fits, where each data point is randomised follow-
 3987 ing a Gaussian distribution with mean and width equal to the nominal value and
 3988 statistical uncertainty, respectively. Then the simulated dimuon p_T spectrum is
 3989 weighed, event-by-event, to match each of the generated random p_T distributions,
 3990 and in each case, the double ratio of efficiencies is computed. The RMS of the one
 3991 hundred efficiency double ratio values is taken as the systematic uncertainty.

3992 These three sources of uncertainties are summed in quadrature. In this case, the
 3993 largest relative uncertainty on the double ratio of charmonium yields amounts to 20%.

3994 4.2.8.3 Uncertainty on the subtraction of nonprompt charmonia

3995 The nominal method used to subtract the nonprompt charmonium contamination relies
 3996 on simulations to determine the expected fraction of prompt and nonprompt charmonia
 3997 passing and failing the $\ell_{J/\psi}$ selection. To determine the uncertainty on this procedure, a
 3998 set of 2D fits are employed using the same procedure employed in Ref. [244], which is
 3999 similar to the one presented in this chapter.

4000 The 2D fits are performed in two dimuon invariant mass ranges: 2.2-3.5 GeV/ c^2 and
 4001 3.3-4.4 GeV/ c^2 . The first one is used to extract the fraction of nonprompt J/ψ mesons
 4002 in p-p and Pb-Pb data, while the second range is used to derive the nonprompt $\psi(2S)$
 4003 meson fraction from p-p data only. The prompt charmonium yields are then computed
 4004 using the nonprompt charmonium fractions extracted from the 2D fits ($f_\psi^{\text{NP},\text{2D}}$), as given
 4005 by:

$$N_{\psi}^{\text{P},2\text{D}} = \left(1 - f_{\psi}^{\text{NP},2\text{D}}\right) N_{\psi}^{\text{tot}} \quad (4.42)$$

where N_{ψ}^{tot} is the total number of charmonia extracted from the nominal fits.

In the case of $\psi(2\text{S})$ mesons in Pb-Pb collisions, the number of prompt $\psi(2\text{S})$ mesons is derived according to:

$$N_{\psi(2\text{S}),\text{PbPb}}^{\text{P},2\text{D}} = N_{\psi(2\text{S}),\text{PbPb}}^{\text{P,nominal}} \times \left(\frac{N_{\psi(2\text{S}),\text{pp}}^{\text{P},2\text{D}}}{N_{\psi(2\text{S}),\text{pp}}^{\text{P,nominal}}} \right) \quad (4.43)$$

where $N_{\psi(2\text{S})}^{\text{P,nominal}}$ is the number of prompt $\psi(2\text{S})$ mesons determined in the nominal case, as presented in Section 4.2.5.3.

The double ratio is then recomputed using the prompt charmonium yields derived from Eq. (4.42) and Eq. (4.43). The difference between the double ratio of charmonium yields when accounting for the nonprompt charmonium contamination using the nominal method and using 2D fits, is taken as a systematic uncertainty. The largest relative uncertainty is found to be 17.7%.

4.3 Results

This section presents the measurements of the charmonium production in Pb-Pb and p-p collisions at $\sqrt{s_{\text{NN}}} = 5.02 \text{ TeV}$. The results of the nonprompt fraction of J/ψ mesons are shown in Section 4.3.1. In Section 4.3.2, the measurements of the normalised cross sections of J/ψ -meson production in p-p and Pb-Pb collisions, are reported. The nuclear modification factor of J/ψ mesons and the double ratio of prompt $\psi(2\text{S})$ over J/ψ meson yields are presented in Section 4.3.3 and Section 4.3.4, respectively.

4.3.1 Nonprompt fraction of J/ψ mesons

The fraction of J/ψ mesons coming from b-hadron decays is measured in p-p and Pb-Pb collisions at $\sqrt{s_{\text{NN}}} = 5.02 \text{ TeV}$, for different dimuon rapidity and p_{T} intervals. The nonprompt J/ψ -meson fraction is extracted by performing 2D fits to the $m^{\mu\mu}$ and $\ell_{\text{J}/\psi}$ distributions in data. The extracted fractions are corrected for detector acceptance and efficiency, in each analysis bin and collision system, according to:

$$b_{\text{J}/\psi} = b_{\text{J}/\psi}^{\text{raw}} \left(\frac{(\mathcal{A}_{\text{J}/\psi} \times \epsilon_{\text{J}/\psi})^{\text{P}}}{b_{\text{J}/\psi}^{\text{raw}} (\mathcal{A}_{\text{J}/\psi} \times \epsilon_{\text{J}/\psi})^{\text{P}} + (1 - b_{\text{J}/\psi}^{\text{raw}}) (\mathcal{A}_{\text{J}/\psi} \times \epsilon_{\text{J}/\psi})^{\text{NP}}} \right) \quad (4.44)$$

4.3. RESULTS

where $b_{J/\psi}^{\text{raw}}$ is the nonprompt J/ψ -meson fraction determined from the data fits, and $(\mathcal{A}_{J/\psi} \times \epsilon_{J/\psi})^P$ and $(\mathcal{A}_{J/\psi} \times \epsilon_{J/\psi})^{\text{NP}}$ are the acceptance times efficiency factors for prompt and nonprompt J/ψ mesons, respectively. The systematic uncertainty of the acceptance and efficiency corrections, and the statistical uncertainty from the 2D fits, are propagated to the measured nonprompt J/ψ -meson fraction.

Figure 4.27 shows the $b_{J/\psi}$ results as a function of dimuon p_T and rapidity, measured in p-p and Pb-Pb collisions. The nonprompt fraction of J/ψ mesons is observed to not vary significantly with respect to rapidity. However, it depends strongly on $p_T^{\mu\mu}$, increasing from ~ 0.2 at $p_T^{\mu\mu} \approx 6.5 \text{ GeV}/c$ to ~ 0.6 at $p_T^{\mu\mu} > 30 \text{ GeV}/c$. The $b_{J/\psi}$ measurements are also seen to be slightly larger in Pb-Pb compared to p-p collisions at $p_T^{\mu\mu} < 20 \text{ GeV}/c$. Considering the significant $b_{J/\psi}$ fraction measured at high p_T , these results reaffirm the need to distinguish the contributions from prompt and nonprompt J/ψ mesons, in order to disentangle the hot nuclear matter effects that impact the production of charmonia and b hadrons.

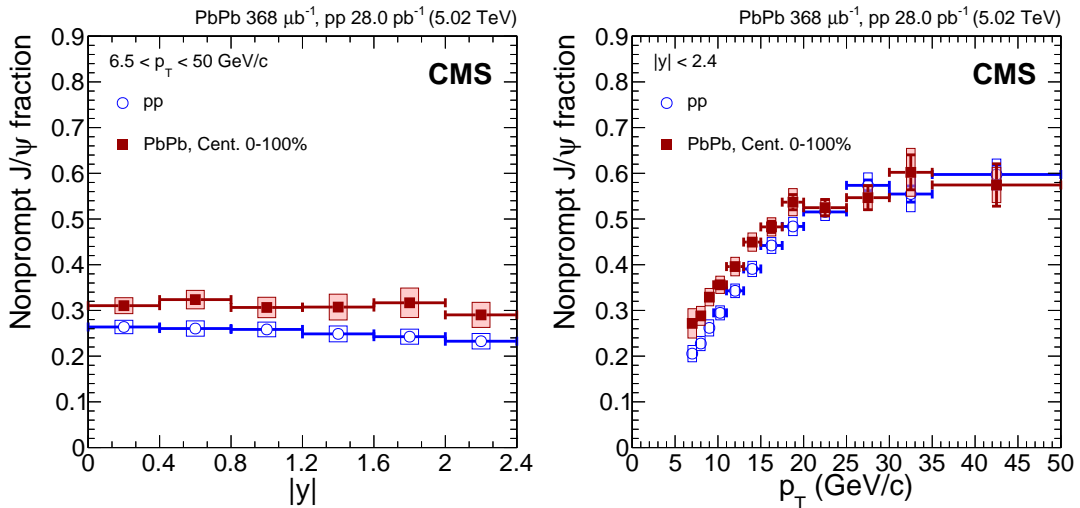


Figure 4.27: Nonprompt fraction of J/ψ mesons measured in p-p and Pb-Pb collisions, as a function of dimuon rapidity (left) and p_T (right). The boxes (bars) represent the systematic (statistical) uncertainties. Figures published in Ref. [231].

4.3.2 Cross section of prompt and nonprompt J/ψ mesons

The J/ψ -meson production cross sections are derived from the measured number of prompt and nonprompt J/ψ mesons as:

$$N_{J/\psi} = \frac{N_{J/\psi}^{\text{raw}}}{(\mathcal{A}_{J/\psi} \times \epsilon_{J/\psi})} \quad (4.45)$$

where $N_{J/\psi}^{\text{raw}}$ is the number of prompt or nonprompt J/ψ mesons extracted from the 2D fits to the $m^{\mu\mu}$ and $\ell_{J/\psi}$ distributions in data, and $\epsilon_{J/\psi}$ and $\mathcal{A}_{J/\psi}$ are the corresponding J/ψ -meson efficiency and acceptance, respectively. In the case of p-p collisions, the production cross section of prompt and nonprompt J/ψ mesons decaying into $\mu^+\mu^-$ is computed as follows:

$$B(J/\psi \rightarrow \mu^+\mu^-) \frac{d^2\sigma_{J/\psi}^{\text{pp}}}{dp_T^{\mu\mu} dy^{\mu\mu}} = \frac{1}{\mathcal{L}_{\text{pp}}} \left(\frac{N_{J/\psi}^{\text{pp}}}{\Delta p_T^{\mu\mu} \Delta y^{\mu\mu}} \right) \quad (4.46)$$

where B represents the branching ratio of $J/\psi \rightarrow \mu^+\mu^-$ decays, $N_{J/\psi}^{\text{pp}}$ is the number of prompt or nonprompt J/ψ mesons measured in p-p collisions, $\mathcal{L}_{\text{pp}} = 28.0 \pm 0.6 \text{ pb}^{-1}$ is the recorded integrated luminosity of the p-p data sample, and $\Delta p_T^{\mu\mu}$ and $\Delta y^{\mu\mu}$ are the widths of the dimuon p_T and rapidity intervals in which the measurement is performed.

In order to directly compare the Pb-Pb measurements with those from p-p collisions, the $J/\psi \rightarrow \mu^+\mu^-$ cross section in Pb-Pb collisions is presented in the following way:

$$B(J/\psi \rightarrow \mu^+\mu^-) \frac{d^2\sigma_{J/\psi}^{\text{PbPb}}}{dp_T^{\mu\mu} dy^{\mu\mu}} = \frac{1}{\langle T_{\text{AA}} \rangle \cdot N_{\text{MB}}} \left(\frac{N_{J/\psi}^{\text{pp}}}{\Delta p_T^{\mu\mu} \Delta y^{\mu\mu}} \right) \quad (4.47)$$

where $N_{\text{MB}} = (2.37 \pm 0.05) \times 10^9$ represents the efficiency-corrected number of minimum bias events sampled by the analysis trigger and $\langle T_{\text{AA}} \rangle = 5.61^{+0.16}_{-0.19}$ is the nuclear-overlap function integrated over the 0 – 100% centrality range. The centrality-integrated T_{AA} is equal to $A^2/\sigma_{\text{PbPb}}^{\text{inel}}$, where $A = 208$ is the atomic number of Pb ions and $\sigma_{\text{PbPb}}^{\text{inel}} = N_{\text{MB}}/\mathcal{L}_{\text{PbPb}}$ is the total PbPb inelastic cross section.

The systematic uncertainties that impacts the measurement of the prompt and nonprompt $J/\psi \rightarrow \mu^+\mu^-$ cross sections in p-p and Pb-Pb collisions are:

- The uncertainty on the J/ψ -meson extraction. It is associated to the parametrisation of the dimuon $m^{\mu\mu}$ and $\ell_{J/\psi}$ distributions, and it is determined by varying the different components of the 2D fit model as described in Sections 4.2.7.1 and 4.2.7.2.
- The uncertainty on the efficiency estimation. It includes the uncertainties due to the TnP corrections applied to the efficiency, the J/ψ -meson p_T and rapidity weighing applied to the simulated dimuons, and the statistics of the simulated samples, as detailed in Section 4.2.7.3.

- The uncertainty on the measurement of the number of minimum bias events N_{MB} probed by the dimuon trigger, which corresponds to 2%.
- The uncertainty on the p-p integrated luminosity. It has been derived by the CMS collaboration and corresponds to 2.3% [245].
- The uncertainty on the $\langle T_{\text{AA}} \rangle$ computation. The $\langle T_{\text{AA}} \rangle$ relative asymmetric uncertainty in the centrality range 0 – 100% is $[-3.4\%, +2.8\%]$.

The global uncertainties (i.e. the same across all measurements) of the J/ψ -meson cross sections correspond to: the p-p integrated luminosity uncertainty of 2.3% for p-p collisions, and the $\langle T_{\text{AA}} \rangle$ and N_{MB} uncertainties, which quadrature sums to a relative asymmetric uncertainty of $[-3.9\%, +3.4\%]$, for Pb-Pb collisions.

The results of the J/ψ -meson cross sections, measured in p-p and Pb-Pb collisions are presented in Figure 4.28. The J/ψ -meson cross sections decrease rapidly towards higher $p_T^{\mu\mu}$ values, with the same trend between prompt and nonprompt J/ψ mesons, and between both collisions systems. The measurements as a function of rapidity are seen to decrease when approaching the forward region ($|y^{\mu\mu}| > 1.2$), and similar trends are also observed between the different measurements.

4.3.3 Nuclear modification factor of J/ψ mesons

The modification of the prompt and nonprompt production of J/ψ mesons in Pb-Pb collisions is studied by measuring the nuclear modification factor, computed from the ratio of PbPb-to-pp cross sections presented in the previous section. The nuclear modification factor of J/ψ mesons is defined as:

$$R_{\text{AA}}^{J/\psi} = \left(\frac{d^2\sigma_{J/\psi}^{\text{PbPb}} / dp_T^{\mu\mu} dy^{\mu\mu}}{d^2\sigma_{J/\psi}^{\text{pp}} / dp_T^{\mu\mu} dy^{\mu\mu}} \right) = \frac{\mathcal{L}_{\text{pp}}}{\langle T_{\text{AA}} \rangle \cdot N_{\text{MB}} \cdot \Delta_{\text{cent}}} \left(\frac{N_{J/\psi}^{\text{PbPb}}}{N_{J/\psi}^{\text{pp}}} \right) \quad (4.48)$$

where Δ_{cent} is the fraction of the total hadronic inelastic cross section sampled in the measured centrality range (e.g. 0.3 for 70–100%). The measurements of the J/ψ -meson nuclear modification factor are performed as a function of the dimuon p_T , rapidity and the average number of participants $\langle N_{\text{part}} \rangle$.

The global uncertainties that enters in the measurement of the nuclear modification factor depends on which variable is used to bin the data. On the one hand, if the results are measured differentially in centrality, the global uncertainties include the statistical

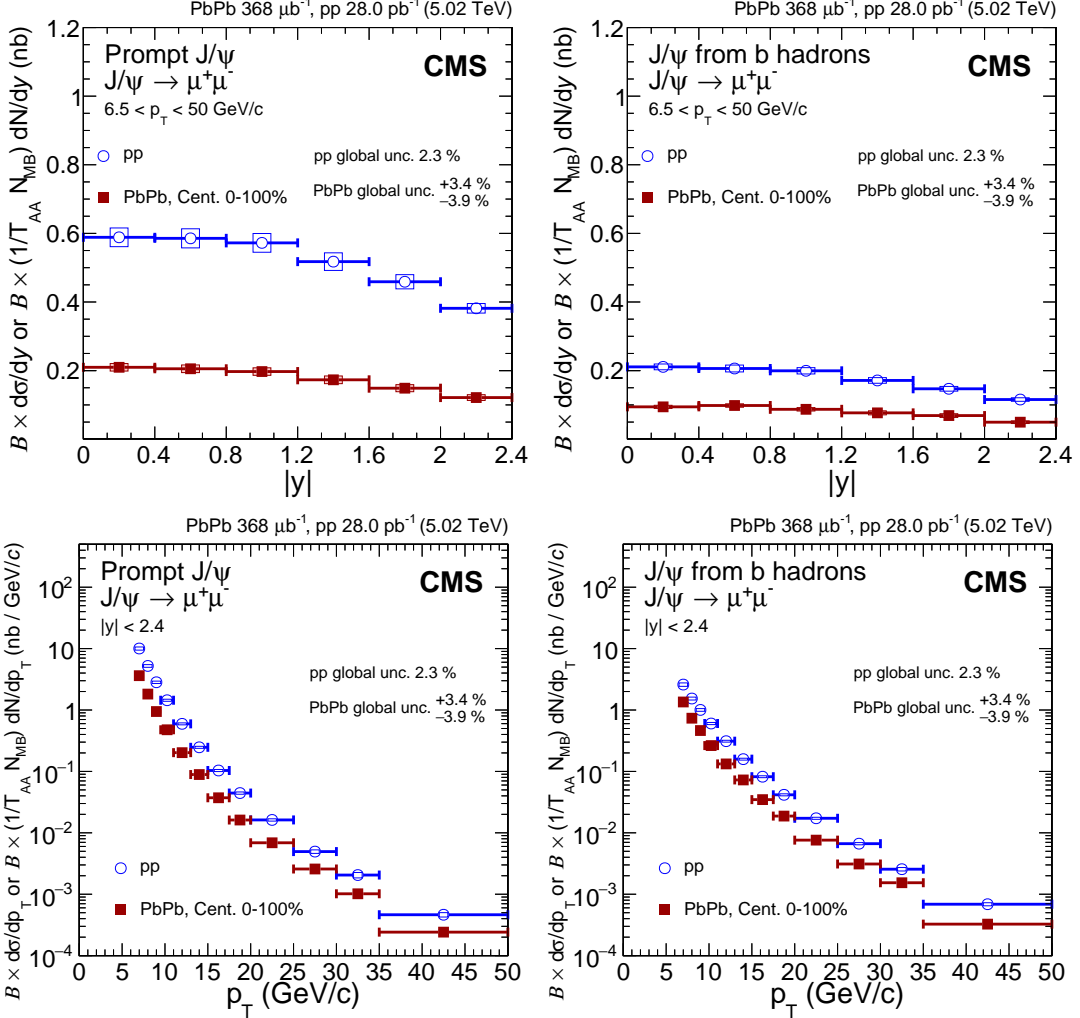


Figure 4.28: Differential cross section of the production of prompt (left) and nonprompt (right) J/ψ mesons decaying into $\mu^+\mu^-$, as a function of dimuon rapidity (top) and p_T (bottom) in p-p (blue open circles) and Pb-Pb (red squares) collisions. The boxes (bars) represent the systematic (statistical) uncertainties. The global relative uncertainties are written in the plots. Figures published in Ref. [231].

and systematic uncertainty of the J/ψ -meson cross section in p-p collisions, and the N_{MB} uncertainty of the Pb-Pb data. On the other hand, if the measurements are performed in different $p_T^{\mu\mu}$ or $y^{\mu\mu}$ intervals, then the global uncertainty includes the p-p integrated luminosity uncertainty, the Pb-Pb N_{MB} uncertainty and the uncertainty on the $\langle T_{\text{AA}} \rangle$ corresponding to the centrality range probed. The $\langle T_{\text{AA}} \rangle$ uncertainties are found to vary from 2% in central Pb-Pb collisions to 16% in the most peripheral ones, as presented in Table 4.8.

4107 **4.3.3.1 Prompt J/ ψ -meson R_{AA}**

4108 The R_{AA} results as a function of $p_T^{\mu\mu}$, rapidity and $\langle N_{\text{part}} \rangle$ are shown in Figure 4.29. The
 4109 measurements are compared with the CMS results derived at $\sqrt{s_{\text{NN}}} = 2.76 \text{ TeV}$ and found
 4110 to be in agreement within uncertainties.

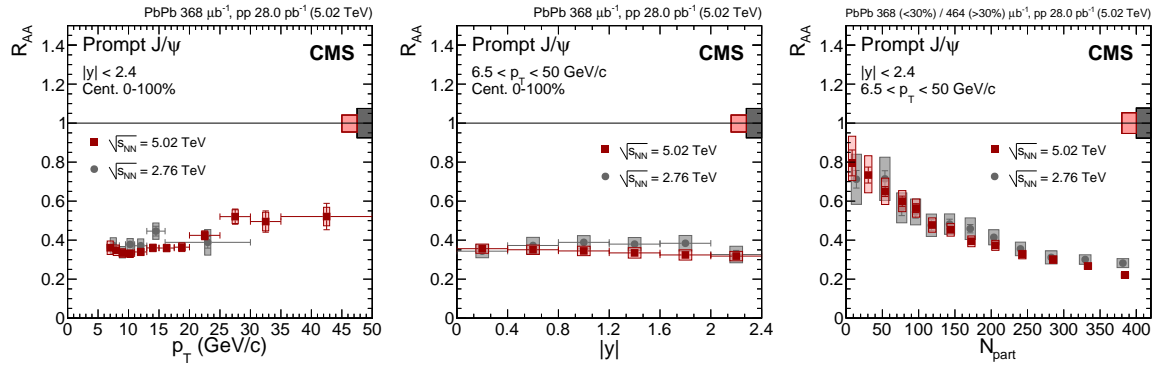


Figure 4.29: Nuclear modification factor of prompt J/ψ mesons measured at $\sqrt{s_{\text{NN}}} = 2.76 \text{ TeV}$ [244] (grey circles) and $\sqrt{s_{\text{NN}}} = 5.02 \text{ TeV}$ [231] (red squares), as a function of dimuon p_T (left), rapidity (middle) and $\langle N_{\text{part}} \rangle$ (right). The boxes (bars) represent the systematic (statistical) uncertainties. The size of the global relative uncertainties are depicted in the boxes plotted at $R_{\text{AA}} = 1$. Figures published in Ref. [231].

4111 The prompt J/ψ -meson R_{AA} is less than unity in all measurements, which means that
 4112 prompt J/ψ mesons are suppressed in Pb-Pb collisions. It is observed that the dependence
 4113 on $p_T^{\mu\mu}$ is mostly flat at $p_T^{\mu\mu} > 6.5 \text{ GeV}/c$, except in the highest p_T intervals ($p_T^{\mu\mu} > 25 \text{ GeV}/c$),
 4114 where the prompt J/ψ -meson suppression is seen to be weaker. Moreover, the prompt
 4115 J/ψ mesons are more suppressed toward central collisions, which is consistent with the
 4116 picture of colour-screening due to the QGP.

4117 Double-differential results as a function of $p_T^{\mu\mu}$ and $\langle N_{\text{part}} \rangle$ are displayed in Fig-
 4118 ure 4.30. The $p_T^{\mu\mu}$ dependence is presented for the mid- ($|y^{\mu\mu}| < 0.6$) and most forward
 4119 ($2.0 < |y^{\mu\mu}| < 2.4$) rapidity regions, while the measurements as a function of $\langle N_{\text{part}} \rangle$ are
 4120 shown in two dimuon p_T intervals: $3 < p_T^{\mu\mu} < 6.5 \text{ GeV}/c$ and $6.5 < p_T^{\mu\mu} < 50 \text{ GeV}/c$, at for-
 4121 ward rapidity. An indication of less suppression is seen in central collisions ($\langle N_{\text{part}} \rangle > 200$,
 4122 corresponding to 0-30% centrality) for lower $p_T^{\mu\mu}$ values ($3.0 < p_T^{\mu\mu} < 6.5 \text{ GeV}/c$). Such
 4123 reduction in the J/ψ -meson suppression could be caused by possible contributions from
 4124 regenerated charmonia due to the hot medium.

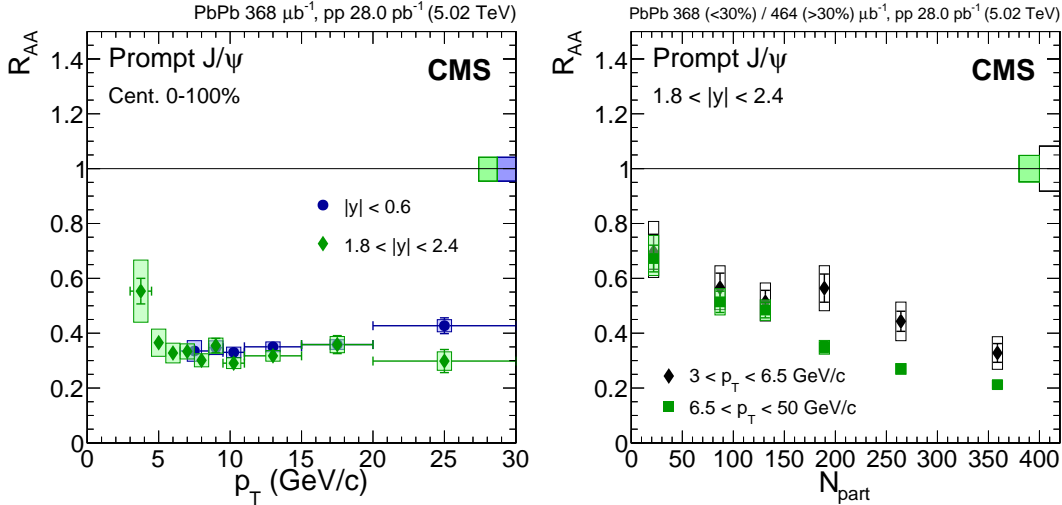


Figure 4.30: Nuclear modification factor of prompt J/ψ mesons. Left: as a function of $p_T^{\mu\mu}$ in the mid- and most forward rapidity regions. Right: as a function of $\langle N_{part} \rangle$ at $3 < p_T^{\mu\mu} < 6.5$ GeV/c and $6.5 < p_T^{\mu\mu} < 50$ GeV/c, in the $1.8 < |y^{\mu\mu}| < 2.4$ rapidity region. The boxes (bars) represent the systematic (statistical) uncertainties. The size of the global relative uncertainties are depicted in the boxes plotted at $R_{AA} = 1$. Figures published in Ref. [231].

4.3.3.2 Nonprompt J/ψ -meson R_{AA}

The suppression of b hadrons is probed by the nuclear modification factor of nonprompt J/ψ mesons. The nonprompt J/ψ -meson results as a function of p_T , rapidity and $\langle N_{part} \rangle$ are compared to the corresponding ones obtained at $\sqrt{s_{NN}} = 2.76$ TeV in Figure 4.31. The measurements at both collision energies are also found to be in good overall agreement.

The b hadrons are suppressed in all measurements and the nonprompt J/ψ -meson R_{AA} decreases towards high $p_T^{\mu\mu}$ reaching a value of $R_{AA} \approx 0.4$. The suppression is observed to not vary significantly with respect to rapidity. In addition, the suppression of b hadrons becomes stronger for more central collisions. The nonprompt J/ψ -meson nuclear modification factor varies from $R_{AA} \approx 0.7$ in the most peripheral centrality bin (50 – 100%) to $R_{AA} \approx 0.4$ for the most central Pb-Pb collisions (0 – 10%).

In Figure 4.32, the R_{AA} of nonprompt J/ψ mesons is presented as a function of $p_T^{\mu\mu}$ in the mid- and forward rapidity regions (left), and $\langle N_{part} \rangle$ in two $p_T^{\mu\mu}$ intervals (right). A hint of stronger suppression is seen in the highest p_T interval ($6.5 < p_T^{\mu\mu} < 50$ GeV/c) as a function of $\langle N_{part} \rangle$, which could originate from parton energy loss (i.e. jet quenching) of bottom quarks in the QGP medium as detailed in Section 1.2.4.3. More differential studies can be found in Ref. [231].

4.3. RESULTS

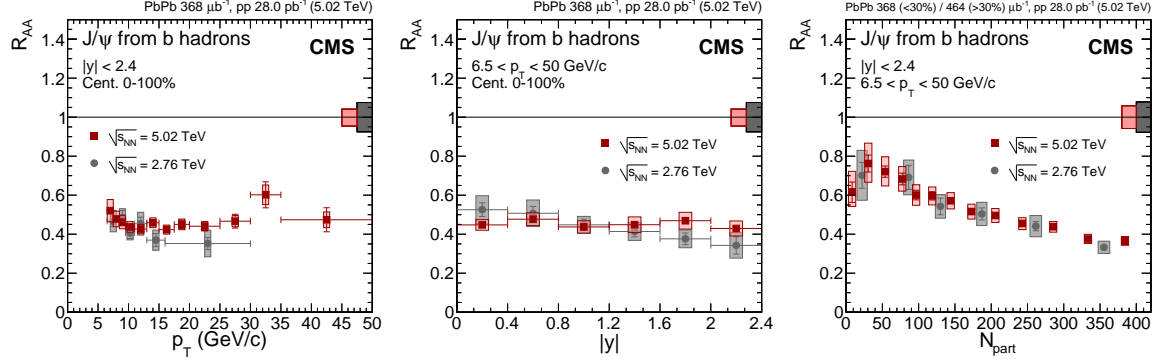


Figure 4.31: Nuclear modification factor of nonprompt J/ψ mesons measured at $\sqrt{s_{NN}} = 2.76\text{TeV}$ [244] (grey circles) and $\sqrt{s_{NN}} = 5.02\text{TeV}$ [231] (red squares), as a function of dimuon p_T (left), rapidity (middle) and $\langle N_{\text{part}} \rangle$ (right). The boxes (bars) represent the systematic (statistical) uncertainties. The size of the global relative uncertainties are depicted in the boxes plotted at $R_{\text{AA}} = 1$. Figures published in Ref. [231].

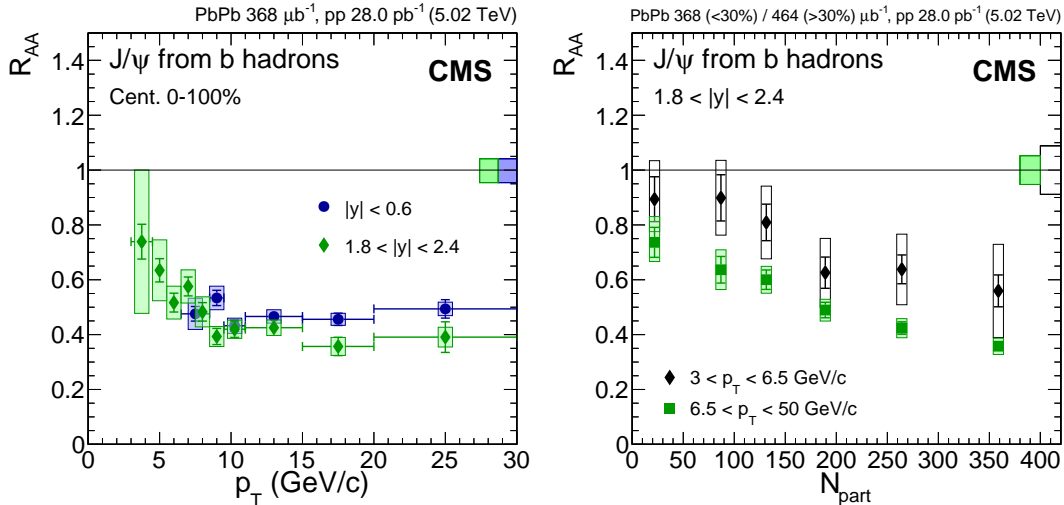


Figure 4.32: Nuclear modification factor of nonprompt J/ψ mesons. Left: as a function of $p_T^{\mu\mu}$ in the mid- and most forward rapidity regions. Right: as a function of $\langle N_{\text{part}} \rangle$ in two $p_T^{\mu\mu}$ intervals at forward rapidity. The boxes (bars) represent the systematic (statistical) uncertainties. The size of the global relative uncertainties are depicted in the boxes plotted at $R_{\text{AA}} = 1$. Figures published in Ref. [231].

4.3.4 Double ratio of prompt $\psi(2S)$ /J/ ψ yields

The double ratio of prompt $\psi(2S)$ over J/ψ meson yields, $(N_{\psi(2S)}/N_{J/\psi})_{\text{PbPb}}/(N_{\psi(2S)}/N_{J/\psi})_{\text{pp}}$, is derived from the $\psi(2S)$ -to- J/ψ yields ratios measured in p-p and Pb-Pb collisions, as detailed in Section 4.2.5. The systematic uncertainties that affects the measurement of

4146 the double ratio of prompt charmonium yields are:

- 4147 • The uncertainty on the extraction of the $\psi(2S)$ -to- J/ψ yields ratios, derived from
4148 the parametrisation of the $m^{\mu\mu}$ distribution in p-p and Pb-Pb collisions. This
4149 uncertainty is found to be less than 0.02 (0.11) from the p-p (Pb-Pb) data fits.
- 4150 • The uncertainty on the cancellation of the prompt charmonium efficiencies. This
4151 uncertainty is seen to vary between 0.01 and 0.05, except at $3 < p_T^{\mu\mu} < 6.5$ GeV/c,
4152 where it seen to be 0.10.
- 4153 • The uncertainty on the subtraction of the nonprompt charmonium contamination,
4154 which is less than 0.07.

4155 The results of the $(N_{\psi(2S)}/N_{J/\psi})_{\text{PbPb}}/(N_{\psi(2S)}/N_{J/\psi})_{\text{pp}}$, as a function of $p_T^{\mu\mu}$, are presented
4156 in Figure 4.33. Since the values of the double ratios of prompt charmonium yields and the
4157 prompt J/ψ -meson R_{AA} are below unity in all measurements, the prompt $\psi(2S)$ mesons
4158 are more suppressed than the prompt J/ψ mesons in Pb-Pb collisions. This is consistent
4159 with a sequential suppression of charmonia in the QGP. The results at mid- and forward
4160 rapidity regions are compatible within uncertainties, and no significant dependence is
4161 seen as a function of $p_T^{\mu\mu}$.

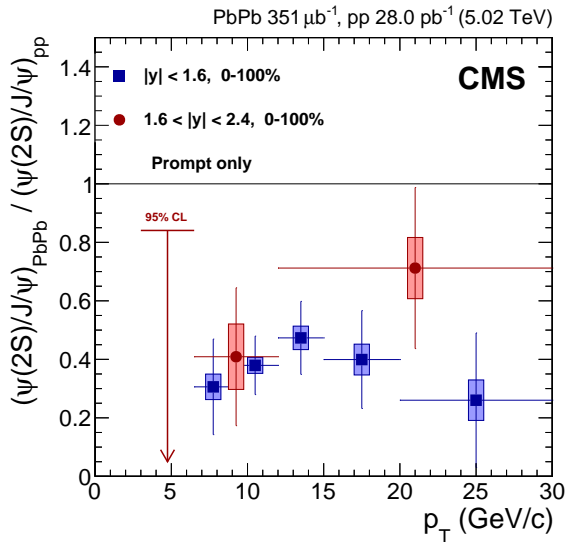


Figure 4.33: Double ratio of prompt $\psi(2S)$ over J/ψ meson yields as a function of the dimuon p_T , at $|y^{\mu\mu}| < 1.6$ (squares) and $1.6 < |y^{\mu\mu}| < 2.4$ (circles). The horizontal lines denote the widths of the p_T intervals. The bars (boxes) represent the statistical (systematic) uncertainties, while the arrows indicate the 95% CL interval where the measurement is consistent with zero. Figures published in Ref. [232].

4.3. RESULTS

4162 The measurements of the double ratio of prompt charmonium yields are also per-
 4163 formed for different centrality intervals, as shown in terms of $\langle N_{\text{part}} \rangle$ in Figure 4.34,
 4164 separately for mid-rapidity (left) and forward rapidity (right). The results do not ex-
 4165 hibit a clear dependence with respect to $\langle N_{\text{part}} \rangle$. Moreover, the double ratios measured
 4166 in the 20 – 100% centrality range at forward rapidity and the most central collisions
 4167 (0 – 20%) at mid-rapidity, are consistent with zero. The results at $\sqrt{s_{\text{NN}}} = 5.02 \text{ TeV}$ are
 4168 compared with the previous CMS measurement at $\sqrt{s_{\text{NN}}} = 2.76 \text{ TeV}$. On the one hand, the
 4169 results with respect to $\langle N_{\text{part}} \rangle$ at both energies are observed to be compatible in the mid-
 4170 rapidity region at $6.5 < p_{\text{T}}^{\mu\mu} < 30 \text{ GeV}/c$. On the other hand, the measurements extending
 4171 to lower $p_{\text{T}}^{\mu\mu}$ intervals ($3 < p_{\text{T}}^{\mu\mu} < 30$) in the forward rapidity region are strongly re-
 4172 duced at $\sqrt{s_{\text{NN}}} = 5.02 \text{ TeV}$ compared to $\sqrt{s_{\text{NN}}} = 2.76 \text{ TeV}$, and the enhancement present at
 4173 $\sqrt{s_{\text{NN}}} = 2.76 \text{ TeV}$ for the most central collisions is not seen at $\sqrt{s_{\text{NN}}} = 5.02 \text{ TeV}$. The differ-
 4174 ence in the centrality-integrated interval, between $\sqrt{s_{\text{NN}}} = 2.76 \text{ TeV}$ and $\sqrt{s_{\text{NN}}} = 5.02 \text{ TeV}$,
 4175 corresponds to roughly 3 standard deviations.

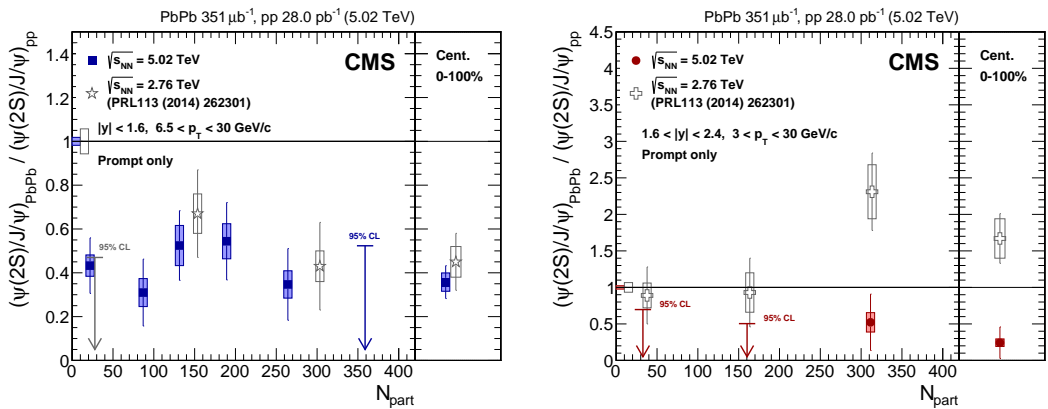


Figure 4.34: Comparison of the double ratio of prompt $\psi(2S)$ over J/ψ meson yields measured at $\sqrt{s_{\text{NN}}} = 2.76 \text{ TeV}$ [228] and $\sqrt{s_{\text{NN}}} = 5.02 \text{ TeV}$ [232], as a function of the dimuon p_{T} (left) and Pb-Pb collision centrality (right), at $|y^{\mu\mu}| < 1.6$ (squares) and $1.6 < |y^{\mu\mu}| < 2.4$ (circles). The horizontal lines denotes the widths of the p_{T} intervals. The bars (boxes) represent the statistical (systematic) uncertainties, while the arrows indicate the 95% CL interval where the measurement is consistent with zero. Figures published in Ref. [232].

4176 A possible interpretation of the double ratio results is provided by Ralf Rapp and
 4177 Xiaojian Du in Ref. [246], using a transport model approach. According to Rapp and
 4178 Du, the enhancement observed at $\sqrt{s_{\text{NN}}} = 2.76 \text{ TeV}$ could be a signature of sequential
 4179 regeneration of charmonia. They propose that $\psi(2S)$ mesons are regenerated later in the
 4180 medium evolution, where the larger collective flow shifts their transverse momentum

4181 to $p_T > 3$ GeV/c, while the J/ψ mesons are mainly regenerated earlier at lower p_T [230].
4182 However, at higher collisions energies, the p_T spectrum of the regenerated J/ψ mesons is
4183 shifted to $p_T > 3$ GeV/c due to the increase in transverse flow, leading to the suppression
4184 pattern observed at $\sqrt{s_{NN}} = 5.02$ TeV.

CONCLUSION

4186 The understanding of the cold nuclear matter effects, arising from the sole presence of
 4187 nuclei, is crucial in order to characterise the quark-gluon plasma (QGP) produced in
 4188 heavy-ion collisions. Among these effects, one that impacts the production of particles
 4189 formed in the initial hard scattering is the nuclear modification of the parton distribution
 4190 functions (PDF). Due to the non-perturbative behaviour of the strong interactions,
 4191 the PDFs can not be determined theoretically and instead are parametrised using
 4192 experimental data. Weak bosons provide good measurements of the PDF modifications
 4193 in nuclear collisions since they do not interact strongly with the medium. Thanks to
 4194 the high collision energy available at the Large Hadron Collider (LHC), it has become
 4195 possible to measure the production of weak bosons in heavy-ion collisions. The LHC
 4196 collaborations have studied the weak boson production in p-Pb at $\sqrt{s_{\text{NN}}} = 5.02 \text{ TeV}$, where
 4197 hints of nuclear modifications of the PDFs were observed in the forward rapidity region,
 4198 although the free-proton PDF calculations were also consistent with the measurements
 4199 within the statistical precision of the data.

4200 In the scope of this thesis, I measured the W-boson production in p-Pb collisions at
 4201 $\sqrt{s_{\text{NN}}} = 8.16 \text{ TeV}$ with the Compact Muon Solenoid detector and required the systematic
 4202 uncertainties to be largely decreased. Compared to previous measurements at $\sqrt{s_{\text{NN}}} =$
 4203 5.02 TeV , the analysis benefits from an increased W-boson statistics due to the higher
 4204 beam energy and integrated luminosity. The measured W-boson production is found
 4205 to be in good agreement with the EPPS16 and nCTEQ15 nuclear PDF sets. On the
 4206 other hand, the W-boson measurements significantly disfavoured the CT14 free-proton
 4207 PDF calculations, revealing unambiguously the presence of nuclear modifications in the
 4208 production of electroweak bosons, for the first time. Considering the smaller size of the
 4209 measured uncertainties, compared to the model calculations, the W-boson measurements
 4210 have the potential to constrain the parametrisations of the quark nuclear PDFs.

4211 The hot nuclear matter effects caused by the QGP are probed in this thesis through
 4212 the study of the charmonium production in heavy-ion collisions. Two related analyses
 4213 were presented in the second part of the manuscript: the production of prompt and

4214 nonprompt J/ψ mesons, and the nuclear modification of $\psi(2S)$ mesons relative to J/ψ
4215 mesons, in Pb-Pb collisions at $\sqrt{s_{NN}} = 5.02\text{ TeV}$.

4216 Prompt and nonprompt J/ψ mesons are found to be suppressed in all measurements.
4217 Their nuclear modification factor (R_{AA}) is observed to depend on centrality, being more
4218 suppressed towards more central collisions, while no significant dependence on rapidity
4219 is seen. On the one hand, an indication of weaker suppression is observed for prompt
4220 J/ψ mesons, in the lowest transverse momentum (p_T) interval ($3 < p_T < 6.5 \text{ GeV}/c$) and
4221 most central collisions (0-30%), which may originate from J/ψ regeneration. Also, for
4222 the first time, a hint of less suppression of prompt J/ψ mesons is seen in the highest
4223 p_T range ($p_T > 25 \text{ GeV}/c$) compared to the intermediate p_T range ($6.5 < p_T < 25 \text{ GeV}/c$),
4224 which may reflect the energy loss of initial partons fragmenting into J/ψ mesons. On
4225 the other hand, the nonprompt J/ψ -meson suppression is seen to be more pronounced at
4226 high p_T , likely caused by jet quenching of bottom quarks. In the overlapping range, the
4227 measured J/ψ -meson R_{AA} is compatible with previous measurements at $\sqrt{s_{NN}} = 2.76\text{ TeV}$.

4228 The measurement of the $(N_{\psi(2S)}/N_{J/\psi})_{\text{PbPb}}/(N_{\psi(2S)}/N_{J/\psi})_{\text{pp}}$ double ratio in Pb-Pb at
4229 $\sqrt{s_{NN}} = 5.02\text{ TeV}$ shows that the $\psi(2S)$ mesons are more suppressed than J/ψ mesons,
4230 which is consistent with the sequential suppression of charmonia in the QGP. Compar-
4231 isons with measurements at $\sqrt{s_{NN}} = 2.76\text{ TeV}$ show a good agreement of the double ratio
4232 at high p_T in the mid-rapidity region. On the contrary, extending the p_T range down to
4233 3 GeV/c in the forward rapidity region shows a stronger reduction of the double ratio
4234 at $\sqrt{s_{NN}} = 5.02\text{ TeV}$ compared to $\sqrt{s_{NN}} = 2.76\text{ TeV}$, where the two measurements deviates
4235 by almost 3 standard deviations in the centrality-integrated interval. A sequential re-
4236 generation of charmonia has been suggested to explain the double ratio results at both
4237 collision energies.



RESULTS OF THE FITS FOR THE W BOSON ANALYSIS

The results of the fits to the p_T^{miss} distribution in data are shown in Figure A.1 for $W^- \rightarrow \mu^- \bar{\nu}_\mu$ events, in Figure A.2 for $W^+ \rightarrow \mu^+ \nu_\mu$ events, and in Figure A.3 for the η_{CM}^μ -inclusive range.

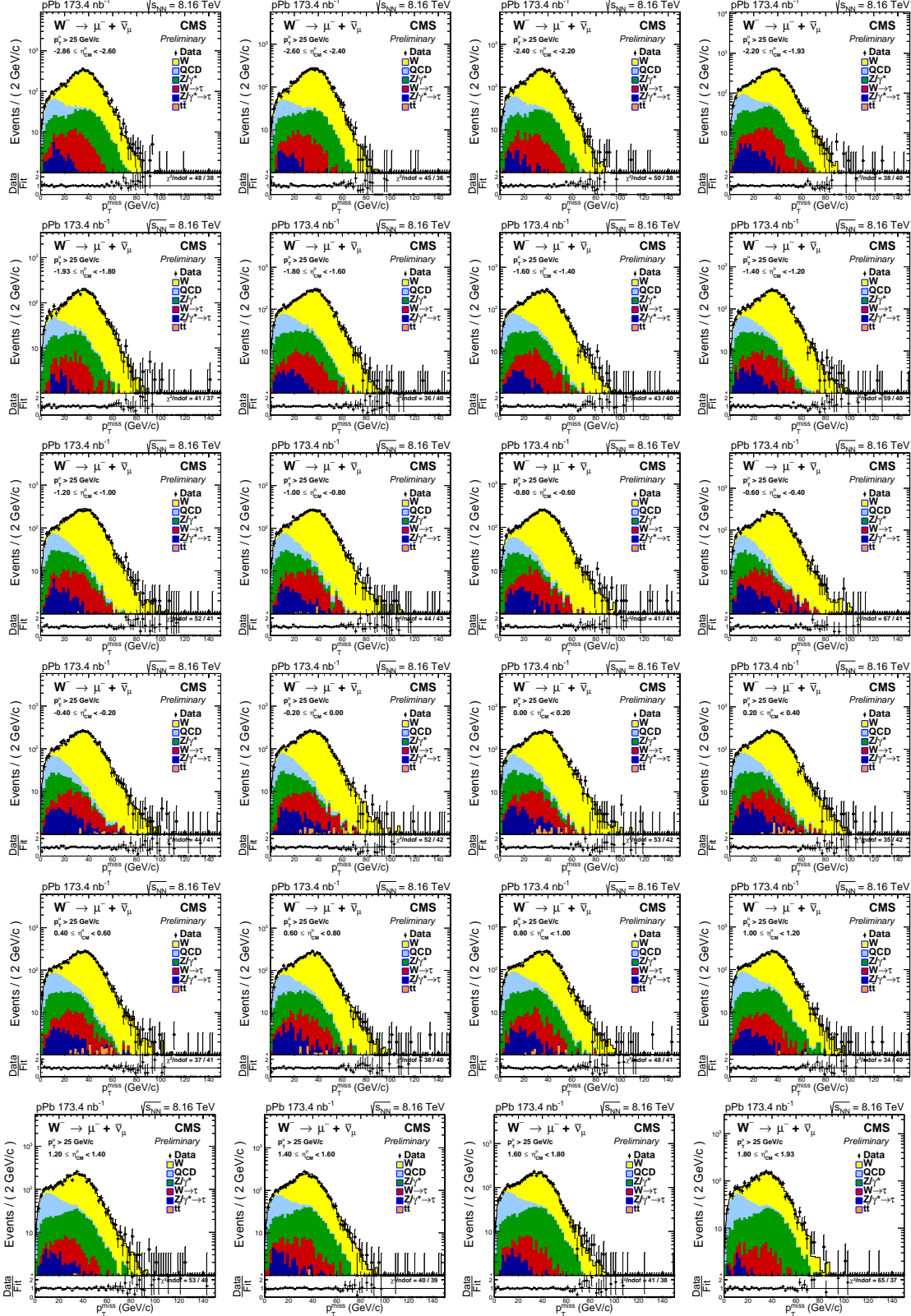


Figure A.1: The p_T^{miss} distribution for $W^- \rightarrow \mu^- \bar{\nu}_\mu$ events within each fitted η_{CM}^μ range, shown in logarithmic scale. Unbinned fits to the data (black points) are performed with six contributions, stacked from top to bottom: $W^+ \rightarrow \mu^+ \nu_\mu$ (yellow), QCD multijet (light blue), $Z/\gamma^* \rightarrow \mu^+ \mu^-$ (green), $W^+ \rightarrow \bar{\tau} \nu_\tau$ (red), $Z/\gamma^* \rightarrow \tau \bar{\tau}$ (dark blue) and $t\bar{t}$ (orange). Error bars represent statistical uncertainties. The lower panels display the data divided by the result of the fit, for each η_{CM}^μ range. The χ^2 test value over the number of degrees of freedom is also shown.

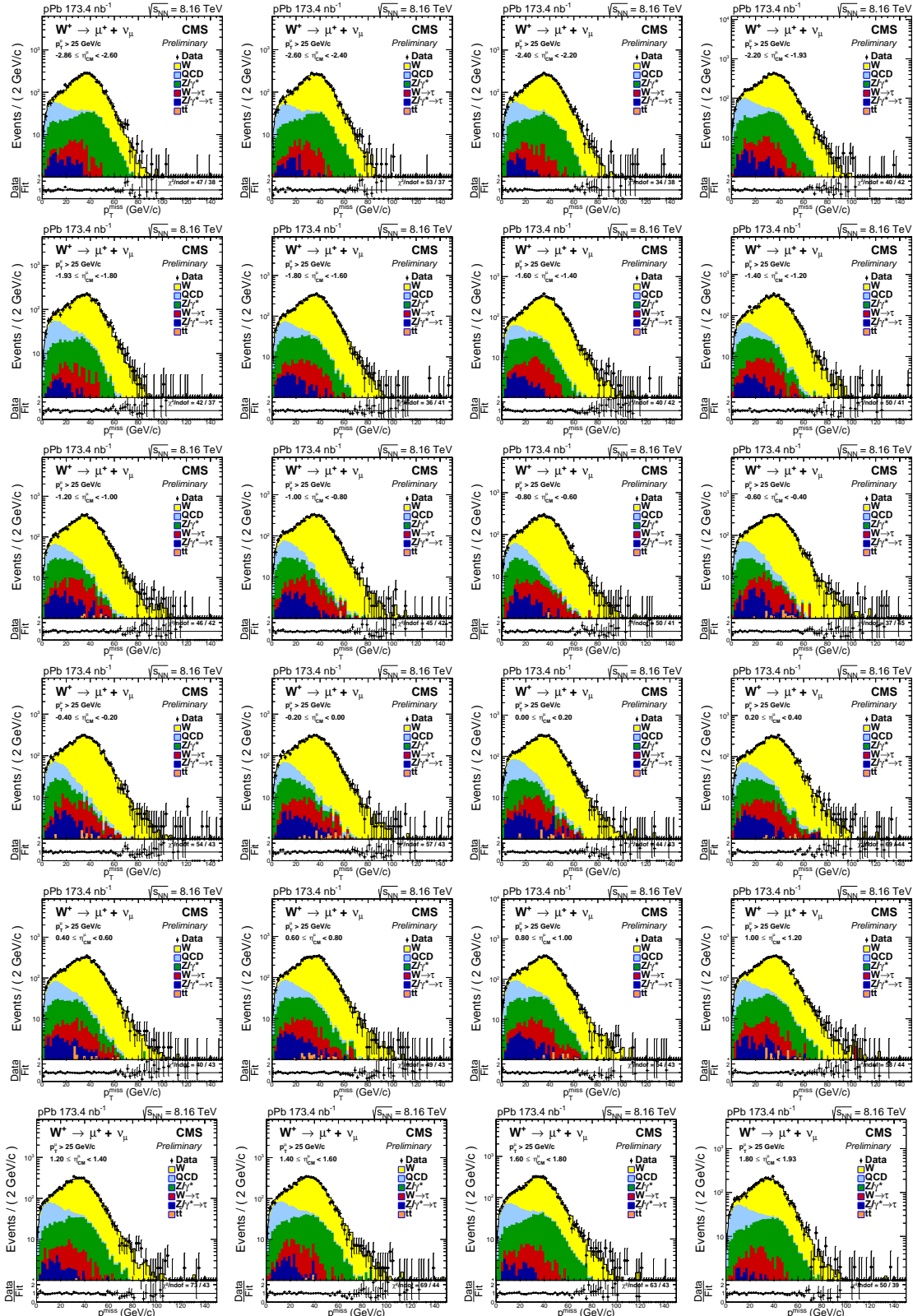


Figure A.2: The p_T^{miss} distribution for $W^+ \rightarrow \mu^+ \nu_\mu$ events within each fitted η_{CM}^μ range, shown in logarithmic scale. Unbinned fits to the data (black points) are performed with six contributions, stacked from top to bottom: $W^+ \rightarrow \mu^+ \nu_\mu$ (yellow), QCD multijet (light blue), $Z/\gamma^* \rightarrow \mu^+ \mu^-$ (green), $W^+ \rightarrow \bar{\tau} \nu_\tau$ (red), $Z/\gamma^* \rightarrow \tau \bar{\tau}$ (dark blue) and $t\bar{t}$ (orange). Error bars represent statistical uncertainties. The lower panels display the data divided by the result of the fit, for each η_{CM}^μ range. The χ^2 test value over the number of degrees of freedom is also shown.

APPENDIX A. RESULTS OF THE FITS FOR THE W BOSON ANALYSIS

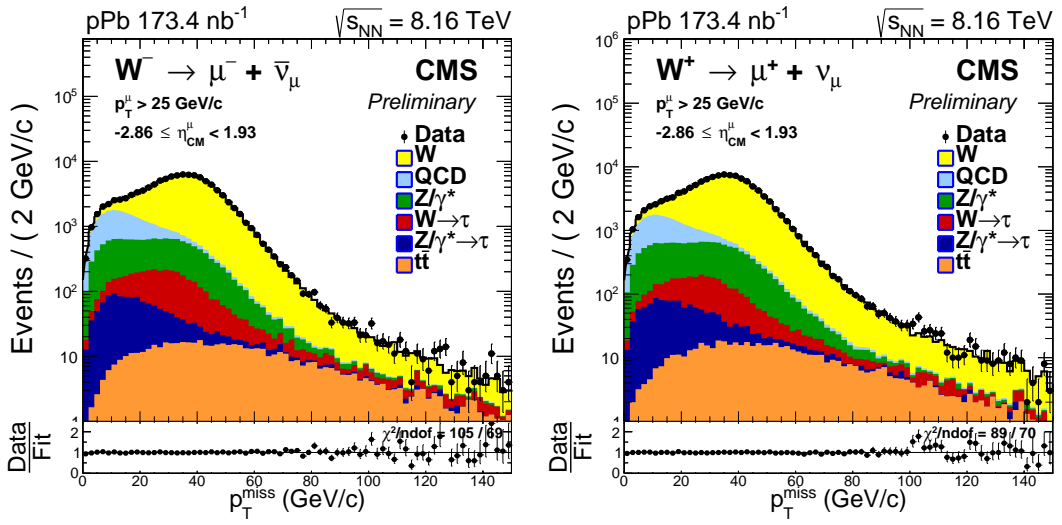


Figure A.3: The p_T^{miss} distribution for $W^+ \rightarrow \mu^+ \nu_\mu$ (left) and $W^- \rightarrow \mu^- \bar{\nu}_\mu$ (right) events within the η_{CM}^μ -inclusive range, shown in logarithmic scale. Unbinned fits to the data (black points) are performed with six contributions, stacked from top to bottom: $W \rightarrow \mu \nu_\mu$ (yellow), QCD multijet (light blue), $Z/\gamma^* \rightarrow \mu^+ \mu^-$ (green), $W \rightarrow \tau \nu_\tau$ (red), $Z/\gamma^* \rightarrow \tau \bar{\tau}$ (dark blue) and $t\bar{t}$ (orange). Error bars represent statistical uncertainties. The lower panels display the data divided by the result of the fit, for each η_{CM}^μ range. The χ^2 test value over the number of degrees of freedom is also shown.



ANALYSIS BINS USED IN THE CHARMONIA ANALYSES

This appendix summarises the different bins in which the J/ψ -meson R_{AA} and $\psi(2S)$ -to- J/ψ double ratio analyses are performed. The binning used for the measurement of the J/ψ -meson R_{AA} as a function of centrality is listed in Table B.1, while the one used as a function of dimuon p_T in different rapidity and centrality intervals are presented in Table B.2 and Table B.3, respectively. Regarding the measurement of the double ratio of charmonium yields, the different analysis bins are summarised in Table B.4.

$ y $	p_T [GeV/c]	Centrality [%]	Pb-Pb dataset
[0.0,0.6]	[6.5,50.0]	0-10	HIONiaDoubleMu0
[0.0,0.6]	[6.5,50.0]	10-20	HIONiaDoubleMu0
[0.0,0.6]	[6.5,50.0]	20-30	HIONiaDoubleMu0
[0.0,0.6]	[6.5,50.0]	30-40	HIONiaPeripheral30100
[0.0,0.6]	[6.5,50.0]	40-50	
[0.0,0.6]	[6.5,50.0]	50-100	
[0.6,1.2]	[6.5,50.0]	0-10	HIONiaDoubleMu0
[0.6,1.2]	[6.5,50.0]	10-20	HIONiaDoubleMu0
[0.6,1.2]	[6.5,50.0]	20-30	HIONiaDoubleMu0
[0.6,1.2]	[6.5,50.0]	30-40	HIONiaPeripheral30100
[0.6,1.2]	[6.5,50.0]	40-50	
[0.6,1.2]	[6.5,50.0]	50-100	
[1.2,1.8]	[6.5,50.0]	0-10	HIONiaDoubleMu0
[1.2,1.8]	[6.5,50.0]	10-20	HIONiaDoubleMu0
[1.2,1.8]	[6.5,50.0]	20-30	HIONiaDoubleMu0
[1.2,1.8]	[6.5,50.0]	30-40	HIONiaPeripheral30100
[1.2,1.8]	[6.5,50.0]	40-50	
[1.2,1.8]	[6.5,50.0]	50-100	
[1.8,2.4]	[3.0,6.5]	0-10	HIONiaDoubleMu0
[1.8,2.4]	[3.0,6.5]	10-20	HIONiaDoubleMu0
[1.8,2.4]	[3.0,6.5]	20-30	HIONiaDoubleMu0
[1.8,2.4]	[3.0,6.5]	30-40	HIONiaPeripheral30100
[1.8,2.4]	[3.0,6.5]	40-50	
[1.8,2.4]	[3.0,6.5]	50-100	
[1.8,2.4]	[6.5,50.0]	0-10	HIONiaDoubleMu0
[1.8,2.4]	[6.5,50.0]	10-20	HIONiaDoubleMu0
[1.8,2.4]	[6.5,50.0]	20-30	HIONiaDoubleMu0
[1.8,2.4]	[6.5,50.0]	30-40	HIONiaPeripheral30100
[1.8,2.4]	[6.5,50.0]	40-50	
[1.8,2.4]	[6.5,50.0]	50-100	
[0.0,2.4]	[6.5,50.0]	0-5	HIONiaDoubleMu0
[0.0,2.4]	[6.5,50.0]	5-10	HIONiaDoubleMu0
[0.0,2.4]	[6.5,50.0]	10-15	HIONiaDoubleMu0
[0.0,2.4]	[6.5,50.0]	15-20	HIONiaDoubleMu0
[0.0,2.4]	[6.5,50.0]	20-25	HIONiaDoubleMu0
[0.0,2.4]	[6.5,50.0]	25-30	HIONiaDoubleMu0
[0.0,2.4]	[6.5,50.0]	30-35	HIONiaPeripheral30100
[0.0,2.4]	[6.5,50.0]	35-40	
[0.0,2.4]	[6.5,50.0]	40-45	
[0.0,2.4]	[6.5,50.0]	45-50	
[0.0,2.4]	[6.5,50.0]	50-60	
[0.0,2.4]	[6.5,50.0]	60-70	
[0.0,2.4]	[6.5,50.0]	70-100	HIONiaPeripheral30100

Table B.1: Summary of the bin boundaries used in the J/ψ -meson R_{AA} analysis as a function of centrality for different rapidity regions.

$ y $	p_T [GeV/c]	Centrality [%]	Pb-Pb dataset
[0.0, 0.6]	[6.5, 8.5]	0-10	HIONiaDoubleMu0
[0.0, 0.6]	[8.5, 9.5]	10-20	HIONiaDoubleMu0
[0.0, 0.6]	[9.5, 11.0]	20-30	HIONiaDoubleMu0
[0.0, 0.6]	[11.0, 15.0]	30-40	HIONiaDoubleMu0
[0.0, 0.6]	[15.0, 50.0]	40-50	HIONiaDoubleMu0
[0.6, 1.2]	[6.5, 8.5]	0-100	HIONiaDoubleMu0
[0.6, 1.2]	[8.5, 9.5]	0-100	HIONiaDoubleMu0
[0.6, 1.2]	[9.5, 11.0]	0-100	HIONiaDoubleMu0
[0.6, 1.2]	[11.0, 15.0]	0-100	HIONiaDoubleMu0
[0.6, 1.2]	[15.0, 50.0]	0-100	HIONiaDoubleMu0
[1.2, 1.6]	[6.5, 7.5]	0-100	HIONiaDoubleMu0
[1.2, 1.6]	[7.5, 8.5]	0-100	HIONiaDoubleMu0
[1.2, 1.6]	[8.5, 9.5]	0-100	HIONiaDoubleMu0
[1.2, 1.6]	[9.5, 11.0]	0-100	HIONiaDoubleMu0
[1.2, 1.6]	[11.0, 15.0]	0-100	HIONiaDoubleMu0
[1.2, 1.6]	[15.0, 50.0]	0-100	HIONiaDoubleMu0
[1.6, 2.4]	[3.0, 4.5]	0-100	HIONiaDoubleMu0
[1.6, 2.4]	[4.5, 5.5]	0-100	HIONiaDoubleMu0
[1.6, 2.4]	[5.5, 6.5]	0-100	HIONiaDoubleMu0
[1.6, 2.4]	[6.5, 7.5]	0-100	HIONiaDoubleMu0
[1.6, 2.4]	[7.5, 8.5]	0-100	HIONiaDoubleMu0
[1.6, 2.4]	[8.5, 9.5]	0-100	HIONiaDoubleMu0
[1.6, 2.4]	[9.5, 11.0]	0-100	HIONiaDoubleMu0
[1.6, 2.4]	[11.0, 15.0]	0-100	HIONiaDoubleMu0
[1.6, 2.4]	[15.0, 50.0]	0-100	HIONiaDoubleMu0
[0.0, 2.4]	[6.5, 7.5]	0-100	HIONiaDoubleMu0
[0.0, 2.4]	[7.5, 8.5]	0-100	HIONiaDoubleMu0
[0.0, 2.4]	[8.5, 9.5]	0-100	HIONiaDoubleMu0
[0.0, 2.4]	[9.5, 11.0]	0-100	HIONiaDoubleMu0
[0.0, 2.4]	[11.0, 13.0]	0-100	HIONiaDoubleMu0
[0.0, 2.4]	[13.0, 15.0]	0-100	HIONiaDoubleMu0
[0.0, 2.4]	[15.0, 20.0]	0-100	HIONiaDoubleMu0
[0.0, 2.4]	[20.0, 30.0]	0-100	HIONiaDoubleMu0
[0.0, 2.4]	[30.0, 50.0]	0-100	HIONiaDoubleMu0

Table B.2: Summary of the bin boundaries used in the J/ψ -meson R_{AA} analysis as a function of p_T for different rapidity regions.

$ y $	p_T [GeV/c]	Centrality [%]	Pb-Pb dataset
[0.0,2.4]	[6.5, 7.5]	0-10	HIONiaDoubleMu0
[0.0,2.4]	[7.5, 8.5]	0-10	HIONiaDoubleMu0
[0.0,2.4]	[8.5, 9.5]	0-10	HIONiaDoubleMu0
[0.0,2.4]	[9.5, 11.0]	0-10	HIONiaDoubleMu0
[0.0,2.4]	[11.0, 13.0]	0-10	HIONiaDoubleMu0
[0.0,2.4]	[13.0, 15.0]	0-10	HIONiaDoubleMu0
[0.0,2.4]	[15.0, 20.0]	0-10	HIONiaDoubleMu0
[0.0,2.4]	[20.0, 50.0]	0-10	HIONiaDoubleMu0
[0.0,2.4]	[6.5, 7.5]	10-30	HIONiaDoubleMu0
[0.0,2.4]	[7.5, 8.5]	10-30	HIONiaDoubleMu0
[0.0,2.4]	[8.5, 9.5]	10-30	HIONiaDoubleMu0
[0.0,2.4]	[9.5, 11.0]	10-30	HIONiaDoubleMu0
[0.0,2.4]	[11.0, 13.0]	10-30	HIONiaDoubleMu0
[0.0,2.4]	[13.0, 15.0]	10-30	HIONiaDoubleMu0
[0.0,2.4]	[15.0, 20.0]	10-30	HIONiaDoubleMu0
[0.0,2.4]	[20.0, 50.0]	10-30	HIONiaDoubleMu0
[0.0,2.4]	[6.5, 7.5]	30-100	HIONiaPeripheral30100
[0.0,2.4]	[7.5, 8.5]	30-100	HIONiaPeripheral30100
[0.0,2.4]	[8.5, 9.5]	30-100	HIONiaPeripheral30100
[0.0,2.4]	[9.5, 11.0]	30-100	HIONiaPeripheral30100
[0.0,2.4]	[11.0, 13.0]	30-100	HIONiaPeripheral30100
[0.0,2.4]	[13.0, 15.0]	30-100	HIONiaPeripheral30100
[0.0,2.4]	[15.0, 20.0]	30-100	HIONiaPeripheral30100
[0.0,2.4]	[20.0, 50.0]	30-100	HIONiaPeripheral30100

Table B.3: Summary of the bin boundaries used in the J/ψ -meson R_{AA} analysis as a function of p_T for different centrality intervals.

$ y $	p_T [GeV/c]	Centrality [%]	Pb-Pb dataset
[0,1.6]	[6.5,30]	0-10	HIONiaDoubleMu0
[0,1.6]	[6.5,30]	10-20	HIONiaDoubleMu0
[0,1.6]	[6.5,30]	20-30	HIONiaDoubleMu0
[0,1.6]	[6.5,30]	30-40	HIONiaPeripheral30100
[0,1.6]	[6.5,30]	40-50	HIONiaPeripheral30100
[0,1.6]	[6.5,30]	50-100	HIONiaPeripheral30100
[1.6,2.4]	[3,30]	0-20	HIONiaDoubleMu0
[1.6,2.4]	[3,30]	20-40	HIONiaDoubleMu0
[1.6,2.4]	[3,30]	40-100	HIONiaPeripheral30100
[0,1.6]	[6.5,9]	0-100	HIONiaDoubleMu0
[0,1.6]	[9,12]	0-100	HIONiaDoubleMu0
[0,1.6]	[12,15]	0-100	HIONiaDoubleMu0
[0,1.6]	[15,20]	0-100	HIONiaDoubleMu0
[0,1.6]	[20,30]	0-100	HIONiaDoubleMu0
[1.6,2.4]	[3,6.5]	0-100	HIONiaDoubleMu0
[1.6,2.4]	[6.5,12]	0-100	HIONiaDoubleMu0
[1.6,2.4]	[12,30]	0-100	HIONiaDoubleMu0

Table B.4: Summary of the bin boundaries used in the $\psi(2S)$ -to- J/ψ double ratio analysis.

BIBLIOGRAPHY

- [1] A. G. Stahl Leiton, “nPDF studies with electroweak bosons in pPb collisions at 8.16 TeV with the CMS detector”, XXVII International Conference on Ultrarelativistic Nucleus-Nucleus Collisions (Quark Matter 2018): Venice, Italy, May 14-19, 2018, 2018, unpublished. [[Cited on page 2.](#)]
- [2] A. G. Stahl Leiton, “nPDF studies with electroweak bosons in pPb collisions with the CMS detector”, XXXIX International Conference on High Energy Physics (ICHEP 2018): Seoul, Korea, July 4-11, 2018, 2018, unpublished. [[Cited on page 2.](#)]
- [3] CMS Collaboration, “Constraints on nuclear parton distributions from W boson production in pPb collisions at $\sqrt{s_{NN}} = 8.16$ TeV”, Tech. Rep. CMS-PAS-HIN-17-007, CERN, Geneva, 2018. [[Cited on page 2.](#)]
- [4] CMS Collaboration, A. M. Sirunyan *et al.*, “Relative Modification of Prompt $\psi(2S)$ and J/ψ Yields from pp to PbPb Collisions at $\sqrt{s_{NN}} = 5.02$ ÅTeV”, *Phys. Rev. Lett.* **118** (2017), no. 16, 162301, arXiv:1611.01438. [[Cited on page 2.](#)]
- [5] CMS Collaboration, A. M. Sirunyan *et al.*, “Measurement of prompt and nonprompt charmonium suppression in PbPb collisions at 5.02 TeV”, *Eur. Phys. J. C* **78** (2018), no. 6, 509, arXiv:1712.08959. [[Cited on page 2.](#)]
- [6] CMS Collaboration, A. G. Stahl, “Charmonium production in pp, pPb and PbPb collisions with CMS”, in “Proceedings, Hot Quarks 2016: Workshop for Young Scientists on the Physics of Ultrarelativistic Nucleus-Nucleus Collisions (HQ2016): South Padre Island, Texas, September 12-17, 2016”, vol. 832, p. 012031. 2017. [[Cited on page 2.](#)]
- [7] CMS Collaboration, A. G. Stahl Leiton, “Charmonium production in pPb and PbPb collisions at 5.02 TeV with CMS”, in “Proceedings, 2017 European Physical

BIBLIOGRAPHY

- Society Conference on High Energy Physics (EPS-HEP 2017): Venice, Italy, July 5-12, 2017”, p. 196. 2017. [Cited on page 2.]
- [8] E. Fermi, “Sulla quantizzazione del gas perfetto monoatomico”, *Rendiconti Lincei* **3** (1926) 145. [Cited on page 4.]
- [9] P. A. M. Dirac, “On the theory of quantum mechanics”, *Proceedings of the Royal Society of London A: Mathematical, Physical and Engineering Sciences* **112** (1926), no. 762, 661,
<http://rspa.royalsocietypublishing.org/content/112/762/661.full.pdf>.
[Cited on page 4.]
- [10] W. Pauli, “”, *Zeitschrift für Physik* **31** (1925), no. 1, 765. [Cited on page 4.]
- [11] S. N. Bose, “Plancks Gesetz und Lichtquantenhypothese”, *Zeitschrift für Physik* **26** (1924), no. 1, 178. [Cited on page 4.]
- [12] A. Einstein, “Quantentheorie des einatomigen idealen Gases”, *Sitzungber. Kgl. Akad. Wiss.*, 1924 261. [Cited on page 4.]
- [13] **Belle** Collaboration, A. Bondar *et al.*, “Observation of two charged bottomonium-like resonances in Y(5S) decays”, *Physical Review Letters* **108** (2012), no. 6, 122001, arXiv:1110.2251. [Cited on page 5.]
- [14] **LHCb** Collaboration, R. Aaij *et al.*, “Observation of $J/\psi p$ Resonances Consistent with Pentaquark States in $\Lambda_b^0 \rightarrow J/\psi K^- p$ Decays”, *Phys. Rev. Lett.* **115** (2015) 072001, arXiv:1507.03414. [Cited on page 5.]
- [15] P. W. Higgs, “Broken Symmetries and the Masses of Gauge Bosons”, *Phys. Rev. Lett.* **13** (1964) 367. [Cited on pages 5, 68, and 69.]
- [16] F. Englert and R. Brout, “Broken Symmetry and the Mass of Gauge Vector Mesons”, *Phys. Rev. Lett.* **13** (1964) 321. [Cited on pages 5, 68, and 69.]
- [17] **CMS** Collaboration, S. Chatrchyan *et al.*, “Observation of a new boson at a mass of 125 GeV with the CMS experiment at the LHC”, *Phys. Lett. B* **716** (2012) 30, arXiv:1207.7235. [Cited on pages 5 and 68.]
- [18] **ATLAS** Collaboration, G. Aad *et al.*, “Observation of a new particle in the search for the Standard Model Higgs boson with the ATLAS detector at the LHC”, *Phys. Lett. B* **716** (2012) 1, arXiv:1207.7214. [Cited on pages 5 and 68.]

- [19] **Particle Data Group** Collaboration, C. Patrignani *et al.*, “Review of Particle Physics”, *Chin. Phys. C* **40** (2016) 100001. [[Cited on pages 6, 8, 9, 70, 71, 72, 115, 130, 131, 146, 147, 152, 170, 183, 249, 250, and 253.](#)]
- [20] M. Gell-Mann, “The Eightfold Way: A Theory of strong interaction symmetry”, 1961. [[Cited on page 5.](#)]
- [21] Y. Ne’eman, “Derivation of strong interactions from a gauge invariance”, *Nucl. Phys.* **26** (1961) 222, [,34(1961)]. [[Cited on page 5.](#)]
- [22] M. Gell-Mann, “A Schematic Model of Baryons and Mesons”, *Phys. Lett.* **8** (1964) 214. [[Cited on page 5.](#)]
- [23] G. Zweig, “An SU(3) model for strong interaction symmetry and its breaking. Version 2”, *Developments in the Quark Theory of Hadrons* **1** (1964) 22. [[Cited on page 5.](#)]
- [24] O. W. Greenberg, “Spin and Unitary Spin Independence in a Paraquark Model of Baryons and Mesons”, *Phys. Rev. Lett.* **13** (1964) 598. [[Cited on page 5.](#)]
- [25] H. Fritzsch, M. Gell-Mann, and H. Leutwyler, “Advantages of the Color Octet Gluon Picture”, *Phys. Lett. B* **47** (1973) 365. [[Cited on page 5.](#)]
- [26] G. ’t Hooft and M. J. G. Veltman, “Regularization and Renormalization of Gauge Fields”, *Nucl. Phys. B* **44** (1972) 189. [[Cited on page 7.](#)]
- [27] J. L. Kneur and A. Neveu, “ $\Lambda_{\text{MS}}^{\text{QCD}}$ from Renormalization Group Optimized Perturbation”, *Phys. Rev. D* **85** (2012) 014005, arXiv:1108.3501. [[Cited on pages 8 and 14.](#)]
- [28] D. J. Gross and F. Wilczek, “Ultraviolet Behavior of Nonabelian Gauge Theories”, *Phys. Rev. Lett.* **30** (1973) 1343, [,271(1973)]. [[Cited on page 8.](#)]
- [29] H. D. Politzer, “Reliable Perturbative Results for Strong Interactions?”, *Phys. Rev. Lett.* **30** (1973) 1346, [,274(1973)]. [[Cited on page 8.](#)]
- [30] L. V. P. R. de Broglie, “Recherches sur la théorie des quanta”, *Annals Phys.* **2** (1925) 22. [[Cited on page 9.](#)]
- [31] M. N. Chernodub, “Background magnetic field stabilizes QCD string against breaking”, arXiv:1001.0570. [[Cited on pages 10 and 253.](#)]

BIBLIOGRAPHY

- [32] J. D. Bjorken, “CURRENT ALGEBRA AT SMALL DISTANCES”, *Conf. Proc.* **670717** (1967) 55. [[Cited on page 10.](#)]
- [33] J. C. Collins, D. E. Soper, and G. F. Sterman, “Factorization of Hard Processes in QCD”, *Adv. Ser. Direct. High Energy Phys.* **5** (1989) 1, arXiv:hep-ph/0409313. [[Cited on page 11.](#)]
- [34] G. Altarelli and G. Parisi, “Asymptotic Freedom in Parton Language”, *Nucl. Phys. B* **126** (1977) 298. [[Cited on page 11.](#)]
- [35] Y. L. Dokshitzer, “Calculation of the Structure Functions for Deep Inelastic Scattering and e+ e- Annihilation by Perturbation Theory in Quantum Chromodynamics.”, *Sov. Phys. JETP* **46** (1977) 641, [Zh. Eksp. Teor. Fiz. 73, 1216(1977)]. [[Not cited.](#)]
- [36] V. N. Gribov and L. N. Lipatov, “Deep inelastic e p scattering in perturbation theory”, *Sov. J. Nucl. Phys.* **15** (1972) 438, [Yad. Fiz. 15, 781(1972)]. [[Cited on page 11.](#)]
- [37] **ZEUS** Collaboration, S. Chekanov *et al.*, “A ZEUS next-to-leading-order QCD analysis of data on deep inelastic scattering”, *Phys. Rev. D* **67** (2003) 012007, arXiv:hep-ex/0208023. [[Cited on pages 12, 13, and 253.](#)]
- [38] R. Hagedorn, “Statistical thermodynamics of strong interactions at high energies”, *Nuovo Cimento, Suppl.* **3** (1965) 147. [[Cited on page 13.](#)]
- [39] N. R. Council, “Nuclear physics: Exploring the heart of matter”, The National Academies Press, Washington, DC, 2013. [[Cited on pages 15, 18, and 253.](#)]
- [40] M. G. Alford, A. Schmitt, K. Rajagopal, and T. Schäfer, “Color superconductivity in dense quark matter”, *Rev. Mod. Phys.* **80** (2008) 1455, arXiv:0709.4635. [[Cited on page 14.](#)]
- [41] H.-T. Ding, “Recent lattice QCD results and phase diagram of strongly interacting matter”, *Nucl. Phys. A* **931** (2014) 52, arXiv:1408.5236. [[Cited on page 14.](#)]
- [42] A. Bazavov *et al.*, “Equation of state and QCD transition at finite temperature”, *Phys. Rev. D* **80** (2009) 014504, arXiv:0903.4379. [[Cited on page 14.](#)]
- [43] W. Scheid, H. Muller, and W. Greiner, “Nuclear Shock Waves in Heavy-Ion Collisions”, *Phys. Rev. Lett.* **32** (1974) 741. [[Cited on page 15.](#)]

- [44] E. J. Lofgren, “ACCELERATOR DIVISION ANNUAL REPORTS, 1 JULY 1972 12/31/1974”, Tech. Rep. LBL-3835, Lawrence Berkeley Laboratory, United States, 1975. [[Cited on page 16.](#)]
- [45] V. R. Pandharipande, D. Pines, and R. A. Smith, “Neutron star structure: theory, observation, and speculation.”, *Astrophys. J.* **208** (1976) 550. [[Cited on page 16.](#)]
- [46] T. L. Ainsworth, E. Baron, G. E. Brown, J. Cooperstein, and M. Prakash, “Equation of State of Dense Nuclear Matter”, *Nucl. Phys. A* **464** (1987) 740. [[Cited on page 16.](#)]
- [47] CERN, “New State of Matter created at CERN”, 2000. [Online; accessed June 11, 2018]. [[Cited on page 16.](#)]
- [48] W. Fischer, “Run overview of the Relativistic Heavy Ion collider”, 2000. [Online; accessed July 28, 2018]. [[Cited on page 16.](#)]
- [49] **BRAHMS** Collaboration, I. Arsene *et al.*, “Quark gluon plasma and color glass condensate at RHIC? The Perspective from the BRAHMS experiment”, *Nuclear Physics A* **757** (2005) 1, arXiv:nucl-ex/0410020. [[Cited on page 17.](#)]
- [50] **PHENIX** Collaboration, K. Adcox *et al.*, “Formation of dense partonic matter in relativistic nucleus-nucleus collisions at RHIC: Experimental evaluation by the PHENIX collaboration”, *Nuclear Physics A* **757** (2005) 184, arXiv:nucl-ex/0410003. [[Not cited.](#)]
- [51] **STAR** Collaboration, J. Adams *et al.*, “Experimental and theoretical challenges in the search for the quark gluon plasma: The STAR Collaboration’s critical assessment of the evidence from RHIC collisions”, *Nuclear Physics A* **757** (2005) 102, arXiv:nucl-ex/0501009. [[Not cited.](#)]
- [52] B. B. Back *et al.*, “The PHOBOS perspective on discoveries at RHIC”, *Nuclear Physics A* **757** (2005) 28, arXiv:nucl-ex/0410022. [[Cited on page 17.](#)]
- [53] M. L. Miller, K. Reygers, S. J. Sanders, and P. Steinberg, “Glauber modeling in high energy nuclear collisions”, *Annual Review of Nuclear and Particle Science* **57** (2007) 205, arXiv:nucl-ex/0701025. [[Cited on pages 18 and 19.](#)]
- [54] U. W. Heinz, “The Strongly coupled quark-gluon plasma created at RHIC”, *J. Phys. A* **42** (2009) 214003, arXiv:0810.5529. [[Cited on pages 22 and 253.](#)]

BIBLIOGRAPHY

- [55] R. Snellings, “Elliptic Flow: A Brief Review”, *New J. Phys.* **13** (2011) 055008, arXiv:1102.3010. [[Cited on pages 22 and 23.](#)]
- [56] P. Kovtun, D. T. Son, and A. O. Starinets, “Viscosity in strongly interacting quantum field theories from black hole physics”, *Phys. Rev. Lett.* **94** (2005) 111601, arXiv:hep-th/0405231. [[Cited on page 23.](#)]
- [57] J.-Y. Ollitrault, “Relativistic hydrodynamics for heavy-ion collisions”, *Eur. J. Phys.* **29** (2008) 275, arXiv:0708.2433. [[Cited on page 23.](#)]
- [58] P. Braun-Munzinger and J. Stachel, “The quest for the quark-gluon plasma”, *Nature* **448** (2007) 302. [[Cited on pages 23, 24, and 253.](#)]
- [59] **CMS** Collaboration, V. Khachatryan *et al.*, “”, *Journal of High Energy Physics* **09** (2010) 091, arXiv:1009.4122. [[Cited on pages 23, 25, and 254.](#)]
- [60] **PHOBOS** Collaboration, B. Alver *et al.*, “System size dependence of cluster properties from two-particle angular correlations in Cu+Cu and Au+Au collisions at $\sqrt{s_{NN}} = 200$ GeV”, *Physical Review C* **81** (2010) 024904, arXiv:0812.1172. [[Cited on page 24.](#)]
- [61] J. Rafelski and R. Hagedorn, “From Hadron Gas to Quark Matter. 2.”, in “International Symposium on Statistical Mechanics of Quarks and Hadrons Bielefeld, Germany, August 24-31, 1980”, p. 253. 1980. [[Cited on page 25.](#)]
- [62] A. Capella, “Strangeness enhancement in heavy ion collisions”, *Phys. Lett. B* **364** (1995) 175, arXiv:hep-ph/9501331. [[Cited on pages 25 and 26.](#)]
- [63] K. Safarik, “Strangeness production at CERN SPS”, in “Strangeness in quark matter. Proceedings, 5th International Conference, Strangeness 2000, Berkeley, USA, July 20-25, 2000”, vol. 27, pp. 579–583. 2001. [[Cited on page 25.](#)]
- [64] **NA49** Collaboration, A. Mischke *et al.*, “Lambda production in central Pb + Pb collisions at CERN SPS energies”, *J. Phys. G* **28** (2002) 1761–1768, arXiv:nucl-ex/0201012. [[Cited on page 25.](#)]
- [65] **STAR** Collaboration, B. I. Abelev *et al.*, “Enhanced strange baryon production in Au+Au collisions compared to p+p at $\sqrt{s_{NN}} = 200$ GeV”, *Physical Review C* **77** (2008) 044908, arXiv:0705.2511. [[Cited on pages 25, 26, and 254.](#)]

- [66] **ALICE** Collaboration, J. Adam *et al.*, “Enhanced production of multi-strange hadrons in high-multiplicity proton-proton collisions”, *Nature Phys.* **13** (2017) 535, arXiv:1606.07424. [[Cited on pages 26 and 254.](#)]
- [67] M. Cacciari, G. P. Salam, and G. Soyez, “The Anti-k(t) jet clustering algorithm”, *JHEP* **04** (2008) 063, arXiv:0802.1189. [[Cited on page 27.](#)]
- [68] J. D. Bjorken, “Energy Loss of Energetic Partons in Quark - Gluon Plasma: Possible Extinction of High p(t) Jets in Hadron - Hadron Collisions”, 1982. [[Cited on page 27.](#)]
- [69] A. P. S. . A. Stonebraker, “Sketch of jet production in proton-proton and heavy-ion collisions”, 2014. [Online; accessed June 8, 2018]. [[Cited on pages 27 and 254.](#)]
- [70] **PHENIX** Collaboration, A. Adare *et al.*, “Centrality dependence of low-momentum direct-photon production in Au+Au collisions at $\sqrt{s_{NN}} = 200 \text{ GeV}$ ”, *Phys. Rev. C* **91** (2015), no. 6, 064904, arXiv:1405.3940. [[Cited on page 28.](#)]
- [71] B. Betz, “Jet Quenching in Heavy-Ion Collisions - The Transition Era from RHIC to LHC”, *The European Physical Journal A* **48** (2012) 164, arXiv:1211.5897. [[Cited on pages 29 and 254.](#)]
- [72] **ATLAS** Collaboration, G. Aad *et al.*, “Observation of a Centrality-Dependent Dijet Asymmetry in Lead-Lead Collisions at $\sqrt{s_{NN}} = 2.76 \text{ TeV}$ with the ATLAS Detector at the LHC”, *Physical Review Letters* **105** (2010) 252303, arXiv:1011.6182. [[Cited on pages 28, 30, and 254.](#)]
- [73] **CMS** Collaboration, S. Chatrchyan *et al.*, “Observation and studies of jet quenching in PbPb collisions at nucleon-nucleon center-of-mass energy $\sqrt{s_{NN}} = 2.76 \text{ TeV}$ ”, *Physical Review C* **84** (2011) 024906, arXiv:1102.1957. [[Cited on page 28.](#)]
- [74] H. S. Chung, J. Lee, and D. Kang, “Cornell Potential Parameters for S-wave Heavy Quarkonia”, *J. Korean Phys. Soc.* **52** (2008) 1151, arXiv:0803.3116. [[Cited on page 29.](#)]
- [75] T. Matsui and H. Satz, “ J/ψ Suppression by Quark-Gluon Plasma Formation”, *Phys. Lett. B* **178** (1986) 416. [[Cited on pages 30 and 155.](#)]

BIBLIOGRAPHY

- [76] **CMS** Collaboration, A. M. Sirunyan *et al.*, “Suppression of Excited Υ States Relative to the Ground State in Pb-Pb Collisions at $\sqrt{s_{\text{NN}}}=5.02\text{TeV}$ ”, *Phys. Rev. Lett.* **120** (2018), no. 14, 142301, arXiv:1706.05984. [[Cited on pages 30, 31, and 254.](#)]
- [77] **LHCb** Collaboration, R. Aaij *et al.*, “Study of χ_b meson production in p p collisions at $\sqrt{s} = 7$ and 8 TeV and observation of the decay $\chi_b(3P) \rightarrow \Upsilon(3S)\gamma$ ”, *Eur. Phys. J. C* **74** (2014), no. 10, 3092, arXiv:1407.7734. [[Cited on page 31.](#)]
- [78] **NA50** Collaboration, M. C. Abreu *et al.*, “Anomalous J/ψ suppression in Pb-Pb interactions at 158 GeV/c per nucleon”, *Phys. Lett. B* **410** (1997) 337. [[Cited on pages 31 and 157.](#)]
- [79] **NA50** Collaboration, B. Alessandro *et al.*, “A New measurement of J/ψ suppression in Pb-Pb collisions at 158-GeV per nucleon”, *Eur. Phys. J. C* **39** (2005) 335, arXiv:hep-ex/0412036. [[Cited on page 31.](#)]
- [80] **PHENIX** Collaboration, A. Adare *et al.*, “ J/ψ Production vs Centrality, Transverse Momentum, and Rapidity in Au+Au Collisions at $\sqrt{s_{\text{NN}}} = 200$ GeV”, *Physical Review Letters* **98** (2007) 232301, arXiv:nucl-ex/0611020. [[Cited on pages 31 and 157.](#)]
- [81] P. Braun-Munzinger and J. Stachel, “(Non)thermal aspects of charmonium production and a new look at J/ψ suppression”, *Phys. Lett. B* **490** (2000) 196, arXiv:nucl-th/0007059. [[Cited on page 32.](#)]
- [82] L. Yan, P. Zhuang, and N. Xu, “Competition between J/ψ suppression and regeneration in quark-gluon plasma”, *Phys. Rev. Lett.* **97** (2006) 232301, arXiv:nucl-th/0608010. [[Cited on page 32.](#)]
- [83] R. Vogt, “Systematics of heavy quark production at RHIC”, arXiv:hep-ph/0203151. [[Cited on page 32.](#)]
- [84] **ALICE** Collaboration, B. B. Abelev *et al.*, “Centrality, rapidity and transverse momentum dependence of J/ψ suppression in Pb-Pb collisions at $\sqrt{s_{\text{NN}}}=2.76$ TeV”, *Phys. Lett. B* **734** (2014) 314, arXiv:1311.0214. [[Cited on pages 33, 158, and 255.](#)]
- [85] **CMS** Collaboration, S. Chatrchyan *et al.*, “Study of Z production in PbPb and pp collisions at $\sqrt{s_{\text{NN}}}=2.76$ TeV in the dimuon and dielectron decay channels”, *JHEP* **03** (2015) 022, arXiv:1410.4825. [[Cited on pages 33, 34, and 255.](#)]

- [86] A. D. Rosso, “Particle kickers. Aiguiller les particules”, Jun 2014. [[Cited on pages 38 and 255.](#)]
- [87] **ALICE** Collaboration, K. Aamodt *et al.*, “The ALICE experiment at the CERN LHC”, *Journal of Instrumentation* **3** (2008), no. 8, 08002. [[Cited on page 37.](#)]
- [88] **ATLAS** Collaboration, G. Aad *et al.*, “The ATLAS Experiment at the CERN Large Hadron Collider”, *Journal of Instrumentation* **3** (2008), no. 8, 08003. [[Cited on page 38.](#)]
- [89] **CMS** Collaboration, S. Chatrchyan *et al.*, “The CMS Experiment at the CERN LHC”, *Journal of Instrumentation* **3** (2008), no. 8, 08004. [[Cited on pages 38, 41, 45, 46, 47, 53, 255, and 256.](#)]
- [90] **LHCb** Collaboration, A. A. Alves, Jr. *et al.*, “The LHCb Detector at the LHC”, *Journal of Instrumentation* **3** (2008), no. 8, 08005. [[Cited on page 38.](#)]
- [91] J. Jowett *et al.*, “The 2015 Heavy-Ion Run of the LHC”, in “Proceedings, 7th International Particle Accelerator Conference (IPAC 2016): Busan, Korea, May 8-13, 2016”, vol. TUPMW027. 2016. [[Cited on pages 40, 41, and 255.](#)]
- [92] J. Jowett *et al.*, “The 2016 Proton-Nucleus Run of the LHC”, in “Proceedings, 8th International Particle Accelerator Conference (IPAC 2017): Copenhagen, Denmark, May 14-19, 2017”, vol. TUPVA014. 2017. [[Cited on pages 42 and 255.](#)]
- [93] J. M. Jowett, “Colliding Heavy Ions in the LHC”, in “Proceedings, 9th International Particle Accelerator Conference (IPAC 2018): Vancouver, BC, Canada, April 29 - May 4, 2018”, vol. TUXGBD2. 2018. [[Cited on pages 42 and 249.](#)]
- [94] T. Sakuma and T. McCauley, “Detector and Event Visualization with SketchUp at the CMS Experiment”, in “Proceedings, 20th International Conference on Computing in High Energy and Nuclear Physics (CHEP 2013): Amsterdam, The Netherlands, October 14-18, 2013”, vol. 513, p. 022032. 2014. [[Cited on pages 43 and 255.](#)]
- [95] C. Battilana, “The CMS muon system: status and upgrades for LHC Run-2 and performance of muon reconstruction with 13 TeV data”, in “Proceedings, 14th Topical Seminar on Innovative Particle and Radiation Detectors (IPRD16): Siena, Italy, Oct 3-6, 2016”, vol. 12, p. 01048. 2017. [[Cited on page 45.](#)]

BIBLIOGRAPHY

- [96] **CMS** Collaboration, J. Mans, J. Anderson, B. Dahmes, P. de Barbaro, J. Freeman, T. Grassi, E. Hazen, J. Mans, R. Ruchti, I. Schimdt, *et al.*, “CMS Technical Design Report for the Phase 1 Upgrade of the Hadron Calorimeter”, 2012. [[Cited on pages 45, 49, and 255.](#)]
- [97] **CMS** Collaboration, A. Tapper and D. Acosta, “CMS Technical Design Report for the Level-1 Trigger Upgrade”, tech. rep., CERN, 2013. [[Cited on pages 45 and 56.](#)]
- [98] **CMS** Collaboration, A. Benaglia, “The CMS ECAL performance with examples”, in “Proceedings, 13th Topical Seminar on Innovative Particle and Radiation Detectors (IPRD13): Siena, Italy, October 7-10, 2013”, vol. 9, p. 02008. 2014. [[Cited on pages 47 and 255.](#)]
- [99] G. Abbiendi, “The CMS muon system in Run2: preparation, status and first results”, in “Proceedings, 2015 European Physical Society Conference on High Energy Physics (EPS-HEP 2015): Vienna, Austria, July 22-29, 2015”, vol. 234, p. 237. 2016. [[Cited on pages 51 and 255.](#)]
- [100] **CMS** Collaboration, S. Chatrchyan *et al.*, “Performance of the CMS Drift Tube Chambers with Cosmic Rays”, *Journal of Instrumentation* **5** (2010), no. 3, 03015. [[Cited on pages 52 and 256.](#)]
- [101] M. Abbrescia *et al.*, “Beam test results on double-gap resistive plate chambers proposed for CMS experiment”, *Nuclear Instruments and Methods in Physics Research Section A: Accelerators, Spectrometers, Detectors and Associated Equipment* **414** (1998), no. 2, 135. [[Cited on pages 53 and 256.](#)]
- [102] C. Collaboration, “Resistive Plate Chambers”, 2011. [Online; accessed July 7, 2018]. [[Cited on pages 53 and 256.](#)]
- [103] **CMS** Collaboration, V. Khachatryan *et al.*, “The CMS trigger system”, *Journal of Instrumentation* **12** (2017), no. 1, 01020. [[Cited on pages 54 and 55.](#)]
- [104] J. J. Brooke, D. G. Cussans, R. Frazier, G. Heath, D. Machin, and D. Newbold, “The New Global Muon Trigger of the CMS Experiment”, in “Proceedings, 9th Workshop on Electronics for LHC Experiments, Amsterdam, The Netherlands, 29 Sep - 3 Oct 2003”, p. 226. 2003. [[Cited on pages 55 and 256.](#)]
- [105] A. Zabi *et al.*, “Triggering on electrons, jets and tau leptons with the CMS upgraded calorimeter trigger for the LHC RUN II”, in “Proceedings, Topical

Workshop on Electronics for Particle Physics (TWEPP15): Lisbon, Portugal, September 28 - October 02, 2015”, vol. 11, p. 02008. 2016. [[Cited on page 57.](#)]

- [106] J. Fulcher, J. Lingemann, D. Rabady, T. Reis, and H. Sakulin, “The New Global Muon Trigger of the CMS Experiment”, in “Proceedings, 20th IEEE-NPSS Real Time Conference (RT2016): Padua, Italy, June 5-10, 2016”, vol. 64, p. 1467. 2017. [[Cited on page 57.](#)]
- [107] J.-M. André *et al.*, “Performance of the new DAQ system of the CMS experiment for run-2”, in “Proceedings, 2016 IEEE-NPSS Real Time Conference (RT): Padua, Italy, June 6-10, 2016”, p. 1. 2016. [[Cited on page 58.](#)]
- [108] R. Fruhwirth, “Application of Kalman filtering to track and vertex fitting”, *Nuclear Instruments and Methods in Physics Research Section A: Accelerators, Spectrometers, Detectors and Associated Equipment* **262** (1987), no. 2, 444. [[Cited on pages 59 and 60.](#)]
- [109] **CMS** Collaboration, A. M. Sirunyan *et al.*, “Performance of the CMS muon detector and muon reconstruction with proton-proton collisions at $\sqrt{s} = 13$ TeV”, *Journal of Instrumentation* **13** (2018), no. 6, 06015. [[Cited on page 60.](#)]
- [110] D. Barney, “CMS Detector Slice”, CMS Collection., Jan 2016, unpublished. [[Cited on pages 61 and 256.](#)]
- [111] **CMS** Collaboration, A. M. Sirunyan *et al.*, “Particle-flow reconstruction and global event description with the CMS detector”, *JINST* **12** (2017), no. 10, P10003, arXiv:1706.04965. [[Cited on pages 63 and 90.](#)]
- [112] C. Collaboration, “Performance of missing transverse momentum in pp collisions at $\text{sqrt}(s)=13$ TeV using the CMS detector”, Tech. Rep. CMS-PAS-JME-17-001, CERN, Geneva, 2018. [[Cited on page 63.](#)]
- [113] **CMS** Collaboration, V. Khachatryan *et al.*, “Performance of the CMS missing transverse momentum reconstruction in pp data at $\sqrt{s} = 8$ TeV”, *Journal of Instrumentation* **10** (2015), no. 2, 02006. [[Cited on page 63.](#)]
- [114] E. Rutherford, “Uranium radiation and the electrical conduction produced by it”, *Philos. Mag.* **47** (1899) 109. [[Cited on page 66.](#)]

BIBLIOGRAPHY

- [115] J. Chadwick, “Intensitätsverteilung im magnetischen Spektrum von β -Strahlen von Radium B+C”, *Verhandlungen der deutschen physikalischen Gesellschaft* **16** (1914) 383. [[Cited on page 66.](#)]
- [116] J. Chadwick and C. D. Ellis, “A Preliminary Investigation of the Intensity Distribution in the β -Ray Spectra of Radium B and C”, *Proceedings of the Cambridge Philosophical Society* **21** (1922) 274. [[Cited on page 66.](#)]
- [117] W. Pauli, “Fünf Arbeiten zum Ausschliessungsprinzip und zum Neutrino”, Wissenschaftliche Buchgesellschaft, [Abt. Verlag], 1977. [[Cited on page 66.](#)]
- [118] K. Winter, “Neutrino physics”, Cambridge University Press, 1991. [[Cited on page 66.](#)]
- [119] J. Chadwick, “Possible Existence of a Neutron”, *Nature* **129** (1932) 312. [[Cited on page 66.](#)]
- [120] E. Fermi, “Collected Papers of Enrico Fermi”, University of Chicago Press, 1965. [[Cited on page 66.](#)]
- [121] E. Fermi, “Versuch einer Theorie der β -Strahlen. I”, *Zeitschrift für Physik* **88** (1934) 161. [[Cited on page 66.](#)]
- [122] T. D. Lee and C. N. Yang, “Question of Parity Conservation in Weak Interactions”, *Phys. Rev.* **104** (1956) 254. [[Cited on pages 66 and 67.](#)]
- [123] C. S. Wu, E. Ambler, R. W. Hayward, D. D. Hoppes, and R. P. Hudson, “Experimental Test of Parity Conservation in Beta Decay”, *Phys. Rev.* **105** (1957) 1413. [[Cited on page 67.](#)]
- [124] M. Goldhaber, L. Grodzins, and A. W. Sunyar, “Helicity of Neutrinos”, *Phys. Rev.* **109** (1958) 1015. [[Cited on page 67.](#)]
- [125] E. C. G. Sudarshan and R. E. Marshak, “Origin of the Universal VÄA theory”, *AIP Conf. Proc.* **300** (1994) 110, [,0001(1984)]. [[Cited on page 67.](#)]
- [126] J. H. Christenson, J. W. Cronin, V. L. Fitch, and R. Turlay, “Evidence for the 2π Decay of the K_2^0 Meson”, *Phys. Rev. Lett.* **13** (1964) 138. [[Cited on page 67.](#)]
- [127] M. Kobayashi and T. Maskawa, “CP Violation in the Renormalizable Theory of Weak Interaction”, *Prog. Theor. Phys.* **49** (1973) 652. [[Cited on page 67.](#)]

- [128] N. Cabibbo, “Unitary Symmetry and Leptonic Decays”, *Phys. Rev. Lett.* **10** (1963) 531, [,648(1963)]. [[Cited on page 67.](#)]
- [129] S. L. Glashow, J. Iliopoulos, and L. Maiani, “Weak Interactions with Lepton-Hadron Symmetry”, *Phys. Rev. D* **2** (1970) 1285. [[Cited on page 67.](#)]
- [130] **E598** Collaboration, J. J. Aubert *et al.*, “Experimental Observation of a Heavy Particle J ”, *Phys. Rev. Lett.* **33** (1974) 1404. [[Cited on pages 67 and 146.](#)]
- [131] **SLAC-SP-017** Collaboration, J. E. Augustin *et al.*, “Discovery of a Narrow Resonance in e^+e^- Annihilation”, *Phys. Rev. Lett.* **33** (1974) 1406. [[Cited on pages 67 and 146.](#)]
- [132] S. W. Herb *et al.*, “Observation of a Dimuon Resonance at 9.5-GeV in 400-GeV Proton-Nucleus Collisions”, *Phys. Rev. Lett.* **39** (1977) 252. [[Cited on page 67.](#)]
- [133] **CDF** Collaboration, F. Abe *et al.*, “Observation of top quark production in $\bar{p}p$ collisions”, *Phys. Rev. Lett.* **74** (1995) 2626, arXiv:hep-ex/9503002. [[Cited on page 67.](#)]
- [134] P. A. M. Dirac, “The Principles of Quantum Mechanics”, Clarendon Press, 1930. [[Cited on page 67.](#)]
- [135] S. L. Glashow, “The renormalizability of vector meson interactions”, *Nucl. Phys.* **10** (1959) 107. [[Cited on pages 67 and 69.](#)]
- [136] S. Weinberg, “A Model of Leptons”, *Phys. Rev. Lett.* **19** (1967) 1264. [[Cited on page 67.](#)]
- [137] A. Salam, “Weak and Electromagnetic Interactions”, *Conf. Proc. C* **680519** (1968) 367. [[Cited on pages 67 and 69.](#)]
- [138] G. t. Hooft, “Renormalizable Lagrangians for massive Yang-Mills fields”, *Nuclear Physics B* **35** (1971) 167. [[Cited on page 68.](#)]
- [139] G. t. Hooft and M. Veltman, “Regularization and renormalization of gauge fields”, *Nuclear Physics B* **44** (1972) 189. [[Cited on page 68.](#)]
- [140] **Gargamelle Neutrino** Collaboration, F. J. Hasert *et al.*, “Observation of Neutrino Like Interactions without Muon or Electron in the Gargamelle Neutrino Experiment”, *Nucl. Phys. B* **73** (1974) 1. [[Cited on page 68.](#)]

BIBLIOGRAPHY

- [141] C. Rubbia, P. McIntyre, and D. Cline, *Producing Massive Neutral Intermediate Vector Bosons with Existing Accelerators*, p. 683. Vieweg+Teubner Verlag, Wiesbaden, 1977. [[Cited on page 68.](#)]
- [142] S. van der Meer, “Stochastic damping of betatron oscillations in the ISR”, Tech. Rep. CERN-ISR-PO-72-31. ISR-PO-72-31, CERN, Geneva, Aug 1972. [[Cited on page 68.](#)]
- [143] G. Arnison *et al.*, “Experimental observation of isolated large transverse energy electrons with associated missing energy at $\sqrt{s}=540$ GeV”, *Phys. Lett. B* **122** (1983) 103. [[Cited on page 68.](#)]
- [144] M. Banner *et al.*, “Observation of single isolated electrons of high transverse momentum in events with missing transverse energy at the CERN pp collider”, *Phys. Lett. B* **122** (1983) 476. [[Cited on page 68.](#)]
- [145] **UA1** Collaboration, G. Arnison *et al.*, “Experimental Observation of Lepton Pairs of Invariant Mass Around 95-GeV/c**2 at the CERN SPS Collider”, *Phys. Lett. B* **126** (1983) 398, [,7.55(1983)]. [[Cited on page 68.](#)]
- [146] **UA2** Collaboration, P. Bagnaia *et al.*, “Evidence for $Z_0 \rightarrow e^+ e^-$ at the CERN anti-p p Collider”, *Phys. Lett. B* **129** (1983) 130, [,7.69(1983)]. [[Cited on page 68.](#)]
- [147] S. Myers, “The LEP Collider, from design to approval and commissioning”, CERN, Geneva, 1991. Delivered at CERN, 26 Nov 1990. [[Cited on page 68.](#)]
- [148] **DØ Collaboration** Collaboration, V. M. Abazov *et al.*, “Improved W boson mass measurement with the DØ detector”, *Phys. Rev. D* **66** Jul (2002) 012001. [[Cited on page 68.](#)]
- [149] R. R. Wilson, “The Tevatron”, *Phys. Today* **30** (1977) 23. [[Cited on page 68.](#)]
- [150] S. Dulat, T.-J. Hou, J. Gao, M. Guzzi, J. Huston, P. Nadolsky, J. Pumplin, C. Schmidt, D. Stump, and C. P. Yuan, “New parton distribution functions from a global analysis of quantum chromodynamics”, *Phys. Rev. D* **93** (2016) 033006, arXiv:1506.07443. [[Cited on pages 74, 75, 86, and 256.](#)]
- [151] **European Muon** Collaboration, J. J. Aubert *et al.*, “The ratio of the nucleon structure functions F_{2n} for iron and deuterium”, *Phys. Lett. B* **123** (1983) 275–278. [[Cited on page 76.](#)]

- [152] **European Muon** Collaboration, M. Arneodo *et al.*, “Shadowing in Deep Inelastic Muon Scattering from Nuclear Targets”, *Phys. Lett. B* **211** (1988) 493. [[Cited on page 76.](#)]
- [153] H. Paukkunen, “Nuclear PDFs in the beginning of the LHC era”, *Nucl. Phys. A* **926** (2014) 24, arXiv:1401.2345. [[Cited on pages 76 and 256.](#)]
- [154] K. J. Eskola, V. J. Kolhinen, and C. A. Salgado, “The Scale dependent nuclear effects in parton distributions for practical applications”, *Eur. Phys. J. C* **9** (1999) 61, arXiv:hep-ph/9807297. [[Cited on page 77.](#)]
- [155] K. J. Eskola, H. Paukkunen, and C. A. Salgado, “An Improved global analysis of nuclear parton distribution functions including RHIC data”, *JHEP* **07** (2008) 102, arXiv:0802.0139. [[Cited on page 77.](#)]
- [156] K. J. Eskola, H. Paukkunen, and C. A. Salgado, “EPS09: A New Generation of NLO and LO Nuclear Parton Distribution Functions”, *JHEP* **04** (2009) 065, arXiv:0902.4154. [[Cited on page 77.](#)]
- [157] D. de Florian, R. Sassot, P. Zurita, and M. Stratmann, “Global Analysis of Nuclear Parton Distributions”, *Phys. Rev. D* **85** (2012) 074028, arXiv:1112.6324. [[Cited on page 77.](#)]
- [158] K. J. Eskola, P. Paakkinen, H. Paukkunen, and C. A. Salgado, “EPPS16: Nuclear parton distributions with LHC data”, *Eur. Phys. J. C* **77** (2017) 163, arXiv:1612.05741. [[Cited on pages 77, 79, 81, 86, 127, 154, 256, and 261.](#)]
- [159] K. Kovarik *et al.*, “nCTEQ15 - Global analysis of nuclear parton distributions with uncertainties in the CTEQ framework”, *Phys. Rev. D* **93** (2016), no. 8, 085037, arXiv:1509.00792. [[Cited on pages 78, 80, and 256.](#)]
- [160] **CMS** Collaboration, S. Chatrchyan *et al.*, “Study of W boson production in PbPb and pp collisions at $\sqrt{s_{NN}} = 2.76$ TeV”, *Phys. Lett. B* **715** (2012) 66, arXiv:1205.6334. [[Cited on page 80.](#)]
- [161] **CMS** Collaboration, S. Chatrchyan *et al.*, “Study of Z boson production in PbPb collisions at $\sqrt{s_{NN}} = 2.76$ TeV”, *Phys. Rev. Lett.* **106** (2011) 212301, arXiv:1102.5435. [[Cited on page 80.](#)]

BIBLIOGRAPHY

- [162] **ATLAS** Collaboration, G. Aad *et al.*, “Measurement of the production and lepton charge asymmetry of W bosons in Pb+Pb collisions at $\sqrt{s_{\text{NN}}} = 2.76$ TeV with the ATLAS detector”, *Eur. Phys. J. C* **75** (2015), no. 1, 23, arXiv:1408.4674. [[Cited on page 80.](#)]
- [163] **ATLAS** Collaboration, G. Aad *et al.*, “Measurement of Z boson Production in Pb+Pb Collisions at $\sqrt{s_{\text{NN}}} = 2.76$ TeV with the ATLAS Detector”, *Phys. Rev. Lett.* **110** (2013), no. 2, 022301, arXiv:1210.6486. [[Cited on page 80.](#)]
- [164] **ALICE** Collaboration, S. Acharya *et al.*, “Measurement of Z^0 -boson production at large rapidities in Pb-Pb collisions at $\sqrt{s_{\text{NN}}} = 5.02$ TeV”, *Phys. Lett. B* **780** (2018) 372, arXiv:1711.10753. [[Cited on page 82.](#)]
- [165] **ATLAS** Collaboration, G. Aad *et al.*, “ Z boson production in p+Pb collisions at $\sqrt{s_{\text{NN}}} = 5.02$ TeV measured with the ATLAS detector”, *Phys. Rev. C* **92** (2015), no. 4, 044915, arXiv:1507.06232. [[Cited on pages 82 and 257.](#)]
- [166] **ALICE** Collaboration, J. Adam *et al.*, “ W and Z boson production in p-Pb collisions at $\sqrt{s_{\text{NN}}} = 5.02$ TeV”, *JHEP* **02** (2017) 077, arXiv:1611.03002. [[Cited on pages 83 and 257.](#)]
- [167] **CMS** Collaboration, V. Khachatryan *et al.*, “Study of W boson production in pPb collisions at $\sqrt{s_{\text{NN}}} = 5.02$ TeV”, *Phys. Lett. B* **750** (2015) 565, arXiv:1503.05825. [[Cited on pages 83, 84, 130, and 257.](#)]
- [168] CMS Collaboration, “CMS luminosity measurement using 2016 proton-nucleus collisions at nucleon-nucleon center-of-mass energy of 8.16 TeV”, Tech. Rep. CMS-PAS-LUM-17-002, CERN, Geneva, 2018. [[Cited on pages 85, 126, 137, 138, and 260.](#)]
- [169] C. A. Salgado *et al.*, “Proton-Nucleus Collisions at the LHC: Scientific Opportunities and Requirements”, *Journal of Physics G: Nuclear and Particle Physics* **39** (2012), no. 1, 015010, arXiv:1105.3919. [[Cited on page 85.](#)]
- [170] S. Frixione, P. Nason, and C. Oleari, “Matching NLO QCD computations with Parton Shower simulations: the POWHEG method”, *JHEP* **11** (2007) 070, arXiv:0709.2092. [[Cited on page 86.](#)]
- [171] P. Nason, “A New method for combining NLO QCD with shower Monte Carlo algorithms”, *JHEP* **11** (2004) 040, arXiv:hep-ph/0409146. [[Not cited.](#)]

- [172] S. Alioli, P. Nason, C. Oleari, and E. Re, “A general framework for implementing NLO calculations in shower Monte Carlo programs: the POWHEG BOX”, *JHEP* **06** (2010) 043, arXiv:1002.2581. [[Cited on page 86.](#)]
- [173] L. Barze, G. Montagna, P. Nason, O. Nicrosini, and F. Piccinini, “Implementation of electroweak corrections in the POWHEG BOX: single W production”, *JHEP* **04** (2012) 037, arXiv:1202.0465. [[Cited on pages 86 and 133.](#)]
- [174] L. Barze, G. Montagna, P. Nason, O. Nicrosini, F. Piccinini, and A. Vicini, “Neutral-current Drell–Yan with combined QCD and electroweak corrections in the POWHEG BOX”, *Eur. Phys. J. C* **73** (2013) 2474, arXiv:1302.4606. [[Cited on page 86.](#)]
- [175] S. Frixione, P. Nason, and G. Ridolfi, “A Positive-Weight Next-to-Leading-Order Monte Carlo for Heavy Flavour Hadroproduction”, *JHEP* **09** (2007) 126, arXiv:0707.3088. [[Cited on page 86.](#)]
- [176] T. Sjöstrand, S. Ask, J. R. Christiansen, R. Corke, N. Desai, P. Ilten, S. Mrenna, S. Prestel, C. O. Rasmussen, and P. Z. Skands, “An Introduction to PYTHIA 8.2”, *Comput. Phys. Commun.* **191** (2015) 159, arXiv:1410.3012. [[Cited on pages 87 and 161.](#)]
- [177] **CMS** Collaboration, S. Chatrchyan *et al.*, “Study of the underlying event at forward rapidity in pp collisions at $\sqrt{s} = 0.9, 2.76$, and 7 TeV”, *JHEP* **04** (2013) 072, arXiv:1302.2394. [[Cited on pages 87 and 161.](#)]
- [178] **GEANT4** Collaboration, S. Agostinelli *et al.*, “GEANT4: A Simulation toolkit”, *Nucl. Instrum. Meth. A* **506** (2003) 250. [[Cited on pages 87 and 161.](#)]
- [179] T. Pierog, I. Karpenko, J. M. Katzy, E. Yatsenko, and K. Werner, “EPOS LHC: Test of collective hadronization with data measured at the CERN Large Hadron Collider”, *Phys. Rev. C* **92** (2015) 034906, arXiv:1306.0121. [[Cited on page 87.](#)]
- [180] **CMS** Collaboration, A. M. Sirunyan *et al.*, “Pseudorapidity distributions of charged hadrons in proton-lead collisions at $\sqrt{s_{\text{NN}}} = 5.02$ and 8.16 TeV”, *JHEP* **01** (2018) 045, arXiv:1710.09355. [[Cited on page 87.](#)]
- [181] **CMS** Collaboration, A. M. Sirunyan *et al.*, “Observation of top quark production in proton-nucleus collisions”, *Phys. Rev. Lett.* **119** (2017) 242001, arXiv:1709.07411. [[Cited on pages 88, 115, 131, and 249.](#)]

BIBLIOGRAPHY

- [182] B. H. Armstrong, “Spectrum line profiles: The Voigt function”, *J. Quant. Spectrosc. Radiat. Transfer* **7** (1967) 61. [[Cited on page 109.](#)]
- [183] CMS Collaboration, “Muon performance studies in 2016 pPb data”, Tech. Rep. CMS-HIN-AN-17-137, CERN, Geneva, 2017. [[Cited on pages 110, 111, 258, and 259.](#)]
- [184] W. Verkerke and D. P. Kirkby, “The RooFit toolkit for data modeling”, *eConf C* **0303241** (2003) 186, arXiv:physics/0306116. [[Cited on pages 120 and 168.](#)]
- [185] A. Buckley, J. Ferrando, S. Lloyd, K. Nordström, B. Page, M. Rüfenacht, M. Schönherr, and G. Watt, “LHAPDF6: parton density access in the LHC precision era”, *Eur. Phys. J. C* **75** (2015) 132, arXiv:1412.7420. [[Cited on page 127.](#)]
- [186] R. Boughezal, J. M. Campbell, R. K. Ellis, C. Focke, W. Giele, X. Liu, F. Petriello, and C. Williams, “Color singlet production at NNLO in MCFM”, *Eur. Phys. J. C* **77** (2017) 7, arXiv:1605.08011. [[Cited on pages 130 and 140.](#)]
- [187] S. Alioli, P. Nason, C. Oleari, and E. Re, “NLO vector-boson production matched with shower in POWHEG”, *JHEP* **07** (2008) 060, arXiv:0805.4802. [[Cited on page 134.](#)]
- [188] S. Okubo, “Phi meson and unitary symmetry model”, *Phys. Lett.* **5** (1963) 165. [[Cited on page 146.](#)]
- [189] G. Zweig, “An SU(3) model for strong interaction symmetry and its breaking. Version 2”, in “DEVELOPMENTS IN THE QUARK THEORY OF HADRONS. VOL. 1. 1964 - 1978”, D. Lichtenberg and S. P. Rosen, eds., p. 22. 1964. [[Not cited.](#)]
- [190] J. Iizuka, “Systematics and phenomenology of meson family”, *Prog. Theor. Phys. Suppl.* **37** (1966) 21. [[Cited on page 146.](#)]
- [191] J.-M. Richard, “An introduction to the quark model”, in “Ferrara International School Niccolo Cabeo 2012: Hadronic spectroscopy Ferrara, Italy, May 21-26, 2012”. 2012. arXiv:1205.4326. [[Cited on pages 147 and 261.](#)]
- [192] M. B. Einhorn and S. D. Ellis, “Hadronic Production of the New Resonances - Are Gluons Important?”, *Phys. Rev. Lett.* **34** (1975) 1190–1193. [[Cited on page 148.](#)]

- [193] C.-H. Chang, “Hadronic Production of J/ψ Associated With a Gluon”, *Nucl. Phys. B* **172** (1980) 425. [[Cited on page 148.](#)]
- [194] A. Andronic *et al.*, “Heavy-flavour and quarkonium production in the LHC era: from proton- \bar{p} to heavy-ion collisions”, *Eur. Phys. J. C* **76** (2016), no. 3, 107, arXiv:1506.03981. [[Cited on pages 148, 153, 157, and 251.](#)]
- [195] J. P. Lansberg, “ J/ψ , ψ' and ν production at hadron colliders: A Review”, *Int. J. Mod. Phys. A* **21** (2006) 3857, arXiv:hep-ph/0602091. [[Cited on page 148.](#)]
- [196] S. J. Brodsky and J.-P. Lansberg, “Heavy-Quarkonium Production in High Energy Proton-Proton Collisions at RHIC”, *Phys. Rev. D* **81** (2010) 051502, arXiv:0908.0754. [[Cited on page 148.](#)]
- [197] **CDF** Collaboration, F. Abe *et al.*, “Production of J/ψ mesons from χ_c meson decays in $p\bar{p}$ collisions at $\sqrt{s} = 1.8$ TeV”, *Phys. Rev. Lett.* **79** (1997) 578. [[Cited on page 148.](#)]
- [198] **Quarkonium Working Group** Collaboration, N. Brambilla *et al.*, “Heavy quarkonium physics”, arXiv:hep-ph/0412158. [[Cited on pages 148, 149, and 150.](#)]
- [199] H. Fritzsch, “Producing Heavy Quark Flavors in Hadronic Collisions: A Test of Quantum Chromodynamics”, *Phys. Lett. B* **67** (1977) 217. [[Cited on page 148.](#)]
- [200] F. Halzen, “CVC for Gluons and Hadroproduction of Quark Flavors”, *Phys. Lett. B* **69** (1977) 105. [[Cited on page 148.](#)]
- [201] R. Gavai, D. Kharzeev, H. Satz, G. A. Schuler, K. Sridhar, and R. Vogt, “Quarkonium production in hadronic collisions”, *Int. J. Mod. Phys. A* **10** (1995) 3043, arXiv:hep-ph/9502270. [[Cited on page 149.](#)]
- [202] J. F. Amundson, O. J. P. Eboli, E. M. Gregores, and F. Halzen, “Quantitative tests of color evaporation: Charmonium production”, *Phys. Lett. B* **390** (1997) 323, arXiv:hep-ph/9605295. [[Cited on page 149.](#)]
- [203] **CDF** Collaboration, A. Abulencia *et al.*, “Measurement of $\sigma_{\chi_{c2}} B(\chi_{c2} \rightarrow J/\psi \gamma) / \sigma_{\chi_{c1}} B(\chi_{c1} \rightarrow J/\psi \gamma)$ in $p\bar{p}$ collisions at $\sqrt{s} = 1.96$ -TeV”, *Phys. Rev. Lett.* **98** (2007) 232001, arXiv:hep-ex/0703028. [[Cited on page 149.](#)]

BIBLIOGRAPHY

- [204] **CMS** Collaboration, S. Chatrchyan *et al.*, “Measurement of the relative prompt production rate of chi(c2) and chi(c1) in $p\bar{p}$ collisions at $\sqrt{s} = 7$ TeV”, *Eur. Phys. J. C* **72** (2012) 2251, arXiv:1210.0875. [[Cited on page 149.](#)]
- [205] V. Cheung and R. Vogt, “Polarized Heavy Quarkonium Production in the Color Evaporation Model”, *Phys. Rev. D* **95** (2017), no. 7, 074021, arXiv:1702.07809. [[Cited on page 149.](#)]
- [206] G. T. Bodwin, E. Braaten, and G. P. Lepage, “Rigorous QCD predictions for decays of p wave quarkonia”, in “The Fermilab Meeting DPF 92. Proceedings, 7th Meeting of the American Physical Society, Division of Particles and Fields, Batavia, USA, November 10-14, 1992. Vol. 1, 2”, p. 1063. 1992.
arXiv:hep-ph/9211253. [[Cited on page 149.](#)]
- [207] J. P. Lansberg, “On the mechanisms of heavy-quarkonium hadroproduction”, *Eur. Phys. J. C* **61** (2009) 693, arXiv:0811.4005. [[Cited on pages 151 and 261.](#)]
- [208] **ATLAS** Collaboration, G. Aad *et al.*, “Measurement of the differential cross-sections of prompt and non-prompt production of J/ψ and $\psi(2S)$ in $p\bar{p}$ collisions at $\sqrt{s} = 7$ and 8 TeV with the ATLAS detector”, *Eur. Phys. J. C* **76** (2016), no. 5, 283, arXiv:1512.03657. [[Cited on page 151.](#)]
- [209] B. Paul, M. Mandal, P. Roy, and S. Chattapadhyay, “Systematic study of charmonium production in p-p collisions at LHC energies”, *J. Phys. G* **42** (2015), no. 6, 065101, arXiv:1411.6783. [[Not cited.](#)]
- [210] R. Sharma and I. Vitev, “High transverse momentum quarkonium production and dissociation in heavy ion collisions”, *Phys. Rev. C* **87** (2013), no. 4, 044905, arXiv:1203.0329. [[Not cited.](#)]
- [211] Y.-Q. Ma and R. Venugopalan, “Comprehensive Description of J/ψ Production in Proton-Proton Collisions at Collider Energies”, *Phys. Rev. Lett.* **113** (2014), no. 19, 192301, arXiv:1408.4075. [[Cited on page 151.](#)]
- [212] Z. Sun and H.-F. Zhang, “Reconciling charmonium production and polarization data in the midrapidity region at hadron colliders within the nonrelativistic QCD framework”, *Chin. Phys. C* **42** (2018), no. 4, 043104, arXiv:1505.02675. [[Cited on page 151.](#)]

- [213] H. S. Shao, H. Han, Y. Q. Ma, C. Meng, Y. J. Zhang, and K. T. Chao, “Yields and polarizations of prompt J/ψ and $\psi(2S)$ production in hadronic collisions”, *JHEP* **05** (2015) 103, arXiv:1411.3300. [[Cited on page 151.](#)]
- [214] **CMS** Collaboration, C. Collaboration, “Production of prompt and nonprompt J/ψ mesons in jets in pp collisions at $\sqrt{s} = 5.02$ TeV”, 2018. [[Cited on page 151.](#)]
- [215] **LHCb** Collaboration, R. Aaij *et al.*, “Study of J/ψ Production in Jets”, *Phys. Rev. Lett.* **118** (2017), no. 19, 192001, arXiv:1701.05116. [[Cited on page 151.](#)]
- [216] **LHCb** Collaboration, R. Aaij *et al.*, “First observation of $B_s^0 \rightarrow J/\psi f_0(980)$ decays”, *Phys. Lett. B* **698** (2011) 115, arXiv:1102.0206. [[Cited on pages 152 and 261.](#)]
- [217] P. Braun-Munzinger and J. Stachel, “Charmonium from Statistical Hadronization of Heavy Quarks: A Probe for Deconfinement in the Quark-Gluon Plasma”, *Landolt-Bornstein* **23** (2010) 424, arXiv:0901.2500. [[Cited on page 153.](#)]
- [218] B. Alver, M. Baker, C. Loizides, and P. Steinberg, “The PHOBOS Glauber Monte Carlo”, arXiv:0805.4411. [[Cited on page 153.](#)]
- [219] F. Arleo, S. Peigné, and T. Sami, “Revisiting scaling properties of medium-induced gluon radiation”, *Phys. Rev. D* **83** (2011) 114036, arXiv:1006.0818. [[Cited on page 154.](#)]
- [220] F. Arleo and S. Peigné, “Heavy-quarkonium suppression in p-A collisions from parton energy loss in cold QCD matter”, *JHEP* **03** (2013) 122, arXiv:1212.0434. [[Not cited.](#)]
- [221] S. Peigné, F. Arleo, and R. Kolevatov, “Coherent medium-induced gluon radiation in hard forward $1 \rightarrow 1$ partonic processes”, *Phys. Rev. D* **93** (2016), no. 1, 014006, arXiv:1402.1671. [[Cited on page 154.](#)]
- [222] J. W. Cronin, H. J. Frisch, M. J. Shochet, J. P. Boymond, R. Mermod, P. A. Piroue, and R. L. Sumner, “Production of hadrons with large transverse momentum at 200, 300, and 400 GeV”, *Phys. Rev. D* **11** (1975) 3105. [[Cited on page 155.](#)]
- [223] **ALICE** Collaboration, J. Adam *et al.*, “Rapidity and transverse-momentum dependence of the inclusive J/ψ nuclear modification factor in p-Pb collisions at $\sqrt{s_{NN}} = 5.02$ TeV”, *JHEP* **06** (2015) 055, arXiv:1503.07179. [[Cited on pages 155, 156, and 261.](#)]

BIBLIOGRAPHY

- [224] P. Braun-Munzinger and J. Stachel, “Charmonium from Statistical Hadronization of Heavy Quarks: A Probe for Deconfinement in the Quark-Gluon Plasma”, *Landolt-Bornstein* **23** (2010) 424, arXiv:0901.2500. [[Cited on page 157.](#)]
- [225] P. Braun-Munzinger and J. Stachel, “(Non)thermal aspects of charmonium production and a new look at J/ψ suppression”, *Phys. Lett. B* **490** (2000) 196, arXiv:nucl-th/0007059. [[Cited on page 157.](#)]
- [226] L. Grandchamp, R. Rapp, and G. E. Brown, “In medium effects on charmonium production in heavy ion collisions”, *Phys. Rev. Lett.* **92** (2004) 212301, arXiv:hep-ph/0306077. [[Cited on page 157.](#)]
- [227] **NA50** Collaboration, B. Alessandro *et al.*, “psi-prime production in Pb-Pb collisions at 158-GeV/nucleon”, *Eur. Phys. J. C* **49** (2007) 559, arXiv:nucl-ex/0612013. [[Cited on page 157.](#)]
- [228] **CMS** Collaboration, V. Khachatryan *et al.*, “Measurement of Prompt $\psi(2S) \rightarrow J/\psi$ Yield Ratios in Pb-Pb and p-p Collisions at $\sqrt{s_{NN}} = 2.76$ TeV”, *Phys. Rev. Lett.* **113** (2014), no. 26, 262301, arXiv:1410.1804. [[Cited on pages 158, 159, 211, 262, and 265.](#)]
- [229] **ALICE** Collaboration, J. Adam *et al.*, “Differential studies of inclusive J/ψ and $\psi(2S)$ production at forward rapidity in Pb-Pb collisions at $\sqrt{s_{NN}} = 2.76$ TeV”, *JHEP* **05** (2016) 179, arXiv:1506.08804. [[Cited on page 158.](#)]
- [230] X. Du and R. Rapp, “Sequential Regeneration of Charmonia in Heavy-Ion Collisions”, *Nucl. Phys. A* **943** (2015) 147, arXiv:1504.00670. [[Cited on pages 158 and 212.](#)]
- [231] **CMS** Collaboration, A. M. Sirunyan *et al.*, “Measurement of prompt and nonprompt charmonium suppression in PbPb collisions at 5.02 TeV”, *Eur. Phys. J. C* **78** (2018), no. 6, 509, arXiv:1712.08959. [[Cited on pages 159, 203, 206, 207, 208, 209, 264, and 265.](#)]
- [232] **CMS** Collaboration, A. M. Sirunyan *et al.*, “Relative Modification of Prompt $\psi(2S)$ and J/ψ Yields from pp to PbPb Collisions at $\sqrt{s_{NN}} = 5.02$ TeV”, *Phys. Rev. Lett.* **118** (2017), no. 16, 162301, arXiv:1611.01438. [[Cited on pages 159, 210, 211, and 265.](#)]

- [233] D. J. Lange, “The EvtGen particle decay simulation package”, *Nucl. Instrum. Meth. A* **462** (2001) 152–155. [[Cited on page 161.](#)]
- [234] CMS Collaboration, V. Khachatryan *et al.*, “Event generator tunes obtained from underlying event and multiparton scattering measurements”, *Eur. Phys. J. C* **76** (2016), no. 3, 155, arXiv:1512.00815. [[Cited on page 161.](#)]
- [235] I. P. Lokhtin and A. M. Snigirev, “A Model of jet quenching in ultrarelativistic heavy ion collisions and high-p(T) hadron spectra at RHIC”, *Eur. Phys. J. C* **45** (2006) 211, arXiv:hep-ph/0506189. [[Cited on page 161.](#)]
- [236] CMS Collaboration, “Centrality and Event Plane reconstruction for PbPb collisions at 5 TeV in 2015”, Tech. Rep. CMS-HIN-AN-15-080, CERN, Geneva, 2015. [[Cited on pages 165, 166, 251, and 262.](#)]
- [237] T. Speer, K. Prokofiev, R. Fruhwirth, W. Waltenberger, and P. Vanlaer, “Vertex fitting in the CMS tracker”, 2006. [[Cited on page 170.](#)]
- [238] R. Fruhwirth, W. Waltenberger, and P. Vanlaer, “Adaptive vertex fitting”, *J. Phys. G* **34** (2007) 343. [[Cited on page 170.](#)]
- [239] CMS Collaboration, S. Chatrchyan *et al.*, “Description and performance of track and primary-vertex reconstruction with the CMS tracker”, *JINST* **9** (2014), no. 10, P10009, arXiv:1405.6569. [[Cited on page 170.](#)]
- [240] J. C. Mason and D. C. Handscomb, “Chebyshev Polynomials”, CRC Press, 2002. [[Cited on page 172.](#)]
- [241] M. Pivk and F. R. Le Diberder, “SPlot: A Statistical tool to unfold data distributions”, *Nucl. Instrum. Meth. A* **555** (2005) 356, arXiv:physics/0402083. [[Cited on page 174.](#)]
- [242] CMS Collaboration, “Muon performance studies in 2015 5.02TeV pp and PbPb Data”, Tech. Rep. CMS-HIN-AN-16-048, CERN, Geneva, 2016. [[Cited on pages 189, 190, and 263.](#)]
- [243] K. S. Cranmer, “Kernel estimation in high-energy physics”, *Comput. Phys. Commun.* **136** (2001) 198, arXiv:hep-ex/0011057. [[Cited on page 197.](#)]
- [244] CMS Collaboration, V. Khachatryan *et al.*, “Suppression and azimuthal anisotropy of prompt and nonprompt J/ψ production in PbPb collisions at

BIBLIOGRAPHY

- $\sqrt{s_{\text{NN}}} = 2.76 \text{ TeV}$ ", *Eur. Phys. J. C* **77** (2017), no. 4, 252, arXiv:1610.00613.
[Cited on pages 201, 207, 209, 264, and 265.]
- [245] CMS Collaboration, "CMS Luminosity Calibration for the pp Reference Run at $\sqrt{s} = 5.02 \text{ TeV}$ ", Tech. Rep. CMS-PAS-LUM-16-001, CERN, Geneva, 2016. [Cited on page 205.]
- [246] X. Du and R. Rapp, " $\psi(2S)$ Production at the LHC", in "Proceedings, 16th International Conference on Strangeness in Quark Matter (SQM 2016): Berkeley, California, United States", vol. 779, p. 012042. 2017. arXiv:1609.04868. [Cited on page 211.]

LIST OF TABLES

1.1 Basic properties of quarks, leptons and bosons from the SM. The table includes the mass, electric charge, spin and type of interactions of each particle. The values are taken from Ref. [19].	6
2.1 LHC beam parameters during the highest luminosity physics fills. The luminosity values are averages for CMS. Information extracted from Ref. [93].	42
3.1 Experimental values of the mass, width and branching fractions of weak bosons extracted from the PDG [19].	71
3.2 Summary of the information of EPS09, EPPS16 and nCTEQ15 nuclear PDFs.	81
3.3 Simulated NLO samples used for the W-boson measurement in p-Pb at 8.16 TeV. The listed cross sections are the POWHEG NLO cross sections scaled by $A_{\text{Pb}} = 208$, except for the $t\bar{t}$ production cross section which is taken from the CMS measurement in p-Pb at 8.16 TeV [181].	88
3.4 Relative difference between the corrected and simulated signal efficiencies as a function of the generated muon η_{CM} , separated in negative and positive charged muons.	114
3.5 QCD background parameters extrapolated to $I^\mu = 0.03$. The results are presented for positive and negative charged muons in the η_{CM}^μ -inclusive range.	118
3.6 Event yields of $W^- \rightarrow \mu^- \bar{\nu}_\mu$ and background processes, extracted from the fits to the p_T^{miss} distribution in each muon η_{CM}^μ region. All analysis selection criteria are applied including the muon $p_T > 25$ GeV/c. All uncertainties shown are statistical only.	122
3.7 Event yields of $W^+ \rightarrow \mu^+ \nu_\mu$ and background processes, extracted from the fits to the p_T^{miss} distribution in each muon η_{CM}^μ region. All analysis selection criteria are applied including the muon $p_T > 25$ GeV/c. All uncertainties shown are statistical only.	123

3.8 Corrected event yields of $W^- \rightarrow \mu^- \bar{\nu}_\mu$, given for each muon η_{CM}^μ bin. All analysis selection criteria are applied including the muon $p_T > 25$ GeV/c. The muon efficiency has been corrected by applying the tag-and-probe corrections, HF energy weights and vector boson p_T weights, event by event. All uncertainties shown are statistical only.	124
3.9 Corrected event yields of $W^+ \rightarrow \mu^+ \nu_\mu$, given for each muon η_{CM}^μ . All analysis selection criteria are applied including the muon $p_T > 25$ GeV/c. The muon efficiency has been corrected by applying the tag-and-probe corrections, HF energy weights and vector boson p_T weights, event by event. All uncertainties shown are statistical only.	125
3.10 The RMS of the set of QCD background parameters extrapolated along all η_{CM}^μ regions.	129
3.11 QCD shape parameters extrapolated to the average muon isolation point $iso = 0.08$	129
3.12 Maximum uncertainty of the measured observables determined for each category. The uncertainties of the $W \rightarrow \mu \nu_\mu$ differential cross sections are relative while for the forward-backward ratios and muon charge asymmetry are absolute.	134
3.13 Results of the χ^2 statistical test between the measurements and the theory calculations from the CT14 PDF, CT14+EPPS16 nPDF and CT14+nCTEQ15 nPDF models. The value of the χ^2 , the number of degrees of freedom (ndf) and the χ^2 probability (Prob.), are presented for the $W^\pm \rightarrow \mu^\pm \nu_\mu$ differential cross sections, the muon charge asymmetry, the $W^\pm \rightarrow \mu^\pm \nu_\mu$ forward-backward ratios, and the charge-summed forward-backward ratio, respectively.	142
4.1 The width and mass of charmonium states below the $D\bar{D}$ -meson pair mass. Information taken from Ref. [19].	146
4.2 Branching ratios for decays of J/ψ and $\psi(2S)$ mesons. Information taken from Ref. [19].	147
4.3 Branching ratios for inclusive charmonium decays of b-hadron mixtures ($B^\pm/B^0/B_s^0/b$ -baryon) determined from measurements at LHC, LEP, Tevatron and SppS. Information taken from Ref. [19].	152
4.4 Fragmentation fractions of bottom quarks into b hadrons measured at Tevatron in $p\bar{p}$ collisions at $\sqrt{s} = 1.96$ TeV and at LEP in $Z \rightarrow b\bar{b}$ decays. Information taken from Ref. [19].	152

4.5 Binding energy and radius of J/ψ , $\chi_c(1P)$ and $\psi(2S)$ mesons. Information taken from Ref. [194].	157
4.6 Total integrated luminosity of each dataset used in the analysis of the charmonium nuclear modification in p-p and Pb-Pb collisions at $\sqrt{s_{\text{NN}}} = 5.02 \text{ TeV}$	161
4.7 Simulations used in the analysis of the charmonium production in Pb-Pb and p-p collisions at 5.02 TeV.	162
4.8 Values of the centrality-integrated number of participants $\langle N_{\text{part}} \rangle$ and nuclear overlap factor $\langle T_{\text{AA}} \rangle$, determined in the different collision centrality ranges used in the analysis. Information taken from the private Ref. [236].	166
4.9 Parameters extracted from the prompt J/ψ -meson simulation and used to constrain the double Crystal Ball functions in each differential and integrated rapidity region. The parameters fixed to simulation in both Pb-Pb and p-p data fits are shown in bold blue colour, while those fixed to simulation only on Pb-Pb data are displayed in bold red colour. The $f_{J/\psi}$ values from simulation are only used to initialise them in the data fits.	172
4.10 Results of the LLR test used to determine the order of the Chebyshev function for the background $\mu^+ \mu^-$ invariant mass fitted in Pb-Pb data within $0.6 < y^{\mu\mu} < 1.2$ and $9.5 \leq p_T^{\mu\mu} < 11 \text{ GeV}/c$. The LLR test results of which the χ^2 probability determined for two consecutive orders ($M = N + 1$ and $M = N + 2$) are higher than 5% are highlighted in bold.	173
4.11 Parameters extracted for the double Crystal Ball function from the prompt J/ψ -meson p-p simulation after applying the $\ell_{J/\psi}$ selection. The values shown correspond to the p_T -centrality integrated fits. The CB parameters fixed to simulation when performing the data fits are shown in bold font.	184
4.12 Relative width used in the Gaussian penalty functions for the tail parameters $\alpha_{J/\psi}$ and n , and the ratio of CB widths. The Gaussian width is shown relative to the nominal parameter value.	194
B.1 Summary of the bin boundaries used in the J/ψ -meson R_{AA} analysis as a function of centrality for different rapidity regions.	220
B.2 Summary of the bin boundaries used in the J/ψ -meson R_{AA} analysis as a function of p_T for different rapidity regions.	221
B.3 Summary of the bin boundaries used in the J/ψ -meson R_{AA} analysis as a function of p_T for different centrality intervals.	222
B.4 Summary of the bin boundaries used in the $\psi(2S)$ -to- J/ψ double ratio analysis.	223

LIST OF FIGURES

1.1 Feynman diagrams of the QCD vertices for quark-gluon coupling (left), triple-gluon self-coupling (middle) and quadri-gluon self-coupling (right).	7
1.2 Feynman diagrams of 1-loop contributions to pQCD.	8
1.3 Summary of measurements of α_s as a function of the energy scale Q . Figure taken from the PDG [19]	9
1.4 Sketch of the gluon string breaking between a quark Q and an anti-quark \bar{Q} due to $q\bar{q}$ pair creation. Figure taken from Ref. [31].	10
1.5 Feynman diagram of deep inelastic scattering of electrons against protons. .	12
1.6 Next-to-leading order QCD fits to the to the ZEUS F_2 structure function data from 1996, 1997 and proton fixed-target at HERA. The error bands of the fit represent the total experimental uncertainty from both correlated and uncorrelated sources. Figure taken from Ref. [37].	13
1.7 Feynman diagram of the Drell-Yan process.	13
1.8 Sketch of the QCD phase diagram for nuclear matter. The solid lines show the phase boundaries and the solid circle represents the critical point. Figure taken from Ref. [39].	15
1.9 Illustration of two nucleus with impact parameter b before (left) and after (right) colliding. Figure taken from Ref. [39].	18
1.10 Schematic representation of the optical Glauber model geometry.	19
1.11 Sketch of the evolution of a relativistic heavy-ion collision.	20
1.12 Sketch of the elliptic flow produced in non-central heavy-ion collisions. Figure taken from Ref. [54].	22
1.13 Elliptic flow distribution of as a function of transverse momentum for π^\pm mesons, K_s^0 mesons, antiprotons and Λ baryons measured by STAR collaboration in Au-Au collisions at $\sqrt{s_{NN}} = 200$ GeV. The results are compared with relativistic hydrodynamic calculations. Figure taken from Ref. [58].	24

1.14 3D display of the $\Delta\eta$ - $\Delta\phi$ correlation function between two charged particles with $1 \text{ GeV}/c < p_T < 3 \text{ GeV}/c$, measured by the CMS collaboration in high multiplicity ($N \geq 110$) p-p collisions at $\sqrt{s} = 7 \text{ TeV}$. Figure taken from Ref. [59].	25
1.15 Left: Distribution of the yield of inclusive protons and strange baryons, measured by the STAR collaboration in Au-Au collisions at $\sqrt{s_{\text{NN}}} = 200 \text{ GeV}$ (solid symbols) and by the NA57 collaboration in Pb-Pb collisions at $\sqrt{s_{\text{NN}}} = 17.3 \text{ GeV}$ (empty symbols), relative to the corresponding yield in p-p (at RHIC) or p-Be (at SPS) collisions scaled by N_{part} . Figure from Ref. [65]. Right: Distribution of the p_T -integrated yield ratios of strange hadrons to pions as a function of the average charged-particle multiplicity measured in $ \eta < 0.5$ by the ALICE collaboration in p-p, p-Pb and Pb-Pb collisions at $\sqrt{s} = 7 \text{ TeV}$, $\sqrt{s_{\text{NN}}} = 5.02 \text{ TeV}$ and $\sqrt{s_{\text{NN}}} = 2.56 \text{ TeV}$, respectively. Figure from Ref. [66].	26
1.16 Sketch of the production mechanism of two jets in proton-proton (top) and heavy-ions (bottom) collisions. Figure taken from Ref. [69].	27
1.17 Distribution of the nuclear modification factor R_{AA} of direct photons, pions, η mesons and charged hadrons, measured at RHIC in central Au-Au collisions at $\sqrt{s_{\text{NN}}} = 200 \text{ GeV}$. Theoretical predictions of radiative parton energy loss are also included. Figure taken from Ref. [71].	29
1.18 Dijet asymmetry measured by the ATLAS collaboration in lead-lead collisions at $\sqrt{s_{\text{NN}}} = 2.76 \text{ TeV}$ (points) and proton-proton collisions at $\sqrt{s} = 7 \text{ TeV}$ (open circles). The top panel shows the dijet asymmetry distributions and unquenched HIJING with superimposed PYTHIA dijets (solid yellow histograms), as a function of collision centrality. The bottom panel shows the distribution of the azimuthal angle between the two jets $\Delta\phi$, for data and HIJING+PYTHIA, also as a function of centrality. Figure taken from Ref. [72].	30
1.19 Dimuon invariant mass distribution measured by the CMS collaboration in Pb-Pb collisions at $\sqrt{s_{\text{NN}}} = 5.02 \text{ TeV}$. The total fit (solid blue line), the background component (dot-dashed blue line) and the individual $\Upsilon(1S)$, $\Upsilon(2S)$ and $\Upsilon(3S)$ mass peaks (dotted gray lines) are shown. The dashed red line represents the p-p signal shapes added on top of the Pb-Pb background and normalised to the $\Upsilon(1S)$ mass peak in Pb-Pb. Figure taken from Ref. [76].	31

1.20 Nuclear modification factor of J/ψ meson as a function of transverse momentum measured by the ALICE collaboration in the 0% – 20% most central Pb-Pb collisions at $\sqrt{s_{\text{NN}}} = 2.76$ TeV compared to results from the PHENIX collaboration measured in the 0% – 20% most central Au-Au collisions at $\sqrt{s_{\text{NN}}} = 200$ GeV. Figure taken from Ref. [84].	33
1.21 Nuclear modification factor R_{AA} of $Z \rightarrow e^+e^-$ (blue squares) and $Z \rightarrow \mu^+\mu^-$ (red circles) events as a function of N_{part} measured by the CMS collaboration in Pb-Pb collisions at $\sqrt{s_{\text{NN}}} = 2.56$ TeV. The open points represent the centrality-integrated R_{AA} and the vertical lines (boxes) correspond to statistical (systematic) uncertainties. Figure taken from Ref. [85].	34
2.1 Schematic diagram of the LHC injection chain for protons and Pb nuclei. The proton and Pb ion trajectories are indicated with red and blue arrows, accordingly. The location of each LHC detector is also included.	36
2.2 Schematic diagram of the LHC layout. Figure taken from Ref. [86].	38
2.3 Integrated nucleon-pair luminosity delivered by the LHC to each experiment during Pb-Pb collisions at $\sqrt{s_{\text{NN}}} = 5.02$ TeV. The integrated luminosity of p-Pb collisions at $\sqrt{s_{\text{NN}}} = 5.02$ TeV and Pb-Pb collisions at $\sqrt{s_{\text{NN}}} = 2.76$ TeV are included for comparison. Figure taken from Ref. [91].	41
2.4 Integrated proton-nucleus luminosity delivered by the LHC to each experiment during p-Pb collisions at $\sqrt{s_{\text{NN}}} = 8.16$ TeV (solid lines). The integrated luminosity of p-Pb collisions at $\sqrt{s_{\text{NN}}} = 5.02$ TeV (dashed lines) is included for comparison. Figure taken from Ref. [92].	42
2.5 Cutaway view of the CMS detector in its configuration used during 2015 and 2016. Labels and basic details of each subdetector are included. [94]	43
2.6 Schematic diagram of the coordinate system used in the CMS experiment. . .	44
2.7 View of the CMS tracker in the r - z plane. Each line represents a detector module. Figure taken from Ref. [89].	46
2.8 Schematic layout [89] (left) of the CMS electromagnetic calorimeter, and its corresponding one-quarter geometric view [98] (right).	47
2.9 Geometric view of one quarter of the CMS detector, displaying the subdetectors of the hadron calorimeter: HB, HE, HF and HO. Figure taken from Ref. [96].	49
2.10 Geometric view of one quadrant the CMS detector in the r - z plane. Each chamber of the muon system is shown in blue (RPC), green (CSC) and orange (DT). Figure taken from Ref. [99].	51

2.11 Schematic layout of a DT cell (left) and a DT chamber (right). Figures taken from [100].	52
2.12 Schematic layout of a CSC. Figure taken from [89].	53
2.13 Cross section view (left) [101] and exploded view (right) [102] of a RPC module.	53
2.14 Diagram of the legacy L1 trigger of CMS. Figure taken from Ref. [104].	55
2.15 Diagram of the CMS L1 trigger used in 2016.	57
2.16 Cross section view of the CMS detector showing how particles interact in the CMS. The different types of muon tracks are indicated by boxes. Figure taken from Ref. [110].	61
3.1 Feynman diagram of the decay modes of W^+ (left), W^- (middle) and Z (right) bosons to fermions.	71
3.2 Leading order Feynman diagram of W boson production to final state leptons, from a collision between an incoming proton (p) and a bound nucleon (a) in a Pb nucleus.	72
3.3 Next-to-leading order Feynman diagrams of W boson partonic production to final state leptons.	73
3.4 Schematic diagram of the production of W^- (left) and W^+ (right) bosons to muonic decays. The black arrows represent the particle direction of motion whereas the blue arrows correspond to its spin. The spin of the W^\pm boson points in the direction of the anti-quark.	74
3.5 Results of the CT14 proton PDFs at NNLO derived at $Q = 10\text{ GeV}$ (left) and $Q = 10\text{ GeV}$ (right). Figure taken from Ref. [150].	75
3.6 Illustration of the different nuclear PDF effects. Figure taken from Ref. [153].	76
3.7 Results of the EPPS16 nuclear correction factor R^A for Pb ions at $Q^2 = 10\text{ GeV}^2$. The black curve represents the central fit while the blue bands shows the total uncertainty of the PDF fit. The results are compared against a baseline made by performing the EPPS16 fits on the same datasets used for EPS09. Figure taken from Ref. [158].	79
3.8 Results of the nCTEQ15 full nuclear PDFs for Pb ions f^{Pb} at $Q = 10\text{ GeV}$. Figure taken from Ref. [159].	80
3.9 Comparison between the EPPS16 (black curve with blue band) and the nCTEQ15 (red curves with hatching) nuclear modifications performed at $Q^2 = 10\text{ GeV}^2$. Figure taken from Ref. [158].	81

3.10 Distribution of the production cross section for $Z \rightarrow \mu^+ \mu^-$ measured as a function of the Z-boson rapidity measured in the centre-of-mass frame. Figure taken from Ref. [165].	82
3.11 Distribution of the production cross section for $W^- \rightarrow \mu^- \bar{\nu}_\mu$ (left) and $W^+ \rightarrow \mu^+ \nu_\mu$ (right) measured as a function of the muon rapidity in the centre-of-mass frame. Figure taken from Ref. [166].	83
3.12 Distribution of the production cross section for $W^- \rightarrow \ell^- \bar{\nu}_\ell$ (left) and $W^+ \rightarrow \ell^+ \nu_\ell$ (middle), and the lepton charge asymmetry (right) measured as a function of the lepton pseudorapidity in the laboratory frame. The CT10 PDF calculations with EPS09 (green line) and without (red line) nuclear PDF corrections are included. The bottom panels present the ratio of the CT10+EPS09 (green line) and data (black points) normalised to the CT10 baseline. Figure taken from Ref. [167].	84
3.13 Survival probability of single muons from a $Z/\gamma^* \rightarrow \mu^+ \mu^-$ ($M > 30$ GeV/c 2) simulation, as a function of the muon η_{CM}^μ and p_T^μ , separated in negative (left) and positive (right) charged muons. Muons are required to have $p_T > 25$ GeV/c and $ \eta < 2.4$, match the trigger and pass the isolation and identification criteria.	91
3.14 Flowchart illustrating the way the events are classified	92
3.15 Muon p_T distribution extracted from the W-boson enhanced sample before (left) and after (right) applying the boson p_T weights. The red points correspond to data, while the blue and red filled areas correspond to events from the $W \rightarrow \mu \nu_\mu$ and $Z/\gamma^* \rightarrow \mu^+ \mu^-$ simulations, respectively. The bottom panels shows the ratio of data over simulation.	94
3.16 Distribution of the number of tracks per event (left) and the total energy deposited in the HF calorimeter (right) in $Z \rightarrow \mu^+ \mu^-$ events. The red points and filled area correspond to data and $Z/\gamma^* \rightarrow \mu^+ \mu^-$ simulation, respectively.	96
3.17 Comparison of the p_T^{miss} distribution in data and simulation for $Z \rightarrow \mu^+ \mu^-$ events before (left) and after (right) applying the HF energy weights.	96
3.18 Distribution of the p_T^{miss} in data and simulation for $Z \rightarrow \mu^+ \mu^-$ selected events.	97
3.19 Definition and components of the recoil \vec{u}_T for $Z \rightarrow \mu^+ \mu^-$ events.	98
3.20 Distributions of the $u_{ }$ (top) and u_{\perp} (bottom) recoil components in data (left) and simulation (right). The fit function is based on a weighted sum of two Gaussian distributions as defined in Eq. (3.32). The plots correspond to the q_T^Z bin [3, 4] GeV/c.	99

3.21	Fits of the profile of $-\mu_{\parallel}$ as a function of q_T^Z . The results are derived from $Z \rightarrow \mu^+ \mu^-$ events in data (left) and simulation (right). The yellow band represents the 68% error band of the fit.	100
3.22	Fits of the profile of μ_{\perp} as a function of q_T^Z . The results are derived from $Z \rightarrow \mu^+ \mu^-$ events in data (left) and simulation (right). The yellow band represents the 68% error band of the fit.	101
3.23	Fits to the profile of the $\sigma_{\parallel,1}$ (left), $\sigma_{\parallel,2}$ (middle) and weighed average σ_{\parallel} (right) values of the parallel recoil component as a function of q_T^Z . The results are derived from $Z \rightarrow \mu^+ \mu^-$ events in data (top) and simulation (bottom).	102
3.24	Fits for the $\sigma_{\perp,1}$ (left), $\sigma_{\perp,2}$ (middle) and weighed average σ_{\perp} (right) values of the recoil perpendicular component as a function of q_T . The results are derived from $Z \rightarrow \mu^+ \mu^-$ events in data (top) and simulation (bottom).	103
3.25	A comparison of the p_T^{miss} distribution from $Z \rightarrow \mu^+ \mu^-$ events between data and simulation, before (left) and after (right) calibrating the simulated recoil. The distributions of the simulated HF energy and generated Z-boson p_T have been weighed.	105
3.26	Comparison of the p_T^{miss} distribution in data and simulation for positive-charged muons in the η_{CM}^{μ} -inclusive signal region. The results are shown before (top-left) and after (top-right) applying the recoil calibrations using the nominal scaling method. The result using the alternative smearing method (bottom) is also presented. The distributions of the simulated HF energy and generated Z-boson p_T have been weighed.	106
3.27	Comparison of the signal efficiency derived from the pPb and Pbp $W \rightarrow \mu\nu_{\mu}$ simulations as a function of the generated muon η_{lab} , separated in negative (left) and positive (right) charged muons. The distributions of the simulated HF energy and generated W-boson p_T have been weighed. The bottom panel shows the ratio of Pbp over pPb signal efficiencies.	107
3.28	Simulated signal efficiency derived from the $W \rightarrow \mu\nu_{\mu}$ NLO simulations as a function of the generated muon η_{CM} , separated in negative (left) and positive (right) charged muons. The distributions of the simulated HF energy and generated W-boson p_T have been weighed.	108
3.29	Fits to the tag-probe invariant mass distribution for passing (left) and failing (right) probes, used to measure the STA reconstruction efficiency. The results correspond to the probe kinematic region: $ \eta_{\text{lab}} < 2.4$ and $50 < p_T < 80$ GeV/c. Figures taken from the private Ref. [183].	110

3.30 Muon identification (left) and isolation (right) efficiencies extracted from data (blue) and simulation (red) using the TnP method, as a function of the probe p_T . The bottom panels show the data-to-simulation efficiency ratio. The results of the fits to the efficiencies are also shown. Figures taken from the private Ref. [183].	111
3.31 Muon trigger efficiency extracted from data (blue) and simulation (red) using the TnP method, as a function of the probe η_{lab} . The bottom panel shows the data-to-simulation efficiency ratio. Figure taken from the private Ref. [183]. . .	111
3.32 Corrected signal efficiency as a function of the generated muon η_{CM} , separated in negative (left) and positive (right) charged muons. The yellow and green boxes represents the uncertainty on the signal efficiency due to the TnP statistics and systematics, respectively.	113
3.33 QCD jet background fits to the p_T^{miss} distribution in a control sample of non-isolated muon events corresponding to the muon isolation bins: $0.4 < I^\mu < 0.5$ (left) and $0.8 < I^\mu < 0.9$ (right). The results are shown for positive (top) and negative (bottom) charged muons separately.	117
3.34 Linear fits to the profile of the QCD background parameters: σ_0 (left), σ_1 (middle) and σ_2 (right), with respect to the muon isolation variable I^μ . The results are shown for negative (top) and positive (bottom) charged muons in the η_{CM}^μ -inclusive range. The red points represents the value obtained by linearly extrapolating to $I^\mu = 0.03$	118
3.35 Muon η_{CM}^μ dependence of σ_0 (left), σ_1 (middle) and σ_2 (right) parameters extrapolated to $I^\mu = 0.03$. The results are shown for negative (top) and positive (bottom) charged muons. The red line corresponds to the QCD jet parameter extrapolated in the η_{CM}^μ -inclusive range.	119
3.36 The p_T^{miss} distribution for $W^- \rightarrow \mu^- \bar{\nu}_\mu$ (left) and $W^+ \rightarrow \mu^+ \nu_\mu$ (right) events within the η_{CM}^μ -inclusive range, shown in linear scale. Unbinned fits to the data (black points) are performed with six contributions, stacked from top to bottom: $W \rightarrow \mu \nu_\mu$ (yellow), QCD jet (light blue), $Z/\gamma^* \rightarrow \mu^+ \mu^-$ (green), $W \rightarrow \tau \nu_\tau$ (red), $Z/\gamma^* \rightarrow \tau \bar{\tau}$ (dark blue) and $t \bar{t}$ (orange). The lower panel, on each figure, display the ratio of the measurements over the result of the fit. The χ^2 test value over the number of degrees of freedom is also shown.	121

3.37 Uncertainty corresponding to each category as function of the muon η_{CM} . The plots are divided as: $W^- \rightarrow \mu^- \bar{\nu}_\mu$ (top-left) and $W^+ \rightarrow \mu^+ \nu_\mu$ (bottom-left) differential cross sections, $W^- \rightarrow \mu^- \bar{\nu}_\mu$ (top-middle) and $W^+ \rightarrow \mu^+ \nu_\mu$ (bottom-middle) forward-backward ratios, and finally the charge-summed forward-backward ratio (top-right) and muon charge asymmetry (bottom-right). The uncertainties of the cross sections are relative while for the forward-backward ratios and muon charge asymmetry are absolute. The global luminosity uncertainty of 3.5% is not included.	135
3.38 Correlation matrices for: W^\pm cross section (top-left), $W^\pm R_{FB}$ (top-right), charge-inclusive R_{FB} (bottom-left), and charge asymmetry (bottom-right). The lines in the top plots are used to separate the different muon charge bins.	137
3.39 Differential production cross sections for $W^+ \rightarrow \mu^+ \nu_\mu$ (left) and $W^- \rightarrow \mu^- \bar{\nu}_\mu$ (right), as a function of the muon pseudorapidity in the center-of-mass frame. The brackets represent the statistical and systematic uncertainties summed in quadrature, while the error bars show the statistical uncertainties only. The global luminosity uncertainty of 3.5% [168] is not shown.	138
3.40 Muon charge asymmetry as a function of the muon pseudorapidity in the center-of-mass frame. The brackets represent the statistical and systematic uncertainties summed in quadrature, while the error bars show the statistical uncertainties only.	138
3.41 Forward-backward ratios, for the positive (top-left), negative (top-right) and all (bottom) charged muons. The brackets represent the statistical and systematic uncertainties summed in quadrature, while the error bars show the statistical uncertainties only.	139
3.42 Differential cross sections for $W^+ \rightarrow \mu^+ \nu_\mu$ (left) and $W^- \rightarrow \mu^- \bar{\nu}_\mu$ (right), as a function of the muon η_{CM}^μ . Errors bars represent the statistical uncertainties, while the brackets represent the statistical and systematic uncertainties summed in quadrature. The global luminosity uncertainty of 3.5% is not displayed. Theoretical predictions with (CT14+EPPS16 shown in dashed green line and CT14+nCTEQ15 shown in dashed brown line) and without (CT14, solid red line) PDF nuclear modifications are also shown, with the uncertainty bands. All theory uncertainty bands include the PDF uncertainties.	141

3.43 Muon charge asymmetry of $W \rightarrow \mu\nu_\mu$, given for each muon η_{CM}^μ range. Errors bars represent the statistical uncertainties, while the brackets represent the statistical and systematic uncertainties summed in quadrature. Theoretical predictions with (CT14+EPPS16 shown in dashed green line and CT14+nCTEQ15 shown in dashed brown line) and without (CT14, solid red line) PDF nuclear modifications are also shown, with the uncertainty bands. All theory uncertainty bands include the PDF uncertainties.	142
3.44 Forward-backward ratio of $W \rightarrow \mu\nu_\mu$, given for each muon η_{CM}^μ range separated in negative (top-left), positive (top-right) and all (bottom) charged muons. Errors bars represent the statistical uncertainties, while the brackets represent the statistical and systematic uncertainties summed in quadrature. Theoretical predictions with (CT14+EPPS16 shown in dashed green line and CT14+nCTEQ15 shown in dashed brown line) and without (CT14, solid red line) PDF nuclear modifications are also shown, with the uncertainty bands. All theory uncertainty bands include the PDF uncertainties.	143
4.1 Illustration of the different charmonium decays to lower mass charmonium states. The dashed (solid) lines represent radiative (hadronic) decays. Figure taken from Ref. [191].	147
4.2 Illustration of a colour-singlet (left) and colour-octet (right) Feynman diagram, at leading order (α_s^3), that contributes to the production of quarkonium states. Diagrams taken from Ref. [207].	151
4.3 Feynman diagram of a B_s^0 decay to J/ψ meson. Diagram taken from Ref. [216].	152
4.4 Gluon nuclear PDF modification factor determined with EPPS16 (black curve with blue band) and nCTEQ15 (red curves with hatching) nPDF calculations at $Q^2 = 10 \text{ GeV}^2$. Figure taken from Ref. [158].	154
4.5 Nuclear modification factor of J/ψ mesons as a function of p_T in the backward (top-left), mid (top-right) and forward (bottom) rapidity regions. The bars (boxes) represent the statistical (systematic) uncertainties, while the gray box at unity indicate the size of the global uncertainty. The results are compared to nPDF (EPS09), energy loss (Arleo et al), and gluon saturation (CGC) calculations. Figure taken from Ref. [223].	156

4.6 Double ratio of $\psi(2S)$ over J/ψ yields as a function of $\langle N_{\text{part}} \rangle$, in the mid-rapidity (blue squares) and forward rapidity (red circles) regions. The results integrated in centrality are shown at the rightmost edge. The bars (boxes) represents the statistical (systematic) uncertainties, while the boxes at unity indicate the uncertainties on the p-p measurements. Figure taken from Ref. [228].	159
4.7 Distribution of the total energy deposited in the HF calorimeters in Pb-Pb collisions at 5.02 TeV, for minimum-bias events passing the GEF selection. The different centrality classes are shown. Figure taken from the private Ref. [236].	165
4.8 Centrality distribution of $\mu^+ \mu^-$ events in Pb-Pb collisions passing the GEF cuts (red), with $2.2 < M_{\mu^+ \mu^-} < 4.5 \text{ GeV}/c^2$, for $ y < 1.6$ (left) and $1.6 < y < 2.4$ (right). The distribution of the minimum-bias sample, flat by definition, is shown in black. The limits of the centrality bins used for the $\psi(2S)$ analysis are shown as vertical dashed lines, with the most central (peripheral) range on the right (left). The average centrality in each centrality range is also shown as an arrow, in red and black for the dimuon and minimum-bias datasets, respectively.	165
4.9 Distribution of the ratio of the number of reconstructed, identified and triggered muons over the number of generated muons, as a function of muon p_T and η . The results are derived from the prompt J/ψ simulations corresponding to p-p (left) and Pb-Pb (right) collisions. The red line represents the single muon kinematic cuts.	168
4.10 Results of the 2D fits performed on Pb-Pb data, projected onto the dimuon invariant mass (left) and pseudoproper-decay length (right) variables.	170
4.11 Results of the fits to the $\mu^+ \mu^-$ invariant mass distribution in Pb-Pb (left) and p-p (right) data. The black line represents the total fit model while the blue filled area represents the fitted background shape.	174
4.12 Distributions of the σ_ℓ for signal (red line), background (blue line) and all (green line) dimuons, extracted from Pb-Pb (left) and p-p (right) data. The dashed lines represents the σ_ℓ range used to extract the template histograms. The bottom panel shows the ratio between the data and the total template histogram extracted using the sPlot technique.	176

4.13 Results of the $\ell_{J/\psi}$ resolution fits for signal dimuons in data. The results are presented as a function of $\ell_{J/\psi}/\sigma_\ell$ and the dashed lines represent the fitted range.	177
4.14 Fits to the $\ell_{J/\psi}$ distribution of generated nonprompt $J/\psi \rightarrow \mu^+ \mu^-$ events in Pb-Pb (left) and p-p (right) simulations. The fitted value for $\lambda_B = \lambda_{DSS}$ is shown.	178
4.15 Fits to the $\ell_{J/\psi}$ distribution of background events in Pb-Pb (left) and p-p (right) collision data.	179
4.16 Distribution of $\ell_{J/\psi}$ (left) in the p-p simulations of prompt and nonprompt J/ψ mesons, and an illustration (right) of the way the $\ell_{J/\psi}$ selection threshold is chosen. The results corresponds to the mid-rapidity region $ y^{\mu\mu} < 1.6$	181
4.17 Profile of the $\ell_{J/\psi}$ selection thresholds (green points) with respect to $p_T^{\mu\mu}$, extracted from the J/ψ simulations in the mid-rapidity (left) and forward rapidity (right) regions. The fitted functions (red lines) are also displayed and the values of their parameters are shown in the box.	182
4.18 Efficiency of passing the $\ell_{J/\psi}$ selection as a function of $p_T^{\mu\mu}$ for prompt J/ψ (black points), prompt $\psi(2S)$ (red points) and nonprompt J/ψ (blue points) mesons. The results are extracted from p-p simulations in the mid-rapidity (left) and forward rapidity (right) regions.	183
4.19 Fits to the $m^{\mu\mu}$ distribution in p-p (left) and Pb-Pb (right) collisions. The results correspond to dimuon events derived in p_T -centrality-inclusive region at mid-rapidity after applying the $\ell_{J/\psi}$ selection. The black line represents the total fit model while the blue filled area represents the fitted background shape.	184
4.20 Definition of the different categories of events considered for the subtraction of nonprompt charmonia.	185
4.21 Data-to-simulation ratios of the prompt J/ψ -meson p_T distribution measured in the $ y^{\mu\mu} < 0.6$ rapidity region, in Pb-Pb (left) and p-p (right) collisions.	187
4.22 Acceptance of prompt J/ψ mesons, estimated from simulations, as a function of $p_T^{\mu\mu}$ (left) and $y^{\mu\mu}$ (right). The error bars represents the statistical uncertainties.	188
4.23 Muon trigger efficiencies as a function of the probe p_T . The efficiencies are extracted, using the TnP method, from data (blue) and simulation (red) in Pb-Pb collisions at $1.8 < \eta^\mu < 2.1$ (left) and p-p collisions at $2.1 < \eta^\mu < 2.4$ (right). The bottom panels show the data-to-simulation efficiency ratio. The results of the fits to the efficiencies are also shown. Figures taken from the private Ref. [242].	190

4.24 Corrected efficiencies of prompt J/ψ mesons measured in p-p collisions, as a function of $p_T^{\mu\mu}$ (left) and rapidity (right) in different rapidity regions. The error bars represent statistical uncertainties.	191
4.25 Corrected efficiencies of prompt J/ψ mesons measured in Pb-Pb collisions, as a function of $p_T^{\mu\mu}$ (left) and centrality (right), in different rapidity regions. The error bars represent statistical uncertainties.	192
4.26 Double ratios of prompt charmonium efficiencies as a function of $p_T^{\mu\mu}$ (top) and centrality (bottom), in the rapidity regions: $ y^{\mu\mu} < 1.6$ (left) and $ y^{\mu\mu} > 1.6$ (right). The error bars represent statistical uncertainties.	193
4.27 Nonprompt fraction of J/ψ mesons measured in p-p and Pb-Pb collisions, as a function of dimuon rapidity (left) and p_T (right). The boxes (bars) represent the systematic (statistical) uncertainties. Figures published in Ref. [231].	203
4.28 Differential cross section of the production of prompt (left) and nonprompt (right) J/ψ mesons decaying into $\mu^+ \mu^-$, as a function of dimuon rapidity (top) and p_T (bottom) in p-p (blue open circles) and Pb-Pb (red squares) collisions. The boxes (bars) represent the systematic (statistical) uncertainties. The global relative uncertainties are written in the plots. Figures published in Ref. [231].	206
4.29 Nuclear modification factor of prompt J/ψ mesons measured at $\sqrt{s_{NN}} = 2.76 \text{ TeV}$ [244] (grey circles) and $\sqrt{s_{NN}} = 5.02 \text{ TeV}$ [231] (red squares), as a function of dimuon p_T (left), rapidity (middle) and $\langle N_{\text{part}} \rangle$ (right). The boxes (bars) represent the systematic (statistical) uncertainties. The size of the global relative uncertainties are depicted in the boxes plotted at $R_{AA} = 1$. Figures published in Ref. [231].	207
4.30 Nuclear modification factor of prompt J/ψ mesons. Left: as a function of $p_T^{\mu\mu}$ in the mid- and most forward rapidity regions. Right: as a function of $\langle N_{\text{part}} \rangle$ at $3 < p_T^{\mu\mu} < 6.5 \text{ GeV}/c$ and $6.5 < p_T^{\mu\mu} < 50 \text{ GeV}/c$, in the $1.8 < y^{\mu\mu} < 2.4$ rapidity region. The boxes (bars) represent the systematic (statistical) uncertainties. The size of the global relative uncertainties are depicted in the boxes plotted at $R_{AA} = 1$. Figures published in Ref. [231].	208

4.31 Nuclear modification factor of nonprompt J/ψ mesons measured at $\sqrt{s_{\text{NN}}} = 2.76 \text{ TeV}$ [244] (grey circles) and $\sqrt{s_{\text{NN}}} = 5.02 \text{ TeV}$ [231] (red squares), as a function of dimuon p_T (left), rapidity (middle) and $\langle N_{\text{part}} \rangle$ (right). The boxes (bars) represent the systematic (statistical) uncertainties. The size of the global relative uncertainties are depicted in the boxes plotted at $R_{\text{AA}} = 1$. Figures published in Ref. [231].	209
4.32 Nuclear modification factor of nonprompt J/ψ mesons. Left: as a function of $p_T^{\mu\mu}$ in the mid- and most forward rapidity regions. Right: as a function of $\langle N_{\text{part}} \rangle$ in two $p_T^{\mu\mu}$ intervals at forward rapidity. The boxes (bars) represent the systematic (statistical) uncertainties. The size of the global relative uncertainties are depicted in the boxes plotted at $R_{\text{AA}} = 1$. Figures published in Ref. [231].	209
4.33 Double ratio of prompt $\psi(2S)$ over J/ψ meson yields as a function of the dimuon p_T , at $ y^{\mu\mu} < 1.6$ (squares) and $1.6 < y^{\mu\mu} < 2.4$ (circles). The horizontal lines denotes the widths of the p_T intervals. The bars (boxes) represent the statistical (systematic) uncertainties, while the arrows indicate the 95% CL interval where the measurement is consistent with zero. Figures published in Ref. [232].	210
4.34 Comparison of the double ratio of prompt $\psi(2S)$ over J/ψ meson yields measured at $\sqrt{s_{\text{NN}}} = 2.76 \text{ TeV}$ [228] and $\sqrt{s_{\text{NN}}} = 5.02 \text{ TeV}$ [232], as a function of the dimuon p_T (left) and Pb-Pb collision centrality (right), at $ y^{\mu\mu} < 1.6$ (squares) and $1.6 < y^{\mu\mu} < 2.4$ (circles). The horizontal lines denotes the widths of the p_T intervals. The bars (boxes) represent the statistical (systematic) uncertainties, while the arrows indicate the 95% CL interval where the measurement is consistent with zero. Figures published in Ref. [232].	211
A.1 The p_T^{miss} distribution for $W^- \rightarrow \mu^- \bar{\nu}_\mu$ events within each fitted η_{CM}^μ range, shown in logarithmic scale. Unbinned fits to the data (black points) are performed with six contributions, stacked from top to bottom: $W^+ \rightarrow \mu^+ \nu_\mu$ (yellow), QCD multijet (light blue), $Z/\gamma^* \rightarrow \mu^+ \mu^-$ (green), $W^+ \rightarrow \bar{\tau} \nu_\tau$ (red), $Z/\gamma^* \rightarrow \tau \bar{\tau}$ (dark blue) and $t\bar{t}$ (orange). Error bars represent statistical uncertainties. The lower panels display the data divided by the result of the fit, for each η_{CM}^μ range. The χ^2 test value over the number of degrees of freedom is also shown.	216

LIST OF FIGURES

FIGURE **Page**

